

Contributions to rebar-to-concrete interaction and its structural implications for design and monitoring applications

Présentée le 22 mars 2024

Faculté de l'environnement naturel, architectural et construit
Laboratoire de construction en béton
Programme doctoral en génie civil et environnement

pour l'obtention du grade de Docteur ès Sciences

par

Enrique CORRES SOJO

Acceptée sur proposition du jury

Prof. C. J. D. Fivet, président du jury
Prof. A. Muttoni, directeur de thèse
Prof. A. Sharma, rapporteur
Prof. J. Cairns, rapporteur
Prof. D. M. Ruggiero, rapporteur

Foreword

Enrique Corres' doctoral thesis was prompted by two observations. Firstly, the possibility of using new techniques (e.g., drones and high-resolution image acquisition) to carry out monitoring on engineering structures and load-bearing structures of buildings will generate a large quantity of images of cracks, which will be very useful for assessing the condition of the structure, its structural safety level and its residual resistance to fatigue. However, this large quantity of images will require a method to systematically check whether the cracks observed, with their kinematics (crack opening and sliding), are problematic or not. Secondly, the possibilities offered by new laboratory measurement techniques (Digital Image Correlation and optical fibres bonded to the reinforcing bars) now make it possible to gain a much better understanding of the phenomenon of bond between reinforcing bars and concrete. This improved understanding has made possible the development of a model describing a bond law that is closer to reality and is more grounded in mechanical considerations. Additionally, this improved model enables the calculation of the stresses in the reinforcing bars (and the stress variations in the case of cyclic actions) as a function of the measured kinematics of the crack in a more reliable manner.

This thesis also makes an interesting contribution to the direct in-situ application of Digital Image Correlation measurements, which until now have been used mainly in the laboratories. The comparison of these in-situ measurements with conventional measurements provides a better understanding of the limits of application and the accuracy of these measurements used in the context of structural monitoring, both in the short and long term.

The results of this thesis can have also a significant influence in the assessment of existing structures and potentially in the design of new ones. For these reasons, the outcome of this research, which was supported by the Swiss Federal Road Administration, has a significant practical relevance.

Lausanne, February 2024

Prof. Aurelio Muttoni

Acknowledgments

I have had the pleasure to spend 4 years at the École Polytechnique Fédérale de Lausanne in the Structural Concrete Laboratory IBETON to write this thesis. During these years I had the chance to carry out this research which involved theoretical and experimental work, as well as inspections and measurements on existing structures. Furthermore, I have also had the incredible chance to be involved in teaching and guiding master students with their thesis, which has been a fantastic experience.

This was possible thanks to the opportunity given to me by Prof. Aurelio Muttoni. His passion for the profession and his knowledge and expertise have certainly been of great help during these years. Our discussions have certainly shaped the final outcome of this journey. For this I would like to express my most sincere gratitude.

I would also like to acknowledge the members of the jury for the interesting discussion and for their comments to improve the quality of the thesis: Prof. John Cairns from Heriot-Watt University, Prof. David Ruggiero from EPFL Prof. Akanshu Sharma from Purdue University and Prof. Corentin Fivet from EPFL.

The financial support provided by the Swiss Federal Roads Office (FEDRO) within the framework of the research project AGB 2019/017 has made possible this research and it is greatly appreciated. I am also grateful for the discussions and practical perspective of the members of the commission of the project.

All the support provided by all the members of the Structural Engineering Platform (GIS) has been a major contribution to the experimental works presented in this thesis. I would like to thank Gilles, Luca, Armin, Frédérique, Francois, Gregory, Jonathan and, in particular, Serge and Gérald with whom I had the pleasure to share more time in the lab. Their help and infallible solutions for all sorts of problems were a key component of the successful experimental campaigns presented in this thesis. Moreover, our technical and philosophical discussions definitely entertained many of the hours I spent in the lab.

I would like to thank all my colleagues from IBETON with whom I have shared these years for the technical discussions but mostly for all other sorts of life-related activities: Diego, Frédéric, Marko, Qianhui and Xhemi. I would like to extend a special thanks to Raffaele for his patience and generosity to teach me all there is to know about fibres, DIC and business markets. And I would also like to thank Francesco, Patrick, Max, Julia, Mads, Daniel, Andri, Xinalin and the EESD team for the nice discussions and exchanges we had.

I would like to express my gratitude to Dr. Olivier Burdet for the informatic support during these years, for the recommendations concerning the experimental works and the comments and feedback on the articles, the thesis and general writing. I would also like to thank Yvonne Buehl-Brauch and Jessica Ritzi for their kindness and support on all the logistics for event organization and administrative tasks.

I would also like to thank Travis Rozich for the technical advice on page layout and formatting of the thesis and Xhensi for his translation of the abstract in Italian.

I have to thank all my friends that have supported me all these years becoming my family in Lausanne. I am particularly thankful to Simon and Giulia for their invaluable company, the cooking tips but mostly for their life advice. Also, I must thank my tireless adventure companion that brought me regularly to mountain therapy Davide. At the same time, the discussions and encouragements to stop being the eternal student from old friends have been a constant source of energy. For this I must thank Pablo, Murillo y Nacho.

Last but not least, I am deeply grateful to my family, whose unconditional love, support and encouragements have accompanied me throughout my life journey until this day. To my brother Pol for his unquestionable trust in me and the infinitude of great moments that we have shared. To my mother Diana for her genetical optimism, the moral support and the medical advice through all these years. To my father Hugo for his contagious passion and eagerness to keep learning and understanding.

Thank you all.

Enrique Corres Sojo

Abstract

Bond between reinforcing bars and concrete has been the focus of extensive research over the last century. This is well-justified as the functioning of reinforced concrete intimately depends on the interaction between rebar and concrete, as for example cracking and the development of anchorage forces. The large number of publications on various aspects of bond highlights its complexity. One reason why it is difficult to study bond-related phenomena is that it is a very local mechanism, whose effects are integrated over larger parts of the structure. This can lead to significantly different results for virtually identical tests. Furthermore, bond depends on a large number of parameters. This is probably why studies often address only a few different aspects of bond. Fortunately, recent improvements in measurement techniques have provided additional tools to gain an unprecedented insight on the interaction between rebar and concrete. This has led to new experimental evidence showing that some of the assumptions of current design codes concerning bond need to be improved.

This thesis presents the results of a comprehensive research programme aimed at improving the understanding of the interaction between rebar and concrete. By combining experimental and theoretical investigations, this research aims to add further mechanical considerations to the characterization of bond and to better connect some of the various aspects of this interaction. For this purpose, conventional measurement systems and state-of-the-art measurements were used in simple tests of isolated bars anchored in concrete blocks (pull-out tests), in reinforced concrete tie tensile tests and in full-scale tests on beams.

To investigate the activation of bond stresses in anchorages, an experimental programme of medium-length pull-out tests was performed to study the influence of several parameters commonly appearing in concrete structures. A reference bond-slip relationship based on pull-out test results was proposed. The theoretical work shows that the activation of local bond stresses along the anchorage length can be explained and quantified by a reduction of that reference relationship, caused by the development of cracks along the bar. The second part of this research aims at improving the accuracy and generality of the bond-slip relationship for various conditions. A particular attention was given to provide a mechanical basis for the proposed expressions whenever possible. Lastly, the pertinence of the proposed bond-slip relationship was verified by applying it to cracked concrete elements. For this purpose, an experimental programme composed of reinforced concrete ties and beams was performed. Further data from tests by other researchers was also used for the validation. The proposed relationship satisfactorily describes the activation of bond stresses in the longitudinal and shear reinforcement of the tested members. The experimental results, however, differ from typically assumed values. Given the potential of these new detailed measurement techniques, their pertinence for monitoring cracks in existing structures was also investigated, showing promising results.

Keywords

Anchorage, bond stress, bond-slip relationship, casting conditions, confinement, cracking, Digital Image Correlation, fibre optical sensors, pull-out, splitting, spalling, reinforced concrete

Résumé

L'adhérence entre les barres d'armature et le béton a fait l'objet de nombreuses recherches au cours du siècle dernier. Cela se justifie par le fait que le fonctionnement du béton armé dépend intimement de l'interaction entre les barres d'armature et le béton, comme par exemple la fissuration ou le développement des forces d'ancrage. Le grand nombre de publications sur les différents aspects de l'adhérence met en évidence sa complexité. L'une des raisons pour lesquelles il est difficile d'étudier les phénomènes liés à l'adhérence est qu'il s'agit d'un mécanisme très local, dont les effets sont intégrés dans de plus grandes parties de la structure. Cela peut conduire à des résultats très différents pour des essais pratiquement identiques. En outre, la liaison dépend d'un grand nombre de paramètres. C'est probablement la raison pour laquelle les études se concentrent souvent sur une partie du phénomène de l'adhérence. Heureusement, les améliorations récentes des techniques de mesure ont fourni des outils supplémentaires permettant d'obtenir des informations sans précédent de l'interaction entre l'armature et le béton. Cela a conduit à des résultats expérimentaux montrant que certaines des hypothèses des normes actuelles concernant l'adhérence doivent être améliorées.

Cette thèse présente les résultats d'un programme de recherche visant à améliorer la compréhension de l'interaction entre les barres d'armature et le béton. En combinant des études expérimentales et théoriques, cette recherche vise à ajouter des considérations mécaniques supplémentaires à la caractérisation de l'adhérence et à mieux relier certains des divers aspects de cette interaction. À cette fin, des systèmes de mesure conventionnels et des systèmes de mesure de pointe ont été utilisés dans des essais simples de barres isolées ancrées dans des blocs de béton (essais d'arrachement), dans des essais de traction sur des tirants en béton armé et dans des essais en taille réelle sur des poutres.

Pour étudier l'activation des contraintes d'adhérence dans les ancrages, un programme expérimental d'essais d'arrachement de longueur moyenne a été réalisé. L'influence de plusieurs paramètres couramment variées dans les structures en béton a été investigué. Une loi locale contrainte d'adhérence – glissement a été proposée sur la base des résultats des essais d'arrachement. L'investigation théorique montre que l'activation des contraintes locales d'adhérence sur la longueur de l'ancrage peut être expliquée et quantifiée par une réduction de cette relation de référence, causée par le développement de fissures le long de la barre. La deuxième partie de cette recherche vise à améliorer la précision et la généralité de la relation adhérence-glissement pour différentes conditions. Une attention particulière a été accordée à la fourniture d'une base mécanique pour les expressions proposées dans la mesure du possible. Enfin, la pertinence de la relation adhérence-glissement proposée a été vérifiée avec des résultats des éléments en béton fissurés. À cette fin, un programme expérimental composé de tirants et de poutres a été réalisé. D'autres données provenant d'essais réalisés par d'autres chercheurs ont également été utilisées pour la validation. La relation proposée décrit de manière satisfaisante l'activation des contraintes d'adhérence dans les armatures longitudinales et d'effort tranchant des éléments testés. Les résultats expérimentaux diffèrent toutefois des valeurs généralement admises. Compte tenu du potentiel de ces nouvelles techniques de mesure détaillées, leur

pertinence pour la surveillance des fissures dans les structures existantes a également été étudiée, avec des résultats prometteurs.

Mots clés

Ancrage, arrachement, béton armé, conditions de bétonnage, confinement, contrainte d'adhérence, corrélation d'images numériques, fibres optiques, fissuration, fissures d'éclatement, fissures de fendage.

Resumen

La adherencia entre las barras de armadura y el hormigón ha sido objeto de numerosas investigaciones a lo largo del último siglo. Esto está bien justificado, ya que el funcionamiento del hormigón armado depende íntimamente de la interacción entre la armadura y el hormigón, como por ejemplo en el caso de la fisuración y la resistencia de anclajes. El gran número de publicaciones sobre diversos aspectos de la adherencia pone de manifiesto su complejidad. Una de las razones por las que resulta difícil estudiar los fenómenos relacionados con la adherencia es que se trata de un mecanismo muy local, cuyos efectos actúan en partes más amplias de la estructura. Esto puede dar lugar a resultados muy diferentes en ensayos prácticamente idénticos. Además, la adherencia depende de un gran número de parámetros. Esta es probablemente la razón por la que los estudios suelen limitarse a ciertos de estos parámetros. Afortunadamente, las recientes mejoras en las técnicas de medición han proporcionado herramientas adicionales para obtener una caracterización sin precedentes de la interacción entre la armadura y el hormigón. Esto ha dado lugar a resultados experimentales que demuestran la necesidad de mejorar algunas de las hipótesis relativas a la adherencia adoptadas en las normas de diseño vigentes.

Esta tesis presenta los resultados de un amplio programa de investigación destinado a mejorar la comprensión de la interacción entre las barras de refuerzo y el hormigón. Mediante la combinación de resultados experimentales y consideraciones teóricas, esta investigación pretende incluir más consideraciones mecánicas en la caracterización de la adherencia e interrelacionar mejor algunos de los diversos aspectos de esta interacción. Para ello, se han utilizado sistemas de medición convencionales y mediciones de última generación en ensayos de extracción directa de barras ancladas en bloques de hormigón, en ensayos de tracción de tirantes de hormigón armado y en ensayos a escala real en vigas.

Para investigar la activación de las tensiones de adherencia en los anclajes, se ha llevado a cabo un programa experimental de ensayos de extracción directa con longitudes de anclaje medias para estudiar la influencia de varios parámetros que se varían habitualmente en las estructuras de hormigón. Se ha propuesto una relación adherencia-deslizamiento de referencia basada en los resultados de los ensayos de extracción. El trabajo teórico muestra que la activación de tensiones de adherencia locales a lo largo de la longitud de anclaje puede explicarse y cuantificarse mediante una reducción de dicha relación de referencia, provocada por el desarrollo de fisuras a lo largo de la barra. La segunda parte de esta investigación tiene por objeto mejorar la precisión y la generalidad de la relación adherencia-deslizamiento para diversas condiciones. En la medida de lo posible, se ha prestado especial atención a proporcionar un fundamento mecánico a las expresiones propuestas. Por último, se ha verificado la pertinencia de la relación adherencia-deslizamiento propuesta aplicándola a elementos de hormigón fisurados. Para ello, se llevó a cabo un programa experimental compuesto por tirantes y vigas de hormigón armado. También se utilizaron para la validación otros datos procedentes de ensayos realizados por otros investigadores. La relación propuesta describe satisfactoriamente la activación de las tensiones de adherencia en la armadura longitudinal y de

cortante de los elementos ensayados. Sin embargo, los resultados experimentales difieren de los valores típicamente asumidos. Dado el potencial de estas nuevas técnicas de medición detallada, también se ha investigado su pertinencia para la monitorización de fisuras en estructuras existentes, mostrando resultados prometedores.

Palabras clave

Anclaje, tensión de adherencia, relación adherencia-deslizamiento, confinamiento, fisuración, condiciones de hormigonado, correlación digital de imágenes, mediciones con fibra óptica, ensayo de extracción directa, hormigón armado.

Riassunto

L'aderenza tra le barre di armatura e il calcestruzzo è stato al centro di numerose ricerche nell'ultimo secolo. Ciò è dovuto al fatto che il funzionamento del calcestruzzo armato dipende essenzialmente dall'interazione tra le barre di armatura e il calcestruzzo, come ad esempio la fessurazione e lo sviluppo delle forze di ancoraggio. Molte delle pubblicazioni sui vari aspetti dell'aderenza ne mettono in evidenza la sua complessità. Uno dei motivi per cui lo studio di questo fenomeno è complesso, è legato al fatto che si tratta di un meccanismo molto locale, i cui effetti sono integrati in parti più ampie della struttura. Questo può portare a risultati significativamente diversi per prove virtualmente identiche. Inoltre, dato che l'aderenza dipende da tanti parametri, molto studi spesso si concentrano solo su alcuni aspetti specifici. Tuttavia, i recenti miglioramenti nelle tecniche di misura danno la possibilità di ottenere una visione senza precedenti dell'interazione tra l'armatura e il calcestruzzo. Con l'utilizzo di tali tecniche, nuove prove sperimentali suggeriscono la necessità di migliorare alcune delle ipotesi delle normative attuali relative all'aderenza.

Questa tesi presenta i risultati di un ampio programma di ricerca volto a migliorare la comprensione dell'interazione tra l'armatura e il calcestruzzo. Combinando indagini sperimentali e teoriche, l'obiettivo di questa ricerca è di aggiungere ulteriori considerazioni meccaniche alla caratterizzazione dell'aderenza e di collegare meglio alcuni dei vari aspetti di questa interazione. A tal fine, sono stati utilizzati sistemi di misura convenzionali e misure avanzate su prove semplici di barre di armatura isolate ancorate in blocchi di calcestruzzo (prove di pull-out), su prove di trazione di tiranti in calcestruzzo armato e su prove in scala reale di travi.

Per studiare l'attivazione delle tensioni di aderenza negli ancoraggi, è stato eseguito un programma sperimentale che include prove di pull-out di media lunghezza per studiare l'influenza di diversi parametri comunemente presenti nelle strutture in calcestruzzo. È stata proposta una relazione di riferimento aderenza-scorrimento basata sui risultati delle prove sperimentali di pull-out. Il lavoro teorico mostra che l'attivazione delle tensioni locali dovute all'aderenza lungo l'ancoraggio può essere spiegata e quantificata da una riduzione di tale relazione di riferimento, la quale è causata dallo sviluppo di fessure lungo la barra. Lo scopo della seconda parte di questa ricerca è quello di migliorare l'accuratezza e la generalizzazione della relazione aderenza-scorrimento per diverse condizioni. Particolare attenzione è stata posta nel fornire, ove possibile, una base meccanica delle espressioni proposte. Infine, la pertinenza della relazione aderenza-scorrimento proposta è stata verificata applicandola a elementi in calcestruzzo armato fessurati. A tal fine, è stato eseguito un programma sperimentale composto da tiranti e travi in calcestruzzo armato. Per la validazione sono stati utilizzati anche dati di prove effettuate in precedenza da altri ricercatori. La relazione proposta descrive in modo soddisfacente l'attivazione delle tensioni di aderenza nelle armature longitudinali e nell'armatura a taglio degli elementi testati. Tuttavia, i risultati sperimentali, differiscono dai valori tipicamente assunti. Dato il potenziale di queste nuove tecniche di misurazione

dettagliata, è stata studiato anche il loro utilizzo per il monitoraggio delle fessure in strutture esistenti, con risultati promettenti.

Parole chiave

Ancoraggio, tensioni di aderenza, relazione aderenza-scorrimento, condizioni di getto, confinamento, fessurazione, correlazione digitale di immagini, sensori a fibre ottiche, pull-out, splitting, spalling, calcestruzzo armato

Contents

Chapter 1: Introduction	1
1.1 Context and motivation	2
1.2 Objectives	6
1.3 Scientific contributions	7
1.4 Structure of the thesis	8
1.5 List of publications	9
Chapter 2: Bond of steel reinforcement based on detailed measurements: results and interpretations	11
2.1 Introduction	13
2.2 Experimental programme	16
2.2.1 Series PC01 and PC02	16
2.2.2 Series CM11	22
2.2.3 Data post-processing	22
2.2.4 Failure modes	22
2.3 Experimental results	23
2.3.1 Shrinkage	23
2.3.2 Anchorage resistance	24
2.3.3 Effect of the concrete cover and casting conditions	24
2.3.4 Rib orientation	31
2.3.5 Bar type and orientation	33
2.4 Result discussion	34
2.4.1 Splitting and spalling crack evolution	34
2.4.2 Local bond-slip relationship	36
2.5 Conclusions	42
Appendix 2A: Pull-out test results	44

Appendix 2B: Experimental database	51
Notation	54
Chapter 3: Local bond-slip model based on mechanical considerations	57
3.1 Introduction	59
3.2 Load bearing mechanism and failure modes	62
3.3 Modelling the initial phase and the confined wedge development	64
3.3.1 Confinement demand	64
3.3.2 Confining capacity ensured by the surrounding concrete in tension	67
3.4 Pull-out failure	68
3.4.1 Local concrete strength	68
3.4.2 Pull-out bond strength	73
3.4.3 Slip at maximum bond stress	74
3.5 Proposed bond-slip relationship	78
3.5.1 General expression for monotonic loading	78
3.5.2 Confinement and proposed parameters	78
3.6 Conclusions	81
Appendix 3A: Examples of bond-slip relationships	82
Appendix 3B: Internal pressure model	83
Appendix 3C: Three-dimensional stress field	86
Appendix 3D: Extended experimental database	89
Notation	91
Chapter 4: Estimation of the bar stress based on transverse crack width measurements in reinforced concrete structures	93
4.1 Introduction	95
4.2 Cracking in structural members	97
4.2.1 Slip-based model	97
4.2.2 Additional experimental evidence	99

4.3	Experimental programme	100
4.3.1	Tension test series TC10	100
4.3.2	Beam test series SM10	102
4.3.3	Beam test series SC70	103
4.3.4	Measurement post-processing	105
4.4	Experimental results and discussion	105
4.4.1	Tensile tests	105
4.4.2	Monotonic beam tests	108
4.4.3	Cyclic beam tests	112
4.5	Improvement of the bond-slip relationship	113
4.6	Comparison of the proposed model with the experimental results	117
4.6.1	Average bond stresses	117
4.6.2	Steel stress estimation based on the crack width	118
4.7	Conclusions	120
	Appendix 4A: Analytical expression development	121
	Appendix 4B: Local bond-slip relationships	123
	Notation	125
	Chapter 5: Image-based techniques for initial and long-term characterization of cracks in reinforced concrete structures	127
5.1	Introduction	129
5.2	Initial crack characterization	132
5.2.1	Objective	132
5.2.2	Description of the technique	132
5.2.3	Validation of the technique	132
5.2.4	Recommendations and limits of applicability	134
5.3	Long-term crack monitoring	135
5.3.1	Objective	135
5.3.2	Description of the technique	135
5.3.3	Measurement uncertainty	137
5.3.4	Validation of the technique	141
5.3.5	Recommendations and limits of applicability	143
5.4	In-situ application	144

5.4.1 Existing crack characterization	144
5.4.2 Short-term measurements with DIC	146
5.4.3 Long-term measurements	147
5.5 Conclusions	149
Appendix 5A: Best-fit uniform dilation	151
Appendix 5B: Best-fit rigid body motion	152
Appendix 5C: Reduction factors α and β	153
Notation	154
Chapter 6: Conclusions and outlook	157
6.1 Conclusions	158
6.2 Outlook and future works	159
Bibliography	163
Curriculum Vitae	187

1

Introduction

This chapter contextualizes the content of this thesis and presents the objectives, the main scientific contributions and the list publications resulting from this research.

1.1 Context and motivation

The interaction between reinforcing bars and the surrounding concrete is a fundamental part of the behaviour of concrete structures. Bond stresses develop at the interface between the bar and the concrete when relative displacements between the two materials occur. This relative displacement is often referred to as slip. The bond stresses enable the transmission of longitudinal forces between the two materials. Therefore, bond stresses are a key component in multiple aspects of the structural response of reinforced concrete structures.

In service conditions, bond influences the response of cracked members. The uncracked response of a concrete section is characterized by the compatibility of deformations between the bars and the concrete. Cracks appear when the tensile strength of the concrete is reached. At the location of the crack, the bar takes the tensile force that was previously distributed between the bar and the concrete. Due to bond stresses, the force in the bar is then progressively transferred back to the concrete between cracks, reducing the steel strains, which causes a stiffer behaviour also called tension stiffening. Some aspects of the ultimate capacity of concrete structures are also strongly influenced by bond including the anchorage strength, which determines the minimum requirements for anchorage length, the lap splice strength, which determines the minimum lap splice length and the rotation capacity of plastic hinges, amongst others.

The extensive research on the different aspects of bond indicates the relevance of the topic and, at the same time, its complexity. Initially, reinforcing bars used as reinforcement had either a circular or a square cross section with a smooth surface (plain bars) [Sys99]. Consequently, the first publications on bond focus on this type of bars. Early in the 20th century, it was established that the bond strength of plain bars results from an adhesive and a frictional component [Mör06, Pre09]. Structures with plain bars relied on bends and hooks to ensure the anchorage of the bars [Mör06]. At that time in the United States ribbed (or deformed) and twisted bars were used in cases where the bond of plain bars was considered insufficient [Mör06, Hoo12, Abr13]. During the 20th century, multiple experimental campaigns were performed to identify the optimum rib geometry [Abr13, Cla49, Haj51, Mar81, Sor79]. Some of the rib patterns documented in the literature are shown in Figure 1.1a. The use of ribbed bars became widespread in Europe in the second half of the 20th century [Cai21]. Nowadays, the use of ribbed or indented bars (Figure 1.1b) is required. The geometry of the ribs or indentations are regulated [Eur04, EN105, SIA24].

The response of the interface is typically characterized by the relationship between the local bond-stresses and the slip. This is typically obtained from tests where a bar embedded in the concrete is pulled out [RIL78, EN105]. By using short bonded lengths, the bond stress (τ_b) can be estimated by assuming that the applied force is distributed uniformly around the perimeter of the bar. The slip (δ_{sc}) is measured as the relative displacement between the unloaded end of the bar and the concrete as schematically shown in Figure 1.1c. The local development of bond stresses results from the interaction of the rib lugs and the concrete as well as the internal cracking of the concrete surrounding the bar.

Several bond-slip relationships can be found in the literature, accounting for various parameters and conditions [Reh61, Noa78, Haw82, Eli83, Shi87, Giu91, CEB93, Far95, Den96, Hua96, Idd99, Lau99, Har04, Bam07, FIB13, Lin19]. Some are shown in Figure 1.1d.

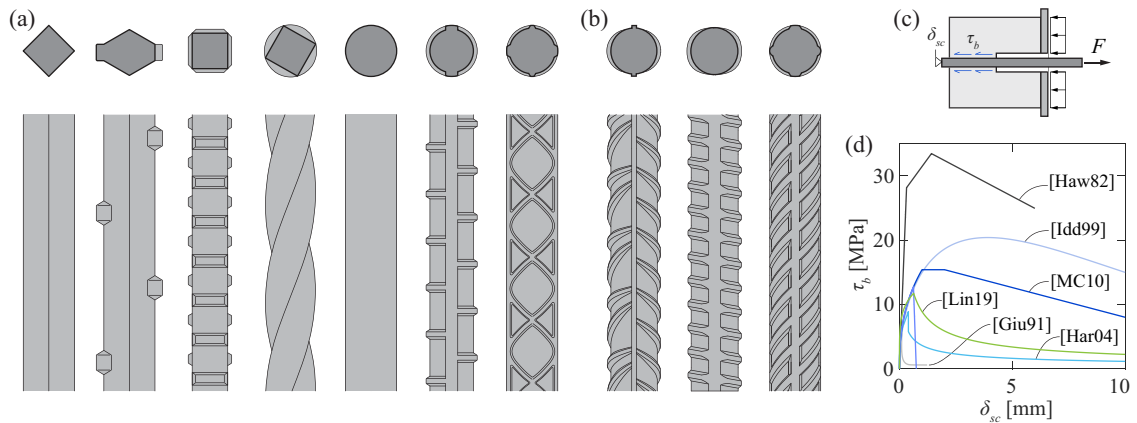


Figure 1.1: Bond of steel reinforcement: (a) examples of early rib geometries [Hoo12, Abr13]; (b) current common rib geometries used in Switzerland; (c) pull-out test; and (d) bond-slip relationships from various authors [Haw82, Idd99, Har04, FIB13, Lin19]

The differences in some of the proposed bond-slip relationships are logical, considering that the interaction is a highly complex and localized phenomenon. For this reason, even in virtually identical tests, considerable variations in the results can be observed. The authors often studied the influence of different parameters which further explains the differences. Furthermore, given the complexity of the bond response, many of the models include empirical factors fitted to the experimental results. Consequently, the proposed relationships might lack generality if they were calibrated on small experimental samples.

For typical bonded lengths in structural members, the slip and bond distributions are far from uniform. In anchorages or lap-splices, the response results from the integration of the local bond stresses along the anchorage length [FIB00, FIB14]. This was measured using bars internally instrumented with strain gauges in the 1950's [Mai51, Dja52]. This technique was used to estimate the local bond-slip relationships at different locations along the bar [Nil72, Shi87].

Similarly, the distribution of bond stresses in cracked zones is not uniform. Due to compatibility conditions, the slip at the point located halfway between the cracks should be close to zero. Consequently, bond stresses are also small in that region. The slip increases towards the crack leading to larger bond stresses. Near the crack, the development of conical cracks originating at the ribs [Got71] prevents the activation of large bond stresses.

Cracking of concrete structures is a topic that has been extensively studied, as it is relevant for their functionality, durability and aesthetics. Van der Esch et al. [Van23] recently published a study categorizing 130 formulations for crack width calculation from 94 publications between 1936 and 2023. Crack formulations aim to predict the crack width as a function of the estimated stresses in the reinforcement. However, they can also be used with the opposite goal: to estimate the steel stress based on the measured crack width. Therefore, the benefits of improving the understanding of bond related mechanisms are twofold.

In crack formulations, bond is often considered as an average constant value. This is pertinent for design purposes, as there is considerable uncertainty in many of the parameters affecting the crack response. For existing structures however, some of these parameters can be obtained through an inspection. In this case, bond becomes one of the main parameters and, therefore, a good estimation of its actual value is essential for an accurate estimation of the stress in the reinforcement.

Cracks are commonly found in the inspection of existing concrete structures and they are often one of the indicators used for structural assessment [DGC12, Zab19, OFR21]. Nevertheless, the evaluation of the safety of a structure based on the presence or absence of cracks is not straightforward. On the one hand, cracks do not necessarily indicate an insufficient level of safety if they are expected based on the structural behaviour and are accounted for in the design. For this reason, crack width formulations and limitations are provided in current design standards [Eur04, FIB13, SIA13]. On the other hand, even small cracks might be a source of concern in structural elements governed by fragile failure modes [Cal18, Zab19, Mon22a].

Considering the long service life of infrastructure and the increase of traffic over the past decades [Cro20] and its expected to grow in the future [Cap13], the needs for monitoring existing structures are likely to increase in coming years. For example, in Switzerland, around 50% of close to 4500 bridges in the national road network will soon reach a service life of 50 years or have already exceeded it [OFR23] (Figure 1.2a). In Germany, that is the case for slightly less than 50% of the 40131 bridges in the national road network [BAS23]. The average age of the 25210 bridges in the national railway system [DB23] is around 72 years [Nar19] (Figure 1.2c). The situation in the United States does not differ substantially. The current count of road bridges included in the National Bridge Inventory amounts to 621851 [USD22]. As it can be observed in Figure 1.2b, around 50% of them have a service life of 50 years or more. Concrete bridges represent 86% of the road bridge population in Germany [BAS23] and 67% in the United States [USD16] (Figure 1.2d).

In recent years, the improvements in detailed measurement techniques such as Digital Image Correlation (DIC) or distributed fibre optical sensors have proven to be useful to understand the rebar-to-concrete interaction in laboratory tests. DIC measurements provide a three-dimensional displacement field over the measured surface. Fibre optical sensors provide strain measurements with high spatial resolutions. Therefore, the combination of these two systems provides highly detailed information about the bar activation and the crack development [Can20, Geh22, Gal22, Lem22]. Recent results using various test set-ups instrumented with conventional [Met14] or detailed measurement techniques [Bad21, Kos22a] have shown discrepancies with one of the commonly used bond-slip relationships [FIB13].

DIC measurements are known to be affected by multiple factors including the relative movements between the camera and the measurement surface, the lighting conditions, or the presence of currents of air between the cameras and the measurement surface. These parameters can be reasonably well controlled under laboratory conditions, and leads to high accuracy measurements in applications of DIC on reinforced concrete elements [Cav15, Can20, Gal22, Mon22a]. When performing similar measurements in situ on existing structures, the measurement conditions can be significantly less favourable, resulting in a lower accuracy.

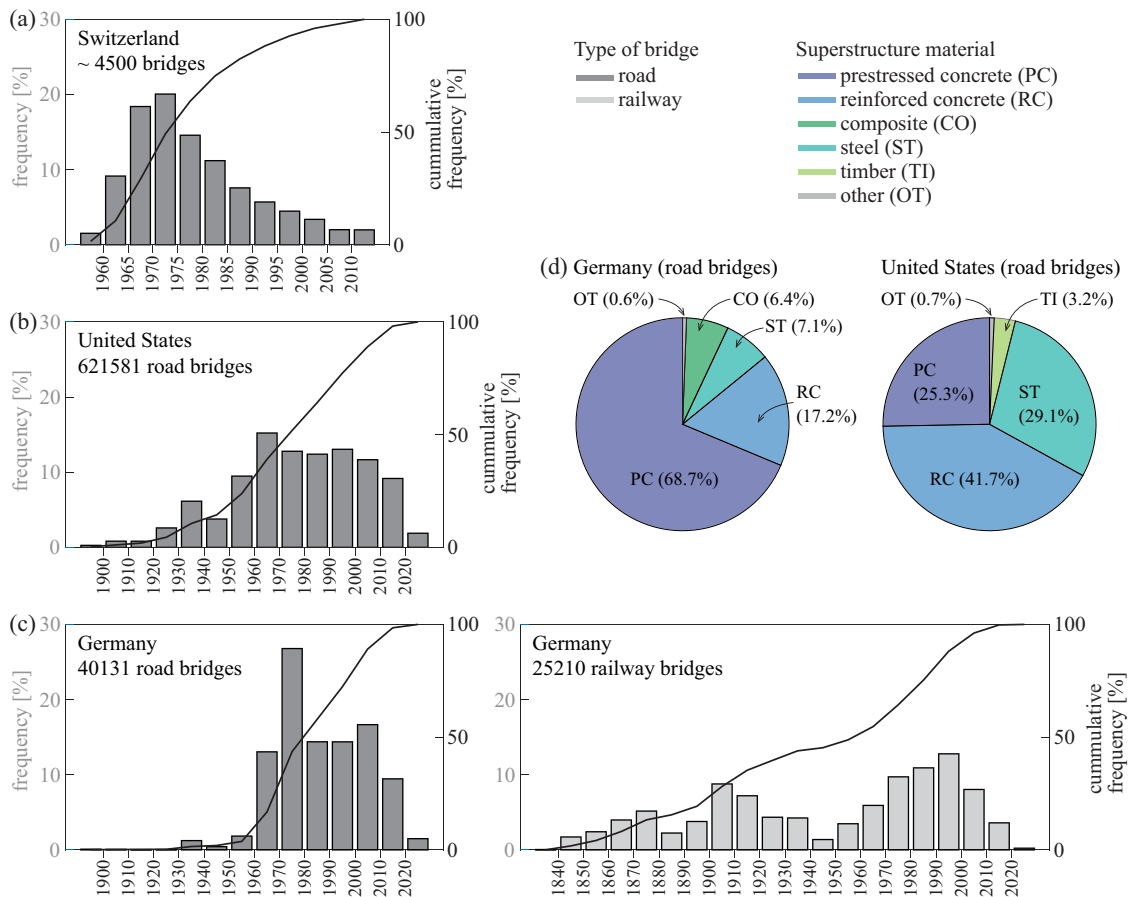


Figure 1.2: Bridge statistics: distribution of bridges as a function of the year of commissioning for (a) road bridges in the national road network in Switzerland [OFR22, OFR23], (b) road bridges in the National Bridge Inventory of the Federal Highway Administration in the United States [USD22], and (c) road bridges [BAS23] and railway bridges [Nar19, DB23] in the national networks in Germany; and (d) distribution of road bridges by superstructure material in Germany [BAS23] and United States [USD16].

Traditional crack measurement systems provide unidirectional information in the direction of the sensor. On the other hand, DIC provides a significant advantage, as the three-dimensional displacement and strain fields allow to detect the crack pattern and crack kinematics (opening and sliding) over large surfaces. Consequently, the use of DIC in existing structures could be useful in cases with complicated crack patterns or where a detailed understanding of the crack kinematics is required. The number of in situ applications of DIC has increased over the past years, showing promising results, but also some limitations of this technique. Fundamentally, cracks that are already present in the reference image cannot be fully characterized. Their evolution can be measured and used to determine the geometry, however, the initial crack kinematics cannot. Furthermore, the assembly and disassembly of the measurement system at each inspection will invariably lead to different relative camera positions in the successive inspections. This

complicates the correlation of images from different inspections, requiring complementary techniques. Furthermore, the limits of application of this technique to measure crack kinematics in-situ are unclear.

In this context, this thesis aims to contribute to the understanding of the bond between steel reinforcement and concrete. As explained in the previous paragraphs, this topic has been extensively studied. However, by making use of state-of-the-art measurements, this thesis presents a detailed investigation of the development of bond in straight bars, contributing to an improvement of the current understanding of the underlying phenomena. The approach adopted includes experimental and theoretical investigations, from pull-out tests to tests on large-scale beams. Moreover, tests to determine the applicability of DIC measurements to existing structures have been performed and complementary techniques have been proposed to overcome some of the limitations.

1.2 Objectives

The main objectives of this research are:

- To contribute to the improvement of the understanding of the interaction between reinforcing bars and concrete and the development of bond stresses in structural members using state-of-the-art measurement techniques.
- To combine the influence of some of the parameters affecting the bond response reported in the literature to increase the generality of bond-slip relationships.
- To do a step forward towards the development of a fully mechanical bond-slip model.
- To clarify the relationship between the development of local bond stresses and the response of longer anchorages.
- To establish a correlation between the observable cracks on inspectable surfaces of concrete specimens and the activation of bond stresses.
- To contribute to the improvement of the understanding of the cracking mechanisms and the development of bond stresses in service conditions.
- To improve the estimation of bond stresses in service conditions, providing coherent values with the bond-slip relationship.
- To test the applicability of DIC measurements in existing structures to characterize crack kinematics.
- To study the use of alternative approaches to overcome the limitations of conventional DIC for the characterization of existing cracks and to perform long-term monitoring of the crack displacements.

1.3 Scientific contributions

The main scientific contributions of this research are:

- An experimental programme of medium length pull-out tests instrumented with detailed measurements to improve the development of bond stresses, including the effect of some parameters that can commonly vary in practice.
- A mechanical model to explain the activated local bond stresses in anchorages with different confinements and casting conditions on the basis of an improved bond-slip relationship for well-confined conditions and the development of spalling and splitting cracks.
- Collection of a database of short pull-out tests in well-confined conditions and good casting position characterized by pull-out failure.
- A local bond-slip relationship for bars in well-confined conditions and good casting position based on mechanical considerations, combining the influence of multiple factors identified in the literature.
- An adaptation of the existing bond-slip relationships in different conditions from the ones mentioned in the previous point, to provide a continuous transition of the effect of the confinement between the different failure modes.
- An experimental programme of 2 reinforced concrete ties and 6 full-scale beam tests instrumented with detailed measurements with different shear reinforcement ratios and types of shear reinforcement, to study the development of cracks and the activation of bond stresses in the flexural and shear reinforcement.
- A proposition of average bond values in service conditions based on the developed bond-slip relationship.
- Validation of the proposed bond values with the results of the aforementioned beam tests and other previous beam tests performed by other authors.
- Comparison of the crack width formulations proposed in current codes and a refined formulation (based on the same principle as the code formulations) for the estimation of the stress in the reinforcement as a function of the measured crack widths.
- An experimental programme in laboratory conditions and in an existing concrete bridge to verify the feasibility of conventional DIC measurements to characterize crack kinematics in-situ and to quantify the influence of different known influencing factors.
- A validation of different available tools to automatically characterize the existing crack geometry and crack kinematics based on digital images from existing concrete structures.

1.4 Structure of the thesis

This thesis includes a general introduction, a compilation of four scientific journal articles and a general conclusion. The thesis is structured in six chapters as described below:

1. Introduction.

This chapter contextualizes the work presented in this thesis and includes the objectives, the main scientific contributions and the list publications resulting from this research.

2. Bond of steel reinforcement based on detailed measurements: results and interpretations.

This chapter presents the results of an experimental programme of medium-length anchorages. This investigation shows that after the correction of the bond-slip relationship in well-confined conditions, the activation of bond stresses along the bonded length can be explained by the development of cracks in the surrounding concrete using the appropriate reduction factor to account for the reduction of the contact surface of the ribs and the concrete.

3. Local bond-slip model based on mechanical considerations.

This chapter presents a local bond-slip relationship for bars in well-confined conditions and good casting conditions based on a thorough review of the literature and some mechanical considerations. The results are validated by comparison against a database of tests from the literature. An adaptation of the current formulations for other confinements is proposed to have a continuous transition between the different failure modes.

4. Estimation of the bar stress based on crack width measurements in reinforced concrete structures.

This chapter presents a study to use crack formulations to estimate the stress in the reinforcement from the crack width measurements. The results of an experimental and theoretical work to study the bond development in structural members is presented. The results from reinforced concrete ties and beams show bond stresses significantly different from the ones assumed in the cracking formulations of current design codes. New values for the average bond stresses for service are proposed using the work presented in the previous chapter and compared with the results of the experimental programme.

5. Image-based techniques to complement digital image correlation for initial and long-term characterization of cracks in reinforced concrete structures.

This chapter studies the use of conventional DIC to characterize the crack geometry and kinematics in existing structures. In order to overcome some of the limitations of this technique, alternative image-based techniques are evaluated to characterize the initial cracks found in the first inspection and to perform long-term monitoring.

6. Conclusion and outlook

This chapter summarizes the general conclusions of this thesis and discusses potential future research.

It is worth mentioning that Chapters 2 to 5 are scientific journal articles. Consequently, each of them has their respective introduction, state-of-the-art of the research in the topic, conclusions, notation and appendixes. A unique bibliography is provided at the end of the thesis.

1.5 List of publications

This research was conducted at the Structural Concrete Laboratory (IBETON) of the Swiss Federal Institute of Technology of Lausanne (EPFL) resulting in the following publications:

- Corres E., Muttoni A. *Long anchorage resistance of reinforcement bars derived from local bond-slip relationships for good and poor bond conditions*, Bond in Concrete 2022, pp. 207-216, Stuttgart, Germany, 2022.
- Corres E., Muttoni A. *Validation of bond models for the crack width estimation based on detailed measurements*, 14th fib International PhD Symposium in Civil Engineering, pp. 138-144, Rome, Italy, 2022.
- Corres E., Muttoni A. *Bond of steel reinforcement based on detailed measurements: Results and interpretations*, Structural Concrete, Vol. 24, No 6, pp. 7173-7204, 2023. (DOI: <https://doi.org/10.1002/suco.202300324>)
- Corres E., Muttoni A. *Local bond-slip model based on mechanical considerations*. [article submitted to Engineering Structures].
- Corres E., Muttoni A. *Estimation of the bar stress based on crack width measurements in reinforced concrete structures*. [article submitted to Structural Concrete].
- Vincens B., Corres E., Muttoni A. *Image-based techniques for initial and long-term characterization of crack kinematics in reinforced concrete structures*. [article submitted to Engineering Structures].

2

Bond of steel reinforcement based on detailed measurements: results and interpretations

This chapter is the post-print version of the article mentioned below, published in Structural Concrete:

Corres E., Muttoni A., Bond of steel reinforcement based on detailed measurements: Results and interpretations, Structural Concrete, Vol.24, No 6, pp. 7173-7204, 2023.

DOI: <https://doi.org/10.1002/suco.202300324>

The work presented in this publication was performed by the author under the supervision of Prof. Aurelio Muttoni who provided constant and valuable feedback, proofreading and revisions of the manuscript. The main contributions of the author to this article and chapter are the following:

- Comprehensive literature review including research and design standards about bond behaviour and its characterization through testing.
- Design, fabrication and testing of 26 pull-out tests with moderate anchorage lengths to investigate the effect of the concrete cover, casting direction, rib geometry and rib orientation.
- Implementation and post-processing of the detailed measurements including Digital Image Correlation and distributed fibre optical sensors.
- Analysis and interpretation of the experimental results.
- Collection of a database of short pull-out tests in well-confined conditions for the characterization of the local bond-slip response for pull-out failure.
- Proposition of an empirical model characterize the main parameters the local bond slip response of anchored bars in well-confined conditions and good casting position.
- Proposition of mechanical factors to explain the local bond slip response of bars in other conditions based on the development of cracks around the bar.
- Redaction of the manuscript of the article, including the production of its figures and tables.

Abstract

Rebar-to-concrete bond is a fundamental aspect of the behaviour of reinforced concrete structures. The characterization of the interface response is challenging due to the complexity of the physical phenomena and the large number of factors affecting it. Locally, the response is characterized by the bond-slip relationship, which is typically obtained experimentally from pull-out tests with short bonded lengths. The behaviour of longer anchorages in structural members differs significantly from short tests as the bond stress distribution is not uniform. In this context, this chapter presents the results of a comprehensive research aiming to establish a better relationship between the local bond-slip response from short pull-out tests and the response of medium-length anchorages. The results of an experimental programme are presented, including the effect of some parameters commonly found in structural applications, such as casting conditions, clear cover, rib geometry and rib orientation. A local bond-slip relationship for well-confined conditions is proposed on the basis of tests carried out by the authors and on the examination of a database on short pull-out tests from the literature. Based on this relationship and some mechanical considerations, the local bond-slip relationship for unconfined conditions can satisfactorily be formulated based on crack-width measurements from the concrete surface. This can be useful for the assessment of existing structures and can be seen as a step forward in the development of a consistent mechanical model for bond.

2.1 Introduction

The transmission of longitudinal forces between straight reinforcement bars and the surrounding concrete is made possible by the bond forces. Consequently, rebar-to-concrete bond is a key parameter in the structural behaviour of reinforced concrete structures at the Serviceability Limit State (SLS) as well as at the Ultimate Limit State (ULS). However, the complexity of the physical phenomena involved in this interaction hinders its characterization.

At a local level, the response is related to the relative displacement between the bar δ_s and the concrete δ_c (slip δ_{sc} , Figures 2.1a and c), which is inherently associated with the interaction of the rib lugs with the concrete and its internal cracking. For this reason, the interface response is typically characterized by the relationship between the slip and the bond stress (τ_b , Figure 2.1d), which is often assumed to be uniformly distributed over the nominal surface of the bar [FIB00]. In structural members, the bond behaviour of the bar is a consequence of the different conditions along the bonded length (Figure 2.1b). In a cracked member, it is sometimes assumed that the midpoint between cracks has no slip, due to compatibility, and that the point at the crack slips by approximately half of the crack width. The reality is more complex, the point between cracks can slip due to the crack sequence and different effects cause a variation of the crack width along the cover [FIB00], as shown in Figure 2.1a. Nevertheless, bond stresses remain relatively small and have a direct influence on the crack width and the so-called tension stiffening (reduction of steel strains due to activation of concrete in tension between two cracks). In an anchorage or in a lap splice, the bond is necessary to transfer the force in the reinforcement to the concrete or to another bar through the concrete. In these cases, the unloaded end of the bar can slip leading to the activation of larger bond stresses, particularly at ULS, as illustrated in Figure 2.1c.

Extensive research on the topic has shown that bond is affected by numerous parameters, including the concrete properties, the bar properties and geometry, the stress-state of both materials, the confinement (provided by the concrete cover, by transverse reinforcement, or by transverse pressure), the relative position of the bar with respect to the casting direction, the type of loading and the test conditions amongst others [FIB00, Lin11]. This complexity is reflected in the broad range of local bond-slip relationships that can be found in literature [Eli83, Shi87, Giu98, Idd99, FIB13].

Current standards account for this complex mechanism and some of the aforementioned parameters in a simplified manner. For instance, in the calculation of the anchorage and lap lengths, a constant bond strength is often assumed as in *fib* Model Code 2010 [FIB13] (MC2010), Eurocode 2 [Eur04] (EC2:2004), or SIA 262:2013 [SIA13]. The drafts for the new generation of standards have opted for another approach, providing the bond length directly on the basis of the steel stress to be activated [Pli22, Eur23, Mut23]. These provisions are based on the expression of *fib* Bulletin 72 [FIB14], where the stress that can be activated in an anchored bar is derived semi-empirically from a statistical study of a large test database. The nonlinearity in the relationship between the steel stress that can be activated and the bond length accounts indirectly for a non-constant distribution of the bond stresses along the bond length. With respect to the crack width formulations at SLS, the code provisions usually consider a rigid-plastic bond-slip relationship where the bond strength is explicitly or implicitly considered in the calculation of the crack spacing and the tension stiffening effect [Eur04, FIB13].

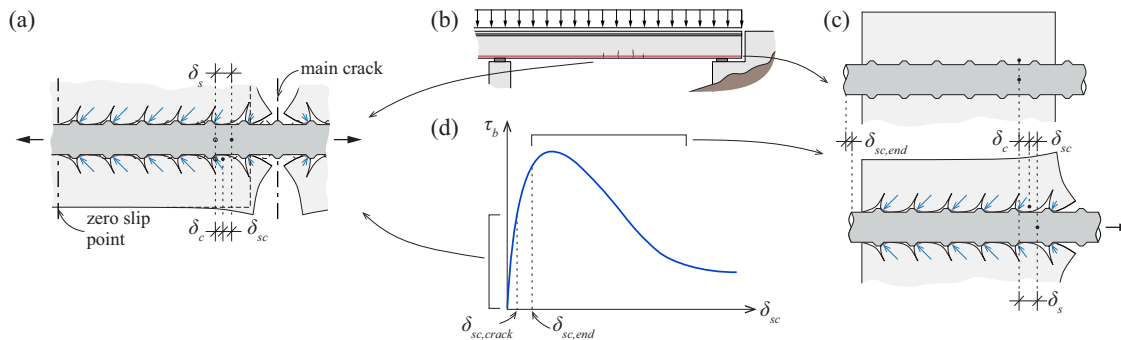


Figure 2.1: Bond in structural members; schematic representation of (a) a cracked region [Got71], (b) a reinforced concrete beam and (c) an end anchorage; and (d) general bond-slip relationship.

MC2010 provides a local bond-slip relationship for ribbed bars subjected to monotonic loading that accounts for the effect of concrete compressive strength, bar diameter, casting conditions (also called bond conditions), concrete cover and confinement. Additional expressions are provided to consider the effect of bar yielding, transverse and longitudinal cracking and other types of loading [FIB13]. The relationship is based on experimental results from pull-out tests in well-confined conditions with short embedment lengths (typically five times the nominal diameter of the bar \varnothing) and a certain unbonded length at the loaded end of the bar to prevent the development of conical cracks [RIL78, Got71]. These relationships are based on the work of Eligehausen et al. [Eli83] and adapted on the basis of the expressions from *fib* Bulletin 72 for low and moderate confinement (so-called splitting failures) [FIB14]. They are applicable to ribbed bars respecting the bond index or relative rib area (f_R) requirements of current standards to ensure a good bond performance (EC2:2004 requires a minimum value of 0.056 for bars with a nominal diameter larger than 12 mm [Eur04]). Metelli et al. [Met14] conducted an experimental programme with 151 pull-out tests to evaluate the effect of the bond index, showing that bars with the minimum bond index can reach higher bond strengths and stiffer responses than the MC2010 relationships. Recent studies using detailed measurement techniques have shown the strain gradients generated in the vicinity of the ribs due to the introduction of the bond forces [Can20], the nonuniform bond stress distribution and its evolution in tests with short bonded lengths between 2 and 5 \varnothing [Kos22, Lem22].

The pertinence of the pull-out test has been questioned, as the stress-state in the materials and the cover may not be representative of structural applications [Cai03]. Another test commonly used for bond research is the beam-end test that provides more flexibility for the concrete cover and bonded length [AST15]. A recent experimental campaign compared the results of pull-out and beam-end tests with a bonded length of 2 \varnothing observing no influence of the test set-up for slip values below 0.1 mm and a 3 to 5% increase of the bond strength for pull-out specimens with comparable confinement [Kos22a]. It must be noted that, being a phenomenon of local nature, the variability observed in experimental results of theoretically identical specimens can be in the range of 1 to 18%, as summarized in Table 2.1.

Table 2.1: Main experimental programme characteristics and coefficient of variation for the maximum bond stress ($\tau_{b,max}$) and its corresponding slip ($\delta_{sc}(\tau_{b,max})$) of identical tests from the literature.

Reference	Test type	Series	Specimens	\emptyset [mm]	l_b/\emptyset [-]	CoV $\tau_{b,max}$	CoV $\delta_{sc}(\tau_{b,max})$
Eligehausen et al. [Eli83]	Pull-out	1.1-1.5	2 or 3	25.4	5	1-12%	2-14%
Tepfers et al. [Tep92]	Ring test	4	5	16	3	7%	23%
Metelli et al. [Met14]	Pull-out	13	7	12	5	15%	
		14	7	20	5	18%	
Moccia et al. [Moc21]	Pull-out	BL5D12-S5	3	12	5	7-10%	8-18%
		BL5D20-S5	3	20	5	2-8%	3-10%

For typical bonded lengths in structural applications, the assumption of a uniform bond distribution is unrealistic. This was experimentally observed already in the 1950's using bars instrumented with strain gauges placed near their axes with various test set-ups [Mai51, Dja52], providing information about the local bond-slip at different positions along the bond length [Nil72, Shi87]. However, the measurement resolution was limited by the minimum spacing between gages.

The improvements in the recent years of fibre optic sensing (FOS) and Digital Image Correlation (DIC) have shown great potential to better understand the bond phenomenon. FOS provides pseudo-continuous strain measurements along the bars with high spatial resolutions and acquisition frequencies. DIC systems allow for detailed measurements of the displacement field over large regions of the specimen's surfaces. Recent works have used this technique to gain better understanding of the local bond-slip relationship and the distribution along bars in different structural members [Can20, Bad21, Lem22].

Several efforts have been done in order to establish a correlation between the local phenomenon and the bond performance in structural members. Balázs [Bal93] proposed a crack width model based on the integration of the local bond-slip relationship proposed in the *fib* Model Code 1990 [CEB93] assumed to be valid over the bar. This model justifies the variation of the average bond strength for different crack widths. Nevertheless, it ignores the effect of proximity to the crack face which leads to lower bond forces due to the development of conical cracks at the rib lugs [Got71]. This effect is often considered by a reduction factor multiplying the local bond stresses with a linear [FIB13] or exponential decrease [Fer07] towards the loaded end of the bar. Furthermore, longitudinal cracking along the bar has been shown to significantly reduce the bond stresses and several models have been proposed to account for this effect [Giu98, Idd99, Gam89, Mah12, Bra16, FIB13].

The approximations with constant bond stress along the bond length are reasonable and practical for many design purposes. Nevertheless, a better understanding of the underlying mechanisms is required to verify the limits of applicability of current expressions, to develop mechanical models

that can more easily be extended to new materials and to refine the design models. This is necessary to build efficient new structures and to better assess the state of existing ones (e.g., for a more refined fatigue verification accounting for the bar-concrete interaction or to estimate the residual resistance of anchorages affected by longitudinal cracks due to corrosion). Furthermore, local bond-slip relationships are used in finite element models. In this context, the aim of the present research is to investigate the bond behaviour in specimens with medium anchorage lengths where conical and longitudinal cracks can develop to establish a better understanding of the effect of visible deteriorations on the concrete surface on the local bond stresses. The influence of some parameters commonly found in structural applications such as concrete cover, casting direction and rib geometry is considered in an experimental programme consisting of 29 pull-out tests instrumented with DIC and FOS. The experimental results show the interaction between the crack development and the local bond stresses that can be activated. On that basis, a local bond-slip model is proposed for well-confined conditions and adjusted based on crack-width measurements to explain the results for low and moderate confinement conditions.

2.2 Experimental programme

An experimental programme was conducted in the Structural Concrete Laboratory of the École Polytechnique Fédérale de Lausanne (Switzerland) to investigate the effect of different parameters on the behaviour of steel reinforcement bars anchored in concrete and the influence of the cracks visible in the surface of the concrete on the local bond-slip relationship. The results of three tests performed by Moccia et al. [Moc21a] (series CM11) are included as well.

2.2.1 Series PC01 and PC02

Specimens

Two series of pull-out tests were conducted using bars with a nominal diameter (\emptyset) of 20 mm: series PC01 with 4 specimens and an anchorage length (l_b) of $10\emptyset$ and series PC02 with 22 specimens and an anchorage length of $15\emptyset$. In all specimens, no deboned length was prepared in the loaded end of the anchorage, with the aim of representing realistic anchorage conditions where conical cracks can develop near the loaded end of the bar. The following parameters were investigated in these series:

- Clear concrete cover c : $1\emptyset \leq c \leq 5\emptyset$.
- Casting position: bars placed horizontally in the formwork were located at the top and bottom position, and bars placed vertically in the formwork were pulled in the same or opposite direction of casting, see Figure 2.2b.
- Rib geometry: three types of bars with ribs composed of two and four lugs were tested.

- Lug orientation: for bars with ribs composed of two lugs, tests were conducted with the lugs oriented parallelly ($//$) or perpendicularly (\perp) to the concrete free surface; the bars with four lugs were placed with the lugs in a 45° disposition with respect to the concrete surface (\times), see Figure 2.2c.

The bars to be tested were embedded in a concrete prism with one dimension corresponding to the anchorage length and the other being 400 mm. The concrete prisms were reinforced in the longitudinal direction with three 18-mm bars to control cracking during the tests as shown in Figure 2.2b. Two reinforcing bars were placed in the region where cracks were expected. One centered bar was placed in the opposite side of the section to prevent unexpected damage to the specimen and to minimise the influence on the development of conical cracks.

The spacing between test bars on the same side of the specimen was 800 mm and their position within opposite sides was shifted by 400 mm. Figure 2.2a shows the geometry of the specimens and the main investigated parameters of the series. Details about the test parameters of each specimen are provided in Table 2.2.

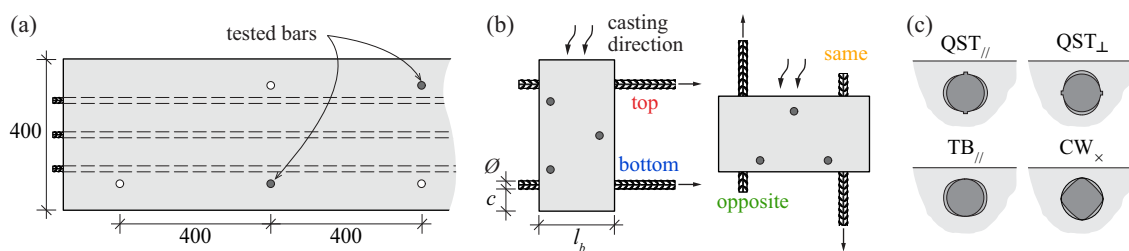


Figure 2.2: Specimen geometry and main investigated parameters of series PC01 and PC02: (a) front elevation of a typical concrete prism containing the test bars; (b) investigated casting positions; and (c) investigated rib geometries and lug orientations (refer to Figure 2.3 for the used symbols describing the rib geometries).

Table 2.2: Series PC01 and PC02 main parameters and experimental results (for definition of parameters, refer to section Notation)

Specimen	\emptyset	l_b/\emptyset	c/\emptyset	Casting	Bar type	Rib orientation	f_c [MPa]	F_{max} [kN]	σ_{sR} [MPa]	$\tau_{b,max}$ [MPa]	$\tau_{b0.1}$ [MPa]	Failure mode
PC0106	20	10	1	top	CW	×	39.5	76.3	243	6.1	4.1	S
PC0108	20	10	1	bottom	CW	×	39.5	87.9	280	7.0	6.4	S
PC0101	20	10	3	top	CW	×	40.6	93.7	298	7.5	6.6	SPO
PC0103	20	10	3	bottom	CW	×	39.5	115.5	368	9.2	7.0	SPO
PC0201	20	15	1	top	QST	//	40.6	96.1	306	5.1	3.4	S
PC0202	20	15	1	top	QST	⊥	40.5	88.5	282	4.7	3.2	S
PC0203	20	15	1	bottom	QST	//	40.7	115.6	368	6.1	5.1	S
PC0204	20	15	1	bottom	QST	⊥	40.7	119.6	381	6.3	5.9	S
PC0205	20	15	3	top	QST	//	40.9	114.8	365	6.1	4.8	SPO
PC0206	20	15	3	top	QST	⊥	40.9	125.5	400	6.7	2.4	SPO
PC0207	20	15	3	bottom	QST	//	41.0	163.5	521	8.7	7.0	SPOy
PC0208	20	15	3	bottom	QST	⊥	40.9	167.3	533	8.9	7.1	SPOy
PC0209	20	15	5	top	QST	//	41.1	158.5	504	8.4	5.8	SPOy
PC0210	20	15	5	top	QST	⊥	41.1	160.5	511	8.5	3.0	SPOy
PC0211	20	15	5	bottom	QST	//	41.2	>171	>545	>9.1	8.3	-
PC0212	20	15	5	bottom	QST	⊥	41.2	>175	>557	>9.3	7.1	-
PC0213	20	15	1	opposite	QST	//	41.3	106.0	337	5.6	5.6	S
PC0214	20	15	3	opposite	QST	//	41.4	157.1	500	8.3	6.6	SPO
PC0215	20	15	5	opposite	QST	//	41.4	163.0	519	8.6	8.1	SPOy
PC0216	20	15	1	same	QST	//	41.5	107.8	343	5.7	5.1	S
PC0217	20	15	3	same	QST	//	41.5	133.9	426	7.1	4.9	SPO
PC0218	20	15	5	same	QST	//	41.5	163.7	521	8.7	7.2	SPOy
PC0220	20	15	5	top	CW	×	41.3	133.5	425	7.1	4.6	SPO
PC0221	20	15	5	bottom	CW	×	41.3	149.8	477	7.9	6.7	SPO
PC0222	20	15	5	top	TB	//	41.2	140.1	446	7.4	5.9	SPO
PC0223	20	15	5	bottom	TB	//	41.3	176.0	560	9.3	8.0	SPO

Note: $\sigma_{sR} = F_{max}/(\pi \cdot \emptyset^2/4)$, $\tau_{b,max} = F_{max}/(\pi \cdot l_b \cdot \emptyset)$.

Abbreviations: S = spalling before yielding of the reinforcement. SPO = splitting induced pull-out before yielding. SPOy = splitting induced pull-out after yielding. - = test stopped after extensive yielding without anchorage failure

Material properties

All specimens from each series were produced from one batch of normal-strength ready-mixed concrete provided by a local supplier with a maximum aggregate size of 16 mm. The concrete was poured in two layers of approximately 200 mm. The compressive strength f_c of the concrete measured on cylinders (height×diameter = 320×160 mm) is indicated in Table 2.2. The tensile strength measured at 28 day by direct tensile tests with the same type of cylinders was 2.6 MPa for series PC01 and 2.5 MPa for series PC02.

Three types of 20-mm diameter steel bars with rib profiles commonly found nowadays in Switzerland were used in the pull-out tests. The stress-strain diagrams are shown in Figure 2.3a. The bars display different characteristics:

- Quenched and self-tempered (QST) bars: hot rolled, quenched and self-tempered bars with a well-defined yield plateau. The ribs are composed of 2 lugs with a non-symmetrical distribution, see Figure 2.3b.
- Cold-worked (CW) bars: cold-worked bars with no clear yield plateau (nominal yield strength determined at 0.2% residual strain). The ribs are composed of 4 lugs disposed symmetrically along the axis of the bar, see Figure 2.3c.
- Threaded bars for reinforced concrete (TB): cold-worked steel bars with no clear yield plateau (nominal yield strength determined at 0.2% residual strain). The ribs are composed of 2 lugs disposed in continuous threads along the axis of the bar, see Figure 2.3d.

The geometrical characteristics of the bar, including the bond index f_R , the maximum rib height $h_{R,max}$, the transverse rib angle β , the transverse rib flank inclination α_R and the transverse rib spacing s_R are obtained from a laser scan of the surface of the bars according to their definition [ISO19]. The average rib height $h_{R,avg}$ is calculated by dividing the projected rib area over the nominal bar perimeter. The clear spacing between ribs c_{clear} is considered as the spacing between consecutive rib flanks at mid-height of the ribs based on the laser scans. The main properties of the bars are summarized in Table 2.3.

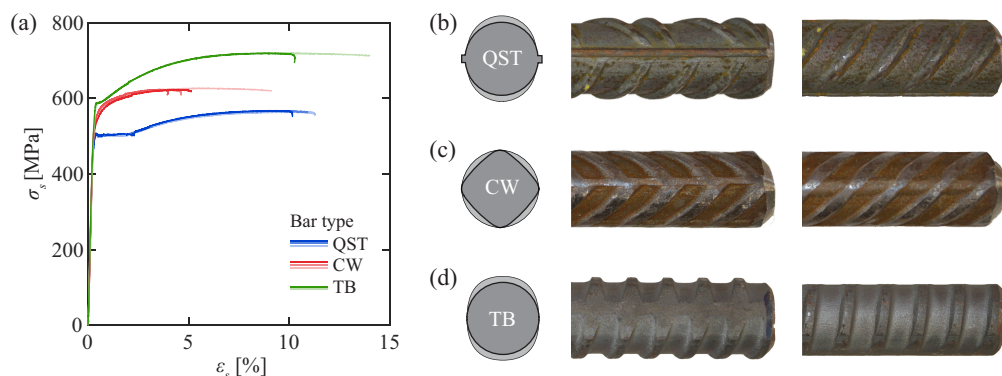


Figure 2.3: Bar characteristics: (a) stress–strain curves; and cross section and pictures of (b) QST bars, (c) CW bars and (d) TB bars.

Table 2.3: Bar mechanical and geometrical properties (for definition of parameters, refer to section Notation)

Type	\emptyset [mm]	f_y [MPa]	f_t [MPa]	Lugs	f_R [-]	$h_{R,avg}$ [mm]	$h_{R,max}$ [mm]	s_R [mm]	c_{clear} [mm]	β [°]	α_R [°]
QST	20	504	567	2	0.075	0.94	1.46	12.63	8.17	52.6	33.9
CW	20	558	625	4	0.079	0.94	1.42	11.91	6.83	42.4	37.5
TB	20	587	726	2	0.089	0.88	1.43	9.90	6.38	80	46.8

Test set-up and test development

All specimens were tested with the bar oriented in the vertical direction as illustrated in Figure 2.4a and b. The bar was clamped with a steel wedge and the pull-out force was exerted through a hinge to minimize bending in the bar. The reaction on the concrete specimens was applied through a steel frame to minimize the influence on the development of concrete cone breakouts. The frame was composed of two UPN 120 profiles and the frame legs were SHS 50×50×5 mm with 70×70×20 mm steel plates welded at the extremities. In each test, the frame was aligned with the axis of the bar. The frame was hinged at the position of the bar to minimize the bending moment in the concrete prism in the bar region. Two 16-mm threaded bars were used to counterbalance the applied force. The tests were conducted by applying the load at constant loading rate reaching the maximum load in 4 to 5 minutes. After the maximum force was reached, the test continued at a constant displacement rate to capture the post-peak response.

Measurements

The force applied to the bar and the reactions on the threaded bars were measured using load cells. The slip between the bar and the concrete at the unloaded end was measured with two LVDTs. The concrete surface parallel to the bar was tracked with DIC (see “DIC area” in Figure 2.4a) using a pair of cameras SVS EVO4070 with a resolution of 4.2 megapixels. The correlation was done using the VIC-3D software [Cor21], with a pixel size of 235 μm for series PC01 and 255 μm for series PC02. The displacement error was 1/75 pixels for in-plane displacements and 1/30 for out-of-plane displacements. The data acquisition frequency was 1 Hz. The reinforcement bars were instrumented using a single fibre optic installed along two opposite sides of the specimen, as illustrated in Figure 2.4b. Polyimide-coated fibres with a diameter of 125 μm were used (Figure 2.4d). The fibres were placed in a groove 1 mm wide and 2 mm deep that runs along the opposite faces of the bars. The position of the grooves was chosen to keep the fibres in a plane perpendicular to the concrete surface, independently of the rib orientation, see Figure 2.4c. The strains were measured using Optical Distributed Sensor Interrogator ODiSI-6100 by Luna Innovations with a strain measurement range of $\pm 12000 \mu\epsilon$ and a measurement accuracy of $\pm 25 \mu\epsilon$ [Lun20]. The spatial resolution of the strain measurements was 0.65 mm and the acquisition frequency varied between 40 and 62.5 Hz. It must be noted that for QST bars with a clear yield plateau, the yielding of the bar leads to strains larger than the measurement range and, therefore, to the loss of the fibre measurements.

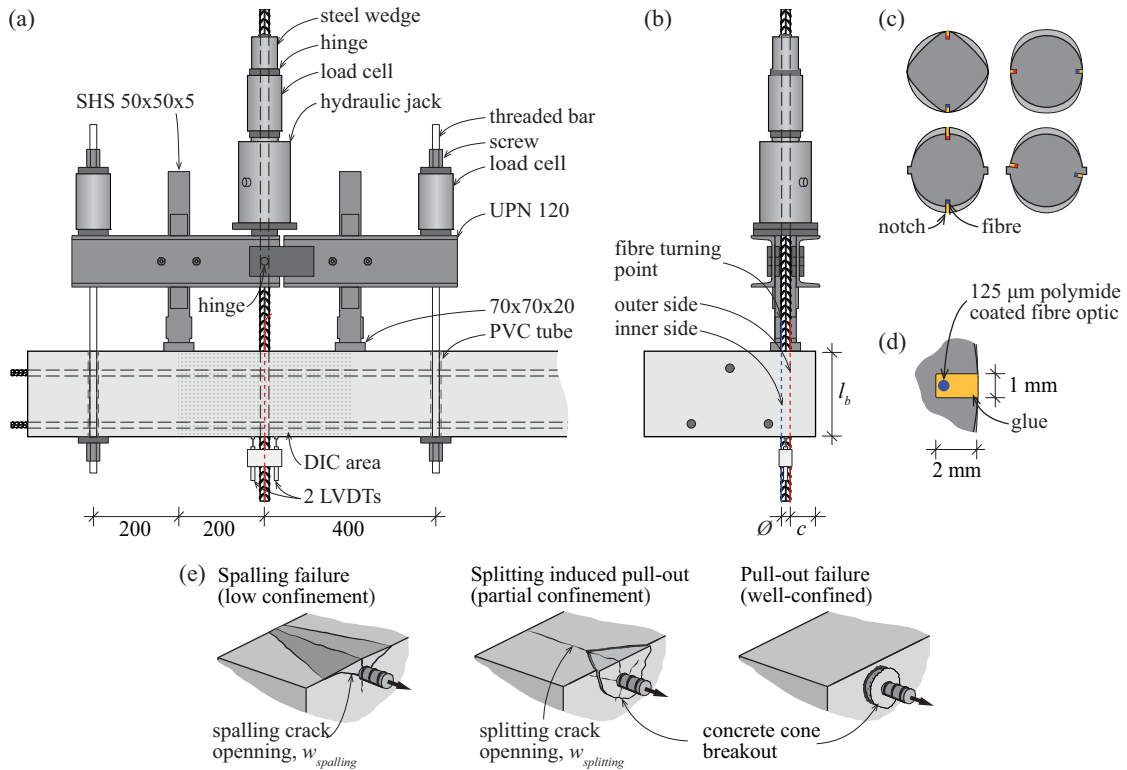


Figure 2.4: Test set-up, measurement systems and typical failure modes in the pull-out tests: (a) front and (b) side elevation of the test set-up; (c) position of fibre optic sensors in the different types of bars; (d) optical fibre detail; and (e) typical failure modes in pull-out tests.

Table 2.4: Series CM11 main parameters and experimental results (for definition of parameters, refer to section Notation)

Specimen	\varnothing	l_b/\varnothing	c/\varnothing	Casting	Bar type	Rib orientation	f_c [MPa]	F_{max} [kN]	σ_{sR} [MPa]	$\tau_{b,max}$ [MPa]	$\tau_{b0.1}$ [MPa]	Failure mode
CM1120	20	10	1	top	QST	⊥	42.3	64.0	204	5.1	2.3	S
CM1128	20	10	1	bottom	QST	⊥	42.3	70.8	225	5.6	5.2	S
CM1124	20	10	3	top	QST	⊥	42.3	94.7	302	7.5	5.4	SPO

Note: $\sigma_{sR} = F_{max}/(\pi \cdot \varnothing^2/4)$. $\tau_{b,max} = F_{max}/(\pi \cdot l_b \cdot \varnothing)$.

Abbreviations: S = spalling before yielding of the reinforcement. SPO = splitting induced pull-out before yielding.

2.2.2 Series CM11

Specimens of the pull-out test series CM11 conducted by Moccia et al. [Moc21a]³³ had the same geometry as specimens from series PC01. The steel bars with a nominal diameter of 20 mm were embedded in a concrete prism 200×400 mm, corresponding to a bonded length of 10Ø. The evaluated parameters in the test series were the concrete cover and the casting conditions. The main properties of the specimens are summarized in Table 2.4. The average concrete strength at the time of the tests was 42.3 MPa. The hot-rolled, quenched and self-tempered steel bars had a distinct yielding plateau, an average yield strength of 521 MPa and a tensile strength of 620 MPa. The ribs were composed of two lugs with a non-symmetric disposition and a bond index $f_R = 0.072$. The tests have been conducted in a similar manner as for series PC (more details can be found in Moccia et al. [Moc21a]).

2.2.3 Data post-processing

The strain measurements along the bonded length show local variations due to the variable cross section of ribbed bars, the potential variable material properties within the cross section, the noise in the measurement system and the transmission of bond forces at the ribs [Can20, Gal21]. These local strain oscillations have to be removed to calculate nominal bond stresses. A moving average filter over a length corresponding to 3 times the rib spacing (around 2 bar diameters) was applied to the raw strain measurements for the analysis of the test results. This distance is similar to the disturbed length observed in pull-out tests of bars with one and two ribs performed by Cantone et al. [Can20]. For the measurement of the strain due to shrinkage, a distance of 10 rib spacings was used. The average strain was computed from the smoothed measurements of the two fibres. The stresses were calculated considering the stress-strain relationship obtained from tensile tests of grooved bare bars with fibres. The pertinence of this assumption was verified with the average strain measurements over a length of 4 rib spacings from the loaded end of the bar outside the concrete (Figure 2.4a). Bond stresses are derived from the smoothed stress profiles using Equation 2.1, which can be obtained from the equilibrium of a differential bar element.

$$\frac{d\sigma_s}{dx} = \frac{4\tau_b}{\emptyset} \quad (2.1)$$

2.2.4 Failure modes

The typical failure modes in pull-out tests and the definitions used in this chapter are illustrated in Figure 2.4e. Regardless of the test conditions, all specimens developed a splitting crack (parallel to the bar and approximately perpendicular to the concrete surface). Specimens with a cover of 1Ø failed by spalling of the concrete cover (failure mode “S” in Tables 2.2 and 2.4) with the propagation of two longitudinal cracks along the bar with a small angle with respect to the concrete surface. Specimens with a cover of 3 and 5Ø displayed a splitting-induced pull-out failure (“SPO”). Some bars with an anchorage length of 15Ø yielded (“SPOy”) and two tests with

QST bars at the bottom of the formwork (good casting conditions) were stopped when the stresses approached the tensile strength of the bar. Detailed crack patterns for all specimens are provided in Appendix 2A.

2.3 Experimental results

2.3.1 Shrinkage

Strain measurements from the fibre optic sensors were recorded 6 hours after the casting (day 0 measurements) and before testing. The measurements from the bar outside the concrete were used to remove the effect of temperature variation, assuming a uniform temperature distribution along the bar. Figures 2.5a and b show the results for specimens PC0206 and 08, including the raw strain measurements (ε_s) from the external (closest to the concrete surface, red curves) and internal fibres (located in the opposite face of the bar, blue curves), the smoothed average stress (σ_s) and the bond stress. In specimen PC0206 (poor casting conditions), the signal presents large strain variations reaching strains over 1.5‰ for the external fibre and regular low amplitude variations for the internal fibre. In specimen PC0208 (good casting conditions), both signals show strain variations reaching approximately 1‰, similar to the measurements by Lemcherreq et al. [Lem22]. The difference can be explained by the presence of plastic settlement voids under bar PC0206, which limit the capacity of the concrete to transfer forces to the bar [Moc21]. The bar in good casting conditions is surrounded by the concrete on all sides, thus causing a similar strain profile on both sides of the bar. Similar trends could be observed in other specimens with the ribs oriented perpendicularly to the concrete surface.

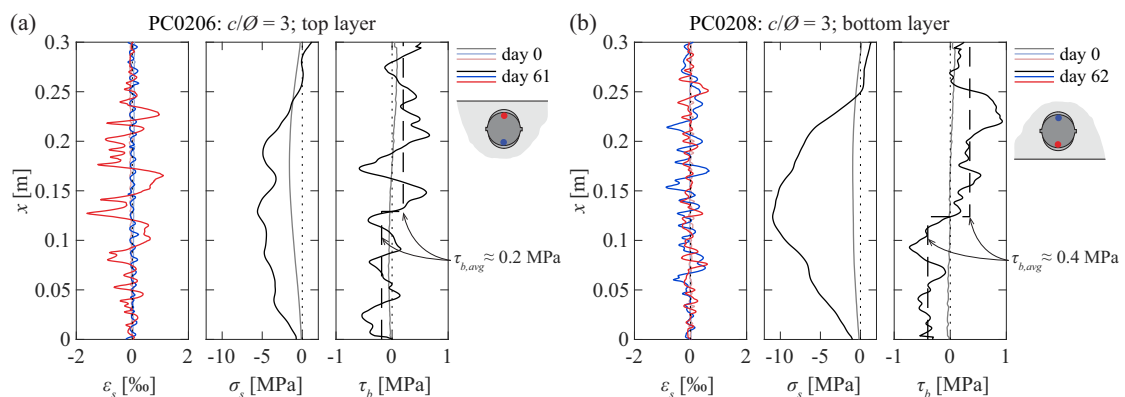


Figure 2.5: Shrinkage-induced effects: distribution along the bonded length of raw strain measurements, axial stresses and bond stresses in the bars for specimens (a) PC0206 and (b) PC0208 (red and blue colours refer to each fibre optic sensor, see sketch, black and grey curves refer to the mean values).

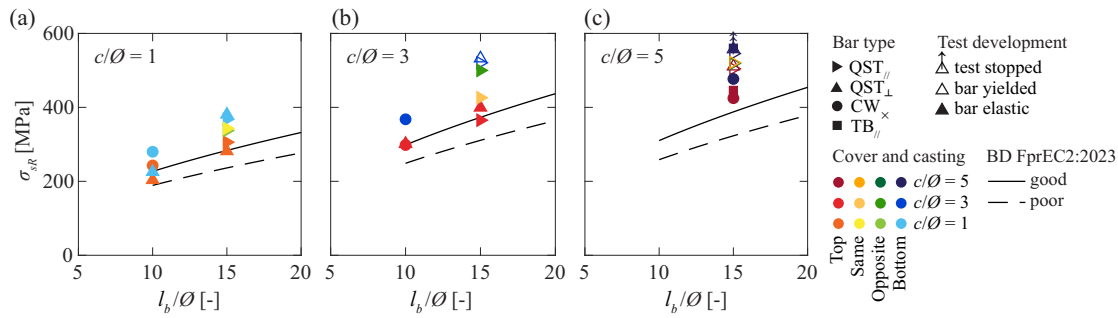


Figure 2.6: Anchorage resistance as a function of the anchorage length for specimens with covers of: (a) $1\emptyset$; (b) $3\emptyset$; and (c) $5\emptyset$.

The fibre measurements were smoothed using a moving average filter over a distance of 10 rib spacings (126 mm). The resulting stress profiles are coherent with those found in literature [Lem22, Bad21a]. The bar in poor casting conditions displays a minimum stress of -5.6 MPa and an average bond stress of 0.2 MPa (average value at each side of the maximum steel stress, see Figure 2.5a) with maximum local values close to 0.5 MPa. For the bar in good casting conditions, the minimum steel stress was -10.9 MPa with an average bond stress of 0.4 MPa, see Figure 2.5b. The results indicate that shrinkage induces smaller axial and bond stresses in the bar in poor casting conditions due to plastic settlement voids. Nevertheless, these results must be considered with care as the peak raw strain measurements are two orders of magnitude larger than the shrinkage strains. Consequently, the results are highly dependent on the smoothing. Further tests are required to confirm these findings.

2.3.2 Anchorage resistance

The anchorage resistance expressed in terms of the maximum stress activated in the bar (σ_{sR}) is represented as a function of the anchorage length in Figures 2.6a to c. The experimental results are compared with the tensile stress that can be developed in the anchorage according to the expression for mean values proposed in the Background Document for the final draft of Eurocode 2 (BD FprEC2:2023) [Eur23, Mut23]. In all specimens, the experimental anchorage resistance was larger than the proposed values.

2.3.3 Effect of the concrete cover and casting conditions

Figure 2.7a shows the average bond stress over the anchorage length ($\tau_{b,avg}$) as a function of the unloaded end slip ($\delta_{sc,end}$) for specimens with an anchorage length of $15\emptyset$ in all the considered casting conditions. The maximum anchorage resistance is reached for good casting conditions (blue), followed by the bars loaded in the opposite direction of casting (green), then by the bars loaded in the casting direction (yellow), and finally the bars in poor casting conditions (red). Specimens with a cover of $1\emptyset$ present a relatively brittle failure with a sudden drop in the force

and the consequent lack of experimental data (dotted lines). The influence of the concrete cover and the casting position on the maximum stress activated in the bar is shown in Figure 2.7b. This difference is caused by the cracks and the voids under the bars due to the plastic settlement of the fresh concrete and the higher porosity of the concrete under the bars [Cla49, Reh61, Mar81, Moc21]. The effect of the confinement and casting position on the anchorage length is included in current standards; however, its effect on cracking at SLS is not [Eur04, FIB13]. Figure 2.7c presents the average bond stress corresponding to a slip at the unloaded end of 0.1 mm ($\tau_{b0.1}$) for the considered covers. Significant variations can be observed due to the other parameters; however, the linear regression (dashed lines) shows an increasing trend for all casting conditions. Therefore, the effect of confinement and casting conditions can be relevant for serviceability verifications. Pérez Caldentey et al. [Pér20] recently proposed an empirical factor for the crack spacing formulation based on the experimental results of four-point bending tests to account for the effect of casting conditions and the effect of cover in poor casting conditions. The results in Figure 2.7c confirm that the cover can influence the bond stresses at SLS in all casting conditions. The new generation of standards includes the effect of casting conditions on the crack width formulation [Eur23].

Figure 2.8 shows the detailed measurements obtained with DIC and FOS along the anchorage length for specimens PC0201, 05 and 09 with QST// bars in poor casting conditions. For each

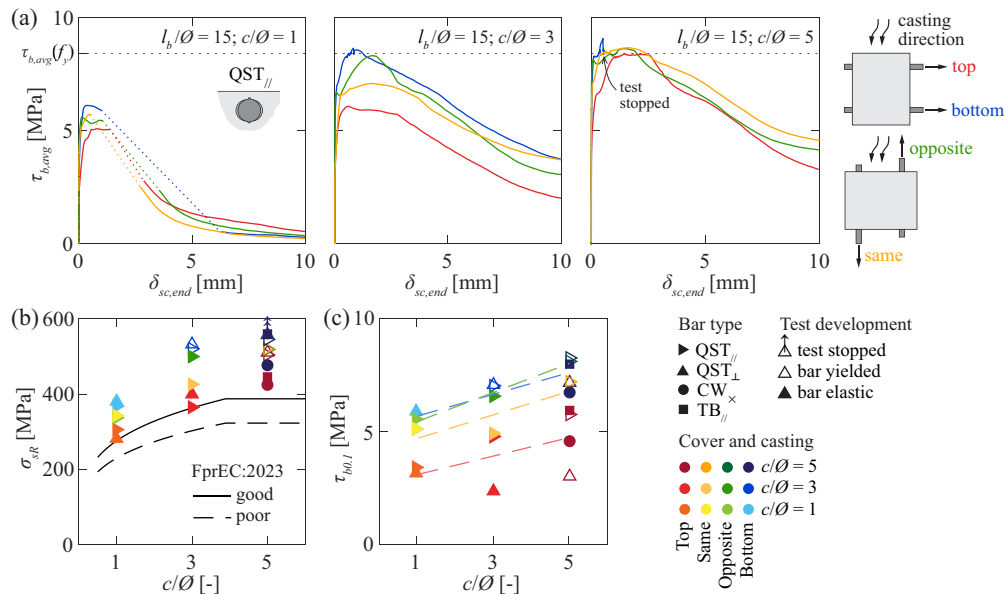


Figure 2.7: Effect of concrete cover and casting conditions: (a) average bond stress-slip relationships for specimens with covers of $1\varnothing$ (PC0201, 03, 13 and 16), $3\varnothing$ (PC0205, 07, 14 and 17) and $5\varnothing$ (PC0209, 11, 15 and 18); (b) anchorage resistance as a function of concrete cover; and (c) average bond stress corresponding to a slip at the unloaded end of 0.1 mm as a function of concrete cover.

specimen, the crack opening at the maximum load (F_{max}) is represented in red and the cracks developed during the post-peak phase are shown in grey in Figures 2.8a, c and e. This information was extracted from the DIC data using the Automatic Crack Detection and Measurement software (ACDM) [Geh22]. Figures 2.8b, d and f display the distribution of raw (light grey curves) and smoothed strains ε_s (red, purple and dark grey curves), smoothed axial stress σ_s , bond stress τ_b , steel δ_s (dotted curves) and concrete displacements δ_c (dashed curves), relative slip δ_{sc} (solid curves) and crack width w for different load levels. The concrete displacement is calculated from the displacement field on the concrete surface measured with DIC. The bar displacement is calculated by adding the slip at the unloaded-end measured with the LVDTs and the integrated strains along the bar. The relative slip is the difference between these two values. The opening of the spalling crack $w_{spalling}$ (solid curves) is assumed to be equal to the out-of-plane displacement of the concrete cover along the bar axis. The opening of the splitting crack $w_{splitting}$ (dashed curves) is measured using the DIC displacements from the concrete surface (for the definition of splitting and spalling cracks used in this chapter, see Figures 2.4e and 2.9d).

For all specimens, the splitting crack appeared first at the loaded end of the bar and propagated towards the unloaded end. Typically, as the load increased, one or more cracks with a “V” shape developed on the concrete surface along the length of the specimen. These cracks probably correspond to the intersection of conical cracks originating at the ribs [Got71] with the concrete surface. The development of these cracks can also be observed in the stepped distribution of concrete displacements. Near the loaded end of the bar, the propagation of these cracks caused the breakout of a conical concrete block (dark grey area in Figures 2.8c and e) causing large displacements and a reduction of the bond stresses. Specimen PC0201 failed by spalling of the cover, the spalled region is indicated with a dark grey hatch in Figure 2.8a.

The axial steel stress distribution shows that for small load levels, larger bond stresses are activated at the loaded end of the bar. As the load increases, the distribution flattens near the loaded end, indicating lower bond stresses in that region. A redistribution of the bond stresses occurs and larger bond stresses are activated near the unloaded end, as observed by other authors [Mai51]. After the maximum load is reached, the concrete cone detachment causes bond stresses to vanish within the corresponding length as can be clearly observed in Figure 2.8d. In specimen PC0209, whose reinforcement yielded at around 95% of the anchorage capacity, the length of the concrete cone breakout along the bar is similar to the region where yielding was detected (Figure 2.8f).

The slip plots indicate that the displacement of the concrete can be neglected until the propagation of the conical cracks reaches the concrete surface. The crack opening plots show that the spalling crack width reaches considerably larger values for the bars with a cover of $1\emptyset$. For specimens with larger covers, the splitting crack widths tend to be larger. An interaction between the concrete cone breakout and the splitting and spalling cracks is observed. Within the region affected by conical cracks, larger spalling crack widths occur due to the displacement of the concrete cover. Concerning the splitting crack, as the bar slides, the partially detached concrete blocks composing the cone are pulled. This causes their rotation in opposite directions in the plane of the concrete surface, reducing the splitting crack width near the intersection of the two cracks. Similar crack patterns and stress distributions were observed in other specimens. The results for all tested specimens can be found in Appendix 2A.

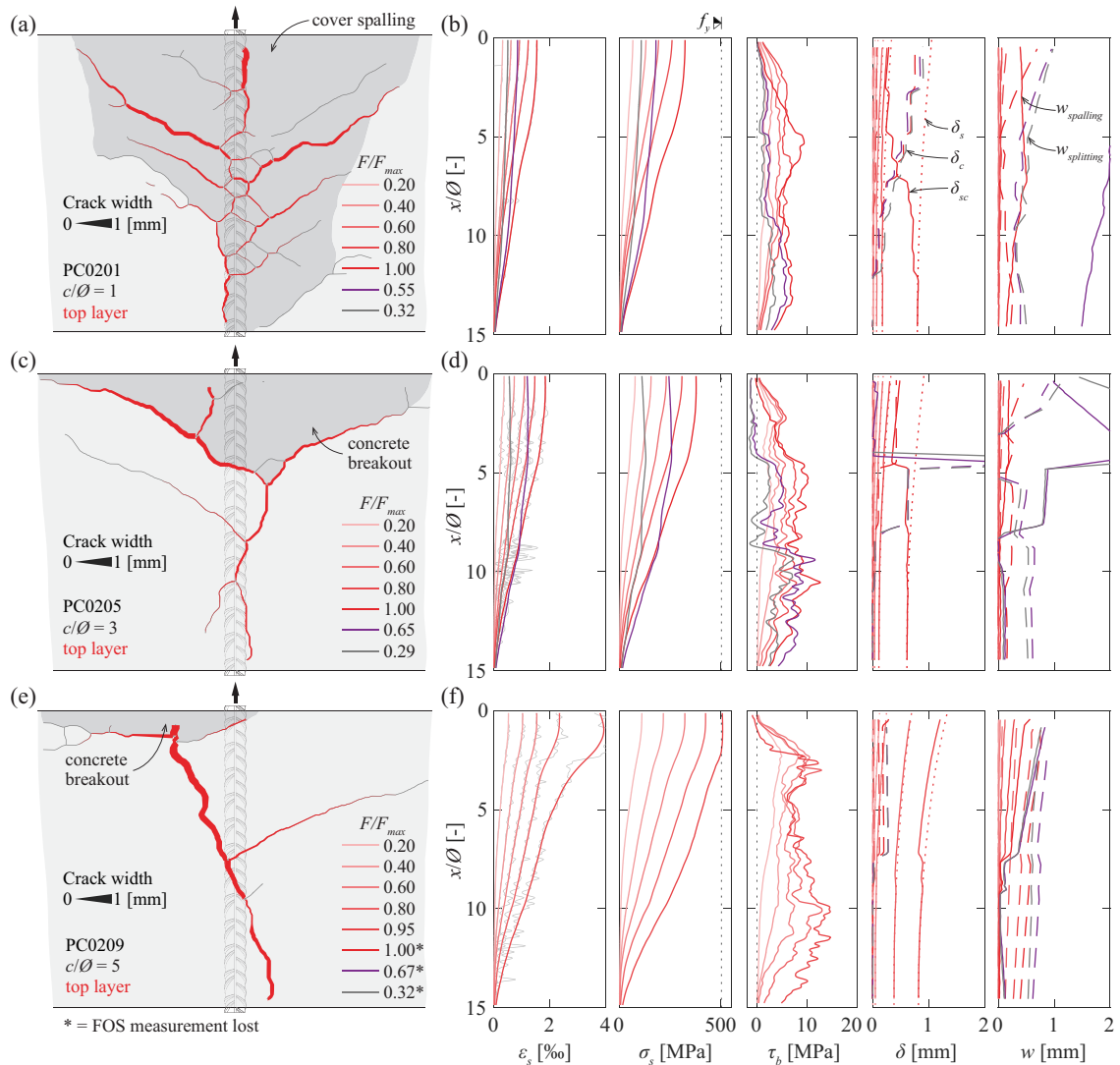


Figure 2.8: Pull-out test detailed measurements: crack pattern and distribution along the anchorage length of axial steel strains, axial steel stresses, bond stresses, slip and crack widths for specimens (a)-(b) PC0201, (c)-(d) PC0205 and (e)-(f) PC0209.

More detailed information about the local response at various positions along the bar can be obtained from the measurements presented in Figure 2.8 by plotting the different values as a function of the local slip. The local bond stress-slip distribution and the evolution of the crack widths at different locations are illustrated in Figure 2.9. The average bond stress as a function of the unloaded and loaded end slips (grey hatch) and the MC2010 local bond-slip relationship (black curves) are represented for comparison. As it can be observed in Figures 2.9a and b, the average response for specimens with a cover of 1 and 3Ø displays a lower peak bond strength than the MC2010 provisions, which is logical as the MC2010 expressions were calibrated with short pull-out tests with a more uniform bond stress distribution. The local bond stress measurements display similar peak values or even higher for the points not affected by the cone breakout. The local measurements display a less brittle post-peak response than the corresponding

relationship according to MC2010 (unconfined splitting failure). This is also probably related to the longer bonded length and the stress redistribution capacity. For the specimen with a cover of $5\varnothing$ (Figure 2.9c), the average response reaches a peak stress close to the MC2010 provision with higher local bond stresses. Points outside the concrete cone breakout display a fairly uniform behaviour. Within the breakout region, the local bond stresses reach lower values and have a more brittle response. The response does not correspond exactly to the reduction of the bond stresses as proposed by MC2010 and other authors [CEB93, Fer07]. They propose a reduction of the bond stress using the factor λ shown in Figure 2.10a, resulting in the bond-slip relationships presented in Figure 2.10b. Instead, the results show a rather similar ascending branch with different maximum bond stresses and post-peak responses closer to the proposal by Eligehausen et al. [Eli83, Kre89] shown in Figure 2.10c.

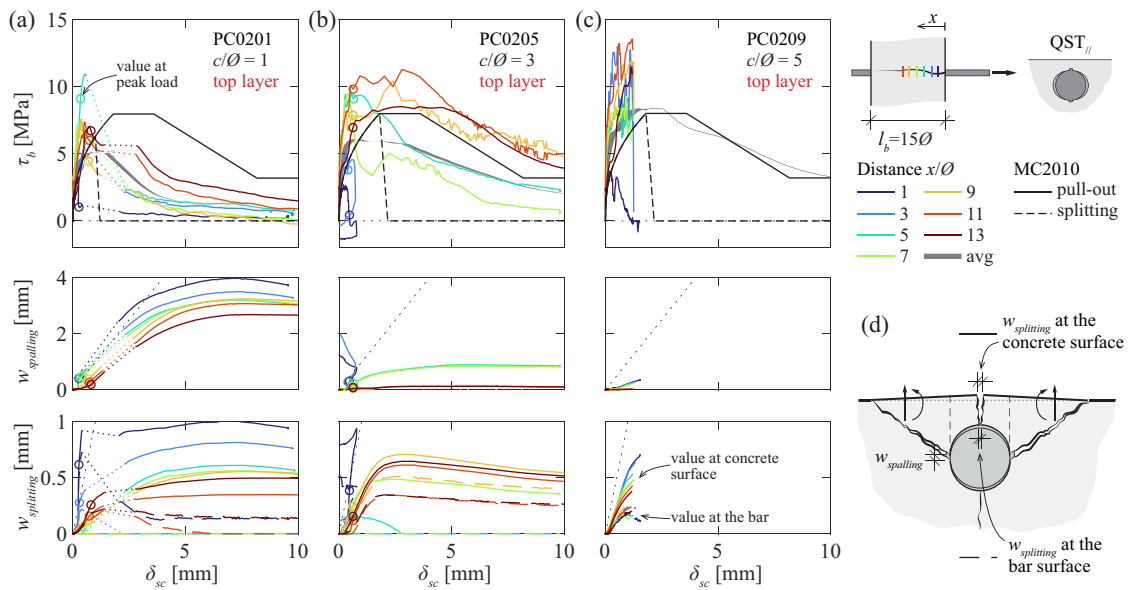


Figure 2.9: Local measurements along the bonded length: local bond-slip, spalling crack opening-slip and splitting crack opening-slip relationships for specimens (a) PC0201, (b) PC0205 and (c) PC0209; and (d) schematic representation of the crack development mechanism.

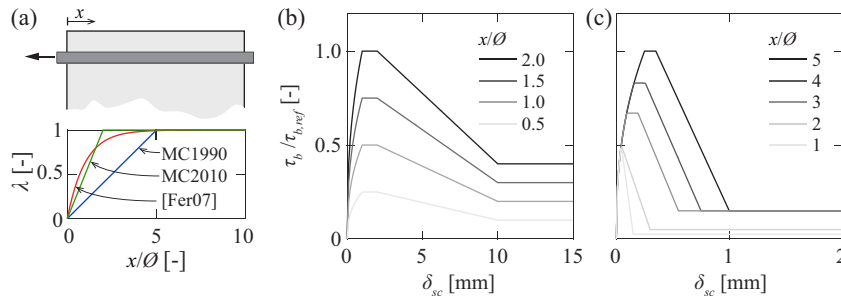


Figure 2.10: Local bond stresses near transverse cracks: (a) variation of the reduction factor λ along the bar from different publications [CEB93, Fer07, FIB13]; (b) resulting bond-slip relationships using the factor λ proposed by MC2010; and (c) bond-slip relationships proposed by Eligehausen et al. [Eli83, Kre89].

In all specimens, the measured response displays higher stiffness in the ascending branch than the MC2010 expressions. One possible explanation for this are the large side covers. In this experimental programme the minimum clear cover (c) was varied; however, the side cover in was constant and typically larger than c . This can lead to a stiffer response and therefore a preferential load bearing direction. The MC2010 expressions do not account for different side covers. Furthermore, the expressions are based on the work of Eligehausen et al. [Eli83] that used mainly bars with a diameter of 25.4 mm. The size effect could also contribute to the difference in the results. Nevertheless, the presented experimental results agree with other recent studies using pull-out tests [Met14], beam-end tests [Kos22a] and concrete ties [Bad21].

It must be noted that the crack patterns represented in Figure 2.8 correspond to the measurements on the concrete surface. The activation of bond forces is directly related to the internal cracking of the concrete around the bar, which can differ from the measurements on the concrete surface. The spalling of the cover causes the rotation of the concrete segments delimited by the splitting and the spalling cracks in a plane perpendicular to the bar, as illustrated in Figure 2.9d. This rotation increases the crack width of the splitting crack on the concrete surface and reduces it at the bar surface. The variation of the crack opening can be estimated by multiplying the rotation at both sides of the crack by the cover. Therefore, the estimated crack width at the bar can be obtained by subtracting the estimated variation from the measurement on the visible concrete face. The pertinence of this estimation was verified and compared with DIC measurements on the surface perpendicular to the bar on the loaded end [Cor22a]. The estimated splitting crack width at the bar is shown with dashed lines in Figure 2.9a to c.

The crack width plots for specimen PC0201 show large spalling crack openings reaching values close to two times the maximum rib height. As the out-of-plane displacements of the cover take place, the width of the splitting crack at the bar is reduced (Figure 2.9a). Specimens with larger covers show smaller spalling openings, particularly for points outside the cone breakout. Specimen PC0205 shows the largest splitting crack widths at the bar surface (close to 0.5 mm) that remain stable during the post-peak phase, see Figure 2.9b. The specimen with a cover of $5\emptyset$ shows the smallest crack openings, see Figure 2.9c.

Figure 2.11a shows the local bond stress corresponding to a local slip of 0.1 mm ($\tau_{b0.1}$) along the anchorage length for specimens with a cover of $3\emptyset$ in different casting conditions. The average value for each specimen is represented with a dashed line. The points closer to the loaded end ($x = 0$), which are affected by the concrete cone breakout, typically display lower secant stiffness, with the exception of the bar loaded along the casting direction (yellow curve), which shows a similar stiffness along most of the bonded length and even higher values near the loaded end. In this case, the loaded end is close to the bottom of the formwork (good casting conditions). Outside the cone breakout region, the specimen in the bottom of the formwork (blue curve) and the specimen loaded against the casting direction (green curve) show similar secant stiffnesses larger than for the other conditions. The local response of the specimen at the top of the formwork (poor casting conditions, red curve) is slightly stiffer than the specimen loaded along the casting direction. This seems reasonable because for the bar at the top of the formwork, the voids caused by the plastic settlement of concrete will be located under the bar; whereas for the vertical bar, they will appear under the ribs along the full perimeter of the bar. Nevertheless, the average response yields similar values as the voids will get smaller in the regions close to the bottom of

the reinforcement. The difference between these two conditions can differ depending on the distance to the bottom of the formwork [Moc21].

The local bond-slip responses for the four considered casting conditions at three locations are shown in Figures 2.11b to d. The results at a distance of $2\varnothing$ from the loaded are within the concrete cone breakout and show a brittle response (Figure 2.11b). The results at 7 and $13\varnothing$ from the loaded end reach larger bond stresses and have a less brittle softening response (Figures 2.11c and d). At each location, the experimental curves show similar behaviours for the different conditions besides the differences in stiffness and peak values. In all cases, the responses are stiffer than the MC2010 relationships. A larger range of slips is shown in Figure 2.12. The trends observed in Figure 2.9 regarding the response in the regions near the loaded end due to the concrete cone breakout remain visible for all the tested conditions.

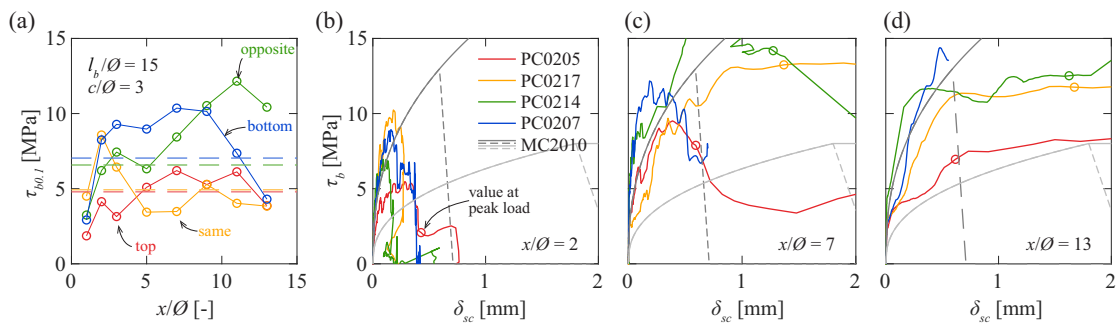


Figure 2.11: Effect of casting position for specimens PC0205, 07, 14 and 17: (a) local bond stress corresponding to a local slip of 0.1 mm along the anchorage length; and local bond-slip relationships at (b) $x/\varnothing = 2$, (c) $x/\varnothing = 7$ and (d) $x/\varnothing = 13$.

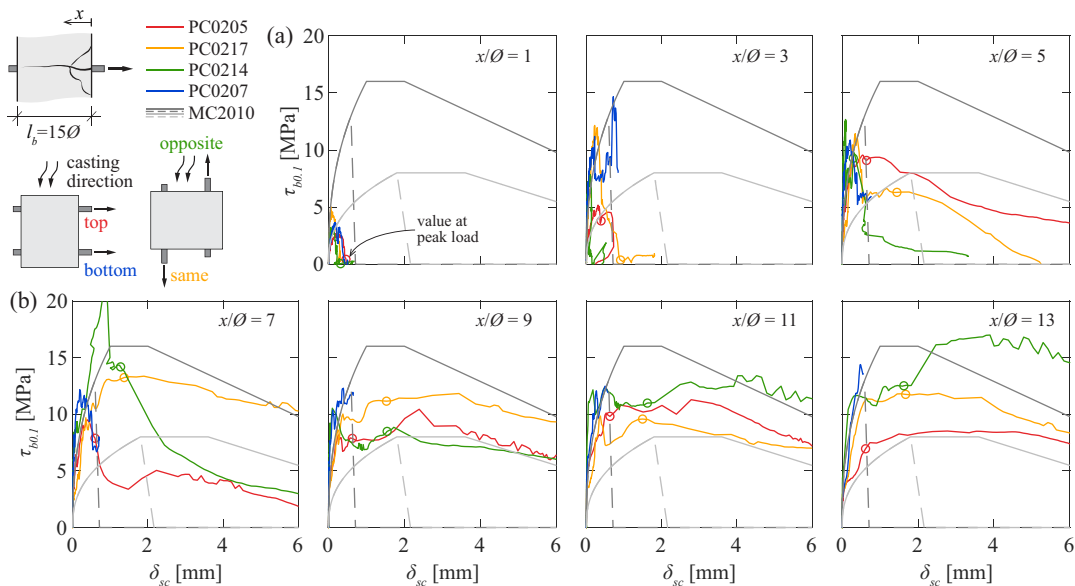


Figure 2.12: Effect of casting position and loading direction on the local bond-slip response from specimens PC0205, 07, 14 and 17 at different positions along the anchorage length: (a) $x/\varnothing = 1, 3$ and 5 ; and (b) $x/\varnothing = 7, 9, 11$ and 13 .

2.3.4 Rib orientation

The measured average bond stresses as a function of the unloaded end slip for specimens with an anchorage length of $15\emptyset$ and different concrete covers are illustrated in Figure 2.13a. The QST bars were placed with two orientations: bars with the ribs oriented parallel to the concrete surface (QST_{//}, solid curves) and bars with the ribs oriented perpendicularly to the surface (QST_⊥, dashed curves). The same general response and failure mode is observed independently of the rib orientation for good (blue curves) and poor casting conditions (red curves). Figure 2.13b shows the influence of the rib orientation on the maximum stress activated in the bar. The results for specimens in good casting conditions show little influence of the rib orientation. For specimens in poor casting conditions with a cover of $1\emptyset$ (spalling failure), the QST_{//} specimen reached an anchorage resistance 9% larger than the QST_⊥. For specimens in poor casting conditions with covers of 3 and $5\emptyset$, the anchorage resistance for QST_{//} bars is, on average, 5% lower.

Figure 2.13c shows that the $\tau_{b0.1}$ is, on average, 67% lower for QST_⊥ specimens in poor casting conditions. The response in good casting conditions shows no difference on average (values of $\pm 15\%$). This can be explained by the presence of plastic settlement voids and the porous concrete layer that, in the case of perpendicular orientation, directly affect the rib placed towards the bottom of the formwork. For specimens with ribs oriented parallelly to the concrete, only a lower portion of the lugs is affected by the voids. This effect is not present in bars in good casting conditions, which justifies the lack of uniform tendency and values within typical bond test scatter.

Figure 2.13d illustrates the bond stress distribution along the bar for 5 load levels for specimens with covers of $3\emptyset$. The results show that for loads close to 20% of the anchorage resistance, bars in poor casting conditions activate lower bond stresses but over a longer portion of the bar, particularly for the QST_⊥ bar. This is in good agreement with the differences in stiffness (Figure 2.13c), and can indicate a higher redistribution capacity when the bond-slip relationship is less stiff. Moreover, it can be observed that higher bond stresses are activated near the unloaded end in specimen PC0206 which explains the higher anchorage resistance. The difference in the activation for low load levels can also be observed for specimens with covers of 1 and $5\emptyset$ (see Appendix 2A).

The results seem coherent with the fact that bars with the ribs oriented perpendicularly to the concrete surface will develop a larger component of bursting forces, whereas if the rib lugs are oriented parallelly, there will be a larger component of splitting forces (Figure 2.13e). Consequently, specimens with a failure mode governed by spalling (low confinement) can have a lower anchorage resistance if the ribs are placed perpendicularly to the concrete surface. In good casting conditions, the sudden crack development limits the influence of this effect.

Cairns et al. [Cai95] reported that there is a high probability that rib orientation influences the bond strength, based on an analytical formulation and an experimental programme with lap-splices that favoured splitting failure. Koschemann et al. [Kos22a] conducted an experimental campaign with beam-end tests with bond lengths of $2\emptyset$ investigating the effect of rib orientation on bars with a nominal diameter of 16 mm and rib pattern similar to the QST bars in this publication. The lowest anchorage resistance (around 5%) was observed for specimens with ribs

oriented parallel to the concrete surface and the lugs leading to compression struts towards the concrete surface. The experimental results presented in this chapter indicate that, for specimens with pull-out or splitting-induced pull-out failures, the influence of the rib orientation is larger in the redistribution of bond stresses than in the crack development. Recent studies on lap-splices [Cai22] and anchorages [Cor22] have shown that local bond-slip relationships with lower peak values and stiffness can lead to higher strengths in poor conditions for long anchorage lengths.

It must be noted that the difference in anchorage resistance due to the rib orientation reported in this study and in the literature lies within the typical scatter observed in bond tests. However, the differences in the secant stiffness for small slip values are significant and indicate that the effect of rib orientation is potentially relevant for SLS conditions.

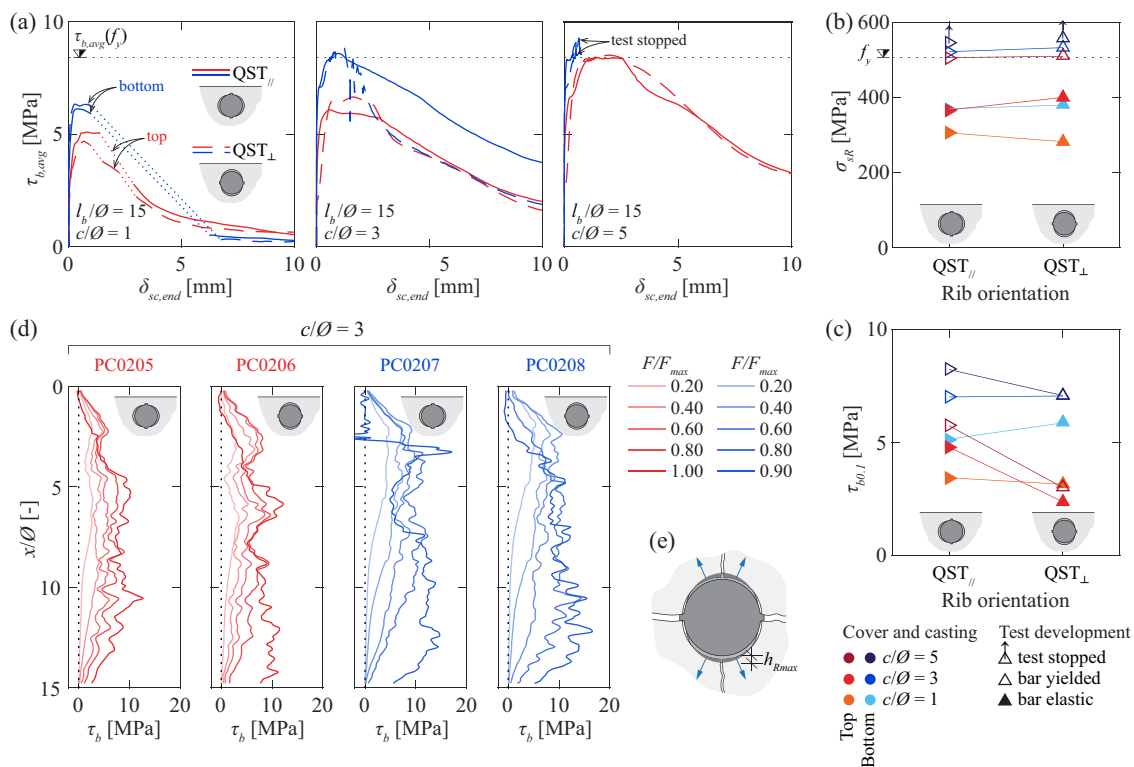


Figure 2.13: Effect of rib orientation: (a) average bond stress-slip relationships for specimens with covers of 1Ø (PC0201 to 04), 3Ø (PC0205 to 08) and 5Ø (PC0209 to 12); (b) anchorage resistance as a function of the rib orientation; (c) average bond stress corresponding to a slip at the unloaded end of 0.1 mm as a function of the rib orientation; (d) local bond stress distribution along the anchorage length for specimens with a cover of 3Ø (PC0205 to 08); and (e) schematic representation of the rib orientation effect.

2.3.5 Bar type and orientation

Figure 2.14a presents the average bond stress as a function of the unloaded end slip for specimens with an anchorage length of $10\varnothing$ and a cover of $1\varnothing$. The results indicate that the anchorage resistance of the QST_\perp bars is lower than for CW bars: 19% for good (blue curves) and 16% for poor casting conditions (red curves). The stiffness follows the same trend, being lower for QST_\perp specimens: 18% for good and 44% for poor casting conditions. This could be explained by the difference in orientation, given the similar geometrical characteristics of these bars. CW bars were placed with the lugs in a 45° disposition with respect to the direction of the concrete surface, therefore generating a lower bursting force component and being less susceptible to the effect of plastic settlement voids. The results for specimens with a cover of $3\varnothing$ in poor casting conditions show similar peak bond stresses and lower secant stiffness, see Figure 2.14b.

Figure 2.14c shows the average bond stress as a function of the unloaded end slip for specimens with an anchorage length of $15\varnothing$ and cover of $5\varnothing$. For good and poor casting conditions, the QST bars developed the largest anchorage resistance (around 19% higher in poor casting conditions), followed by the TB bars (5% and 17% higher in poor and good casting conditions respectively) and the CW bars. The difference in the bond indices of the bars does not correlate with the results, as the bar with the lowest bond index (QST) activates the highest bond stresses. In well-confined conditions, the pull-out failure occurs by shearing off the concrete keys between the ribs and increasing the rib spacing leads to larger bond strengths, as observed by other authors that tested bars with the same rib geometry and different spacings [Tep92, Met14]. As indicated in Table 2.3, QST bars have the largest clear spacing amongst the considered bars, followed by CW and TB bars (8.17, 6.83 and 6.38 mm, respectively). This explains the highest results for QST bars. The width of the rib can influence the results as the ratio of c_{clear}/s_R determines the proportion of the perimeter per unit of length occupied by concrete keys: 0.65 for QST bars, 0.57 for CW bars and 0.64 for TB. Another factor influencing the bond behaviour is the transverse rib angle (β), as previously observed by Soretz et al. [Sor79], who reported a small increase in the bond performance with increasing inclination of the lugs using pull-out tests on cubes. The higher transverse rib angle for TB bars can increase the bond strength. Consequently, the differences in the measured responses are likely the result of the combination of the aforementioned effects.

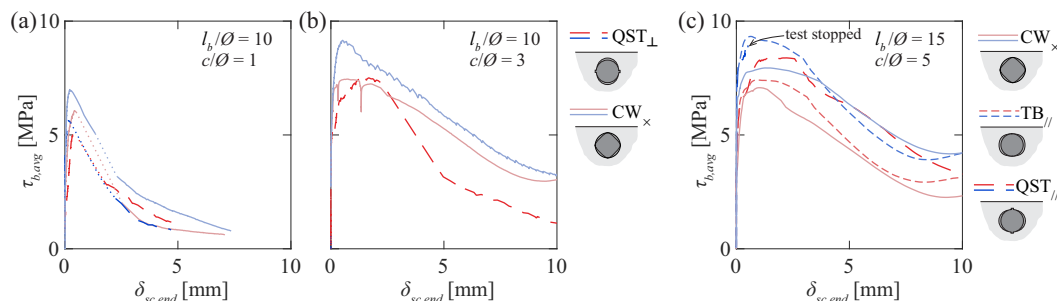


Figure 2.14: Effect of rib geometry: average bond stress-slip relationships for specimens with covers of (a) $1\varnothing$ (CM1120, 28, PC0106 and 08), (b) $3\varnothing$ (CM1124, PC0101 and 03) and (c) $5\varnothing$ (PC0209, 11, 20, 21, 22 and 23)

2.4 Result discussion

2.4.1 Splitting and spalling crack evolution

Figure 2.15 shows the evolution of the spalling crack opening (solid curves) and of the splitting crack opening at the bar surface (dashed curves) as a function of the local slip at different locations along the bar for different specimens. As shown in Figures 2.15a and b, specimens with low confinement display similar trends regardless of the type of bar, anchorage length and casting conditions. For small slip values (around 0 to 0.1 mm), both crack openings remain small and comparable. For larger slip values, the spalling crack becomes significantly larger in most specimens, particularly after the peak load is reached (circles). The crack widths are comparable to the local slip values within a distance of around $7\emptyset$ from the loaded end and gradually decrease for locations closer to the unloaded end. However, the values at the peak load are considerably larger for the specimens in poor casting conditions. This indicates a lower stiffness in the spalling mechanism, which can be explained by the presence of plastic settlement cracks [Moc21]. In good casting conditions, the cracks develop and propagate suddenly close to the peak load, which explains the more brittle behaviour. Only small differences can be observed due to the rib orientation. Specimens with $QST_{//}$ bars (PC0201 and 03) display slightly larger splitting crack widths than QST_{\perp} specimens (PC0202 and 04).

Figure 2.15c presents the results for specimens with a cover of $3\emptyset$ and show a clear effect of the conical cracks noticeable in the sudden change of tendency of the spalling crack propagation. For example, in specimen PC0205, the concrete cone breakout causes large spalling cracks at 1 and $3\emptyset$ from the loaded end and a second conical crack causes an increase in the spalling crack width after the peak load for locations at 5 and $7\emptyset$ (see Figures 2.8c and d). For the rest of the locations, the splitting crack increases almost linearly with the slip and very small spalling openings are measured. The fibre signal is lost before the maximum force for specimens PC0207 to 12.

Figure 2.15d shows the results for specimens with a cover of $5\emptyset$. For most locations, both splitting and spalling cracks follow a fairly uniform tendency and with smaller crack widths than specimens with a cover of $3\emptyset$. It must be noted that for similar slip values, specimens with larger covers reach higher bond stresses, as shown in Figure 2.7a. No clear trend can be observed due to the rib orientation.

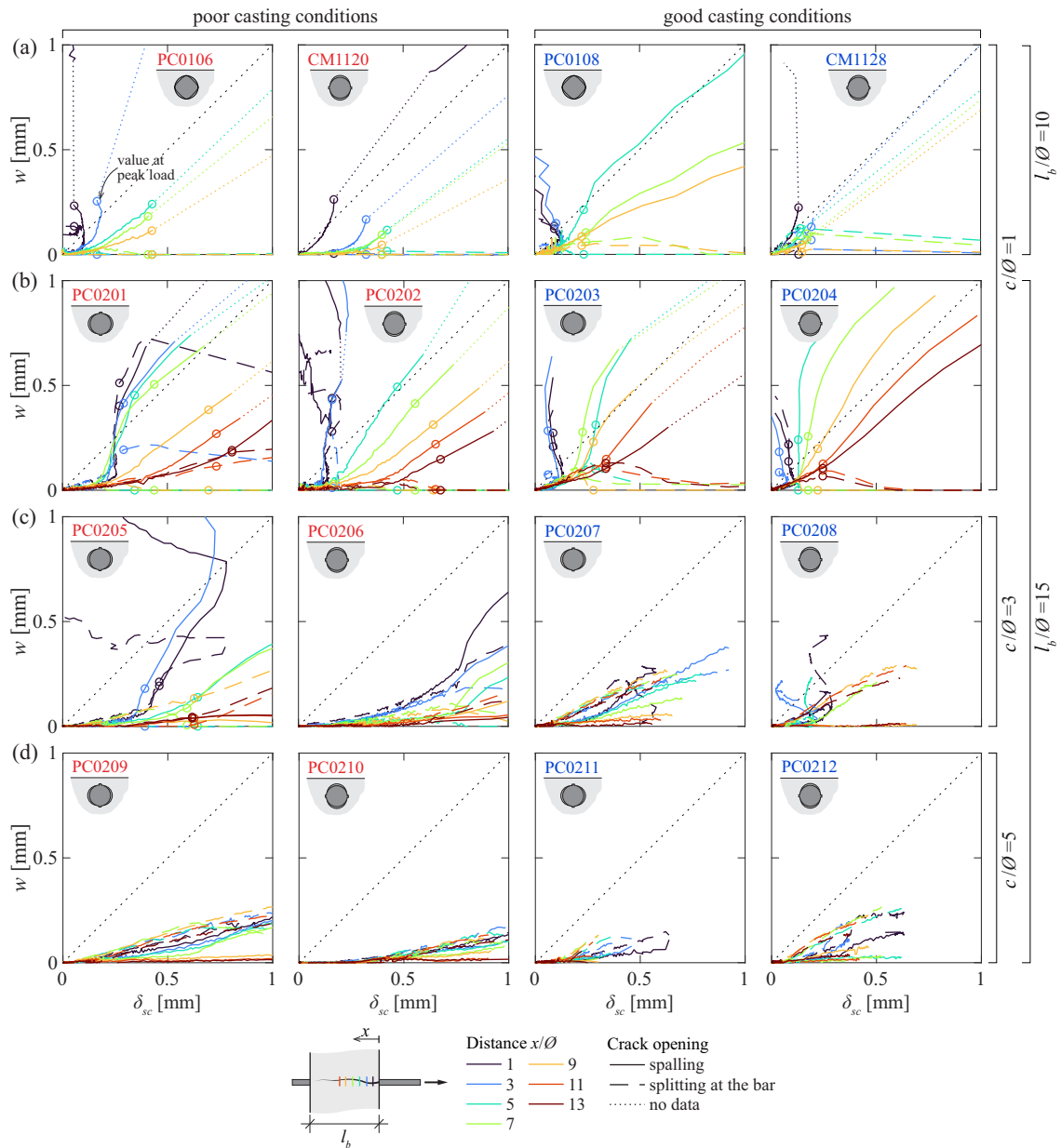


Figure 2.15: Spalling crack opening and splitting crack opening at the bar surface as a function of the local slip for specimens with covers of: (a) 1Ø and $l_b/\text{Ø} = 10$ (CM1120, 28, PC0106 and 08), (b) 1Ø and $l_b/\text{Ø} = 15$ (PC0201 to 04), 3Ø and $l_b/\text{Ø} = 15$ (PC0205 to 08) and 5Ø and $l_b/\text{Ø} = 15$ (PC0209 to 12)

2.4.2 Local bond-slip relationship

Bond-slip relationship proposed in MC2010

The bond-slip relationship for pull-out failure from MC2010 has been used as starting point for the model proposed in this chapter. The relationship is composed of four branches as shown in Figure 2.16.

As discussed in the previous sections, recent experimental evidence shows some differences with respect to the MC2010 formulation. The experimental results presented in this chapter for the case of pull-out failure are limited due to the yielding of the reinforcement. Therefore, only results from the ascending branch are available. For this reason, the main studied parameters of the response in the following sections concern the ascending branch. Some of the parameters of the response proposed in MC2010 that govern the post-peak response are accepted:

- α : exponent of the ascending branch with a recommended value of 0.4
- τ_{bf} : frictional bond stress with a value of $0.4 \cdot \tau_{b,max}$
- δ_{sc2} : slip corresponding to the end of the plateau with a value $2 \cdot \delta_{sc1}$
- δ_{sc3} : slip corresponding to the end of the descending branch with a value equal to c_{clear}

These parameters have not been explicitly validated. Nevertheless, the results presented in the following sections indicate that they provide a reasonable representation of the response and are accepted without further validation.

Well-confined conditions

The pre-peak response is controlled by the maximum bond stress $\tau_{b,max}$ and the corresponding slip $\delta_{sc}(\tau_{b,max})$. A database of experimental results from the literature with short bonded lengths, well-confined conditions (MC2010 considers well-confined conditions without transverse reinforcement for $c \geq 5\emptyset$) and reported pull-out failure has been collected. All details are provided in Table 2.6 of Appendix 2B. The experimental slip at the maximum bond stress is considered equal to the slip at the end of the ascending branch of the local bond-slip relationship (δ_{sc1} , see definitions in Figure 2.16).

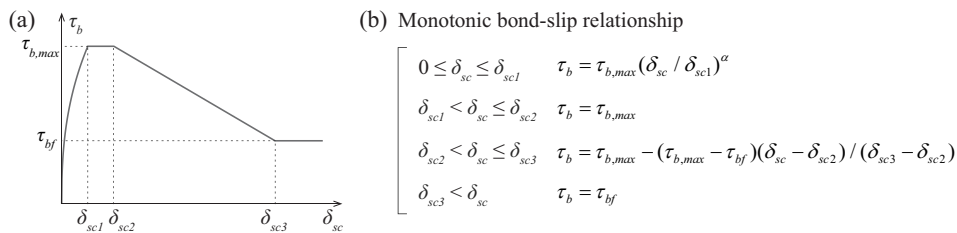


Figure 2.16: Bond-slip relationship for well-confined conditions according to MC2010: (a) parameter definition; and (b) mathematical definition of the segments.

Concerning the bond strength for good casting conditions, Huang et al. [Hua96] proposed a linear relationship between the compressive strength of concrete and the bond strength based on experimental results with normal and high-strength concrete. This relationship was then adjusted to include the size effect of the bar diameter by Bamonte et al. [Bam07]. Nevertheless, based on the existing tests, it seems that a linear relationship tends to overestimate the bond strength for higher concrete compressive strengths. For this reason, accounting also for other considerations [Moc20a], an empirical relationship with a lower exponent is proposed on the basis of the existing experimental results:

$$\tau_{bmax} = 0.53 f_{cm} \left(\frac{30}{f_{cm}} \right)^{1/6} \left(\frac{20}{\varnothing} \right)^{1/6} \quad (2.2)$$

With respect to the slip at maximum bond stress, Eligehausen et al. [Eli83] observed that it is influenced by the concrete compressive strength and by the clear spacing between ribs. Tepfers et al. [Tep92] proposed an inversely proportional relationship between the peak slip and the bond index. Various linear relationships based on the clear rib spacing have been proposed by other authors [Har95, Zha17, Lin19]. On the basis of the existing tests, the ratio between clear rib spacing and bar diameter seems to have a nonnegligible influence. Based on these considerations, the following expression is proposed:

$$\delta_{sc1} = 0.09 (c_{clear} \varnothing)^{1/2} \left(\frac{30}{f_{cm}} \right)^{1/3} \left(\frac{0.07}{f_R} \right)^{1/3} \quad (2.3)$$

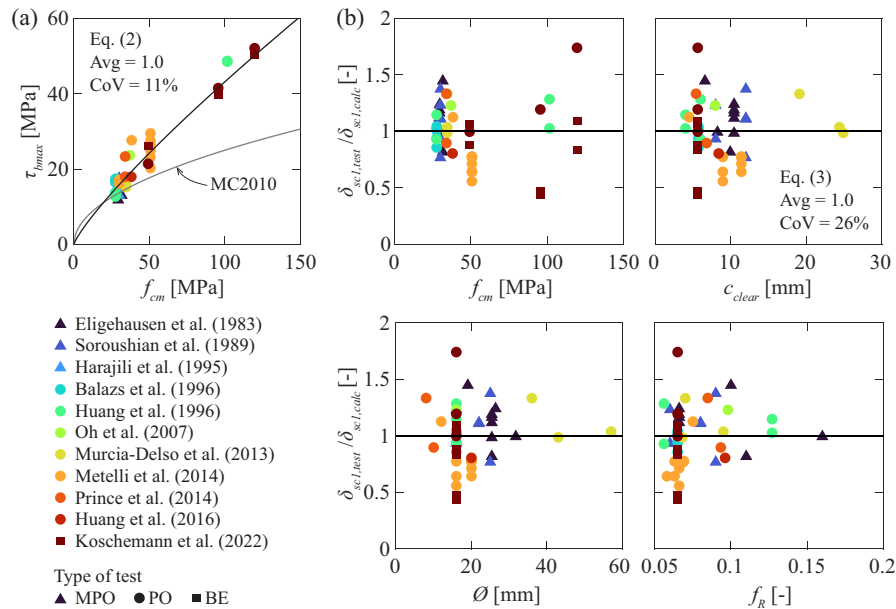


Figure 2.17: Database analysis: (a) maximum local bond stress as a function of the concrete compressive strength; and (b) comparison of measured-to-predicted slip values at the peak bond stress ($\delta_{sc1, test} / \delta_{sc1, calc}$) as a function of the concrete compressive strength, clear rib spacing, bar diameter and bond index (MPO = modified pull-out test, PO = standard pull-out test and BE = beam-end test).

As shown in Figure 2.17a, Equation 2.2 describes better the influence of the compressive concrete strength on the bond strength than the MC2010 provision. Figure 2.17b compares the results of the proposed expression for the slip corresponding to the maximum bond stress with the experimental values. Equation 2.3 shows good agreement with the database results with a reasonable scatter considering the variability in bond results (Table 2.1).

Concerning bars in poor casting conditions, Moccia et al. [Moc20, Moc21] measured the size of the voids under reinforcement bars cast in horizontal position using tomography. They observed larger voids with the increase of the height above the bottom of the formwork and proposed a method for the quantification of the bond strength of horizontal bars in poor casting conditions estimating the size of the voids under the bar using the model by Brantschen et al. [Bra16] that proposes a reduction of the bond strength due to the effect of a longitudinal crack parallel to the bar. The reduction factor is assumed to be proportional to the reduction of the area of contact between the ribs and the surrounding concrete (Figure 2.18a). The reduction factor is calculated using Equation 2.4 on the basis of the crack width (w), the nominal bar diameter (\varnothing), the bond index (f_R) and a proportionality factor ($\kappa_f = 0.75 n_l$) that accounts for the number of lugs that compose the rib (n_l). According to Brantschen et al. [Bra16], the crack opening leads to an additional slip related to the transverse rib flank inclination (α_R) that can be estimated using Equation 2.5 (Figure 2.18b). The void size (in this case equivalent to the crack width) can be estimated using Equation 2.6 on the basis of the plastic settlement strain (s_{ps}) and the height above the bottom of the formwork (h).

$$\eta_2 = \frac{\tau_b}{\tau_{b0}} = \frac{1}{1 + \frac{\kappa_f w}{f_R \varnothing}} \quad (2.4)$$

$$\Delta\delta_{sc} = \frac{w}{2} \cot \alpha_R \leq h_R \cot \alpha_R \quad (2.5)$$

$$w = h \cdot s_{ps} \quad (2.6)$$

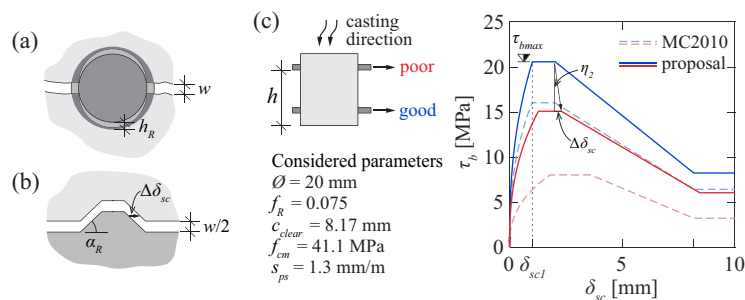


Figure 2.18: Influence of casting conditions in the local bond-slip relationship: schematic representation of the effect of a longitudinal crack along the bar: (a) reduction of the lug contact area and (b) slip increment due to the generated gap for an idealized rib geometry; and (c) proposed expressions for well-confined conditions compared to MC2010. update

Table 2.5 Parameters defining the proposed and the MC2010 local bond-slip relationships for pull-out failure (for definition of parameters, refer to section Notation and Figure 2.18c).

Parameter	Proposed expressions		MC 2010	
	Good casting conditions	Poor casting conditions	Good casting conditions	Poor casting conditions
$\tau_{b,max}$	Eq. 2.2	$\eta_2 \cdot (\text{Eq. 2.2})$	$2.5 \cdot f_c^{1/2}$	$2.5 \cdot \eta_2 \cdot f_c^{1/2}$
τ_{bf}	$0.4 \cdot \tau_{b,max}$	$0.4 \cdot \tau_{b,max}$	$0.4 \cdot \tau_{b,max}$	$0.4 \cdot \tau_{b,max}$
δ_{sc1}	Eq. 2.3	Eq. 2.3 + $\Delta\delta_{sc}$	1.0 mm	1.8 mm
δ_{sc2}	2 · (Eq. 2.3)	2 · (Eq. 2.3) + $\Delta\delta_{sc}$	2.0 mm	3.6 mm
δ_{sc3}	c_{clear}	$c_{clear} + \Delta\delta_{sc}$	c_{clear}	c_{clear}
α^{la}	0.4	0.4	0.4	0.4
η_2	-	Eq. 2.4	-	0.5
$\Delta\delta_{sc}$	-	Eq. 2.5	-	-

^a Parameter α is the exponent for the 1st branch of the relationship

The plastic settlement void will appear on the underside of the bar; therefore, a part of the lugs is likely to remain in contact with the concrete closer to the equator of the bar and on the upper part of the bar. Furthermore, chemical adhesion and friction will act in most of the perimeter of the bar [FIB00]. This is consistent with the absence of large slips for low pull-out forces (Figure 2.9). As the force increases, it is assumed that the bar will tend to centre around the void. Consequently, the reduction factor is calculated assuming a symmetric crack about a horizontal axis. values of the bond stresses. For this reason, the initial slip for poor casting conditions is kept as zero, whereas the other points of the bond-slip relationship are adjusted using Equations 2.4 and 2.5. The parameters defining the proposed local bond-slip relationship are summarized in Table 2.5. The proposal is compared with the original expressions of MC2010 in Figure 2.18c.

Low and moderate confinement

The experimental measurements presented in this article show that significant cracking in the bonded region occurs due to bond for covers between 1 and 3 \emptyset . Consequently, for such conditions, the assumption of a reduction of the bond strength solely caused by the existence of one crack parallel to the bar cracks can be unrealistic.

Equation 2.4 is a simplification for practical purposes of the actual variation of the contact surface with one crack. The proportionality factor has been calibrated based on a numerical analysis of bars with different number and types of lugs in order to provide a satisfactory estimation for the possible different orientations [Bra16a].

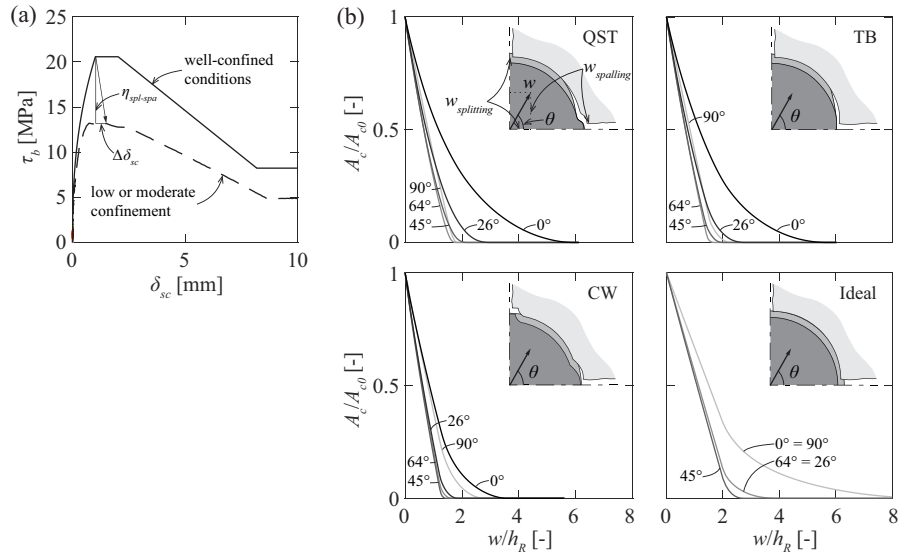


Figure 2.19: Local bond-slip relationship for low or moderate confinement: (a) schematic representation of the proposed reduction factor; and (b) rib contact surface reduction for different crack kinematics for QST, TB, CW bars and an idealized rib geometry.

For low and moderately confined bars, the experimental results have shown the presence of two sets of cracks approximately parallel to the bar (splitting and spalling cracks). In the following, the ratio between a horizontal splitting component and a vertical spalling component will be defined by the angle θ (Figure 2.19b). The two extreme cases considered by Brantschen et al. [Bra16] correspond to the effect of a single crack: a splitting crack ($\theta = 0^\circ$) or a spalling crack ($\theta = 90^\circ$).

The influence of this parameter in the evolution of the rib contact area (A_c/A_{c0}) for the tested bars and for an idealized geometry is shown in Figure 2.19b. For all considered rib geometries, the largest reductions correspond to angles of 45° or 64° . For the bars with two lugs (QST and TB), the largest reductions are similar to the case of 90° . However, for the CW bar with four lugs and the idealized rib geometry, the reduction is significantly larger for $\theta = 45^\circ$ (splitting and spalling cracks with the identical opening). Consequently, a coefficient κ_m is introduced in Equation 2.4 with a value of 1.3 to account for cases with multiple cracks. The resulting bond strength reduction factor (Figure 2.19a) is:

$$\eta_{spl-spa} = \frac{\tau_b}{\tau_{b0}} = \frac{1}{1 + \frac{\kappa_f \kappa_m w}{f_R \emptyset}} \quad (2.7)$$

Comparison to test results

Figure 2.20a compares the model for well-confined conditions with the local measurements from specimens PC0209 to 12 with a cover of $5\emptyset$. For good casting conditions, the proposal follows

better the measured response within the region not affected by the cone breakout. In this case, the stiffness of the response remains slightly underestimated. The smaller bond stresses measured for specimen PC0212 can be explained by the larger crack widths measured (Figure 2.15d).

The theoretical bond-slip relationship for poor casting conditions plotted in Figure 2.20a has been calculated assuming a plastic settlement of 1.3 mm/m (estimated void size ≈ 0.36 mm) [Moc21]. They show a relatively fine agreement with the test results (average response between the results of the two bar orientations). The local bond-slip measurements from specimens PC0209 and 10 justify the absence of an initial slip in poor casting conditions. Specimen PC0209 (QST_{//}) displays a uniform trend with a shape similar to the curves of MC2010. Specimen PC0210 (QST_⊥) follows a similar trend for bond stresses below 3-4 MPa, after which the trend changes, leading to larger slips for comparable bond stresses. The difference is probably caused by plastic settlement voids that affect more the QST_⊥ bars.

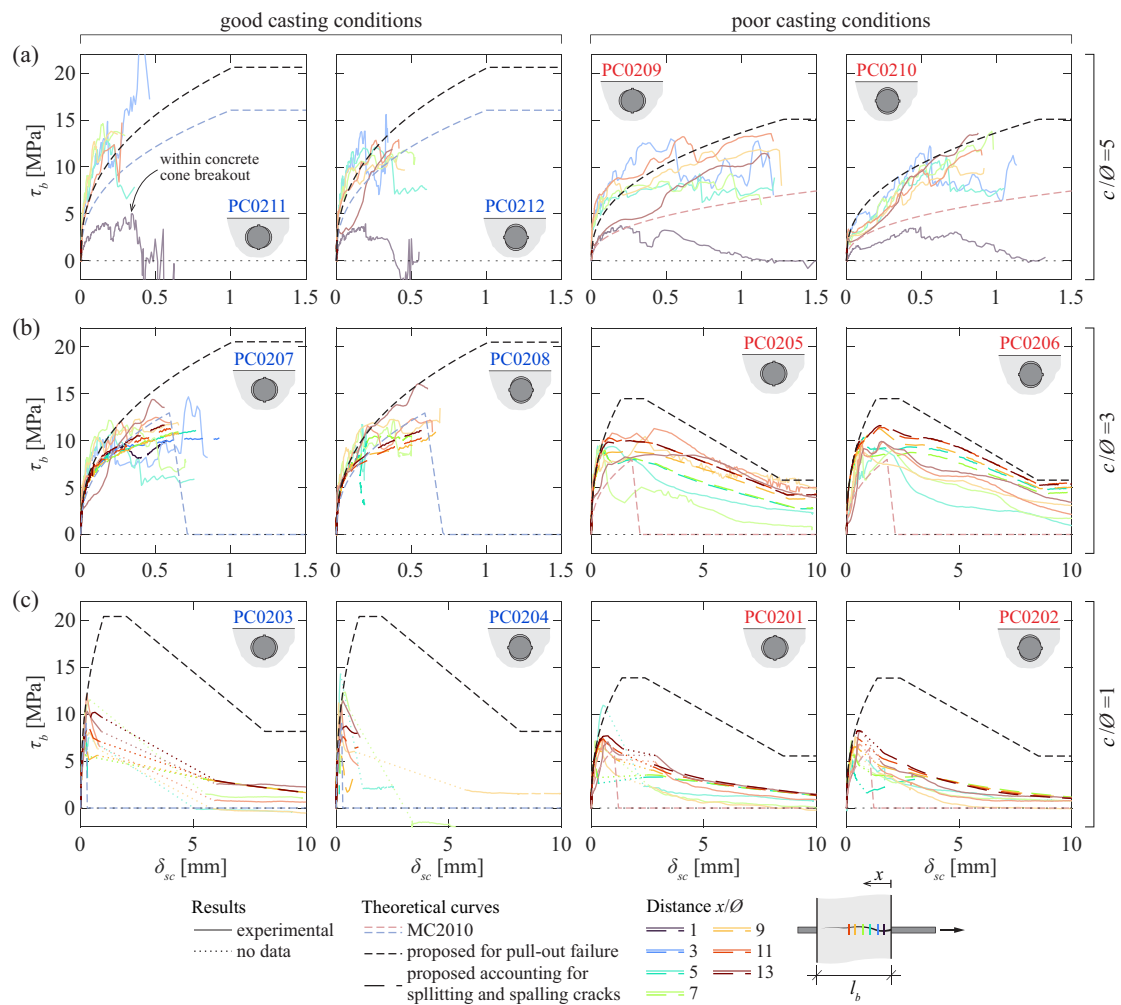


Figure 2.20: Comparison of the analytical model predictions for specimens with covers of: (a) $5\varnothing$ (PC0209-12); (b) $3\varnothing$ (PC0205-08); and (c) $1\varnothing$ (PC0201-04).

For low and moderate confinements, the crack evolution presented in Figures 2.15b and c show comparable splitting and spalling cracks for most of the bonded length, particularly before the peak force. On this basis, Equation 2.7 has been applied for specimens PC0201 to 08 with QST bars using as reference the proposed bond-slip relationship for well-confined conditions (dashed black line) and the local crack opening measurements. The crack width considered in the reduction factor corresponds to the magnitude of the vector addition of the splitting and spalling crack components. The resulting estimated local bond-slip relationships (dashed lines) are displayed in Figures 2.20b and c, and compared with the experimental measurements (solid lines). The results within the concrete cone breakout (typically from the loaded end up to a distance of around 3ϕ and shown in dark grey hatch in Figure 2.8) are not considered, as the assumption of the reference curve is not realistic. In general, the analytical results capture well the tendencies of the experimental measurements, whereas the corresponding local bond-slip relationships provided in MC2010 (light red and blue dashed lines) differ significantly from the experimental results, particularly in the post-peak range.

Describing the bond-slip relationship for unconfined conditions as a function of the measured splitting and spalling cracks can be useful to estimate the steel stress as a function of the measured cracks in case of assessment of existing structures (to estimate the risk of fatigue or the residual resistance of anchorages affected by longitudinal cracks due to corrosion for instance). In addition, this can be seen as a step forward in the development of a fully mechanical model to calculate the bond stress at SLS and the anchorage resistance at ULS in a more rational manner.

2.5 Conclusions

This chapter presents the results of an experimental programme and an analytical investigation to characterize the local bond-slip relationship along anchored bars of medium length and to establish a mechanical model to describe the effect of plastic settlement voids and cracking visible on the concrete surface on the local bond-slip relationship. The main findings of this research are summarized below:

1. The bond behaviour in structural elements is complex and the study of elements with medium and long anchorages is necessary to complement the experiments with short bonded lengths.
2. Fibre optical sensors in combination with DIC have proven to be useful to study the distribution of steel stresses and bond stresses along the anchorage length, the local bond-slip response and the influence of the cracks visible on the concrete surface. The experimental results show that cracking has an unfavourable effect on the bond performance of anchored bars.
3. The effect of concrete cover and casting direction on the bond strength agrees with previous research. The anchorage resistance increases for larger covers. The largest anchorage resistance is obtained for bars in good casing conditions, followed by bars loaded in the opposite direction of casting, and then by the bars loaded in the casting direction. The lowest resistance is obtained for bars in poor casting conditions.

4. The effect of the rib orientation with respect to the concrete surface is more relevant for anchorages with low covers governed by spalling of the concrete cover. In well-confined conditions, the anchorage resistance of bars with similar bond indexes but different rib geometries can differ by more than 15%. In such conditions, the anchorage response is not sufficiently well characterized accounting only for the bond index.
5. In specimens with medium anchorage lengths and moderate or well-confined conditions, the behaviour is less brittle, and the effect of the redistribution of bond forces due to a lower stiffness of the local bond response can lead to a higher anchorage resistance, even if lower local bond stresses are activated.
6. The measured local bond-slip relationships show higher stiffness than the MC2010 expressions for all the tested conditions and parameters. Specimens with a cover of 3ϕ do not display such a brittle post-peak response as the corresponding unconfined splitting failure proposed in MC2010. They failed by splitting induced pull-out developing bond stresses even for slip values similar to the rib spacing.
7. A local bond-slip model for deformed bars with pull-out failure (well-confined conditions) is proposed based on the analysis of a database of tests collected from the literature. The model for poor casting conditions is derived based on mechanical considerations due to the voids under the bar caused by plastic settlement.
8. The differences in the local bond-slip responses for low and moderate confinements, with respect to the pull-out failure, can be explained by the development of spalling cracks (parallel to the bar and approximately parallel to the concrete surface), splitting cracks (parallel to the bar and approximately perpendicular to the concrete surface) and conical cracks leading to concrete cone breakouts near the loaded end of the bar.
9. For these phenomena, a simple model is proposed to quantify the bond strength reduction as a function of the measured opening of longitudinal cracks in the bonded region.

Appendix 2A: Pull-out test results

Detailed measurements for all tests are provided in this section:

- Figure 2.21: PC0202, PC0203, PC0204 and PC0206
- Figure 2.22: PC0207, PC0208, PC0210 and PC0211
- Figure 2.23: PC0212, PC0213, PC0214 and PC0215
- Figure 2.24: PC0216, PC0217, PC0218 and PC0220
- Figure 2.25: PC0221, PC0222, PC0223 and PC0101
- Figure 2.26: PC0103, PC0106, PC0108, CM1120, CM1128 and CM1124

Results for PC0201, PC0205, PC0209 are provided in Figure 2.8.

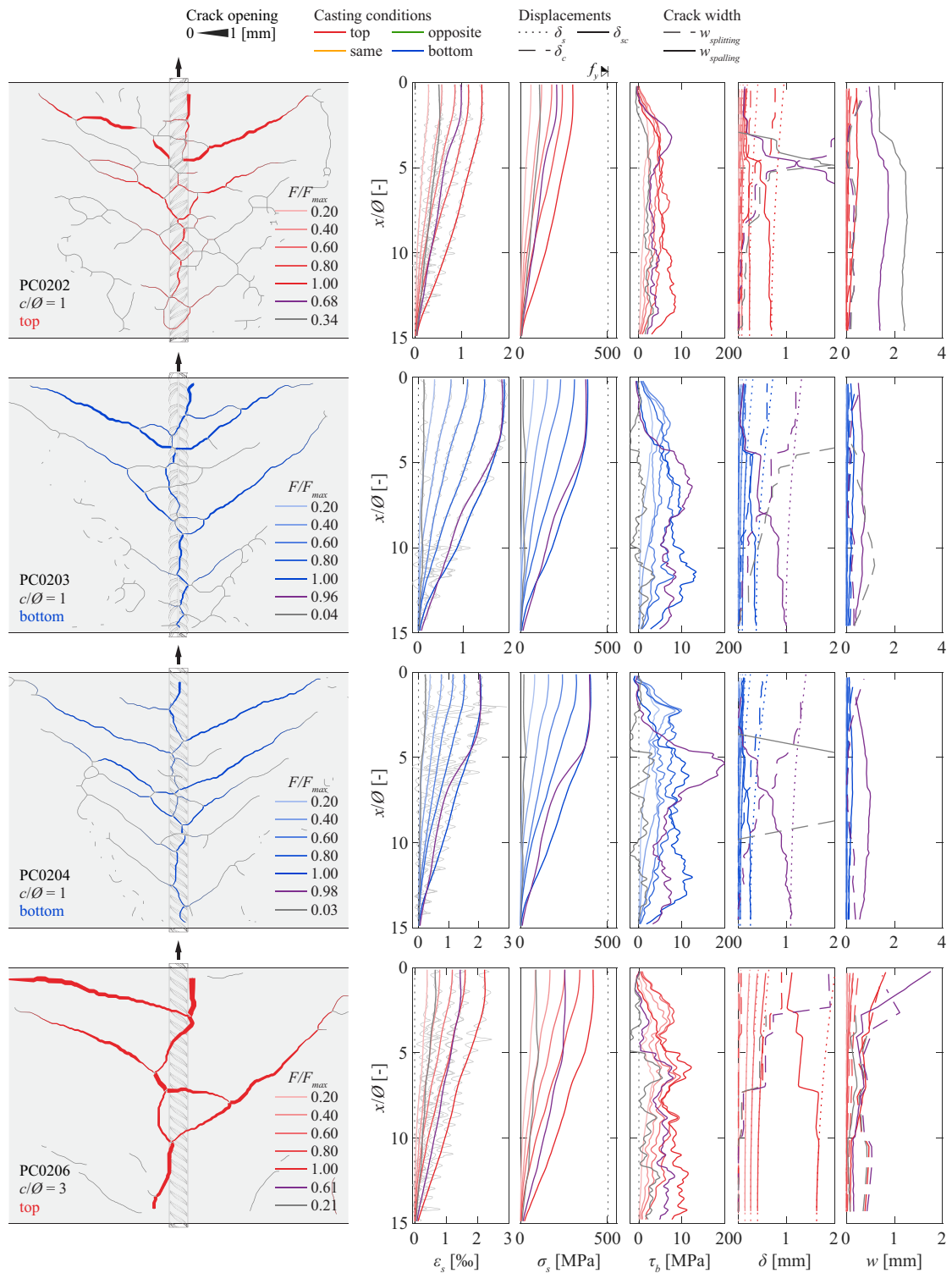


Figure 2.21: Crack pattern and distribution along the anchorage length of axial steel strains, axial steel stresses, bond stresses, slip and crack widths for specimens: PC0202, PC0203, PC0204 and PC0206.

Bond of steel reinforcement based on detailed measurements

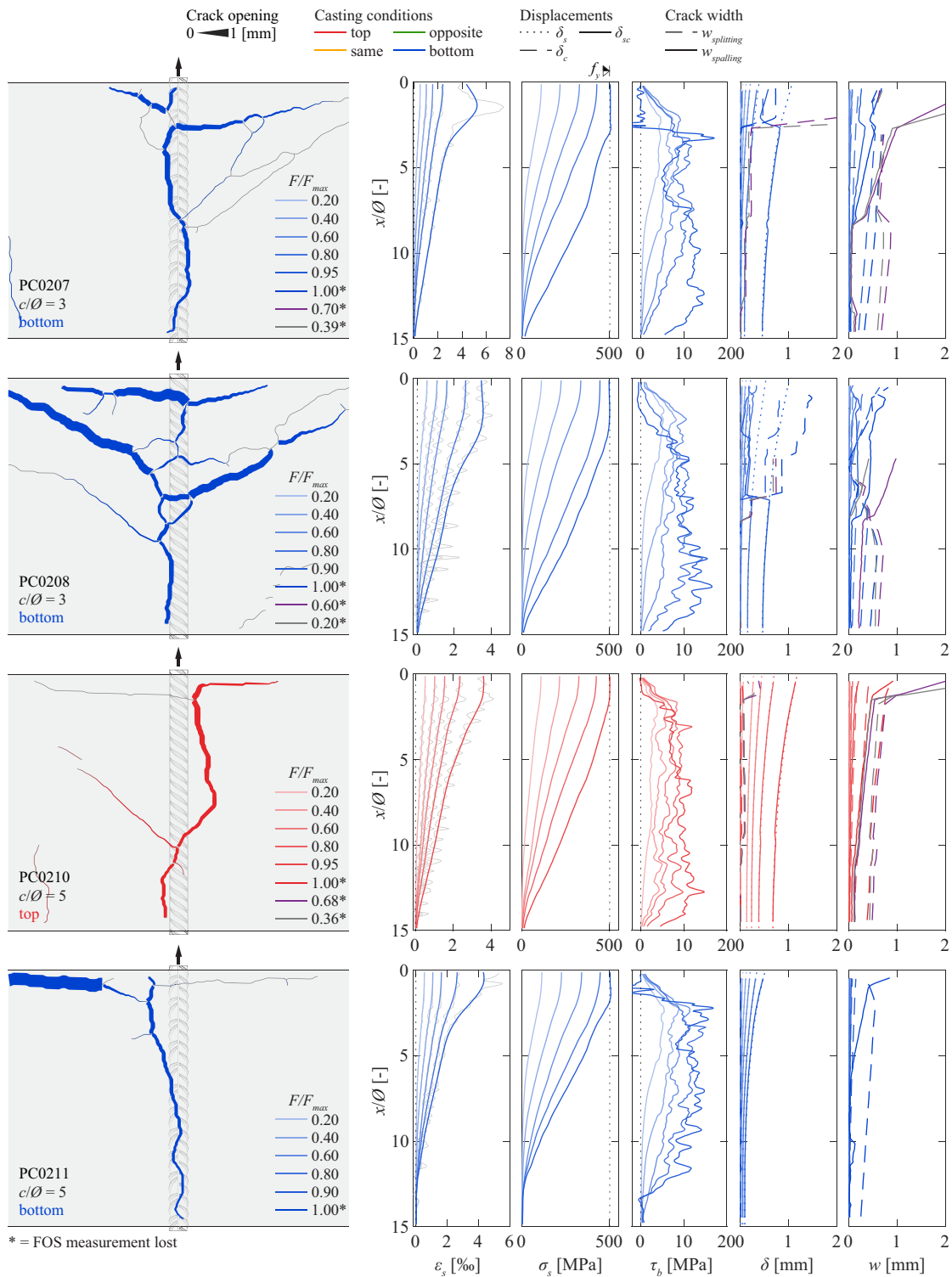


Figure 2.22: Crack pattern and distribution along the anchorage length of axial steel strains, axial steel stresses, bond stresses, slip and crack widths for specimens: PC0207, PC0208, PC0210 and PC0211.

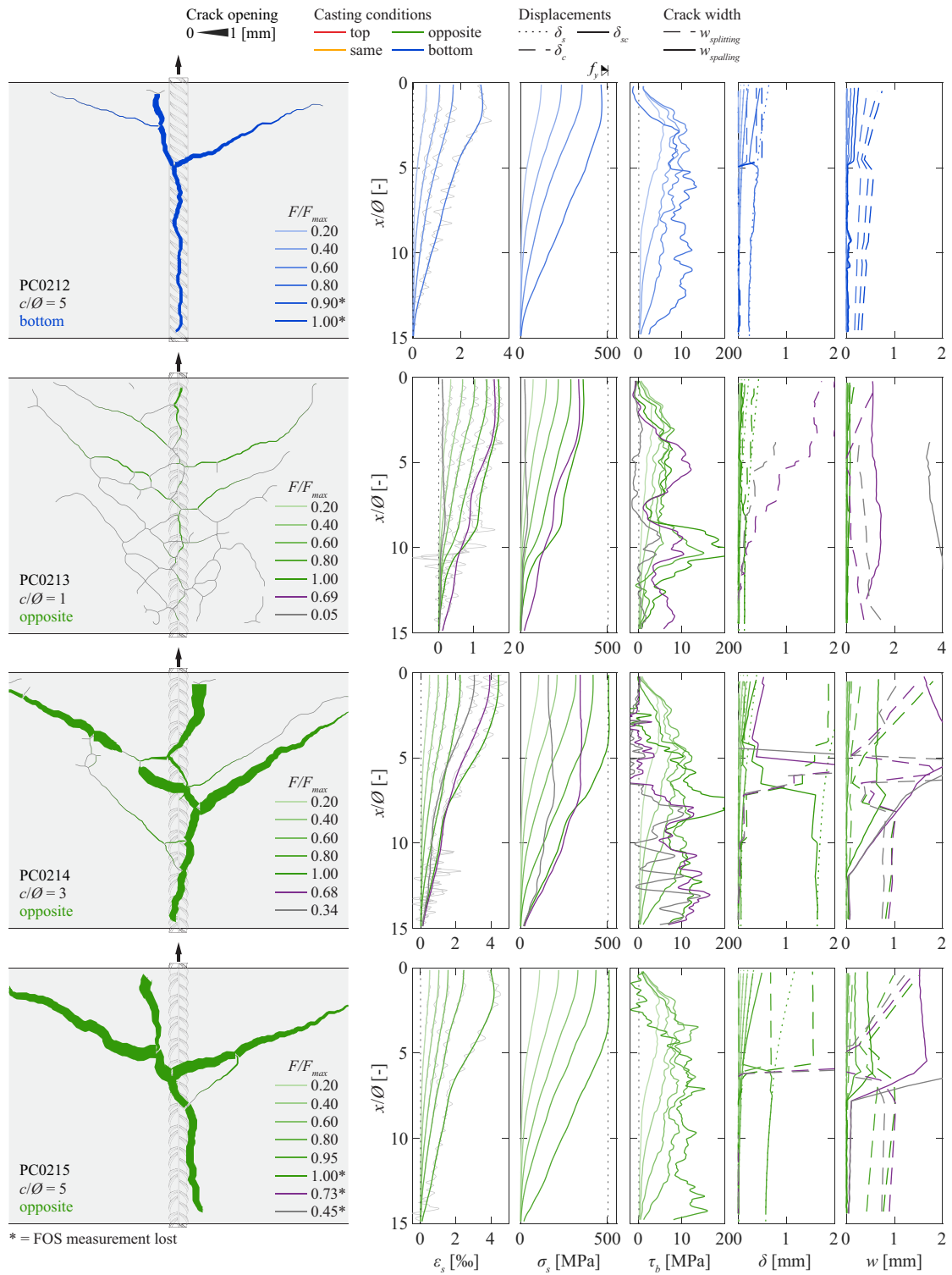


Figure 2.23: Crack pattern and distribution along the anchorage length of axial steel strains, axial steel stresses, bond stresses, slip and crack widths for specimens: PC0212, PC0213, PC0214 and PC0215.

Bond of steel reinforcement based on detailed measurements

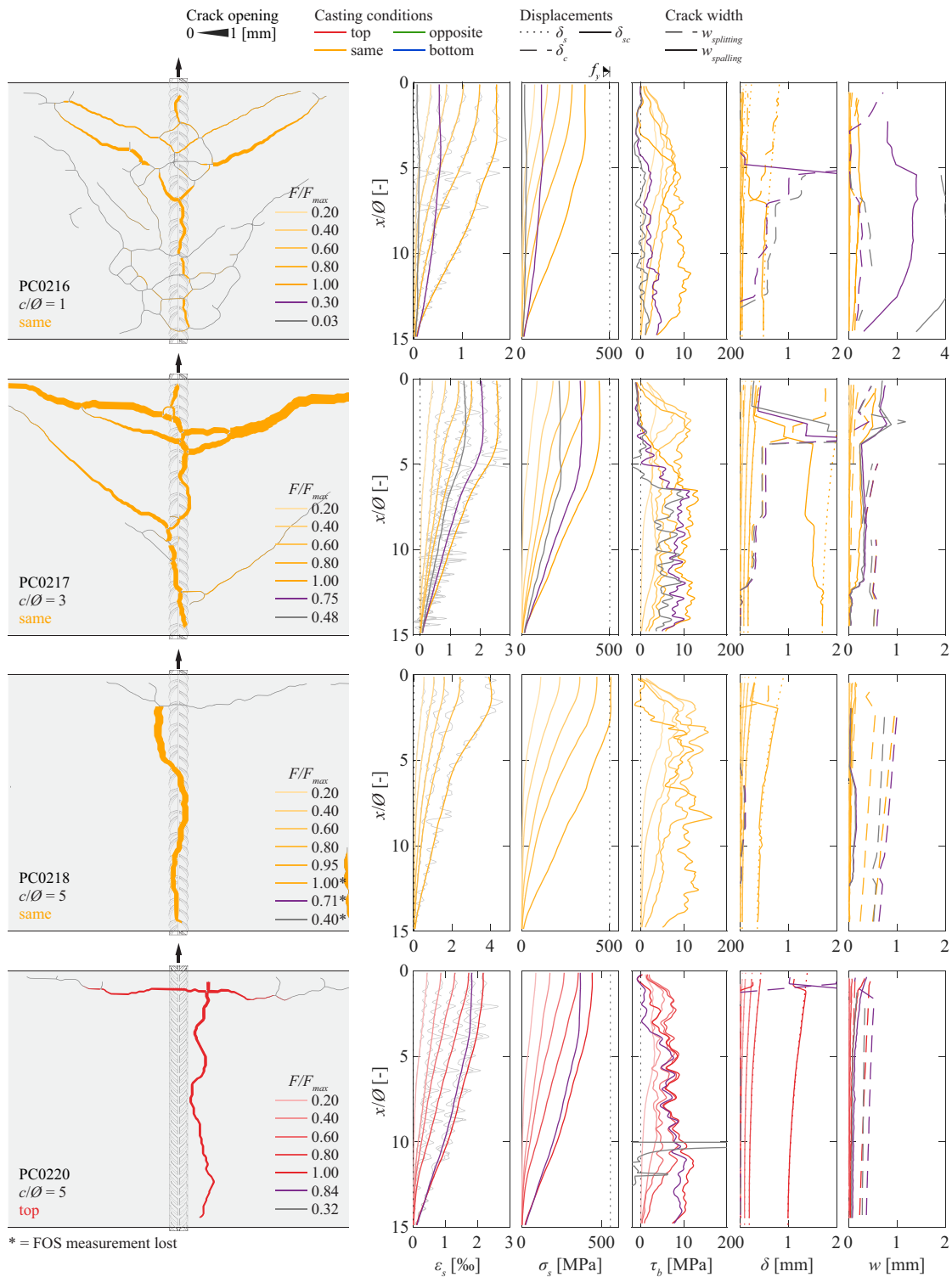


Figure 2.24: Crack pattern and distribution along the anchorage length of axial steel strains, axial steel stresses, bond stresses, slip and crack widths for specimens: PC0216, PC0217, PC0218 and PC0220.

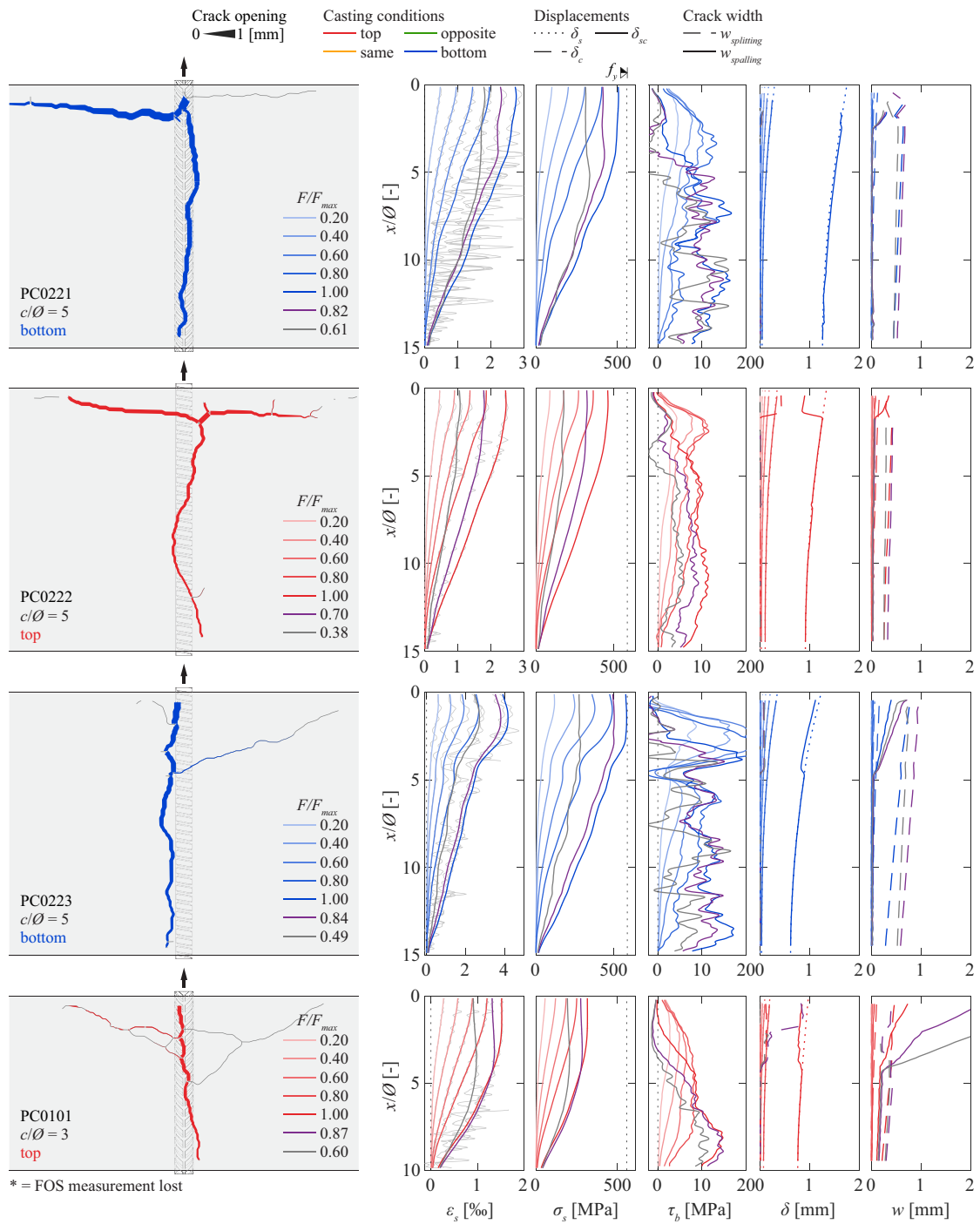


Figure 2.25: Crack pattern and distribution along the anchorage length of axial steel strains, axial steel stresses, bond stresses, slip and crack widths for specimens: PC0221, PC0222, PC0223 and PC0101.

Bond of steel reinforcement based on detailed measurements

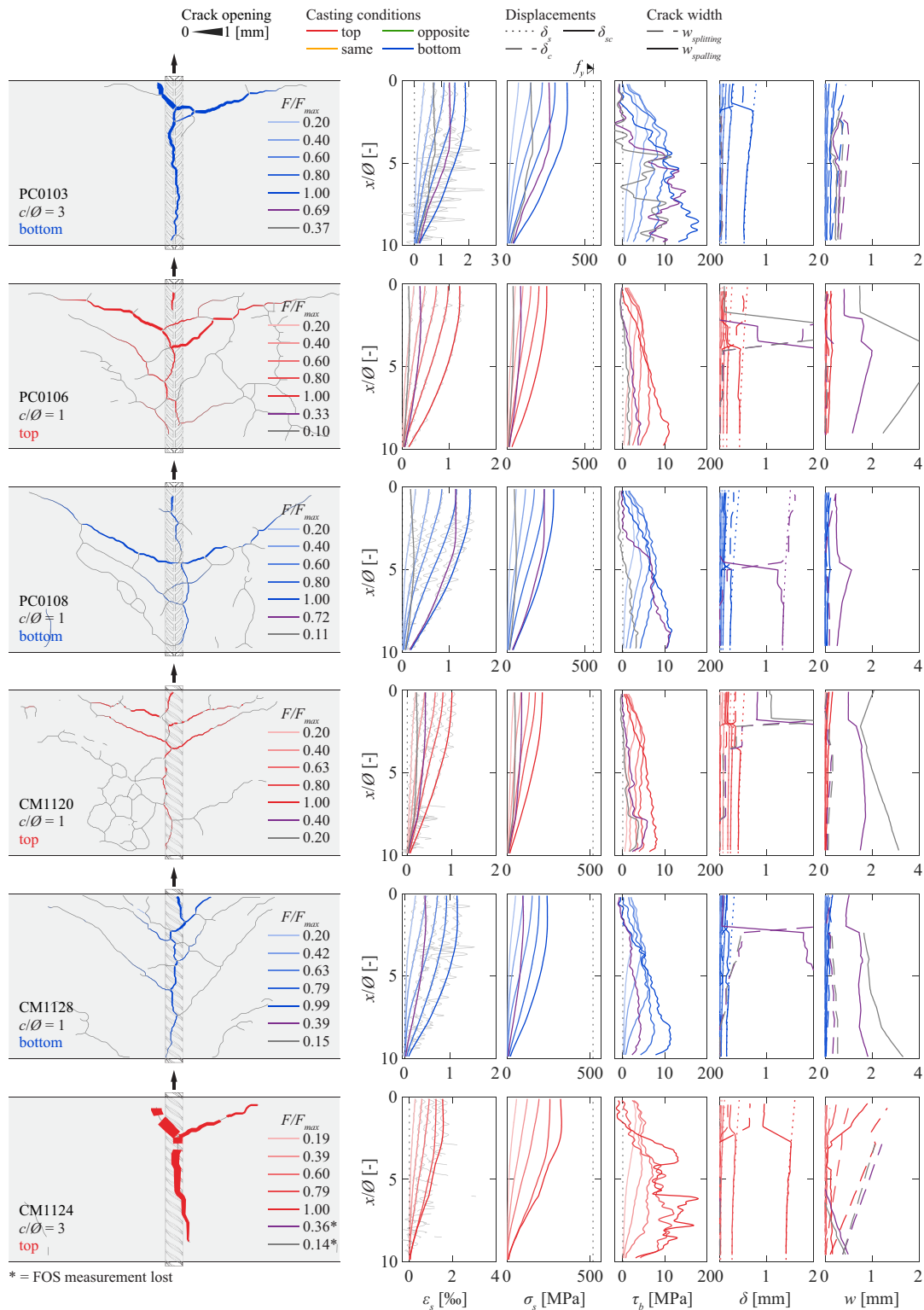


Figure 2.26: Crack pattern and distribution along the anchorage length of axial steel strains, axial steel stresses, bond stresses, slip and crack widths for specimens: PC0103, PC0106, PC0108, CM1120, CM1128 and CM1124.

Appendix 2B: Experimental database

The main parameters of the experimental database of short pull-out tests in well-confined conditions with pull-out failure are provided in Table 2.6. For definition of parameters, refer to section Notation. The references of the considered tests are:

- Eligehausen et al. (1993) [Eli83]
- Soroushian et al. (1989) [Sor89]
- Harajili et al. (1995) [Har95]
- Balazs et al. (1996) [Bal96]
- Huang et al. (1996) [Hua96]
- Oh et al. (2007) [Oh07]
- Murcia-Delso et al. (2013) [Mur13]
- Metelli et al. (2014) [Met14]
- Prince et al. (2014) [Pri13]
- Huang et al. (2016) [Hua16]
- Koschemann et al. (2022) [Kos22a]

Table 2.6: Main parameters of the experimental database of short pull-out tests in well-confined conditions with pull-out failure

Reference	Series	Type of test	Type of bar	n_t	θ [mm]	c/θ	l_b/θ	f_R	s_R [mm]	c_{clear} [mm]	b [mm]	h_R [mm]	θ_s [mm]	n_s	f_c [MPa]	δ_{sc} [mm]	τ_{max} [MPa]	$\delta_{sc,calc}$	$\tau_{b,max,calc}/\tau_{b,max,MC10}$	$\tau_{b,max,calc}/\tau_{b,max,calc}$
Elgehausen et al. (1983)	Series 1.1	MPO	C	3	25.4	2.0	5	0.066	14.0	10.4	3.6	-	25.4	4	29.4	1.79	13.5	1.19	0.99	0.90
	Series 1.2	MPO	C	3	25.4	2.0	5	0.066	14.0	10.4	3.6	-	12.7	4	29.4	1.48	13.6	0.98	1.00	0.91
	Series 1.3	MPO	C	3	25.4	2.0	5	0.066	14.0	10.4	3.6	-	6.35	4	29.4	1.68	11.8	1.12	0.87	0.79
	Series 1.5	MPO	C	3	25.4	2.0	5	0.066	14.0	10.4	3.6	-	12.7	4	29.4	1.75	14.0	1.16	1.03	0.93
	Series 2.1	MPO	C	2	26.4	2.0	5	0.066	14.0	10.4	3.6	-	12.7	4	29.6	1.90	13.7	1.24	1.01	0.92
	Series 3.1	MPO	C	2	19.1	2.0	5	0.100	9.7	6.6	3.1	-	12.7	4	31.6	1.27	15.9	1.45	1.13	0.96
	Series 3.2	MPO	C	2	25.4	2.0	5	0.110	13.4	9.9	3.5	-	12.7	4	31.6	0.99	15.3	0.82	1.09	0.97
	Series 3.3	MPO	C	2	31.8	2.0	5	0.160	13.5	8.2	5.3	-	12.7	4	31.6	1.08	13.0	0.99	0.93	0.85
	#5-1	MPO	C	1	16.0	2.0	5	0.060	10.0	8.0	2.0	2.0	0.6	12.7	4	30.0	1.32	17.6	1.23	1.28
#5-2	MPO	C	1	16.0	2.0	5	0.060	10.0	8.0	2.0	2.0	0.6	12.7	4	30.0	1.00	17.2	0.93	1.26	1.05
Soroushian et al. (1989)	#7-1	MPO	C	1	22.0	2.0	5	0.080	13.6	12.0	1.6	1.2	12.7	4	30.0	1.55	15.7	1.11	1.15	1.01
	#7-2	MPO	C	1	22.0	2.0	5	0.080	13.6	12.0	1.6	1.2	12.7	4	30.0	1.56	14.9	1.12	1.09	0.96
	#8-1	MPO	C	1	25.0	2.0	5	0.090	14.4	12.0	2.4	1.3	12.7	4	30.0	1.10	14.8	0.77	1.08	0.97
	#8-2	MPO	C	1	25.0	2.0	5	0.090	14.4	12.0	2.4	1.3	12.7	4	30.0	1.97	15.1	1.37	1.10	0.99
Harajili et al. (1995)	P2 Vf=0	MPO	C	4	20.0	1.4	3.5	-	8.0	5.9	2.1	-	10	4	30.0	1.46	13.0	-	0.95	0.82
	P1 Vf=0	MPO	C	4	25.0	1.5	3.5	-	15.4	12.2	3.2	-	10	4	30.0	2.96	15.1	-	1.10	0.99
Balazs et al. (1996)	Monotonic	PO	C	1	16.0	2.6	1.25	0.065	8.8	5.7	3.0	-	-	-	27.6	0.78	13.7	0.86	1.05	0.90
	Monotonic	PO	C	1	16.0	2.6	1.25	0.065	8.8	5.7	3.0	-	-	-	27.6	0.85	13.7	0.94	1.04	0.89
	Monotonic	PO	C	1	16.0	2.6	1.25	0.065	8.8	5.7	3.0	-	-	-	27.6	0.95	16.4	1.04	1.25	1.07
	Monotonic	PO	C	1	16.0	2.6	1.25	0.065	8.8	5.7	3.0	-	-	-	27.6	0.93	17.4	1.02	1.33	1.14
	Monotonic	PO	C	1	16.0	2.6	1.25	0.065	8.8	5.7	3.0	-	-	-	27.6	0.92	17.0	1.01	1.29	1.11
Huang et al. (1996)	N40-K500	PO	C	4	16.0	8.9	2.5	0.056	8.9	6.0	-	-	-	-	27.5	0.91	13.4	0.93	1.02	0.88
	N40-Ks60S	PO	C	3	16.0	8.9	2.5	0.127	7.0	4.0	-	-	-	-	27.5	0.70	12.7	1.15	0.97	0.83
	H40-K500	PO	C	4	16.0	8.9	2.5	0.056	8.9	6.0	-	-	-	-	101.6	0.81	48.5	1.28	1.93	1.07
	H40-Ks60S	PO	C	3	16.0	8.9	2.5	0.127	7.0	4.0	-	-	-	-	101.6	0.40	48.7	1.03	1.93	1.07
Oh et al. (2007)	Monotonic	PO	C	1	16.0	4.2	2	0.098	11.6	8.0	3.6	1.1	-	-	37.0	1.04	23.7	1.23	1.56	1.21
	Series 1	PO	C	1	36.0	12.2	5	0.070	-	19.1	-	-	13	6	34.5	3.00	15.2	1.33	1.04	0.94
	Series 2	PO	C	1	43.0	10.1	5	0.068	-	24.9	-	-	13	7	34.5	2.80	16.2	0.99	1.10	1.03
Murcia-Delso et al. (2013)	Series 3	PO	C	2	57.0	7.5	5	0.095	-	24.4	-	-	13	9	34.5	3.00	17.6	1.04	1.20	1.18

Reference	Series	Type of test	Type of bar	n_i	θ [mm]	c/θ	l/θ	f_r	s_r [mm]	c_{clear} [mm]	b [mm]	h_R [mm]	θ_s [mm]	n_s	f_c [MPa]	δ_{scl} [mm]	τ_{max} [MPa]	$\delta_{scl,low}/\delta_{scl,calc}$	$\tau_{hmax,steel}/\tau_{hmax,MC10}$	$\tau_{hmax,steel}/\tau_{hmax,calc}$	
Metelli et al. (2014)	Series 4-30	PO	M	1	12.0	4.5	5	0.075	6.0	4.5	1.5	0.5	-	-	38.3	0.67	27.6	1.13	1.79	1.31	
	Series 8-62	PO	M	1	16.0	4.5	5	0.063	11.0	9.0	2.0	0.5	-	-	50.7	0.72	25.0	0.77	1.40	0.98	
	Series 8-63	PO	M	1	16.0	4.5	5	0.058	11.0	9.0	2.0	0.5	-	-	50.7	0.62	26.6	0.64	1.50	1.05	
	Series 8-64	PO	M	1	16.0	4.5	5	0.066	11.0	9.0	2.0	0.5	-	-	50.7	0.52	27.5	0.56	1.54	1.08	
	Series 9-69	PO	M	1	20.0	4.5	5	0.066	13.9	11.4	2.5	0.5	-	-	50.7	0.83	29.5	0.71	1.66	1.20	
	Series 9-70	PO	M	1	20.0	4.5	5	0.069	13.9	11.4	2.5	0.5	-	-	50.7	0.88	25.1	0.77	1.41	1.02	
	Series 9-71	PO	M	1	20.0	4.5	5	0.063	13.9	11.4	2.5	0.5	-	-	50.7	0.76	20.3	0.64	1.14	0.83	
	Series 9-72	PO	M	1	20.0	4.5	5	0.069	13.9	11.4	2.5	0.5	-	-	50.7	0.89	23.1	0.78	1.30	0.94	
	Series 18-135	PO	C	1	40.0	4.5	5	0.072	-	-	-	-	-	-	30.1	2.53	17.2	-	1.25	1.21	
	Series 18-136	PO	C	1	40.0	4.5	5	0.072	-	-	-	-	-	-	30.1	2.00	16.1	-	1.17	1.14	
	Prince et al. (2014)	A8R0	PO	C	3	8.0	5.8	5	0.085	5.9	5.4	1.2	-	-	-	34.0	0.71	23.3	1.33	1.60	1.14
		A10R0	PO	C	3	10.0	4.5	5	0.093	7.5	6.8	1.2	-	-	-	34.0	0.58	18.0	0.90	1.23	0.91
Huang et al. (2016)	S000-P000-II-C	PO	C	1	20.0	3.3	3	0.096	10.4	8.4	2.0	1.0	6	4	38.0	0.78	18.0	0.80	1.16	0.93	
	C40-PO	PO	C	3	16.0	5.8	2	0.065	9.6	5.6	4.0	1.1	-	-	49.2	0.74	21.4	1.00	1.22	0.86	
	C40-BE-4	BE	C	3	16.0	4.0	2	0.065	9.6	5.6	4.0	1.1	6	2	49.2	0.79	26.1	1.06	1.49	1.05	
	C40-BE-3	BE	C	3	16.0	3.0	2	0.065	9.6	5.6	4.0	1.1	6	2	49.2	0.65	26.1	0.88	1.49	1.05	
	C80-PO	PO	C	6	16.0	5.8	2	0.065	9.6	5.6	4.0	1.1	-	-	95.6	0.71	41.5	1.19	1.70	0.96	
	C80-BE-4	BE	C	3	16.0	4.0	2	0.065	9.6	5.6	4.0	1.1	6	2	95.6	0.28	40.6	0.47	1.66	0.94	
	C80-BE-3	BE	C	3	16.0	3.0	2	0.065	9.6	5.6	4.0	1.1	6	2	95.6	0.26	39.6	0.44	1.62	0.92	
	C120-PO	PO	C	6	16.0	5.8	2	0.065	9.6	5.6	4.0	1.1	-	-	119.7	0.96	52.1	1.74	1.90	1.00	
	C120-BE-4	BE	C	3	16.0	4.0	2	0.065	9.6	5.6	4.0	1.1	6	2	119.7	0.60	50.2	1.09	1.84	0.96	
	C120-BE-3	BE	C	7	16.0	3.0	2	0.065	9.6	5.6	4.0	1.1	6	2	119.7	0.46	50.3	0.83	1.84	0.97	
All tests																	Avg *	1.00	1.31	1.00	
																		CoV *	26%	23%	11%

Type of test: PO = pull-out test; MPO = modified pull-out test; BE = beam-end test

Type of bar: C = commercial; M = machined

* Average value and coefficient of variation calculated without weighted values on the basis of multiple specimens

Notation

Lower case Latin characters

b	rib width
c	clear concrete cover
c_{clear}	clear rib spacing
f_c	cylinder compressive strength of concrete
f_R	bond index
f_t	tensile strength of reinforcement
f_y	yield strength of reinforcement
h	distance from the bar surface to the bottom of the formwork
$h_{R,avg}$	average rib height
$h_{R,max}$	maximum rib height
l_b	bonded length
n_l	number of lugs that compose the rib
n_s	number of transverse reinforcement stirrups
n_t	number tests
s_{ps}	plastic settlement strain
s_R	transverse rib spacing
w	crack width
x	coordinate

Upper case Latin characters

A_c	rib contact area
F_{max}	maximum pull-out force

Lower case Greek characters

α	exponent for the ascending branch of the bond-slip relationship of MC2010
α_R	transverse rib flank inclination
β	transverse rib angle
δ_s	bar displacement
δ_c	concrete displacement
δ_{sc}	relative slip
$\delta_{sc}(\tau_{b,max})$	slip corresponding to the maximum bond stress
$\delta_{sc,end}$	relative slip at the unloaded end of the bar
δ_{sc1}	slip at the end of the ascending branch of the local bond-slip relationship
δ_{sc2}	slip at the end of the plateau of the local bond-slip relationship
δ_{sc3}	slip at the beginning of the residual frictional branch
ϵ_s	bar axial strain
η_2	bond stress reduction factor for poor casting conditions
$\eta_{spl-spa}$	bond stress reduction factor due to splitting and spalling cracks
θ	ratio between splitting and spalling components of the crack width
κ_f	proportionality factor

κ_m	factor to account for the presence of multiple cracks
σ_s	bar axial stress
σ_{sR}	maximum stress at the loaded end of the bar
τ_b	bond stress
τ_{b0}	reference bond stress
$\tau_{b0.1}$	bond stress corresponding to a slip at the unloaded end of 0.1 mm
τ_{bf}	residual frictional bond strength
$\tau_{b,avg}$	average bond stress over the bonded length
$\tau_{b,max}$	maximum bond stress

Other characters

\emptyset	bar diameter
\emptyset_s	transverse stirrup bar diameter

Bond of steel reinforcement based on detailed measurements

3

Local bond-slip model based on mechanical considerations

This chapter is the pre-print version of the article mentioned below, submitted to Engineering Structures:

Corres E., Muttoni A., *Local bond-slip model based on mechanical considerations*, [article submitted to Engineering Structures].

The work presented in this publication was performed by the author under the supervision of Prof. Aurelio Muttoni who provided constant and valuable feedback, proofreading and revisions of the manuscript. The main contributions of the author to this article and chapter are the following:

- Comprehensive literature review including research and design standards about the bond-slip relationship.
- Extension of the database presented in Chapter 2 of short pull-out tests in well-confined conditions.
- Interpretation and integration of the different phenomena and factors involved in the interaction between the reinforcement and the concrete.
- Proposal of the expressions to estimate the pull-out bond strength and the correspondent slip.
- Adaptation of the fib Model Code 2010 bond-slip relationships to provide a gradual transition and to cover the different confinement conditions.
- Redaction of the manuscript of the article and production of its figures and tables.

Abstract

Bond between reinforcing bars and concrete is an important part of the behaviour of reinforced concrete structures. The interface response is typically characterized by the bond stress-slip relationship. Several relationships can be found in the literature accounting for different parameters. In many cases, the expressions are calibrated with the experimental databases, resulting in a wide variety of analytical relationships and factors that are strongly affected by the selected experiments in the database. In this chapter, a thorough review of the literature is presented to identify the relevant parameters influencing the bond-slip relationship. On this basis, a bond-slip relationship for well-confined conditions is proposed combining analytical models for some aspects of the response and mechanical considerations to explain the considered factors. The results are compared with a database of 151 tests in well-confined conditions showing good agreement with the results. Additionally, expressions for other confinement conditions are proposed by adapting the model of the *fib* Model Code 2010 to provide a transition between the unconfined and the well-confined regimes.

3.1 Introduction

Bond forces appear at the interface between reinforcing bars and concrete when relative displacement (defined as slip) occurs between the two materials. These forces play a crucial role in the behaviour of reinforced concrete structures at the serviceability and ultimate limit states, influencing cracking, tension stiffening, rotational capacity of plastic hinges or lap splice and anchorage strength amongst other phenomena. The relevance of bar-to-concrete bond is reflected in the extensive research conducted on the topic [CEB77, ACI92, FIB00, ACI03, ACI12, FIB14, FIB22]

The interface response is typically characterized at the local level by the relationship between the bond stress τ_b and the slip δ_{sc} (see Figure 3.1a). It is generally obtained from pull-out tests with short bonded lengths (l_b), typically five bar diameters, where the bond stress distribution can be assumed to be uniform [FIB00]. Figure 3.1b shows the geometry of the standard pull-out test [RIL78, EN105]. Another frequent alternative is the beam-end test schematically represented in Figure 3.1c [AST15, Met23]. Ribbed bars are widely used in Europe since the 1950s and replaced the previously used plain or twisted bars [Cai21]. Nowadays, the most common solution are ribbed bars and, less frequently, indented bars. For this reason, this article focuses on ribbed bars.

For ribbed bars, the main force transfer mechanism is the mechanical interlock of the lugs and the concrete leading to stress concentrations near the lugs [CEB79, FIB00]. Recently, with the use of distributed fibre optical sensors, the stress peaks at the lugs can be measured [Can20, Gal21]. The local response is directly related to the cracking of the concrete surrounding the bar triggered by the presence of the ribs [FIB00]. Consequently, it is a local phenomenon highly influenced by the properties of the concrete in the vicinity of the rib, including the distribution of aggregates [Oke20]. This is reflected in the considerable variability in the results of virtually identical tests, that display coefficients of variation reaching 18% for the maximum bond stress and 23% for the corresponding slip [Tep92, Met14, Cor23].

The experimental results show the influence of a large number of parameters. There is good agreement on the favourable effect of the confinement on the bond strength. This can be provided by the concrete cover (c), by transverse reinforcement (passive confinement) or by transverse pressure (active confinement). Three categories of confinement are often considered in the literature: well-confined, moderately-confined and unconfined, that lead to different bond slip responses and failure modes [FIB00], as shown in Figure 3.1a. For low confinement conditions (thin cover and no transverse reinforcement), splitting cracks propagate through the cover and cause a brittle failure of the specimen. For moderate confinements (larger covers and/or some transverse reinforcement), the reinforcement prevents the brittle failure and larger bond stresses are developed. In well-confined conditions (large covers and/or heavy transverse reinforcement), the concrete keys between the bar rib lugs are sheared off causing the so-called pull-out failure, leading to a relatively ductile bond-slip response.

The effect of casting conditions is known since first half of the 20th century [Abr13, Cla49]. For short bonded lengths, due to bleeding and plastic settlement voids the bond-slip response of bars cast near the top of the formwork (poor casting conditions) display smaller bond strengths and a

less stiff response that when they are placed in the bottom of the formwork (good casting conditions), see Figure 3.1a [FIB13, Moc20, Moc21, Cai22].

In general, the bar and rib geometry influence the bond performance. The nominal bar diameter (\varnothing) is calculated based on the weight per unit of length [EN105] whereas in ribbed bars, the actual shaft diameter (\varnothing_s) is smaller than the nominal value. Figure 3.1d shows the maximum rib height $h_{R,max}$, the transverse rib spacing s_R , the transverse rib angle β_R , the transverse rib flank inclination α_R and the transverse rib width b_R , as defined in the standard [ISO19]. The relative rib area or bond index is the ratio between the projection of the rib area on the cross section of the bar (A_R) over the nominal contact area between the bar and the surrounding concrete (surface of a cylinder with diameter \varnothing and height s_R), as defined in Equation 3.1 [ISO19].

$$f_R = \frac{A_R}{\pi \cdot \varnothing \cdot s_R} \quad (3.1)$$

Another relevant parameter is the clear rib spacing ($s_{R,clear}$); however, this parameter is not clearly defined in the standards. In this chapter, it is measured as the indentation width [ISO19] at the top of the rib.

The influence of the bar diameter or size effect is known and reflected in the current formulations for anchorage and lap strength [Eur04, FIB14, Sch18]. Several experimental programmes reported a decrease in the normalized strength and stiffness of the local bond response for larger bar diameters in well-confined conditions [Mar81, Eli83, Met14, Lem23]. Soroushian et al. [Sor89] proposed a linear reduction of the bond strength with the diameter. Bamonte et al. [Bam07] proposed a reduction factor using the size effect law proposed by Bazant et al. [Baz95].

The effect of the rib geometry depends on the confinement. For well-confined conditions, the response is mostly governed by the bond index when comparing different rib heights and spacings [Reh61, Sor79]. An increase of the stiffness and bond strength with the bond index has been observed in multiple experimental campaigns [Mar81, Eli83, Los79, Met14].

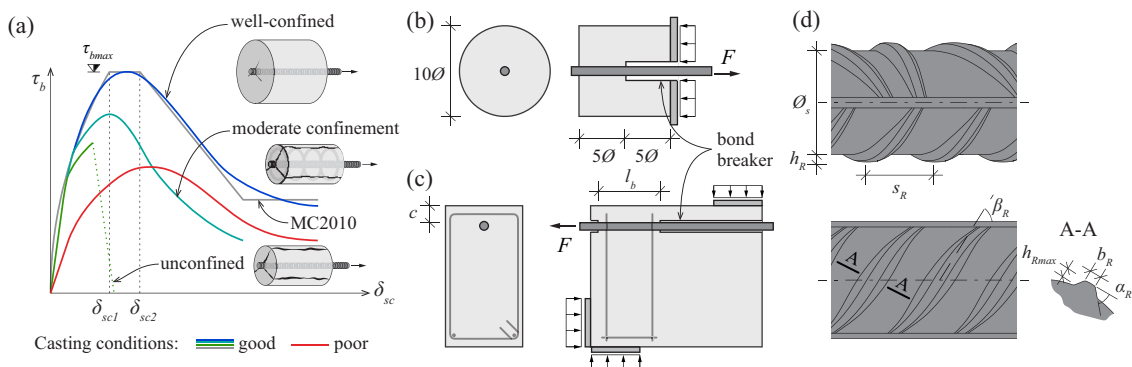


Figure 3.1: Bond-slip response: (a) bond-slip relationship for different confinements and casting conditions; (b) pull-out test; (c) beam-end test; and (d) rib geometry definitions.

For conditions governed by splitting of the concrete cover, Losberg et al. [Los79] observed that the bond index had little influence in the results. Darwin et al. [Dar93] reported that the stiffness increased with the bond index in all tested conditions; whereas, the strength showed almost no difference in unconfined conditions and increased for bars with confinement. Cairns et al. [Cai95] observed an increase in the bond strength of lap splices with small confinement and concluded that bars with larger bond index generate less bursting forces which can trigger splitting and spalling failures. They proposed an analytical model that justified these results. The same effect was observed by Metelli et al. [Met14] who measured smaller transverse deformations in the concrete pull-out cubes for larger f_R with $\varnothing 20$ bars.

Other influencing parameters that have been identified in previous research with smaller influence are the transverse rib angle [Sor79] and the rib orientation with respect to the splitting plane [Cai95, Kos22a]. Due to the friction, the rib face inclination does not have an influence for angles required in current standards [Lut67, EN105].

Eligehausen et al. [Eli83] proposed a bond-slip relationship that was adapted in the *fib* Model Code 1990 [CEB93] for well-confined and unconfined conditions. The *fib* Model Code 2010 (MC2010) [FIB13] further adapted the relationship (schematically shown in grey in Figure 3.1a) and included expressions for cases with stirrups. The bond strength in well-confined conditions ($c \geq 5\varnothing$) is a function of the square root of the concrete compressive strength (f_{cm}). The ratio between the bond strength in poor and good casting conditions is $\eta_2 = 0.5$ according to MC2010 [FIB13]. The formulation for splitting failure (unconfined and moderately confined conditions) are based on the semi-empirical expressions of *fib* Bulletin 72 [FIB14] that account for the effect of the concrete strength, the size effect of the bar diameter, the confinement and a factor for poor bond conditions $\eta_2 = 0.7$. Experimental results on high-strength concrete by Huang et al. [Hua96] showed that the bond strength was underestimated by the *fib* Model Code 1990 proposal. They proposed a linear increase of the bond strength with f_{cm} based on these results. Other proposals based on fitting of different experimental results can be found in the literature [Far95, Lau99]. Recently, Lin et al. [Lin19] proposed a model where the pull-out strength corresponds to the proposal of *fib* Bulletin 72 [FIB14] and with a peak slip dependent on the clear rib spacing based on the results of a database.

Tepfers [Tep73] proposed a mechanical model to calculate the confining capacity provided by concrete in tension surrounding the anchored bar assuming elastic, elastic cracked and plastic stress distributions. The model was then adapted by other researchers assuming an elastic cracked cohesive behaviour [Van90, Gam94, Nog95, Den96], elastic plastic behaviour [Sch98] and elastic plastic cohesive behaviour [Gam98]. The bond strength is typically calculated using an empirical factor or by fitting the inclination of the concrete struts which carry the bond stresses whose radial component is in equilibrium with the confinement stresses according to Tepfers model [Tep73].

Cairns et al. [Cai95] proposed an analytical expression to calculate the splitting forces exerted by the concrete wedge in front of the rib assuming a Mohr-Coulomb failure criterion and a fixed wedge angle related to the internal friction angle. Using a similar approach, Choi et al. [Cho17] proposed a model for splitting failures where the wedge angle is calculated by equating the bond force resisted by the confinement and the bond force that corresponds to the shear failure at the wedge surface assuming a shear strength of $0.2 \cdot f_c'$ [ACI02]. Other authors have proposed anchorage strength expressions based on limit analysis [Hes84, And89, Nie11].

The large number of proposed models in the literature indicates the complexity of the bar-to-concrete interaction. The power-law formulations found in the literature display a wide variety of coefficients and exponents (see Appendix 3A). The models found in the literature often account for different influencing parameters based on the parameters considered in the experimental tests used for the calibration. Therefore, there is an interest in clarifying the main influencing parameters and combining them to provide a more general bond-slip relationship, profiting from the large amount of experimental results reported in the literature.

In this context, this chapter proposes a bond-slip model based on mechanical considerations and experimental evidence. This research is based on an extensive literature review to provide an overview of the bond mechanism and to propose an expression to estimate the bond-slip response of bars in good casting conditions. A large database with 151 tests was collected for validation and derivation of some of the considered factors, with the aim of maximizing the generality of the proposed relationships.

3.2 Load bearing mechanism and failure modes

The typical local bond stress-slip relationship for different confinements is shown qualitatively in Figure 3.2a. For very low slips, the resulting bond stresses ($\tau_b < 0.2-0.8 f_{ct}$) are transferred to the concrete by chemical adhesion and micromechanical interaction of the microscopical roughness of steel bars [FIB00]. The range of slips where these forces govern is around 5-10 μm [CEB79, Giu91].

Beyond this limit, the force transfer occurs mostly through the interlocking of the rib lugs and the initially uncracked concrete [Eli83, FIB00], as represented in Figure 3.2c. The resulting concrete struts have a longitudinal (in equilibrium with bond) and a radial component in equilibrium with tensile hoop stresses in the tangential direction [Tep73], see Figure 3.2b. High compressive stresses develop in the contact zone between the lug and the concrete. Tensile stresses triggered by the corner of the lugs develop in this zone causing internal conical cracks which decrease the stiffness of the response [CEB79, FIB00] as illustrated in Figure 3.2d. Internal cracks with an inclination of around 60° were first observed experimentally by Goto [Got71] extending up to $\sim 2\emptyset$ from the ribs [Got80]. These cracks have been detected also using tomography [Li10] or visually in specimens with modified geometries [Lei18, Oke20]. These observations are consistent with finite element simulations [Ma76, Li10].

For larger bond stresses ($\tau_b = 1-3 f_{ct}$), longitudinal splitting cracks parallel to the bar axis appear due to the tensile stresses in the tangential direction [FIB00], see Figure 3.2e. When the stresses in the concrete struts approach the compressive strength at the bar interface, the concrete is crushed and creates a wedge of confined concrete that increases the splitting forces. Rehm [Reh61] reported that the length of the crushed wedge along the bar axis is about 5-7 times the rib height. Lutz et al. [Lut67] observed face angles of $30-40^\circ$ in tests with a single rib. Darwin et al. [Dar93] measured angles of $17-40^\circ$ in beam-end tests with splitting failure.

Gambarova et al. [Gam89] performed some tests specifically designed to replicate a bar geometry but in a planar stress-state to be able to analyse the crushing and micro-cracking around the

concrete shear keys using the Moiré pattern technique. They observed that the conical cracks extended up to a distance equal to the maximum aggregate size and concluded that near the peak load, the slip (close to 1 mm) was mostly caused by the crushing and shearing-off of the concrete keys whereas the contribution of the conical cracks was minor.

In unconfined conditions, splitting longitudinal cracks propagate through the cover and cause a brittle failure of the specimen [FIB00, Moc21a]. With larger covers and/or moderate transverse reinforcement, brittle failures are prevented, leading to the splitting-induced pull-out failure [FIB00]. The bond strength is however diminished due to the development of the splitting longitudinal cracks [Bra16, Cor23]. In well-confined conditions (heavy transverse reinforcement and/or $c \geq 5\phi$ [FIB13]), the inclined compression struts carrying the bond stress reach the compressive concrete strength at the cylindrical surface outside the ribs leading to the pull-out failure, see Figure 3.2f.

Direct visual observations can provide useful information about the pull-out failure mechanism. Tests without concrete in some regions where the bar and the interface can be directly observed are useful to understand the evolution of the internal cracking [Gam89]. In this regard, the modified pull-out tests performed by Leibovich et al. [Lei18] or the modified tensile tests performed by Okeil et al. [Oke20] instrumented with Digital Image Correlation (DIC) show the development of cracks around the bar and the differences between the response of cement paste and concrete. Nevertheless, the precise quantitative data might be influenced by the modified test conditions. Dybel et al. [Dyb21] obtained X-ray images of a core extracted after the failure and unloading of the specimen. The splitting cracks and sliding surface between the ribs could be observed but the conical cracks starting at the rib lugs were not observed. The observations in specimens after the end of the test might fail to detect thin cracks that close after unloading or detect cracks formed during the specimen preparation.

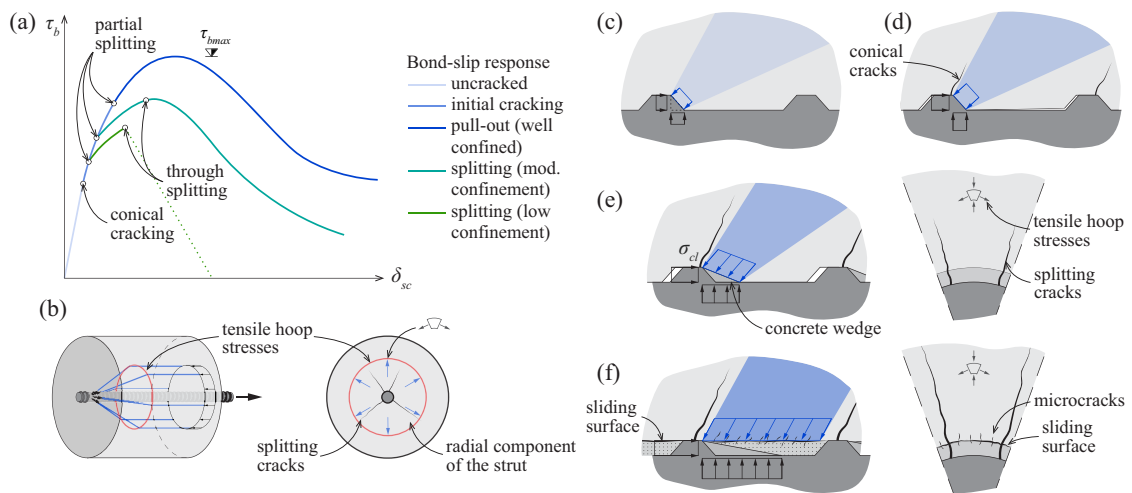


Figure 3.2: Bond load bearing mechanism: (a) relevant changes in the bond-slip relationship; (b) stresses generated in a pull-out test; and schematic representation of (c) the initial rib-concrete interlocking, (d) conical crack development, (e) splitting crack development and (f) pull-out failure.

A mechanism sharing many common points with the pull-out of bars is the response of concrete shear-keys. Two significant differences are the scale of the phenomenon and the bidimensional behaviour of the elements, which leads to planar failures. Consequently, in the case of shear keys, the failure can be directly observed and, at the same time, there is no confinement in the out-of-plane direction. The cracking sequence observed on the visible surface starts with the propagation of a single curvilinear crack from one of the wedge corners (analogous to the conical cracks observed by Goto [Got71]) and is followed by multiple thinner cracks within the strut caused by its crushing. At failure, the thinner cracks coalesced due to the highly localized shear strains. This was visually observed by several authors [Kos83, Bak90] and recently measured using DIC [Sor18]. The difference between plane stress behaviour in the shear keys and three-dimensional behaviour of the concrete zone between bar ribs justifies the different reached strength, but the failure mechanism seems to be similar.

3.3 Modelling the initial phase and the confined wedge development

3.3.1 Confinement demand

Once the concrete in the inclined compression field (struts) near the ribs (region A in Figure 3.3a) reaches the uniaxial compressive strength, compressive confinement stresses are required in that zone to further increase the bond stress. These confinement stresses in the tangential direction must be in equilibrium with an additional activation of the confinement reinforcement or with additional tensile tangential stresses in the concrete around the bar. The latter can lead eventually to spalling or splitting failures. Assuming an ideal cylindrical rib and neglecting the friction between the reinforcing bar and the concrete, the longitudinal compressive concrete stress in region A is [Reh69]:

$$\sigma_{cAl} = \frac{\tau_b}{f_R} \quad (3.2)$$

where τ_b is the nominal bond stress and f_R is the bond index. Since f_R lies between 0.04 and 0.15, the compressive stress according to Equation 3.2 can reach several times the compressive concrete strength (for $f_{cm} = 40$ MPa and $f_R = 0.075$ crushing would occur for $\tau_b = 3$ MPa). In order to reach larger bond stresses, which is typically the case for pull-out failures, the confined wedge must undergo a triaxial stress state. In this case, significant triaxial strengths can be reached, as for instance in well-confined partially loaded areas (up to $\sim 15f_{cm}$, see [Spi59, Lie89]), under the plate of headed bars [Fur91] or at the inner side of bent reinforcing bars in tension [Mon22].

The enhancement of the concrete strength due to confinement in region A can be quantified assuming the concrete as a Mohr-Coulomb material with the yield criterion expressed in principal stresses described by Equation 3.3:

$$Y = \sigma_1 (1 + \sin \varphi) - \sigma_3 (1 - \sin \varphi) - 2f_{coh} \cos \varphi \leq 0 \quad (3.3)$$

where $\sigma_1 \geq \sigma_2 \geq \sigma_3$, φ is the internal friction angle of concrete and f_{coh} is the cohesion. Assuming that the confined concrete wedge is at yielding, $\varphi = \text{atan}(3/4)$ and $f_{coh} = f_{cm}/4$ [Nie11], the yield criterion can be expressed using Equation 3.4:

$$\sigma_{cA3} = -f_{cm} + 4 \cdot \sigma_{cA1} \quad (3.4)$$

where $\sigma_{cA1} = \sigma_{cA2}$ are the two principal compressive confinement stresses in radial and tangential direction, respectively.

A more realistic stress state in region A can be obtained if the friction between the bar shaft and concrete is accounted for. In this case, the shear stress along the shaft τ_s and the radial concrete pressure σ_{cAr} fulfil Equation 3.5:

$$\tau_s = -\mu_s \cdot \sigma_{cAr} \quad (3.5)$$

where μ_s is the friction coefficient between steel and concrete. For radial stresses $\sigma_{cBr} < f_{cm}$, μ_s can be assumed equal to 0.47 [Bal90]. Due to friction, the principal concrete stresses σ_{cA3} have an inclination θ_A with respect to the bar axis. The stress components in region A can be determined on the basis of equilibrium using the Mohr's circle of Figure 3.3a:

$$\sigma_{cA1} = \sigma_{cA3} \cos^2 \theta_A + \sigma_{cA1} \sin^2 \theta_A \quad (3.6)$$

$$\sigma_{cAr} = \sigma_{cA3} \sin^2 \theta_A + \sigma_{cA1} \cos^2 \theta_A \quad (3.7)$$

$$\tau_s = (\sigma_{cA1} - \sigma_{cA3}) \cdot \cos \theta_A \cdot \sin \theta_A \quad (3.8)$$

The bond stress τ_b , assumed to be uniformly distributed along the nominal bar diameter in the tangential direction and the rib spacing (s_R) in the longitudinal direction, can be obtained considering the shear stress along the part of the shaft in contact with the wedge and the longitudinal stress σ_{cA1} acting on the rib height h_R :

$$\tau_b = \frac{h_R}{\varnothing \cdot s_R} \left[\frac{\varnothing}{\tan \gamma} \tau_s - (\varnothing + h_R) \sigma_{cA1} \right] \quad (3.9)$$

Assuming that the wedge is in equilibrium with a compressive strut (region B in Figure 3.3a) with a principal stress of f_{cm} , the system of Equation 3.4-3.9 can be solved, yielding the results presented in Figures 3.3b and c. This demonstrates that, as already shown by Cairns et al. [Cai95], the bond strength has two components: a ‘‘cohesion term’’, which depends on the compressive concrete strength and the rib geometry, and a ‘‘frictional term’’, which depends on the radial confinement stress. It can be observed that the bond index f_R has a non-negligible influence on the required confinement radial stress σ_{cAr} . For the same bond stress, lower confining radial stresses are required for bars with larger f_R . These results agree with the model for splitting by Cairns et al. [Cai95] and experimental results in well-confined conditions [Met14]. It has to be noted that the case without friction between the steel bar and the concrete requires very large confinement stresses.

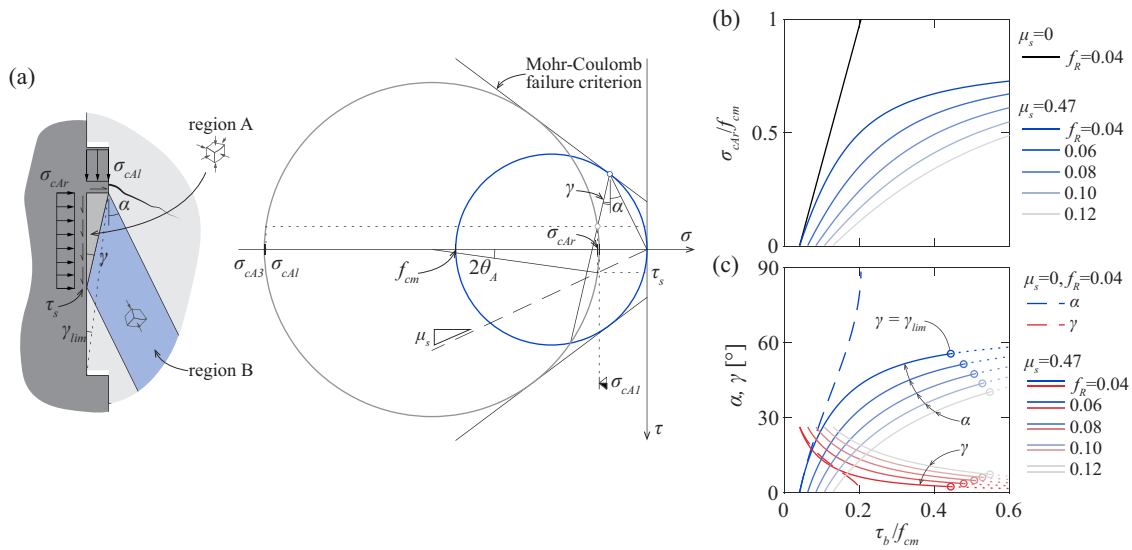


Figure 3.3: Initial phase: (a) stress field and correspondent Mohr circles; (b) normalized radial stress in the wedge as a function of the bond stress; and (c) inclination of stress field B α and wedge angle γ as a function of the bond stress (considered mechanical parameters $f_{cm} = 40$ MPa, $\varnothing = 20$ mm, $S_R = 12$ mm, $S_{R,clear} = 10$ mm).

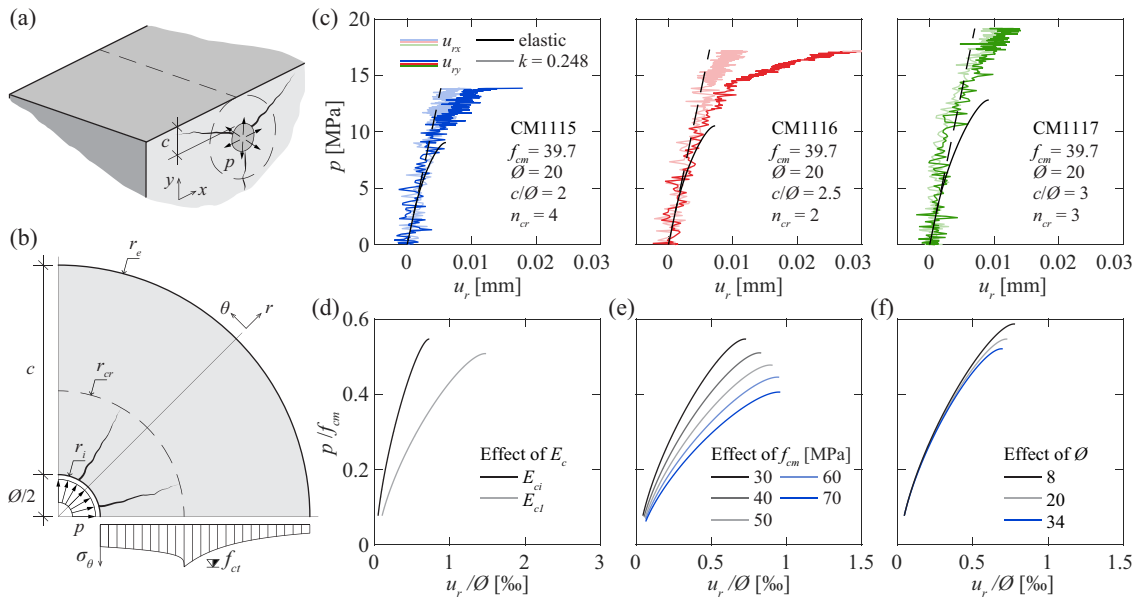


Figure 3.4: Inner pressure response: schematic representation of (a) CM11 test series and (b) the considered analytical model; (c) experimental results from series CM11; and normalized results from the analytical model considering the influence of (d) E_c , (e) f_{cm} and (f) \varnothing (reference mechanical parameters $f_{cm} = 30$ MPa, $\varnothing = 20$ mm, $c/\varnothing = 5$, $n_{cr} = 3$).

The equilibrium conditions yield also the inclination of the stress field B (α , blue curves in Figure 3.3c) and the wedge angle (γ , red curves in Figure 3.3c). A geometrical limit for this mechanism is reached when $\gamma = \gamma_{lim}$. (minimum wedge angle due to the rib geometry as shown in Figure 3.3a). This is indicated by the circular markers in Figure 3.3c. Interestingly, the results shown in Figure 3.3c are similar to the ones measured on tests and derived analytically with an interlocking model by Tirassa et al. [Tir21], and have the same order as the estimations from ring tests by Tepfers et al. [Tep92].

3.3.2 Confining capacity ensured by the surrounding concrete in tension

As explained in the introduction, several models have been proposed to explain the response of a concrete cylinder under internal pressure. In this section, the model of Van der Veen [Van90] was used because it considers a continuous softening response [Rei84] which can be solved analytically. The radial displacements have been calculated using the assumptions proposed by Den Ujil et al. [Den96].

Figure 3.4b shows a schematic representation of the pressure model for the axisymmetric case. Details on the formulation can be found in Appendix 3B. The results of the model are compared in Figure 3.4c with the experimental measurements of three pressure tests from series CM11 performed by Moccia et al. [Moc21a] on the practical non-axisymmetric case shown in Figure 3.4a. Internal pressure was applied in cylindrical openings ($\varnothing = 20$ mm) with variable clear cover (c), as illustrated in Figure 3.4a (the cases with good casting conditions are shown). The radial displacement at the opening surface (u_r) was measured using DIC along the x (solid line) and y (dashed line) directions shown in Figure 3.4a. The number of cracks in each test at failure (n_{cr}) is indicated in Figure 3.4c. Each figure includes the elastic solution (black dashed line) and the analytical solution of the model ($k = 0.248$, black solid line). The analytical solution is calculated assuming the same clear cover as in the pressure tests (see Figure 3.4a). The calculations are performed using the tensile concrete strength and the mean tangent modulus of elasticity ($E_{ci} = E_{cm}$) according to MC2010 [FIB13].

In general, the results capture well the experimental trends. However, the model underestimates the stiffness of the response and the maximum pressure. This is reasonable since the analytical solution refers to an axisymmetric case whereas the measurements have been conducted in a non-axisymmetric situation. For the same cover (c), the cracks in the actual case of Figure 3.4a can extend beyond the idealized cylinder of Figure 3.4b without causing the failure of the specimen, justifying the larger experimental peak pressures. Logically, an increase of the cover leads to an increase of the maximum pressure [Van90].

The axisymmetric model is useful to study the effect of different parameters. The normalized results (applied pressure over compressive strength and radial displacement over internal diameter \varnothing) are shown in Figures 3.4d to f. As explained in the previous section, in the case of bond, the radial pressure represents only one component of the actual stress that is transferred through the inclined compression field. The inclined compressive stress might approach the concrete compressive strength in the region near the wedge, thus the assumption of the tangent modulus

of stiffness might not be pertinent. For this reason, the results of the model assuming both the secant and the tangential modulus of elasticity [FIB08, Pop73] are compared in Figure 3.4d. As shown in Figure 3.4e, the normalized strength and stiffness are reduced for increasing compressive strengths due to the fact that the tensile strength and the elastic modulus of concrete do not increase linearly with f_{cm} . This strength reduction is accounted for in current splitting formulations [FIB14, FIB13].

Figure 3.4f shows that the model has a size effect as indicated by Van der Veen [Van90]. This can be explained by the fact that, for larger diameter bars and similar longitudinal crack depths, the perimeter on which the cracking strain acts is larger. In consequence, crack widths are larger and the residual tensile stresses are smaller, leading to lower maximum pressures. Furthermore, this is coherent with experimental results from inner pressure tests [Moc21a] and pull-out tests [Mar81, Eli83, Sor89, Bam07, Met14, FIB14, Lem23].

It must be noted that according to the model, for $c = 5\varnothing$, the maximum radial pressures are within 0.4 to $0.6 \cdot f_{cm}$. Based on the model presented in the previous section, if friction is neglected, the maximum bond stresses that could be reached are around $0.2 \cdot f_{cm}$. These values are far from the experimental observations, as it will be discussed in the following sections.

Unfortunately, these solutions are difficult to generalize for practical cases and for the related governing splitting or spalling mechanisms. Some authors have proposed models to account for multiple bars and more realistic failure mechanisms [FIB14, Moc21a].

3.4 Pull-out failure

3.4.1 Local concrete strength

If the confinement around the bar is sufficient to prevent the splitting failure, the stress in the inclined compression field can reach its capacity and the pull-out failure occurs by shearing off the concrete keys between the ribs.

Some studies have shown that the pull-out resistance is influenced by the rib spacing. Rehm [Reh61] and Cantone et al. [Can20] performed pull-out tests where only one rib was activated and with different spacings and rib heights (one test by Cantone et al. [Can20] had a single rib). Figure 3.5a shows the results of these experimental campaigns in terms of the applied force (F) as a function of the slip at the unloaded end of the bar. The responses for the same rib height (same colour tone) and different rib spacings follow the same ascending branch from which the curves eventually diverge. For larger rib spacings, the force that can be activated increases. Some tests with very large spacings ($h_R/S_{R,clear} = 1/15$ or $2/15$, dashed lines) failed by splitting of the concrete cube. This indicates that the initial mechanism is the same up to a point where the rib spacing interferes and becomes the limiting factor.

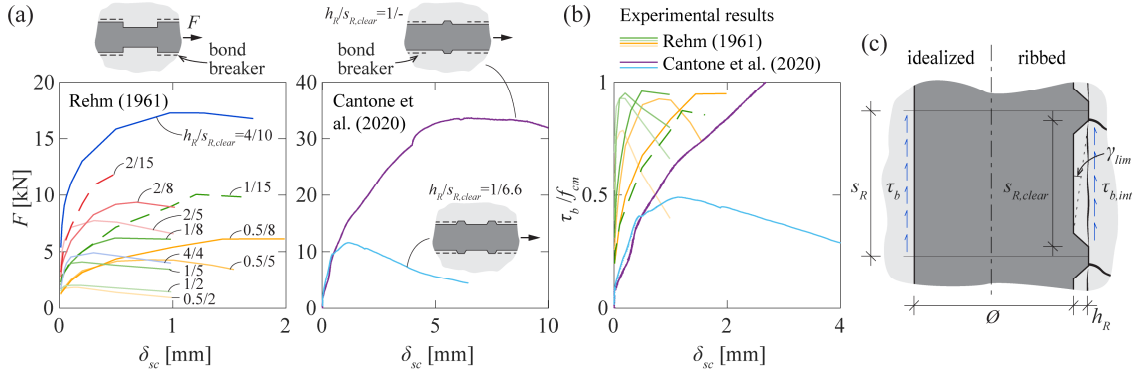


Figure 3.5: Single rib pull-out test results: (a) force-slip and (b) normalized bond stress-slip relationship [Reh61, Can20]; and (c) schematic representation of the idealized bond and the actual interface stresses.

This seems coherent with the mechanism proposed in Section 3.3.1 with an obvious limit being the inclination of the wedge (γ_{lim} in Figure 3.5c). This angle is determined by the clear rib spacing, the rib width and the rib flank inclination. Assuming that the crushing in front of the ribs is the main cause of the slip, the limit angle is likely to be even larger. Furthermore, for most rib geometries, if γ_{lim} was reached, the strut will conflict with the next rib lug or with the potential conical cracks. This is consistent with the fact that these angles are smaller than the observed experimental values [Reh61, Lut67, Dar93].

Figure 3.5b shows the nominal bond stress (calculated on the basis of the rib spacing) as a function of the unloaded-end slip. The results indicate that when the rib spacing is sufficiently large, the nominal bond stresses can reach values close or larger than $0.5f_{cm}$. This is coherent with experimental results from standard pull-out tests [Hua96, Met14]. Assuming an inclination of the stress field of $\alpha = 45^\circ$ with respect to the bar axis, this would correspond to a stress in the strut of f_{cm} ($0.5 = \sin\alpha \cdot \cos\alpha$). However, it must be noted that typical rib geometries have a certain width and, therefore, the surface where concrete stresses can be transferred to the rib is smaller than the full rib spacing (see length $s_{R,clear}$ in Figure 3.5c).

A database of short pull-out tests in well-confined conditions collected by the authors [Cor23] is extended in this publication (a summary can be found in Appendix 3D). Based on this database, the average ratio of the actual shear resisting perimeter $\pi \cdot (\varnothing + 2h_R) s_{R,clear}$ to the nominal one $\pi \cdot \varnothing \cdot s_R$ is around 82%. Consequently, the shear stress along the actual interface ($\tau_{b,int}$) must be approximately 20% larger as per Equation 3.10:

$$\tau_{b,int} = \tau_b \frac{\varnothing \cdot s_R}{(\varnothing + 2h_R) s_{R,clear}} \approx \frac{\tau_b}{0.8} = 1.2\tau_b \quad (3.10)$$

As explained in the previous sections, approaching pull-out failure, the internal splitting and conical cracks have developed. Consequently, the capacity for confinement stresses provided by the surrounding concrete might be hindered. Three possible explanations have been found for the higher stresses.

Matrix strength enclosed between the aggregates

Concrete is a complex composite material composed of aggregates and hardened cement paste, where the bond between them is likely the weakest link [Wal80, Zha97]. It is often modelled as a two-phase material for practical reasons [Zha97, Niel1]. Some experimental results show that the cement matrix strength is higher than the uniaxial concrete compressive strength, particularly for small aggregate volumes (20-30%) [Gil61, Sto75]. The ratio of matrix to concrete strength decreases for normal aggregate volumes (>60%). Furthermore, Hansen [Han95] observed that the response of the matrix is brittle under uniaxial compression and ductile under triaxial compression. The experimental data shows a decrease in the ratio of matrix to concrete strength for larger concrete strengths [Dah92, Gia92].

These results agree with the work of Walraven [Wal80, Wal81], that proposed a model to estimate the stress that could be transferred through a crack through aggregate interlock. In this context, he proposed an empirical formula (Equation 3.11, see also Figure 3.6b) to determine the matrix yielding strength as a function of the uniaxial concrete strength calibrated with an experimental campaign of push-off tests. This value corresponds to the average strength of the inhomogeneous material enclosed between the aggregates.

$$\sigma_{pu} = 6.39 \cdot f_{c,cube}^{0.56} \approx 7.24 \cdot f_{cm}^{0.56} \quad (3.11)$$

Given the typical rib dimensions and aggregate sizes, it is likely that the concrete in contact with the ribs is composed mainly of matrix and granular components of the smallest size [Gam89, Oke20], see Figure 3.6a. The conditions are similar to those in the tests by Walraven [Wal80], which could explain the activation of stresses larger than the uniaxial concrete compressive strength for normal strength concrete.

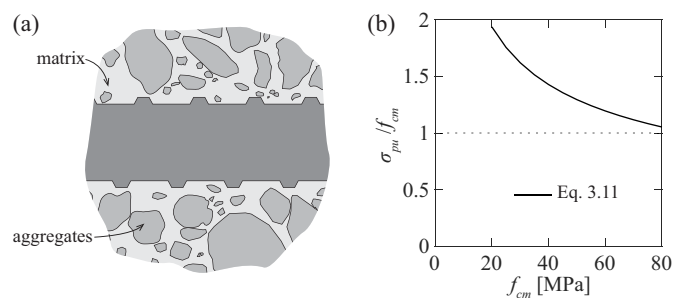


Figure 3.6: Local concrete strength: (a) schematic representation of concrete near the rib lugs; and (b) matrix yielding strength as a function of concrete compressive strength according to Equation 3.11 [Wal81]

Three-dimensional confinement

As already explained, the confining pressure increases the compressive strength of concrete. The bearing capacity of partially loaded areas is a clear example of this phenomenon where stresses significantly larger than the uniaxial compressive strength can be activated [Au60, Niy73, Lie89]. Based on limit analysis, Chen et al. [Che69] proposed different discontinuous stress fields for various load distributions acting on unreinforced concrete blocks, concluding that if tensile strength was neglected, the bearing pressure cannot exceed the uniaxial concrete compressive strength. They proposed a trapezoidal discontinuous stress field where a certain confining stress can be activated under the loaded area based on the spreading of the stresses and the tensile strength of the concrete. Recently, Markić et al. [Mar22] proposed a simplified stress field that can account for pressure and stirrup confinement. The model was further developed for the analysis of concrete ties by Galkovski et al. [Gal23].

The conditions in the case of pull-out failure are slightly different from the aforementioned cases. The propagation of splitting cracks might prevent the development of hoop stresses (other than those transferred through the cracks) near the bar, see Figure 3.7a. Moreover, the conical cracks originating at the lugs might prevent the transfer of radial confinement stresses in the immediate vicinity of the wedge. The large cover provides sufficient confinement to prevent the splitting failure and the reaction force is transferred through compression in the lower part of the concrete specimen to the support plates. These conditions are more similar to well-confined anchorages [Kos22a]. For this reason, an alternative stress field has been developed to account for the three-dimensional confinement that can be activated around the wedge. The modified Mohr-Coulomb failure criterion with tension cut-off at f_{ct} [Che69, Mar22, Gal23] is considered.

The geometry of the bar is approximated by a polygon circumscribed in the equivalent uniform rib as illustrated in Figure 3.7b, where the angle covered by each sector is ξ . The initial unconfined strut phase ends when the wedge angle reaches γ_{lim} . Until this point, the forces exerted by the bar on wedge A can be equilibrated by a single strut with a compressive stress of f_{cm} as explained in Section 3.3.1. In order to activate larger bond stresses, a triaxial stress state is required on the wedge contact surface (green region in Figures 3.7d to f). This can be achieved by spreading of the stresses in two directions: in the longitudinal direction (xy plane, see Figure 3.7e) and the in tangential direction (see Figure 3.7f). The spreading in the longitudinal direction is limited by the stress fields from the previous and following rib. The spreading in the tangential direction is limited by the assumed angle ζ . Consequently, the confinement is provided by the tensile stresses within each sector and no hoop stresses are required in the region near the bar.

The analytical development of this model is presented in Appendix 3C. Considering a bar with a nominal diameter $\varnothing = 20$ mm, bond index $f_R = 0.08$, rib spacing of $s_R = 12$ mm, clear rib spacing $s_{R,clear} = 11$ mm, concrete compressive strength $f_{cm} = 40$ MPa, the limit angle $\gamma_{lim} \approx 7.5^\circ$ is reached for $\tau_b/f_{cm} = 0.35$. Figure 3.7d shows the resulting stress field for the considered parameters. Figure 3.7c shows the evolution of stresses in regions A and B as a function of the bond stress. The maximum bond stress that can be activated without infringing the yield criterion and respecting the geometrical constraints is $\tau_b/f_{cm} = 0.41$. The geometry of the proposed stress fields depends on the rib geometry and, consequently, so does the maximum bond stress. Nevertheless, for multiple tested cases the radial confinement can only justify a partial increase of the bond stress.

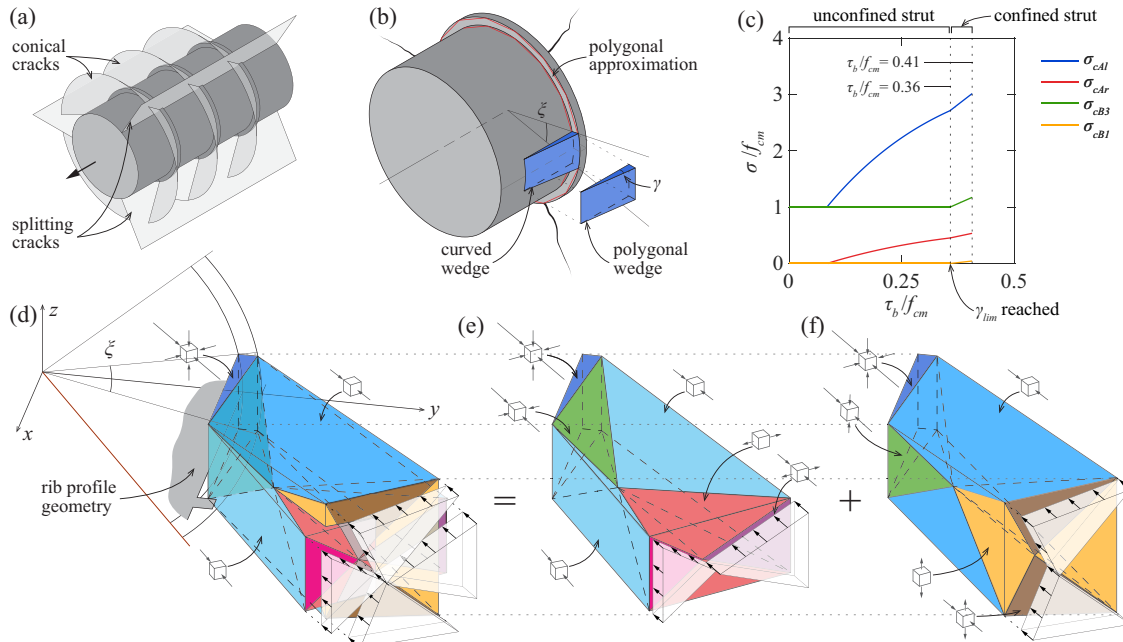


Figure 3.7: Three-dimensional confinement: (a) schematic representation of the cracks around the bar; (b) polygonal bar approximation; (c) wedge and contact stress evolutions; (d) 3D stress fields; (e) spreading in the longitudinal direction; and (f) spreading in the tangential direction.

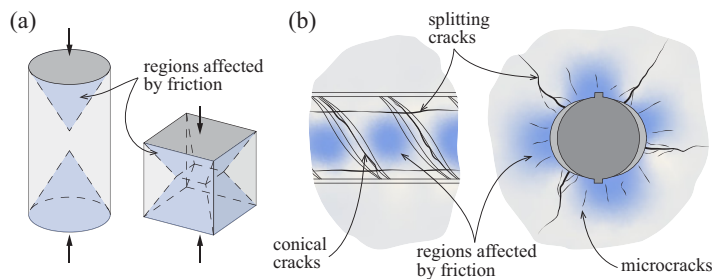


Figure 3.8: Schematic representations of the influence of friction: (a) in compressive tests of cylinders and cubes; and (b) in the sectors delimited by the cracks.

Friction

In compression tests on cubic and cylindric specimens, the friction between the test equipment and the concrete induces lateral stresses, therefore affecting the results of the tests [Elw95], as schematically shown in Figure 3.8a. At a smaller scale, the segment of concrete in contact with

the wedge is geometrically constrained by the splitting cracks and the conical cracks, as illustrated in Figure 3.8b. When the load in the strut approaches f_{cm} , small longitudinal cracks appear causing a lateral expansion with a progressive increase of the Poisson ratio [Vec92]. Due to the cracks around the concrete, a certain part of the concrete can expand towards the cracks. However, in the central region, the friction between the wedge and the concrete might generate some transverse stresses and locally increase the compressive strength of the concrete.

3.4.2 Pull-out bond strength

Based on these considerations, it is likely that a combination of the three aforementioned effects justify the experimental results. It is proposed that the compression field at the actual resisting perimeter can activate a principal compressive stress of $\sigma_3 = -1.2f_{cm}$ and secondary compressive confinement stresses of $\sigma_1 = \sigma_2 = -0.05f_{cm}$, with an inclination $\alpha = 45^\circ$. These values are slightly larger than those activated in the studied stress fields and could be justified by a higher local material strength. The pull-out bond strength is thus defined by Equation 3.12:

$$\tau_{bu,po} = \frac{(\varnothing + 2h_R) \cdot s_{R,clear}}{\varnothing \cdot s_R} \frac{1.2 + 0.05}{2} f_{cm} \left(\frac{30}{f_{cm}} \right)^{1/6} \left(\frac{20}{\varnothing} \right)^{1/8} \quad (3.12)$$

Limited information about the rib geometry in the publications included in the present database is available (Appendix 3D). For instance, clear spacings are rarely provided and when indicated it is not always stated if they are measured at the top of the rib or at its base. Some publications provide a detailed information, but they are a minority. The most complete characterization is generally found for machined bars with uniform axisymmetric ribs, however they are the least representative for real rib geometries. For this reason, the pertinence of Equation 3.12 cannot be fully assessed at the present time. Furthermore, in order to provide a practical expression, Equation 3.12 is adjusted using the average value of the ratio of actual shear resisting perimeter to the nominal one (see Figure 3.5c) from the database (0.82). This results in Equation 3.13:

$$\tau_{bu,po} = 0.5 f_{cm} \left(\frac{30}{f_{cm}} \right)^{1/6} \left(\frac{20}{\varnothing} \right)^{1/8} \quad (3.13)$$

The ratio $30 \text{ MPa}/f_{cm}$ with the exponent of $1/6$ is justified by the decreasing ratio matrix/concrete strength for increasing concrete strength (see Figure 3.6c). This effect is similar to the effective concrete strength accounting for local stress concentrations [Mut89, Moc20]. As shown in Figure 3.9b, the proposed expression provides a reasonable description of the experimental evidence, confirming that the MC2010 [FIB13] underestimates the bond strength for high strength concretes.

The model described in Section 3.3.2 shows a clear size effect depending on the bar diameter, both in the peak pressure and in the stiffness of the response. Even though the peak radial pressure is not the critical parameter in case of pull-out, it is still a fundamental component in the interaction. As it can be observed in Figure 3.4c, for similar normalized radial displacements, larger radial pressures are generated. Figure 3.9a shows the normalized peak pressures (for $u_r/\varnothing \approx 0.7\%$) as a function of the bar diameter. This effect is accounted for in a simplified manner with

the ratio $20 \text{ mm}/\varnothing$ with the exponent of $1/8$. As shown in Figure 3.9c, the size effect in the database is reasonably well captured by the proposed factor in Equation 3.13. A slight ascending trend with the increase of the bond index is observed in the database (see Figure 3.9d) and by some authors in large experimental campaigns with considerable scatter [Bon75, Mar81, Met14]. Nevertheless, despite the fact that the model predicts an influence of the geometry of the ribs and the bond index, based on the comparison with tests, it seems that this effect can be neglected for pull-out failures. The proposal improves the results of MC2010 (Avg.=1.35, CoV=24.9%).

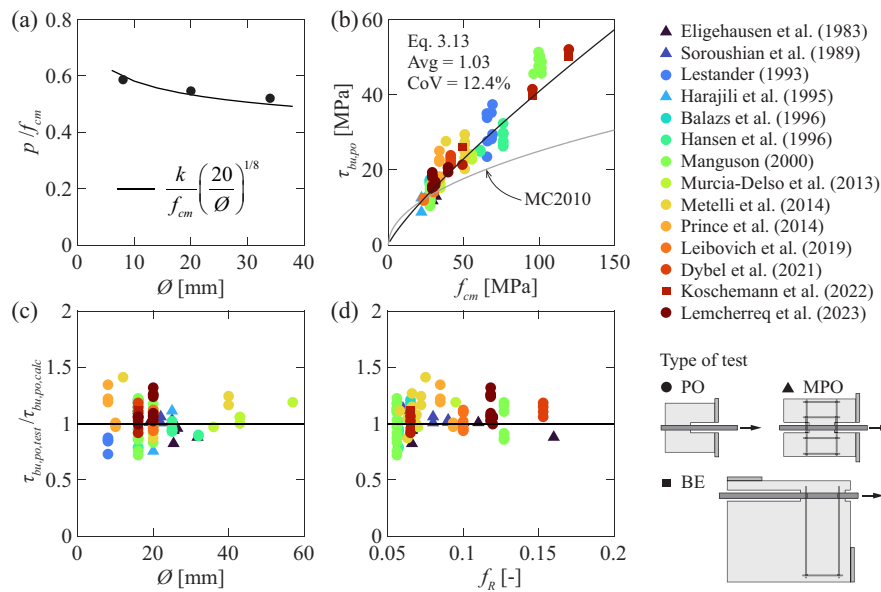


Figure 3.9: Pull-out bond strength: (a) size effect; (b) bond strength as a function of the concrete compressive strength; and ratio of the experimental bond strength over the calculated as a function of the (c) bar diameter and (d) bond index.

3.4.3 Slip at maximum bond stress

As schematically shown in Figure 3.10a, the slip corresponding to the pull-out failure has different contributions. Firstly, the inclined compression field carrying the bond stress deforms elastically leading to a certain longitudinal slip. This contribution is small as the stress in the compression field decreases rapidly with the distance from the bar [Sch84, Sch98]. As soon as the compression stress near the rib approaches the compressive concrete strength f_{cm} , the secant elastic concrete modulus diminishes. When f_{cm} is reached in front of the lug, local crushing occurs. This displacement was estimated using a rigid-plastic strain hardening constitutive law for the concrete by Schober [Sch84] and an elastic-plastic with strain hardening relationship by Schenkel [Sch98]. Furthermore, assuming an idealized uniform rib geometry due to the inclination of the rib (or the wedge), a radial displacement of the concrete generates a gap that causes additional slip [Den96],

see Figure 3.10b. Lastly, a contribution probably related to the shearing of the concrete keys takes place near the pull-out force. This last contribution can be observed in the experimental results shown in Figures 3.5a and b. For each rib height, the force-slip responses have a similar ascending branch independently of the clear rib spacing. At some point, the curves with smaller clear spacings diverge from the ascending branch and reach the peak force. The slip of divergence is smaller for smaller clear spacings.

Lieberum et al. [Lie89] studied the behaviour of concrete under highly concentrated loads, pushing a rigid circular punch into a large concrete block. These tests show the influence of different parameters in the stiffness when local crushing occurs. The results in Figure 3.10c show a stiffer response for larger concrete strength; however, no clear trend can be observed for the applied stress normalized by f_{cm} . The response is stiffer for smaller diameters (Figure 3.10d) similarly to the radial stiffness of the concrete cylinder according to the analytical model (Figure 3.4f).

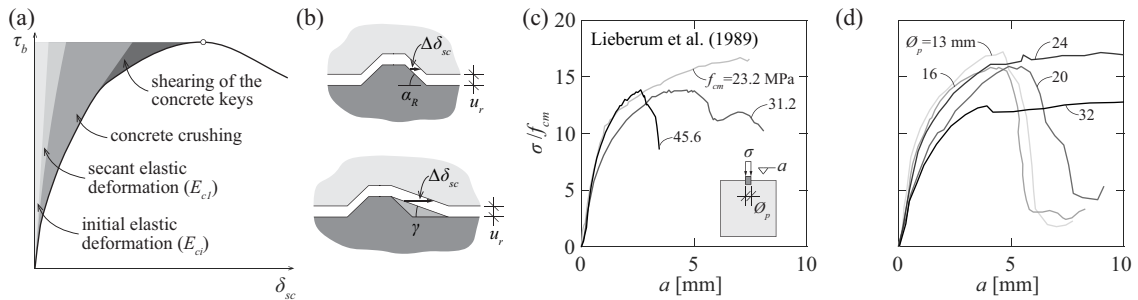


Figure 3.10: Slip in case of pull-out failures: (a) contributions to the total slip before reaching the bond strength; (b) contribution of the radial concrete displacement; (c) influence of f_{cm} and (d) of the punch diameter \varnothing_p in the radial pressure-penetration [Lie89].

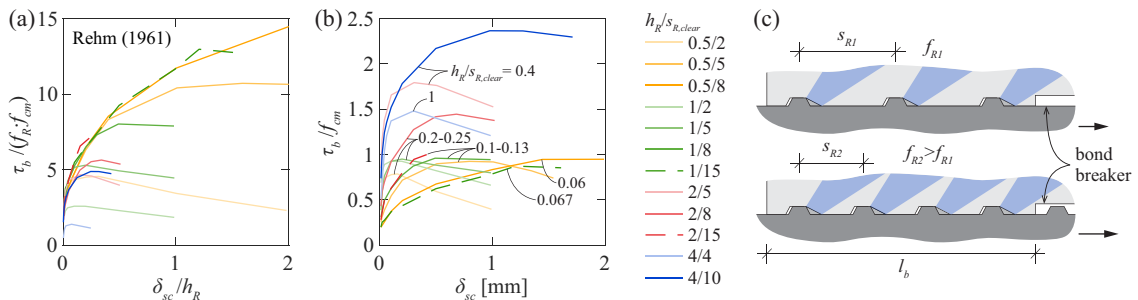


Figure 3.11: Influence of the bond index in the bond-slip stiffness: (a) normalized longitudinal stress as a function of the normalized slip; and (b) nominal bond stress as a function of the slip from single rib tests [Reh61]; and (c) schematic representation of the influence for small bond stresses.

Rehm [Reh61] observed that the first part of the ascending branch bond-slip relationship is fairly uniform, independently of the rib height, if the stress is expressed in terms of the longitudinal compression normal to the rib σ_{cl} (which corresponds to the bond stress divided by the bond index) and the slip is normalized by the rib height h_R , see Figure 3.11a. The author justified this observation arguing that the size of the zone near the rib, where strains concentrate, is more or less proportional to the rib height. For very low spacings, the same stress state cannot develop and failure occurs for lower bond stresses. It must be noted that for relatively large bond stresses, the assumption that all the shear force is carried by the longitudinal stress might not be pertinent according to the model proposed in Section 3.3.1. Figure 3.11b shows the normalised bond stress as a function of the slip. The results show a similar response for similar bond indices as observed by Soretz et al. [Sor79].

Several experimental campaigns show the influence of f_R on the stiffness of the bond-slip response [Reh61, Eli83, Mar81, Dar93, Met14]. This can be explained on the basis of the model proposed in Section 3.3.1. Considering a pull-out test with given bonded length and rib height, the number of bonded ribs depends on the bond index as schematically shown in Figure 3.11c. According to the model, the longitudinal stress determines the radial stress, the corresponding frictional shear component and the geometry of the wedge. Considering the findings of Rehm [Reh61] for relatively low forces, if the longitudinal stress and rib height are the same, the slip should be similar. Due to the fact that there are more ribs, the total external force applied and the nominal bond stress are larger. Additionally, for bars with smaller f_R , the wedge inclination can be smaller which, for the same radial displacement, would lead to larger slips (see Figure 3.10b). For large bond stresses near pull-out failure, the stress state is significantly different. Considerable cracking and crushing can occur and therefore, the influence of f_R is potentially different.

Furthermore, the reality is much more complex due to the actual rib geometries and the heterogeneity of concrete around the ribs, that result in non-uniform bond stress distributions even for short bonded lengths [Kos20, Lem23]. This justifies the large scatter in results and the lack of direct proportionality between the bond index and the stiffness of the response.

The proposed simplified bond-slip relationship, which is adapted from the proposal of MC2010 [Eli83, FIB13], has a plateau between the two slips δ_{sc1} and δ_{sc2} (see Figure 3.1a). The peak slip δ_{sc1} can be estimated with Equation 3.14. It has been assumed that the plateau corresponds to the phase where the shearing contributions take place, until $\delta_{sc2} = 2\delta_{sc1}$ (similarly to MC2010).

$$\delta_{sc1,po} = 1.0 \cdot \frac{\varnothing}{20} \cdot \left(\frac{30}{f_{cm}} \right)^{1/3} \left(\frac{0.08}{f_R} \right)^{1/5} \quad (3.14)$$

Figure 3.12a shows the displacements measured by Lieberum et al. [Lie89] in compression tests with partially loaded areas for a stress close to $4 \cdot f_{cm}$ which corresponds to the longitudinal stress for $\tau_b = 0.5f_{cm}$ according to the model presented in Figure 3.7c. The relationship between displacement and the diameter of the loaded area (\varnothing_p , see sketch in Figure 3.10c) follows a fairly linear trend. Similarly, the radial displacements as a function of the internal pressure estimated with the analytical radial pressure model show a rather linear correlation (Figure 3.12b). Accordingly, a linear relationship has been proposed in Equation 3.14 for the bar diameter.

The concrete compressive strength influences the stiffness of the response. For low bond stresses and for the concrete at a certain distance from the bar, the response will likely remain elastic. Furthermore, the slip results from permanent deformations, crushing and shearing of the concrete near the bar. The quantification of these contributions is difficult due to the limited knowledge and to the fact that the characterization of the concrete is not typically done at this scale. For this reason, a factor is proposed based on the experimental database with an exponent of $1/3$, as it can be observed in Figure 3.12d.

Concerning the influence of the bond index, the comparison with test results shows that an exponent of $1/5$ is a reasonable choice. With this respect, the ratio $h_R/S_{R,clear}$ might be more relevant to the matter. However, the quantification of this ratio is considerably more complex given the typical rib patterns in current reinforcing bars. Consequently, considering that both magnitudes are more or less proportional (typical rib widths are similar), the bond index has been used in the formulation.

The results in Figures 3.12c and d show that the proposed expression captures the general trends of the database. The average ratio of the measured over calculated slip ($\delta_{sc1,test}/\delta_{sc1,calc}$) of 1.11 indicates that the slip is slightly underestimated, which is reasonable as the experimental peak should occur somewhere in the plateau. The coefficient of variation of 28.2% is reasonable given the variability of the results. The proposal improves the results of MC2010 (Avg. = 1.08, CoV = 55%).

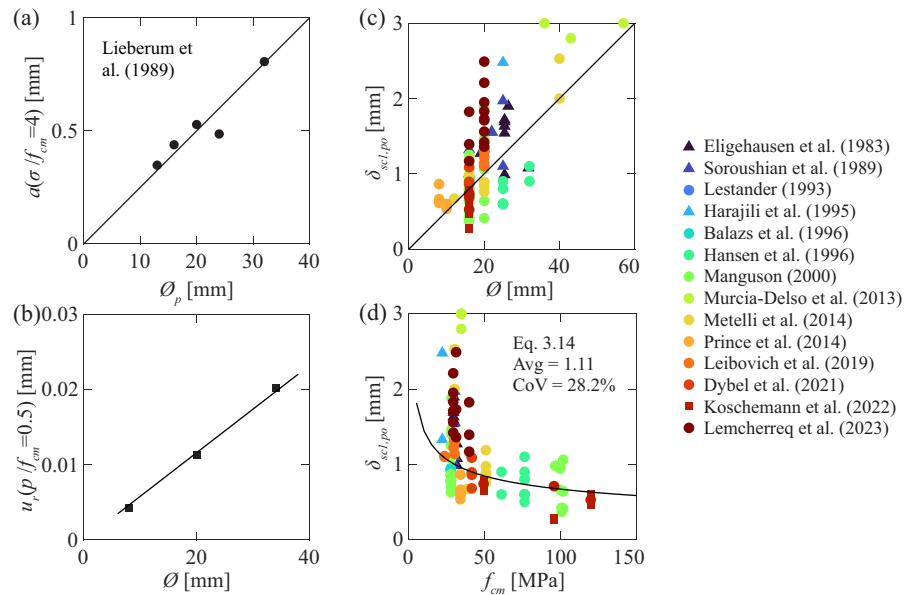


Figure 3.12: Slip at pull-out: influence of the bar diameter in the displacement according to (a) the experimental results of Lieberum et al. [Lie99] and (b) the radial displacement according to the model of Section 3.2; and comparison of the database slip and the proposed expression as a function of (c) the bar diameter and (d) the compressive strength.

3.5 Proposed bond-slip relationship

3.5.1 General expression for monotonic loading

The general expression for the monotonic bond-slip relationship from MC2010 is adopted with some modifications. Four phases are considered: an ascending branch, a plateau and two linear descending branches, as proposed by Huang et al. [Hua96]. The response as a function of the slip is characterized by Equation 3.15.

$$\begin{aligned}
 \tau_b &= \tau_{b,max} (\delta_{sc} / \delta_{sc1})^\alpha && \text{for } 0 \leq \delta_{sc} \leq \delta_{sc1} \\
 \tau_b &= \tau_{b,max} && \text{for } \delta_{sc1} < \delta_{sc} \leq \delta_{sc2} \\
 \tau_b &= \tau_{b,max} - (\tau_{b,max} - \tau_{bf}) (\delta_{sc} - \delta_{sc2}) / (\delta_{sc3} - \delta_{sc2}) && \text{for } \delta_{sc2} < \delta_{sc} \leq \delta_{sc3} \\
 \tau_b &= \tau_{bf} (1 - (\delta_{sc} - \delta_{sc3}) / (\delta_{sc4} - \delta_{sc3})) && \text{for } \delta_{sc3} < \delta_{sc} \leq \delta_{sc4}
 \end{aligned} \tag{3.15}$$

Some of the parameters of the response proposed in MC2010 appear to provide a reasonable representation of the response and are accepted without further validation:

- α : exponent of the ascending branch with a recommended value of 0.4
- τ_{bf} : frictional bond stress with a value of $0.4 \cdot \tau_{b,max}$
- δ_{sc2} : slip corresponding to the end of the plateau with a value $2 \cdot \delta_{sc1}$

3.5.2 Confinement and proposed parameters

In well-confined conditions (blue curve in Figure 3.13b), the maximum bond-stress and the corresponding slip can be determined by Equations 3.13 ($\tau_{b,max} = \tau_{bu,po}$) and 3.14 ($\delta_{sc1} = \delta_{sc1,po}$). The exponent $\alpha = 0.4$ proposed by MC2010 is considered for the ascending branch. After the peak bond stress is reached, the concrete keys are progressively sheared. The slip at the end of the plateau is assumed to be $\delta_{sc2} = 2\delta_{sc1}$. A linear decrease of the bond stresses follows the reduction of the remaining concrete shear key surface [Can20]. The residual bond stress $\tau_{bf} = 0.4\tau_{b,max}$ and $\delta_{sc3} = s_{R,clear}$ proposed by MC2010 are considered. Once the concrete keys are entirely sheared, it is assumed that the residual frictional bond will progressively decrease as the concrete roughness is eroded with the contact of the ribs. A final bond stress of zero at a slip of $\delta_{sc4} = 3s_R$ as proposed by Huang et al. [Hua96] is considered.

For unconfined conditions (green curve in Figure 3.13b), the bond-slip relationship proposed by MC2010 is accepted.

When confinement conditions are between the well-confined and the unconfined conditions, an intermediate response is observed. Koschemann et al [Kos22a] measured bond-slip responses in beam-end tests ($c = 2\emptyset$, without transverse reinforcement) with a smooth transition to the descending branch and no sudden loss of the bond stresses. Similar results were observed in the local bond-slip measurements from pull-out tests ($c \leq 3\emptyset$, no transverse reinforcement) [Cor23].

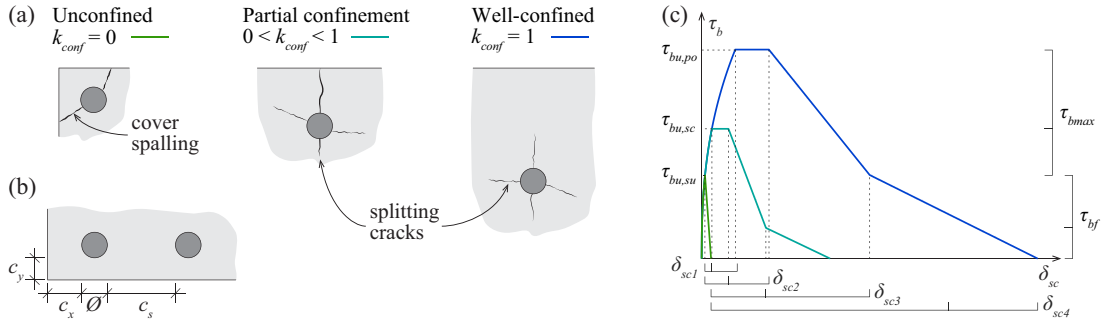


Figure 3.13: Proposed local bond-slip relationship: (a) considered confinements and schematic representation of the failure modes; (b) concrete cover definition; and (c) proposed relationships and defining parameters.

For such cases, the factor to account for the cover and transverse reinforcement proposed in MC2010 is used for the definition of the confinement conditions [FIB13, FIB14]. This factor corresponds to the expression in square brackets in the formula to calculate the peak local bond resistance for splitting failures defined by Equation 3.16 [FIB13]:

$$\tau_{bu,split} = \eta_2 \cdot 6.5 \cdot \left(\frac{f_{cm}}{25} \right)^{0.25} \left(\frac{25}{\varnothing} \right)^{0.2} \left[\left(\frac{c_{min}}{\varnothing} \right)^{0.25} \left(\frac{c_{max}}{c_{min}} \right)^{0.1} + k_m K_{tr} \right] \quad (3.16)$$

where, $c_{min} = \min[c_s/2, c_x, c_y]$ and $c_{max} = \max[c_s/2, c_x]$ (see Figure 3.13b), k_m is a factor that accounts for the efficiency of the reinforcement and K_{tr} is a factor that accounts for the amount of reinforcement as defined in MC2010.

The range of application of this expression is limited to $0.5 \leq c_{min}/\varnothing \leq 3.5$ and $c_{max}/c_{min} \leq 5$ [FIB14]. In order to provide a continuous transition between from unconfined to well-confined conditions, it is assumed that the factor between brackets is valid up to a cover values of $c_{min}/\varnothing = 5$ (minimum required cover for considering pull-out failure according to MC2010). Therefore, the upper limit for the factor is set to 1.5, corresponding to the case of a standard pull-out test ($c_{min}/\varnothing = 5$, $c_{max}/c_{min} = 1$ and $K_{tr} = 0$). A minimum value of 1 is set, that corresponds to the confinement when $c = 1\varnothing$. The normalized factor can be determined using Equation 3.17:

$$k_{conf} = \frac{1}{0.5} \left[\left(\frac{c_{min}}{\varnothing} \right)^{0.25} \left(\frac{c_{max}}{c_{min}} \right)^{0.1} + k_m K_{tr} - 1 \right] \quad k_{conf} \in [0,1] \quad (3.17)$$

Three confinement conditions are defined accordingly, as shown in Figure 3.13a:

- Unconfined conditions: $k_{conf} = 0$, corresponding to small covers ($c = 1\varnothing$) with no transverse reinforcement and failure by cover spalling (failure triggered by the cracks parallel to the bar and approximately parallel to the concrete surface).
- Well-confined conditions: $k_{conf} = 1$, corresponding to large covers ($c \geq 5\varnothing$) and/or sufficient transverse reinforcement, and failure by pull-out.

- Partial confinement: $0 < k_{conf} < 1$, corresponding to other intermediate cases and characterized by splitting induced pull-out (splitting cracks might propagate to the surface of the specimen without causing the failure of the anchorage).

Consequently, the factor k_{conf} is used to interpolate the required parameters of the response between the unconfined and well-confined conditions. The main parameters of the proposed bond-slip relationship for the three types of confinement are summarized in Table 3.1.

The bond-slip response proposed for moderate confinement or unconfined conditions is based on the experimental and analytical works from the literature. These relationships are valid for good bond conditions. Additional research is required for poor bond conditions.

Table 3.1: Bond-slip relationship parameter definition

Parameter	Well-confined	Moderate confinement	Unconfined
Cover ^a	$c \geq 5\varnothing$	$1\varnothing < c < 5\varnothing$	$c = 1\varnothing$
τ_{bu}	$\tau_{bu,po} = 0.5 f_{cm} \left(\frac{30}{f_{cm}} \right)^{1/6} \left(\frac{20}{\varnothing} \right)^{1/8}$	$\tau_{bu,sc} = \tau_{bu,su} + (\tau_{bu,po} - \tau_{bu,su}) k_{conf}$	$\tau_{bu,su} = 7.1 \left(\frac{f_{cm}}{30} \right)^{1/4} \left(\frac{20}{\varnothing} \right)^{1/5}$
τ_{bf}	$0.4 \cdot \tau_{bu}$	$\tau_{bf,sc} = \tau_{bf,po} \cdot k_{conf}$	0
δ_{sc1}	$1.0 \cdot \frac{\varnothing}{20} \cdot \left(\frac{30}{f_{cm}} \right)^{1/3} \left(\frac{0.08}{f_R} \right)^{1/5}$	$\delta_{sc1,sp} = \delta_{sc1,po} \left(\frac{\tau_{bu,sp}}{\tau_{bu,po}} \right)^{1/\alpha}$	$\delta_{sc1,su} = \delta_{sc1,po} \left(\frac{\tau_{bu,su}}{\tau_{bu,po}} \right)^{1/\alpha}$
δ_{sc2}	$2 \cdot \delta_{sc1}$	$\delta_{sc2,sc} = \delta_{sc2,su} + (\delta_{sc2,po} - \delta_{sc2,su}) k_{conf}$	δ_{sc1}
δ_{sc3}	SR_{clear}	$\delta_{sc3,sc} = \delta_{sc3,su} + (\delta_{sc3,po} - \delta_{sc3,su}) k_{conf}$	$1.2 \cdot \delta_{sc1}$
δ_{sc4}	$3 \cdot SR$	$\delta_{sc4,sc} = \delta_{sc4,su} + (\delta_{sc4,po} - \delta_{sc4,su}) k_{conf}$	$1.2 \cdot \delta_{sc1}$
α	0.4	0.4	0.4

^a cover for the case without transverse reinforcement

3.6 Conclusions

This chapter revisits the local bond-slip response of ribbed bars. Through a thorough review of the literature and interpretation of experimental evidence, the pull-out failure mechanism is described. Based on mechanical considerations, models and experimental evidence, the influence of the main parameters in the response is estimated and a modification of available analytical bond-slip relationships is proposed. The main conclusions are listed below:

1. The pull-out failure can be assumed to occur by coalescence of the concrete microcracks that start from the rib edge and developing toward the following rib. The mechanism is similar to the failure of concrete shear keys.
2. A stress-fields model using a Mohr-Coulomb yield criterion is proposed to explain the behaviour of the crushed concrete near the ribs. Cases with and without friction between the reinforcing bar and the concrete are compared. The proposed model explains the variation of the inclination of the concrete struts measured experimentally by other authors.
3. Three possible justifications are proposed to explain the experimental pull-out bond strength that would require an inclined stress field with stresses larger than the concrete compressive strength: (i) local strength of the cement paste confined between the aggregates near the rib lugs higher than the uniaxial compressive concrete strength, (ii) local increase of the strength due to friction between the bar surface and the surrounding concrete, and (iii) three-dimensional confinement. The latter can explain a certain increase of around 15% due to the spreading of the stresses; however, it is not sufficient to explain the total increase. It is therefore considered that a combination of the three effects is present.
4. Two expressions are proposed based on mechanical considerations and experimental evidence to estimate the pull-out bond strength and the corresponding slip considering the influence of: the concrete compressive strength, the bar diameter and the bond index. The results show fairly good agreement with the results from a database collected by the authors.
5. A modification of the fib MC2010 bond-slip relationship for monotonic loading is proposed for well-confined conditions. For other confinements, the proposal is based on analytical works and experimental results from the literature.

Appendix 3A: Examples of bond-slip relationships

Table 3.2 contains some proposed expressions for the bond-slip relationship found in the literature. This summary includes the articles cited in this chapter but several additional models can be found in the literature, see for instance [FIB00].

Table 3.2: Bond-slip relationships from the literature (values in parenthesis provided for high-strength concrete)

Reference	Ascending branch: $\tau_b(\delta_{sc})$ [MPa]	$\delta_{sc,1}$ [mm]	$\delta_{sc,2}$ [mm]	$\delta_{sc,3}$ [mm]
Rehm (1961) [Reh61]	$f_{ccube} \cdot (\varphi \cdot \delta_{sc}^\alpha \pm \psi \cdot \delta_{sc})$			
Noakowski (1978) [Noa78]	$0.58 \cdot f_{cm} \cdot \delta_{sc}^\alpha$			
Eligehausen et al. (1983) [Eli83]	$13.5 \cdot (\delta_{sc1} / \delta_{sc1})^{0.4}$	1.0	3.0	10.5
Noakowski (1988) [Noa88]	$0.95 \cdot f_{cm}^{2/3} \cdot \delta_{sc}^{0.12}$			
Model Code 1990 [CEB93]	$2.5 \cdot f_{ck}^{0.5} \cdot (\delta_{sc1} / \delta_{sc1})^{0.4}$	1.0	3.0	
Farra (1995) [Far95]	$0.4 \cdot f_{cm}^{0.95} \cdot \delta_{sc}^{0.3}$			
Huang et al. (1996) [Hua96]	$0.45 \cdot f_{cm} \cdot (\delta_{sc1} / \delta_{sc1})^{0.4}$	1.0 (0.5)	3.0 (1.5)	SR_{clear}
Laurencet (1998) [Lau99]	$0.22 \cdot f_{cm} \cdot \delta_{sc}^{0.21}$	1.0		
Harajili et al. (2004) [Har04]	$2.57 \cdot (f'_c)^{0.5} \cdot (\delta_{sc1} / \delta_{sc1})^{0.3}$	$0.15 \cdot SR_{clear}$		
Bamonte et al. (2007) [Bam07]	$[0.45 + 1.1(f_{c0}/f_{cm}) (\varnothing/\varnothing)^{\beta}] \cdot f_{cm}$	1.0 (1.0)	2.0 (1.5)	
Nielsen et al. (2011) [Nie11]	$0.12 \cdot v \cdot f_{cm} - 0.28 \cdot v \cdot f_{cm}$			
Model Code 2010 [FIB13]	$2.5 \cdot (f_{cm})^{0.5} \cdot (\delta_{sc1} / \delta_{sc1})^{0.4}$	1.0	2.0	SR_{clear}
Lin et al. (2019) [Lin19]	$13.5 \left(\frac{f_{cm}}{25} \right)^{0.25} \cdot \left(\frac{\varnothing}{l_b} \right)^{0.45} \cdot \left(\frac{25}{\varnothing} \right)^{0.2} \cdot \left[\left(\frac{c_{min}}{\varnothing} \right)^{0.25} \left(\frac{c_{max}}{c_{min}} \right)^{0.1} + k_m K_{tr} \right] \cdot \left(\frac{\delta_{sc}}{\delta_{sc1}} \right)^{0.2}$			$0.12 \cdot SR_{clear}$

Appendix 3B: Internal pressure model

In this appendix the model of Van der Veen [Van90] and the calculation of the radial displacements using the assumptions proposed by Den Ujil et al. [Den96] are presented. The mechanical properties of the concrete are estimated from the fib Model Code 2010 [FIB13] formulations based on the compressive strength (assuming $E_{c0}=21.5$ GPa and $\alpha_E=1$):

$$f_{ct} = 0.3(f_{ck})^{2/3} \quad (3.18)$$

$$E_c = E_{c0} \cdot \alpha_E \cdot (f_{cm} / 10)^{1/3} \quad (3.19)$$

In the elastic range, the solution for thick walled cylinders under internal pressure proposed by Timoshenko [Tim70] assuming that the external pressure is zero is considered. External pressure is considered positive when it acts towards the surface where it is applied. Tensile internal stresses are considered as positive. The resulting expressions are:

$$\begin{aligned} \sigma_r(r) &= \frac{p_i \cdot r_i}{r_e^2 - r_i^2} \left(1 - \frac{r_e^2}{r^2} \right) \\ \sigma_\theta(r) &= \frac{p_i \cdot r_i}{r_e^2 - r_i^2} \left(1 + \frac{r_e^2}{r^2} \right) \\ u(r) &= \frac{p_i \cdot r_i^2}{E_c (r_e^2 - r_i^2)} \left((1 + \nu) \frac{r_e^2}{r} + (1 - \nu)r \right) \end{aligned} \quad (3.20)$$

This leads to the cracking pressure when the tangential stress reaches the tensile strength of concrete proposed by Tepfers [Tep73]:

$$p_{cr} = \frac{r_e^2 - r_i^2}{r_e^2 + r_i^2} f_{ct} \quad (3.21)$$

The elastic cohesive model proposed by Van der Veen [Van90] considers the continuous power function proposed by Reinhardt [Rei84] to represent the softening behaviour of the cracked concrete:

$$\frac{\sigma}{f_{ct}} = 1 - \left(\frac{w}{w_0} \right)^k \quad (3.22)$$

The exponent k is a material constant taken as 0.248 [Van90]. The crack width after which no tensile stresses are transferred through the crack (w_0) is calculated based on the fracture energy is taken as of concrete $G_F = 73f_{cm}^{0.18}$ according to MC2010 [FIB13].

The pressure that can be resisted by the elastic ring that has an internal radius of r_{cr} can be calculated assuming that the tangential stress is reached in the internal face:

$$\begin{aligned}
 \sigma_{\theta}^E(r_{cr}) &= f_{ct} \\
 \sigma_r^E(r_{cr}) &= \frac{r_{cr}^2 - r_e^2}{r_e^2 + r_{cr}^2} f_{ct} \\
 u_r^E(r_{cr}) &= f_{ct} \frac{r_{cr}}{E_c} \left(1 + \nu \frac{r_e^2 - r_{cr}^2}{r_e^2 + r_{cr}^2} \right)
 \end{aligned} \tag{3.23}$$

This pressure at the interface is caused by an acting pressure at the bar surface which causes radial stresses along the cracked disc:

$$p_i^E = \frac{r_{cr}}{r_i} \frac{r_{cr}^2 - r_e^2}{r_e^2 + r_{cr}^2} f_{ct} \tag{3.24}$$

$$\sigma_r^E(r) = p_i^E \frac{r_{cr}}{r} \quad \text{for } r \leq r_{cr} \tag{3.25}$$

At the crack interface, the tangential strain can be calculated from the elastic response. Neglecting the contribution of the radial stress, the elongation of the cylinder fibre at the crack interface can be estimated:

$$\varepsilon_{\theta}^E(r_{cr}) = \frac{1}{E_c} (\sigma_{\theta} - \nu \sigma_r) = \frac{f_{ct}}{E_c} \left(1 + \nu \frac{r_e^2 - r_{cr}^2}{r_e^2 + r_{cr}^2} \right) \approx \frac{f_{ct}}{E_c} \tag{3.26}$$

$$\Delta l_r(r_{cr}) \approx 2\pi r_{cr} \varepsilon_{cr} \tag{3.27}$$

The problem is further simplified assuming that the tangential elongation along the cracked region is uniform, the crack width can be determined based on the tangential deformations:

$$2\pi r_{cr} \varepsilon_{cr} = 2\pi r \varepsilon_{\theta}^C(r) + n w = 2\pi r \varepsilon_{\theta}^C(r) + n w_0 \left(1 - \frac{\sigma_{\theta}^C(r)}{f_{ct}} \right)^{1/k} \tag{3.28}$$

It is assumed that $\varepsilon_{\theta} = \varepsilon_{cr}$ within the cracked region. This might be an overestimation of the tangential deformations, nevertheless, it can partially compensate the assumption of neglecting the contribution of radial stresses in the tangential elongation [Van90, Den96]. Consequently, the crack width distribution along the cover and the tangential stress can be calculated by:

$$w = \frac{2\pi \varepsilon_{cr} (r_{cr} - r)}{n} \tag{3.29}$$

$$\sigma_{\theta}^C(r) = f_{ct} \left[1 - \left(\frac{2\pi \varepsilon_{cr} (r_{cr} - r)}{n w_0} \right)^k \right] \tag{3.30}$$

The radial stress can be determined based on the equilibrium of the tangential stresses along the cracked element:

$$\sigma_r^C(r) = -\frac{1}{r} \int_r^{r_{cr}} \sigma_{\theta}^C(r) \cdot dr = -f_{ct} \frac{r_{cr} - r}{r} \left[1 - \frac{1}{k+1} \left(\frac{2\pi \varepsilon_{cr} (r_{cr} - r)}{n w_0} \right)^k \right] \tag{3.31}$$

$$p_i^C = \sigma_r^C(r_i) = f_{ct} \frac{r_{cr} - r_i}{r_i} \left[1 - \frac{1}{k+1} \left(\frac{2\pi\varepsilon_{cr}}{nw_0} (r_{cr} - r_i) \right)^k \right] = f_{ct} \frac{r_{cr} - r_i}{r_i} \left[1 - C(r_{cr} - r_i)^k \right] \quad (3.32)$$

The internal pressure that can be resisted is the addition of the contributions of the cracked and the uncracked rings:

$$p_i = p_i^E + p_i^C \quad (3.33)$$

The radial displacement along the cracked part can be estimated assuming that the contribution of the tangential strains due to Poisson ratio is small compared with the crack contributions. This must account for the stresses that equilibrate the tangential stresses in the cracked region plus the stresses acting on the elastic ring:

$$u(r) = \frac{1}{E_c} \int_r^{r_{cr}} \sigma_r(r) \cdot dr \quad (3.34)$$

$$u^C(r_i) = \frac{f_{ct}}{E_c} \left[r_{cr} \left(\ln \frac{r_{cr}}{r_i} - 1 \right) + r_i - C \left(r_{cr}^{k+1} \left(\ln \frac{r_{cr}}{r_i} - \frac{1}{k+1} \right) + \frac{r_i^{k+1}}{k+1} \right) \right] \quad (3.35)$$

$$u^E(r_i) = u^E(r_{cr}) + \varepsilon_{cr} r_{cr} \frac{r_e^2 - r_{cr}^2}{r_e^2 + r_{cr}^2} \ln \frac{r_{cr}}{r_i} \quad (3.36)$$

Appendix 3C: Three-dimensional stress field

This appendix includes a detailed calculation of the stress field to account for three-dimensional confinement. The presented solution corresponds to the following parameters: $f_{cm} = 40$ MPa; $\varnothing = 20$ mm; $f_R = 0.08$; $s_R = 12$ mm; $b = 1$ mm; $s_{R,clear} = 11$ mm; $h_{Ravg} = 0.92$; $\gamma_{lim} = 7.5^\circ$. three splitting cracks are considered, and each sector is subdivided in 5 for the polygonal approximation of the bar ($\xi = 24^\circ$).

Radial-longitudinal direction

The Mohr circles and geometry of the stress fields discussed in this section are illustrated in Figures 3.14a and b. The wedge ABC is considered to be on the yielding criteria, therefore:

$$0 = \sigma_1^{ABC} (1 + \sin \varphi) - \sigma_3^{ABC} (1 - \sin \varphi) - 2c \cos \varphi \quad (3.37)$$

For a given imposed angle γ , the combination of principal stresses that leads to a certain bond stress is unique. For the considered conditions, the maximum bond stress that can be activated respecting the yield conditions $\tau_b/f_{cp} = 0.41$, $\sigma_3^{ABC} = -121.6$ MPa, $\sigma_1^{ABC} = -20.4$ MPa ($\sigma_1^{ABC} = -120.6$ MPa, $\sigma_r^{ABC} = -21.4$ MPa, $\tau_s^{ABC} = 10.1$ MPa).

Knowing the imposed angle γ and the pole P^{ABC} , the intersection point P^{BC} can be determined, from the intersection of a line through the pole parallel to the face BC and the intersection of the circle ABC. For the considered conditions $\sigma^{BC} = -25.7$ MPa, $\tau^{BC} = 22.5$ MPa.

The circle for the wedge BCD has to pass through the intersection point to respect equilibrium. Assuming that it is at the yielding criterion the circle can be determined. For the considered conditions $\sigma_3^{BCD} = -46.9$ MPa, $\sigma_1^{BCD} = -1.7$ MPa and $\alpha = 39.2^\circ$.

Establishing the equilibrium of a biaxial stress state (with principal stress q and a secondary stress r) a strut with at a certain angle (α) with the principal stress direction yields Equations 3.38 and 3.39 [Che69].

$$\tan \gamma = \frac{p \cdot \sin \alpha \cdot \cos \alpha}{q - p \cos^2 \alpha} \quad (3.38)$$

$$r = \frac{q \cdot p \cdot \sin^2 \alpha}{q - p \cos^2 \alpha} \quad (3.39)$$

Using these two equations, the spreading of a biaxial stress state can be calculated. First it is subdivided in two struts (CDG and BDF) spreading with angles β_1 and β_2 with respect to the principal directions of wedge BCD. On the other end the struts DGH and DFH transfer compression over surface FHG in the same direction of the resulting applied external force (F^{ABC}) and undergo transverse tension. Imposing the condition to respect the yielding criterion and that there is not overlapping with the stress fields of the previous and the following rib, a solution can be found. For the present case $\beta_1 = \beta_2 = 5^\circ$ has been considered, leading to $\sigma_3^{BFD} = \sigma_3^{CDG} = -39.1$ MPa.

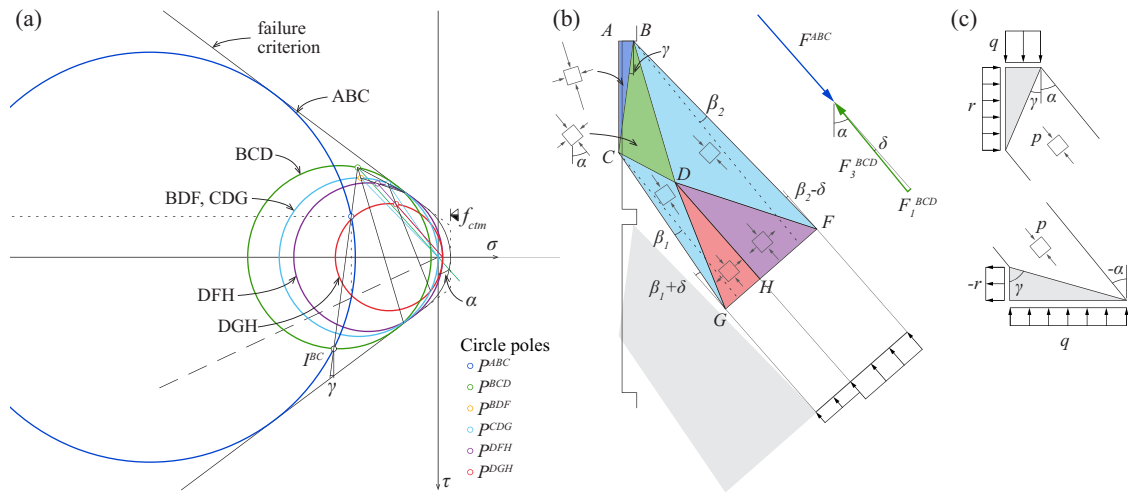


Figure 3.14: Stress field spreading in the radial-longitudinal plane: (a) Mohr circle diagram; (b) stress field geometry; and (c) biaxial stress state equilibrium [Che69].

The reaction at FGH must be in the direction of F^{ABC} . Consequently, the principal directions of the struts CDH and DHF are known. Strut CDG must be deviated by $\beta_1 + \delta$ and strut BDF by $\beta_2 - \delta$. The resulting principal stresses are $\sigma_3^{DGH} = -25.3$ MPa, $\sigma_3^{DFH} = -35.5$ MPa, $\sigma_1^{DGH} = \sigma_1^{DFH} = 1.1$ MPa ($\approx 0.36 f_{ctm}$).

The difference in the principal compression of the struts responds to equilibrium conditions. As the total force in the struts acts in the centre of gravity of the corresponding triangular cross sections, different forces are required to fulfil the equilibrium of moments. However, the equilibrium can only be respected when the struts resulting from the tangential direction are considered.

Tangential direction

The stress in the wedge BCD can be described using the stress tensor expressed in principal directions and using the axis convention presented in Figure 3.15a.

$$\sigma_{BCD} = \begin{bmatrix} \sigma_3 & 0 & 0 \\ 0 & \sigma_1 & 0 \\ 0 & 0 & \sigma_1 \end{bmatrix} \quad (3.40)$$

In order to establish the equilibrium at the interface, the stress tensor has to be rotated. First, a rotation of $\theta_y = -(90 - \alpha - \gamma)$ around the y axis is required (see Figure 3.15a), followed by a second rotation around z' , $\theta'_z = \beta_3$ (see Figure 3.15b). The rotation angle θ'_z is defined by the inclination of the lateral faces of the pyramidal element BCD (see Figure 3.7d) Leading to the rotation matrixes R_y and R'_z .

$$R_y = \begin{bmatrix} \cos\theta_y & 0 & \sin\theta_y \\ 0 & 1 & 0 \\ -\sin\theta_y & 0 & \cos\theta_y \end{bmatrix} ; \quad \sigma_{BCD}^I = R_y \cdot \sigma_{BCD} \cdot R_y^T$$

$$R_z^I = \begin{bmatrix} \cos\theta_z & -\sin\theta_z & 0 \\ \sin\theta_z & \cos\theta_z & 0 \\ 0 & 0 & 1 \end{bmatrix} ; \quad \sigma_{BCD}^{II} = R_z^I \cdot \sigma_{BCD}^I \cdot [R_z^I]^T$$
(3.41)

In the absence of self-weight, the equilibrium across a discontinuity plane is respected when the components normal to the interface plane are the same in the two stress states A and B [Che75], as illustrated in Figure 3.15d. Therefore, the components parallel to axis y'' must remain constant. Using Equation 3.39 and considering $q = -\sigma'_{xx}$, $r = -\sigma'_{yy}$, and $\gamma = \beta_3$, the principal stress $p = -\sigma^{III}_{xx}$ and the angle $\alpha = \psi_3$ of the strut on coordinate system XYZ^{III} . The shear stress τ^{III}_{xz} can be chosen so that the resulting $\tau^{IV}_{yz} = 0$. Lastly, the stress $\sigma^{II}_{zz} = \sigma^{III}_{zz}$, can be chosen so that the corresponding stress tensor in principal directions (XYZ^{IV}) has only compression along axis x^I (see Figure 3.15b). This condition also determines the angle θ^{III}_y . The yielding condition must be verified.

Once the direction and the stress in the strut the spreading can be determined as in the previous section. The geometry has been chosen to reach the tensile stress of the radial-longitudinal direction, resulting in a stress in the spreading strut of -37.1 MPa and a resulting in stress in the direction of the applied force of -28.3 MPa. The resulting stress field is represented in Figures 3.7d and f.

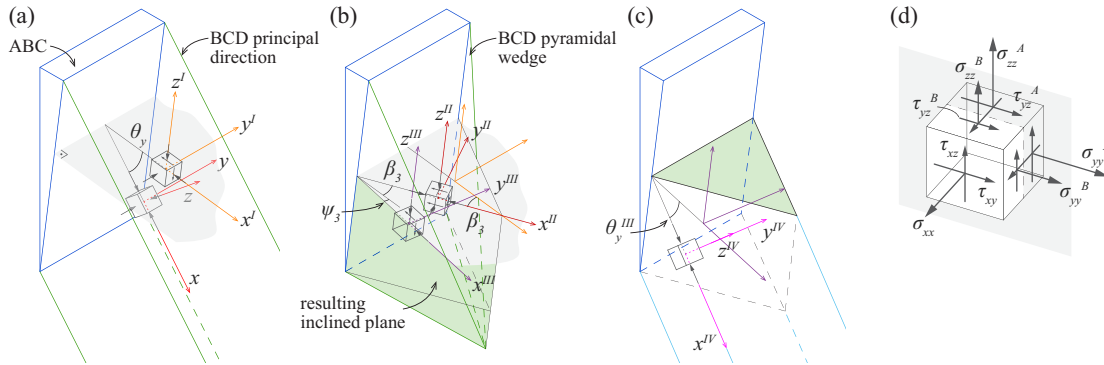


Figure 3.15: Stress field spreading in the tangential direction: transformations (a) from XYZ to XYZ^I , (b) from XYZ^I to XYZ^{II} , (c) from XYZ^{II} to XYZ^{III} ; and (d) interface equilibrium conditions.

Appendix 3D: Extended experimental database

The main parameters of the experimental database of short pull-out tests in well-confined conditions with pull-out failure are provided in Table 3.3. The values provided in the table correspond to the maximum and minimum values for each experimental campaign. For definition of parameters, refer to section Notation. The references of the considered tests are:

- Eligehausen et al. (1993) [Eli83]
- Soroushian et al. (1989) [Sor89]
- Harajili et al. (1995) [Har95]
- Balazs et al. (1996) [Bal96]
- Hansen et al. (1996) [Han96]
- Manguson (2000) [Mag00]
- Murcia-Delso et al. (2013) [Mur13]
- Metelli et al. (2014) [Met14]
- Prince et al. (2014) [Pri13]
- Leibovich et al. (2019) [Lei19]
- Dybel et al. (2021) [Dyb21]
- Koschemann et al. (2022) [Kos22a]
- Lemcherreq et al. (2023) [Lem23]

Table 3.3: Summary of the experimental database of short pull-out tests in well-confined conditions with pull-out failure.

Reference	Type of test	Type	n_t	θ [mm]	c/θ	l_b/θ	f_R	s_R	$s_{R,clear}$	b	h_R	θ_s	n_s	f_{cm} [MPa]	δ_{sc1} [mm]	τ_{bmax} [MPa]	$\tau_{bmax,calc}/\tau_{bmax,MC10}$	$\tau_{bmax,calc}/\tau_{bmax,calc}$	$\delta_{sc1,calc}/\delta_{sc1,calc}$
Eligehausen et al. (1983)	MPO	C	20	19.1 31.8	2.0 2.0	5.0 5.0	0.066 0.160	9.7 14.0	7.4 11.5	2.3 3.2	0.9 2.0	6.4 25.4	4.0 4.0	29.4 31.6	1.0 1.9	11.5 15.9	0.8 1.0	0.8 1.1	0.8 1.4
Soroushian et al. (1989)	MPO	C	6	16.0 25.0	2.0 2.0	5.0 5.0	0.060 0.090	10.0 14.4	8.0 12.0	1.6 2.4	0.6 1.2	12.7 12.7	4.0 4.0	30.0 30.0	1.0 2.0	14.8 17.6	1.0 1.1	1.1 1.3	0.9 1.6
Harajili et al. (1995)	MPO	C	8	20.0 25.0	1.4 1.5	3.5 3.5	- -	8.0 15.4	5.9 12.2	2.1 3.2	- -	10.0 10.0	4.0 4.0	22.0 22.0	1.3 2.5	8.8 12.5	0.8 1.1	0.7 1.1	- -
Balazs et al. (1996)	PO	C	5	16.0 16.0	2.6 2.6	1.3 1.3	0.065 0.065	8.8 8.8	7.4 7.4	1.4 1.4	0.5 0.5	- -	- -	27.6 27.6	0.8 0.9	13.7 17.4	1.0 1.2	1.0 1.3	0.9 1.1
Hansen et al. (1996)	PO	C	10	16.0 32.0	4.0 8.6	3.0 5.0	0.057 0.057	- -	6.5 11.5	- -	- -	- -	- -	61.0 76.2	0.5 1.1	24.9 32.4	0.8 1.0	1.2 1.5	0.6 1.3
Manguson (2000)	PO	C	21	16.0 20.0	8.3 8.9	2.5 2.5	0.056 0.127	7.0 12.2	3.7 7.7	3.3 4.5	0.5 0.8	- -	- -	27.7 101.6	0.4 1.9	10.4 51.4	0.7 1.2	0.8 2.1	0.6 1.7
Murcia-Deliso et al. (2013)	PO	C	5	36.0 57.0	7.5 12.2	5.0 5.0	0.068 0.095	- -	19.1 24.9	- -	- -	13.0 13.0	6.0 9.0	34.5 55.5	- 3.0	15.2 24.1	1.0 1.2	1.0 1.3	1.1 1.7
Metelli et al. (2014)	PO	M	10	12.0 40.0	4.5 4.5	5.0 5.0	0.058 0.075	6.0 13.9	4.5 11.4	1.5 2.5	0.4 0.9	- -	- -	30.1 50.7	0.7 2.5	16.1 29.5	0.9 1.4	1.1 1.8	0.9 1.7
Prince et al. (2014)	PO	C	6	8.0 10.0	4.5 5.8	5.0 5.0	0.085 0.093	5.9 7.5	5.4 6.8	1.2 1.2	0.5 0.7	- -	- -	33.9 33.9	0.5 0.9	17.6 25.1	1.0 1.3	1.2 1.7	1.2 2.3
Leibovich et al. (2019)	PO	M	7	20.0 20.0	4.5 4.5	1.0 4.3	0.100 0.100	15.0 15.0	12.0 12.0	3.0 3.0	1.5 1.5	- -	- -	23.5 30.1	1.1 1.3	11.8 16.9	0.9 1.1	1.0 1.2	1.1 1.4
Dybel et al. (2021)	PO	C	4	16.0 16.0	4.5 4.5	5.0 5.0	0.153 0.153	9.2 9.2	7.4 7.4	1.8 1.8	1.4 1.4	- -	- -	41.4 41.4	0.7 1.1	21.4 23.9	1.1 1.2	1.3 1.5	1.1 1.7
Koschemann et al. (2022)	PO, BE	C	37	16.0 16.0	3.0 5.8	2.0 2.0	0.065 0.065	9.6 9.6	7.3 7.3	2.3 2.3	0.6 0.6	6.0 6.0	2.0 2.0	49.2 119.7	0.3 0.8	21.4 52.1	0.9 1.1	1.2 1.9	0.5 1.3
Lemchenreq et al. (2023)	PO	C	12	16.0 20.0	4.5 5.8	2.0 5.0	- -	9.2 11.0	8.0 10.0	1.0 1.2	- -	- -	- -	29.2 39.7	1.2 2.5	15.0 20.7	1.0 1.3	1.1 1.4	- -
Avg																1.03	1.35	1.11	
CoV:																12.5%	24.9%	28.2%	

Type of test: PO = pull-out test; MPO = modified pull-out test; BE = beam-end test
 Type of bar: C = commercial; M = machined

Notation

Lower case Latin

b_R	rib width
c	clear concrete cover
f_{cm}	cylinder compressive strength of concrete
f_{coh}	cohesion of the concrete in the Mohr-Coulomb failure criteria
f_R	bond index
h_R	rib height
$h_{R,max}$	maximum rib height
l_b	bonded length
p	internal pressure un the pressure tests
n_{cr}	number of splitting cracks observed in the internal pressure tests
n_t	number of tests considered from the corresponding reference in the database
r	radial direction in cylindrical coordinates
r_{cr}	radius of the cracked region of the concrete cylinder
r_e	external radius of the concrete cylinder
r_i	internal radius of the concrete cylinder
s_R	transverse rib spacing
$s_{R,clear}$	clear rib spacing
u_r	radial displacement at the opening surface
x, y	coordinate axes

Upper case Latin

A_R	projection of the rib area on the cross section of the bar
E_{cm}	concrete elastic modulus
F	applied force in a pull-out test
Y	yield criterion

Lower case Greek

α	inclination of the strut B
α_R	transverse rib flank inclination
β_R	transverse rib angle
γ	wedge angle
γ_{lim}	minimum wedge angle due to the rib geometry
δ_{sc}	relative slip
θ_X	inclination of the principal stress components in region X
μ_s	friction coefficient between steel and concrete
$\sigma_1, \sigma_2, \sigma_3$	principal stress components
σ_{cX1}	maximum principal stress in the concrete region X
σ_{cX2}	intermediate principal stress in the concrete region X
σ_{cX3}	minimum principal stress in the concrete region X

σ_{cXl}	stress in the longitudinal direction of the bar in the concrete region X
σ_{cXr}	stress in the radial direction in the concrete region X
σ_{θ}	stress in the tangential direction
τ_b	bond stress
$\tau_{bu,po}$	maximum bond stress for pull-out failure
$\tau_{bu,sc}$	maximum bond stress for splitting with confinement
$\tau_{bu,su}$	maximum bond stress for splitting in unconfined conditions
τ_s	shear stress along the bar shaft
φ	internal friction angle in the Mohr-Coulomb failure criteria

Other characters

\varnothing	bar nominal diameter or diameter of the cylindrical openings in the pressure tests
\varnothing_p	diameter of the punch in the partially loaded areas by Lieberum et al.

4

Estimation of the bar stress based on transverse crack width measurements in reinforced concrete structures

This chapter is the pre-print version of the article mentioned below, submitted for publication to Structural Concrete:

Corres E., Muttoni A., *Estimation of the bar stress based on crack width measurements in reinforced concrete structures*, [article submitted to Structural Concrete].

The work presented in this publication was performed by the author under the supervision of Prof. Aurelio Muttoni who provided constant and valuable feedback, proofreading and revisions of the manuscript. The main contributions of the author to this article and chapter are the following:

- Comprehensive literature review including research and design standards about cracking and the activation of bond stresses in service conditions.
- Design, fabrication and testing of 2 reinforced concrete ties to characterize the activation of bond stresses.
- Design, fabrication and testing of 6 large scale reinforced concrete beam to characterize the activation of bond stresses in members subjected to tension and in the shear reinforcement.
- Implementation and post-processing of the detailed measurements including Digital Image Correlation and distributed fibre optical sensors.
- Analysis and interpretation of the experimental results.
- Further analysis and post-processing of the detailed measurements from the beam test series SC70 (experimental work and first analysis performed by Raffaele Cantone).
- Proposition of a formulation to estimate the activated bond stresses in cracked elements based on the integration of a local bond-slip relationship.
- Verification of the proposed bond stresses and their pertinence to estimate the stress in the reinforcement based on crack width measurements.
- Redaction of the manuscript of the article and production of its figures and tables.

Abstract

Crack width formulations are used to predict the crack width on the basis of the calculated stress in the reinforcement and some geometrical and mechanical parameters. In existing structures, crack width formulations can be used to estimate the stress in the reinforcement from crack width measurements. One of the main sources of uncertainty in this estimation is the crack spacing. However, the spacing between cracks can be measured in existing structures. When the spacing is known, the main source of uncertainty shifts to the bond stresses. Recent experimental results show that the values of the mean bond stress typically considered in code formulations overestimate the actual bond stresses activated in cracked concrete specimens. In this context, this chapter includes the results of an experimental programme consisting of reinforced concrete ties and beams instrumented with Digital Image Correlation and fibre optical measurements. The results confirm the differences with typically assumed bond stresses. A formulation to estimate the bond stresses in service conditions is derived from the results of the numerical integration of a previously developed local bond-slip relationship. Their pertinence for the estimation of the stress in the reinforcement from the measured crack width is evaluated. Satisfactory results are obtained for monotonic loading and for the maximum force in cyclic tests.

4.1 Introduction

Understanding the cracked response of reinforced concrete structures is important, as it influences the stiffness of members (deflections and vibrations) and their water tightness. Furthermore, crack control is important for durability and aesthetic reasons. Accordingly, current design standards such as Eurocode 2 (EC2:2004) [Eur04] or *fib* Model Code 2010 (MC2010) [FIB13] include expressions to estimate the crack width and impose limits based on the environmental exposure and other criteria.

Unsurprisingly, cracks are often found in existing structures and they are often one of the indicators used in visual inspections for structural assessment [Zab19, OFR21]. However, the evaluation of the safety of a structure based on the presence or absence of cracks is not straightforward. On the one hand, cracks do not necessarily indicate an insufficient level of safety if they are expected and coherent with the structural behaviour. On the other hand, small crack openings might not be an indicator of sufficient resistance in cases governed by fragile failure modes [Zab19, Mon22a].

The fatigue assessment of reinforcement bars in existing structures can be conducted in an efficient manner by measuring indirectly the stress variations. This can be conducted by measuring the strain variations in the bar using strain gauges like in steel structures [Tre15]. However, the disturbance of the bond behaviour due to the removal of the concrete cover for gluing the strain gauges can affect the results. An interesting alternative is provided by measuring the crack opening variations using classical or modern techniques such as Digital Image Correlation and calculating the stress variations on the basis of stress-crack openings relationships. However, crack formulations have the opposite goal, that is to estimate the crack width from the calculated reinforcement stress ([Eur04, FIB13]). This often includes simplifying assumptions that might not be pertinent if the formula is used in reverse for bar stress estimation. Moreover, in the case of an existing structure, additional information such as crack spacing, which is an essential parameter in the crack width formulations, or the existence of secondary or splitting cracks can be measured or visually verified.

The first proposed crack width formulae were based on the slip defined as the relative displacement between the steel and the concrete. When the crack appears, compatibility of deformations between the steel and the concrete is lost. The slip activates bond stresses which determine the crack spacing and the tensile stress distributions in the bar and the concrete. Starting in 1936, Saliger [Sal36] proposed a formulation based on this principle to calculate the crack spacing and width in flexural elements with smooth bars assuming a linear bond stress distribution with a maximum at the crack location. Thomas [Tho36] proposed analytical expressions including the effect of shrinkage assuming a parabolic bond stress distribution. A different approach was adopted by Brooms [Bro65], assuming that no slip occurs between the bar and the concrete and that plane sections do not remain plane. In these conditions, tensile stresses develop linearly from the cracks leading to the generation of principal or secondary cracks, depending on whether they reach the surface of the concrete. The resulting crack spacing is proportional to the cover [CEB67]. Ferry-Borges [Fer66] proposed a formulation accounting for both effects that is the base of some of the current code formulae [Eur04, FIB13]. Several crack formulations can be found in the literature using different approaches (thorough reviews of the available models can

be found in [Bor05, Lap18, Van23]). The comparison of 30 formulations performed by Lapi et al. [Lap18] shows that the semi-analytical models of Eurocode 2 [Eur04] and Model Code 10 [FIB13] are amongst the most accurate.

Concerning the bond stresses, Balazs [Bal93] proposed an analytical model based on the integration of the ascending branch of the bond-slip relationship for well-confined conditions from the *fib* Model Code 1990 [CEB93]. A closed form solution was proposed for the crack propagation stage, and a numerical integration was used for the stabilized cracking phase. Based on the analytical integration of a bond-slip relationship [Noa88], Sigrist [Sig95] proposed a rigid plastic bond-slip law with a bond stress equal to $2f_{ctm}$ and f_{ctm} before and after bar yielding, respectively. The considered bond-slip laws [Noa88, CEB93] were derived from a relatively small number of tests. Recent research has shown that the bond-slip relationship from MC2010 captures the general trends of the interface response, but the influence of some parameters is not satisfactorily accounted for [Met14, Bad21, Cor23].

Some attempts have been made to estimate the bar stress from surface crack measurements. Campana et al. [Cam13] used the model by Sigrist [Sig95] to estimate the stresses in the stirrups of beam tests based on crack width measurements; however, the results could not be verified as the stirrups were not instrumented. Calvi [Cal15] proposed a model for the assessment of elements with shear cracks, where the bar strains are estimated from crack width measurements using the expressions for proposed by Shima et al. [Shi87] and the considerations of Maekawa et al. [Mae03]. Brault et al. [Bra15] used this model to predict the strains measured in small beams subjected to bending instrumented with Digital Image Correlation (DIC) and distributed fibre optical sensors glued to the reinforcing bars. The estimated strains have the same order of magnitude as the measurements; however, the trends of the experimental results and the predictions show significant differences. Carmo et al. [Car15] estimated the average steel strain based on the results of ties with internally strain gauged bars and marker photogrammetry. They concluded that this approach is feasible but the accuracy was limited by the camera resolution.

Recent experimental studies using DIC and distributed fibre optical sensors in ties [Can20, Bad21, Gal23a, Lem23a] and beams [Pol19, Can20, Gal22, Mon22a] have shown great potential to improve the understanding of the cracking process and the bar-to-concrete interaction. Some of these results show average bond stress values significantly lower than the code formulations [Gal22, Gal23a]. Fibre optic sensors have proven to be useful to characterise shrinkage induced strains in the reinforcement [Dav17, Bad21a, Gal23a, Lem23a].

Based on these observations and the fact that bond plays a critical role in the cracking response, this chapter investigates the development of bond stresses through analytical and experimental work, with the aim of improving the existing crack formulations to estimate the reinforcement stress based on crack width measurements. Given its mechanical basis, the slip approach is considered in this publication. First, the slip-based model is presented and the influence of the different parameters is evaluated. Secondly, experimental results from tie and beam tests instrumented with DIC and fibre optical sensors on the reinforcement are analysed to better understand the cracking phenomenon and bond development. Lastly, new values for the bond stresses are proposed on the basis of a local bond stress-slip model adapted from Chapter 3. The slip-based model with the proposed bond values are used to estimate the stresses in the experimental results, showing satisfactory results.

4.2 Cracking in structural members

4.2.1 Slip-based model

The mechanical behaviour of a cracked element in tension is typically characterized by the force-average strain response, as shown in Figure 4.1a. The response can be divided in three phases. First, the uncracked response is characterized by compatibility of strains between the bar and the concrete. The crack formation stage begins with the first crack, that appears when the tensile strength of the weakest concrete section is reached, leading to the strain distribution shown in Figure 4.1c. Bond stresses progressively transfer the force from the bar to the surrounding concrete that will eventually reach the cracking strain again at a distance which cannot be shorter than l_{cr} from the 1st crack. When all crack distances are not larger than $2l_{cr}$, new cracks cannot develop (end of the crack formation phase). The minimum and maximum crack spacings (s_{cr}) are thus l_{cr} and $2l_{cr}$, respectively. At this point, the stabilized cracking phase starts, characterized by an increase of the steel strains when the force is further augmented, see Figure 4.1c. This publication focuses on the stabilized cracking stage as it is the most relevant for structural members subjected to external loads.

The slip δ_{sc} corresponds to the difference between the displacements of the steel and the concrete. The slip in the differential element shown in Figure 4.1b can be calculated from the steel (ε_s) and concrete strains (ε_c) using Equation 4.1. The crack width results from the slip at each side of the crack (i.e. the crack spacing s_{cr}) as per Equation 4.2.

$$d\delta_{sc} = (\varepsilon_s - \varepsilon_c)dx \quad (4.1)$$

$$w = \int_{s_{cr}} (\varepsilon_s - \varepsilon_c)dx = s_{cr}(\varepsilon_{sm} - \varepsilon_{cm}) \quad (4.2)$$

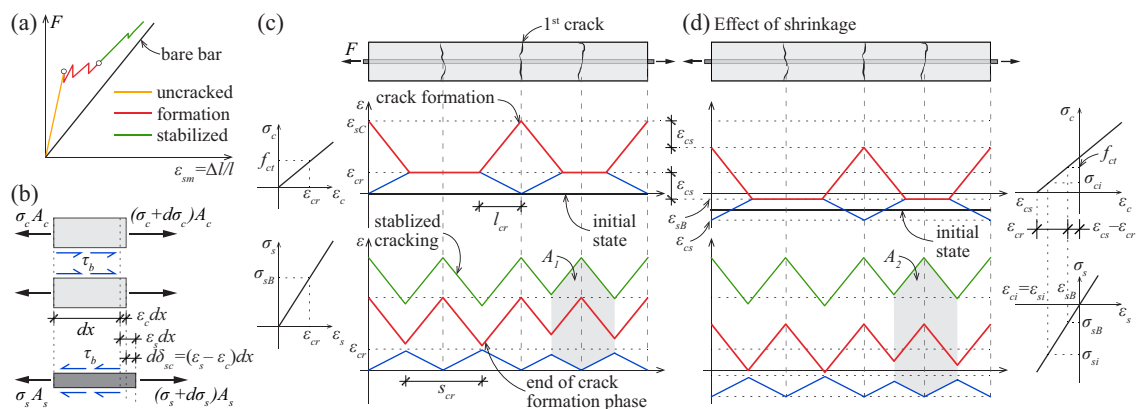


Figure 4.1: Response of a concrete tie: (a) force – average strain diagram; (b) differential tie element; strain distribution in the crack formation phase and the stabilized cracking phase (c) without the effect of shrinkage and (d) accounting for shrinkage.

The stress and strain distributions in the two materials are determined by the external loads and the bond forces. A common approach in numerous crack models is to use a constant bond stress corresponding to the average over the bonded length ($\tau_{b,avg}$). This leads to the diagrams presented in Figure 4.1c where the strain profiles vary linearly. The residual tensile strength of the concrete [Hor91] is neglected.

Shrinkage influences the initial stress and strain distributions (Figure 4.1d) and can reduce the cracking force [Bis01, Gri07]. According to Equation 4.2, the crack width corresponds to the area between the strain profiles of the bar and the concrete (areas A_1 and A_2 in Figures 4.1c and d). The consequence of shrinkage can clearly be observed: for a given stress in the bar, the crack width is larger compared with the case neglecting shrinkage ($A_1 < A_2$). This is reflected in Equation 4.3 that allows to calculate the resulting crack width for a given bar stress in the stabilized cracking phase.

$$w = \frac{s_{cr}}{E_s} \left[\sigma_{sC} - \frac{s_{cr} \tau_{b,avg}}{\emptyset} \frac{1 + (n-1)\rho_t}{1 - \rho_t} - E_s \varepsilon_{cs} \right] \quad (4.3)$$

where, E_s is the elastic modulus of the reinforcement, σ_{sC} is the stress in the reinforcement at the crack location, \emptyset is the bar diameter, $n = E_s/E_c$, ρ_t is the reinforcement ratio of the tie and ε_{cs} is the unrestrained shrinkage strain (considered as a negative value, see Figure 4.1d). The derivation of this expression can be found in Appendix 4A.

This expression is the basis of the maximum crack width formulations in the current codes. MC2010 specifies the average bond strength in the calculation of the length over which slip between concrete and steel occurs. The proposed values for the average bond strength are $1.8f_{ctm}$ for short term loading and $1.35f_{ctm}$ for other types of loading. EC2:2004 does not explicitly mention the average bond stress. A factor to account for the casting position has been proposed [Pér20, Gar22] for the *fib* Model Code 2020 and the new generation of Eurocode 2 [CEN23], which leads to average bond stresses of $2f_{ctm}$ and $1.5f_{ctm}$ in good and poor casting conditions respectively. The proposed expressions for the relative mean strain are similar with a factor which accounts for short or long-term loading. The Tension Chord Model (TCM) [Mar98] uses the same approach assuming a rigid plastic bond-slip relationship with bond stresses of $2f_{ctm}$ and $1f_{ctm}$ before and after yielding of the reinforcement.

Equation 4.3 can be rearranged to provide the stress in the bar as a function of the other variables, resulting in Equation 4.4:

$$\sigma_{sC} = E_s \frac{w}{s_{cr}} + \frac{s_{cr} \tau_{b,avg}}{\emptyset} \frac{1 + (n-1)\rho_t}{1 - \rho_t} + E_s \varepsilon_{cs} \quad (4.4)$$

A sensitivity analysis for a tie with a section of 100×100 mm and a reinforcement bar of $\emptyset 18$ is presented in Figure 4.2. The reference values for the relevant parameters and the tie cross section are shown in Figure 4.2a. The reference value of $s_{cr} = 208$ mm corresponds to the average crack spacing according to MC2010. Figure 4.2a shows the bar stress-crack width diagram according to EC:2004 (dashed black line), MC2010 (solid grey line) and Equation 4.4 (solid black line) for the reference value of the influencing parameters. For a given stress, the code formulations underestimate the crack width compared with Equation 4.3, because the stress variation is calculated assuming the maximum spacing.

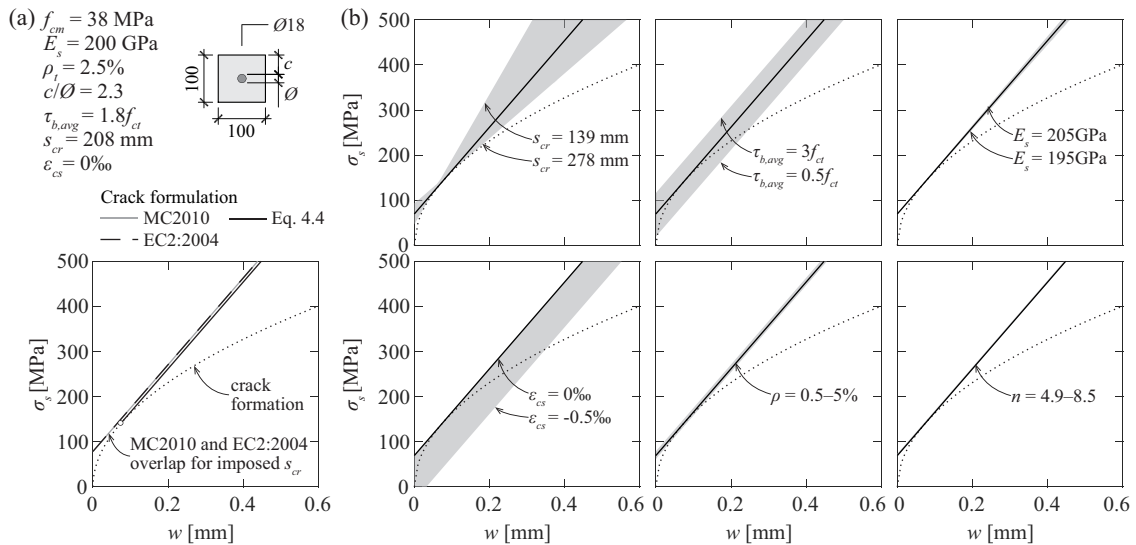


Figure 4.2: Sensitivity analysis of the influencing parameters in the bar stress – crack width relationship: (a) reference parameters and model comparison; and (b) effect of crack spacing, average bond stress, elastic modulus of steel, unrestrained shrinkage strain, reinforcement ratio and elastic moduli ratio.

Figure 4.2b shows the influence of the different parameters. It can be observed that the crack spacing is a crucial parameter. For an existing structure, it can be measured with a certain precision. Shrinkage strains induce compressive stresses in the reinforcement, and have a non-negligible influence on the bar stress for a given crack width. Estimating the shrinkage effects is difficult in simple specimens in laboratory conditions [FIB08], and even more so in real structures. However, concerning the estimation of bar stresses from the measured crack width, it must be noted that neglecting the shrinkage strains leads to an overestimation of the bar stress. This can be considered a conservative estimation of the remaining capacity of the bar. Bond stresses have a relevant contribution particularly for small crack widths. The influence of the other parameters is relatively small for the studied case.

4.2.2 Additional experimental evidence

The reality is slightly more complex than the response of the idealized concrete ties described above. First of all, the bond distribution is not uniform. Due to the propagation of secondary conical cracks developing from the ribs [Got71] which can reach the main crack, bond stresses are significantly reduced near the crack. This is typically accounted for by considering a different bond-slip response near the crack [Eli83, Kre89] or by applying a reduction factor over a certain length [CEB93, Fer07, FIB13]. Due to compatibility of displacements, the slip at the mid-point between cracks has to be zero and, therefore, bond stresses in that region are small.

Several authors have observed that the crack width at the level of the reinforcement is smaller than at the concrete surface [Hus68, Yan89, Bor10]. The difference is often attributed to the

secondary conical cracks [Bor10, Pér13]. Moreover, in cases with relatively small covers, secondary conical cracks can reach the concrete cover during the stabilized cracking phase and eventually propagate across the section, modifying the stress distribution. In such conditions, splitting and spalling cracks can significantly reduce the bond performance of the bar near the crack [Cor23].

4.3 Experimental programme

An experimental programme was conducted in the Structural Concrete Laboratory of the École Polytechnique Fédérale de Lausanne (Switzerland) to investigate the relationship between the crack width and the stress in the reinforcement, and the development of bond stresses in structural elements. Furthermore, results from beam tests from series SM10 by Monney et al. [Mon22a] and SC70 by Cantone et al. [Can20] performed in the same laboratory and instrumented with similar techniques are included in this chapter.

4.3.1 Tension test series TC10

Main parameters and test set-up

Two tension tests were performed on reinforced concrete ties with a square cross section and a length of 1250 mm, see Figure 4.3a. Specimen TC11 had a cross section of 214×214 mm and was reinforced with 4 bars with nominal diameter (\emptyset) of 18 mm, as shown in Figure 4.3b. Specimen TC12 had a single \emptyset 18 centred in a cross section of 100×100 mm. All the details including the clear cover (c) are provided in Table 4.1. The tests were performed using a Trebel Testing Machine with 5 MN capacity in tension at a displacement rate of 0.1 mm/min. Specimen TC11 was loaded monotonically until failure. TC12 was loaded monotonically until $\sigma_{cyc,max} = 275$ MPa, then unloaded until $\sigma_{cyc,min} = 27.5$ MPa. After that, 35 cycles with the same stress range were applied before the tie was loaded until the bar yielded.

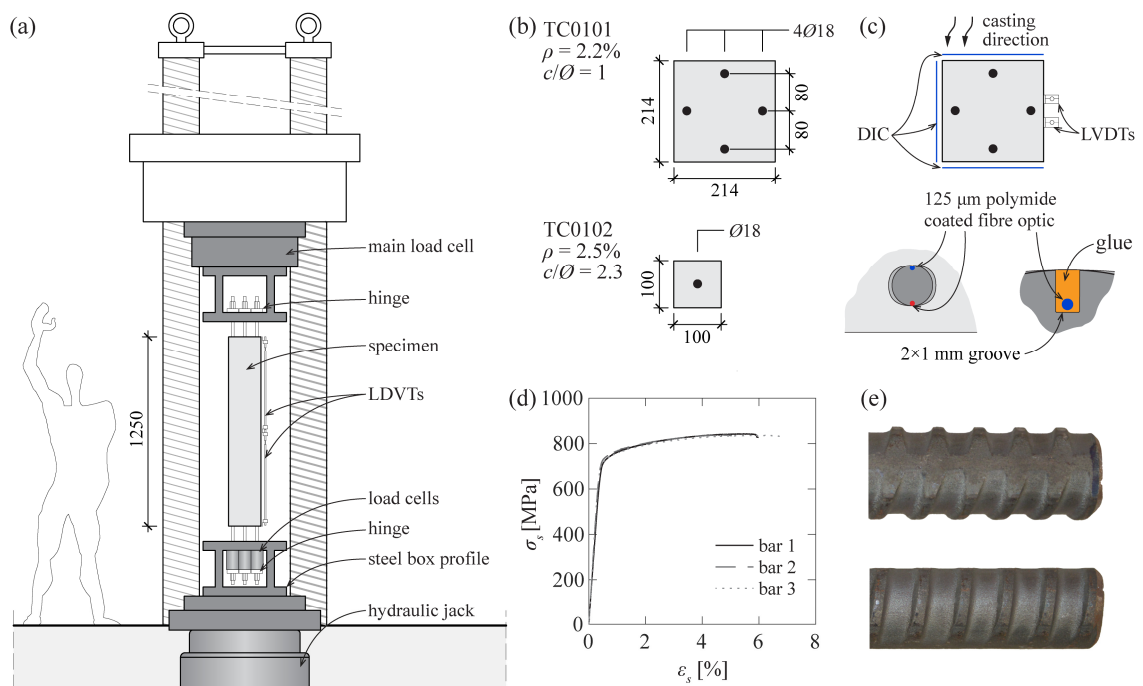
The specimens were cast horizontally, as illustrated in Figure 4.3c, from a single batch of normal-strength ready-mixed concrete provided by a local supplier with a maximum aggregate size of 16 mm. The compressive strength f_{cm} and the tensile strength f_{ctm} of the concrete measured on cylinders (height×diameter = 320×160 mm, direct tensile tests for f_{ctm}) are indicated in Table 4.1.

The longitudinal reinforcement bars were hot rolled high-strength threaded bars with a nominal diameter of 18 mm. As shown in Figure 4.3d, they had no clear yield plateau. The mean value of the yield strength at 0.2% residual strain was 731 MPa. The ribs were composed of two lugs disposed in continuous threads along the axis of the bar, see Figure 4.3e. They were oriented parallelly to the concrete surface, see Figure 4.3c. The geometrical characteristics of the bar were obtained from a laser scan of the surface of the bars [ISO19]: bond index f_R 0.088, maximum rib height 1.13 mm, transverse rib angle 82°, transverse rib flank inclination 46.4° and transverse rib spacing 8.02 mm. The clear rib spacing $s_{R,clear}$ measured at the top of the lugs was 6.34 mm.

Table 4.1: Series TC10 main parameters (see Notation for the definition of the parameters)

Specimen	\emptyset [mm]	bars [-]	ρ [%]	c/\emptyset [-]	Loading type	Age at testing [days]	f_{cm}^a [MPa]	f_{cm}^b [MPa]
TC11	18	4	2.22	1	monotonic	244	43.1	2.5
TC12	18	1	2.54	2.3	cyclic	239	43.1	2.5

^a measured at testing age

^b measured at 28 days

Figure 4.3: Test series TC10: (a) elevation of the test set-up; (b) specimen cross section; (c) measurement systems on the concrete surface and fibre installation for strain measurement; (d) reinforcement bar tensile tests results; and (e) rib profile.

Measurements

Three faces of the ties were tracked using DIC: at the bottom face of the formwork (resolution 20 megapixels and resulting pixel size 277 $\mu\text{m}/\text{pixel}$), at the top face (29 megapixels and 215 $\mu\text{m}/\text{pixel}$) and for a lateral face (5 megapixels, 544 $\mu\text{m}/\text{pixel}$), see Figure 4.3c. The correlation was done using the VIC-3D software [Cor21]. The maximum in plane displacement error was 1/60 pixels. In the face with no DIC measurements, two LVDT's were installed to follow the total elongation.

The reinforcement bars were instrumented by Polyimide-coated optical fibres with a diameter of 125 μm running along two opposite sides of the bar, as shown in Figure 4.3c. A single fibre per bar was placed in grooves (1-mm wide and 2-mm deep) running along opposite faces of the bar. The fibres were oriented in a plane perpendicular to the nearest concrete surface, Figure 4.3c. The strains were measured using Optical Distributed Sensor Interrogator ODiSI-6100 by Luna Innovations with a strain measurement range of $\pm 12,000 \mu\epsilon$ and a measurement accuracy of $\pm 25 \mu\epsilon$ [Lun20]. The spatial resolution of the strain measurements was 0.65 mm, and the acquisition frequency was 10 Hz.

4.3.2 Beam test series SM10

Six three-point bending tests conducted by Monney et al. [Mon22a] and the authors of this publication were used to characterize the cracking response of large-scale elements. Three beam specimens with constant height h of 700 mm and various widths b_w were tested as shown in Figure 4.4b. Each beam had two test regions with the same shear reinforcement consisting of $\emptyset 8$ stirrups placed with a spacing of 200 mm, one with ductility class A and the other with ductility class C according to EC2:2004 [Eur04]. To prevent a failure in the central part, it was reinforced with double $\emptyset 14$ stirrups with a spacing of 150 mm, see Figure 4.4a. The flexural reinforcement was composed of two B500C $\emptyset 34$ bars ($f_{ym} = 561 \text{ MPa}$) and three to six Y1050 $\emptyset 36$ bars ($f_{ym} = 1014 \text{ MPa}$) to provide an approximately constant flexural reinforcement ratio ($\rho_f \sim 1.5\%$). The beams were loaded monotonically until failure using two hydraulic jacks anchored to the strong floor at a loading rate of 10 kN/min. Further details are provided in Table 4.2.

With an effective depth d of 650 mm, the nominal clear cover c_f of the flexural reinforcement was 33 mm ($\sim 1\emptyset_f$), while the nominal clear cover c_w for the stirrups was 25 mm ($3.1\emptyset_w$) as shown in Figure 4.4d. The $\emptyset 34$ bars had a bond index of 0.052 and a clear rib spacing of 16.3 mm. The $\emptyset 8$ type A bars had a bond index of 0.047 and a clear rib spacing of 4.5 mm. The $\emptyset 8$ type C bars had a bond index of 0.069 and a clear rib spacing of 5.1 mm.

Table 4.2: Monotonic test series SM10 main parameters (see Notation for the definition of the parameters)

Test	Shear reinf. ductility class	b_w [mm]	h [mm]	ρ_f [%]	ρ_w [%]	f_{cm} [MPa]	f_{ctm} [MPa]	f_{yw} [MPa]	V_{max}^a [kN]
SM11	A	800	700	1.52	0.063	50.7	3.2	505	603
SM12	C	800	700	1.52	0.063	50.6	3.2	538	610
SM13	A	600	700	1.51	0.084	50.4	3.2	505	540
SM14	C	600	700	1.51	0.084	50.4	3.1	538	639
SM15	A	500	700	1.50	0.101	50.2	3.1	505	454
SM16	C	500	700	1.50	0.101	50.0	3.1	538	515

^a measured shear strength without self-weight

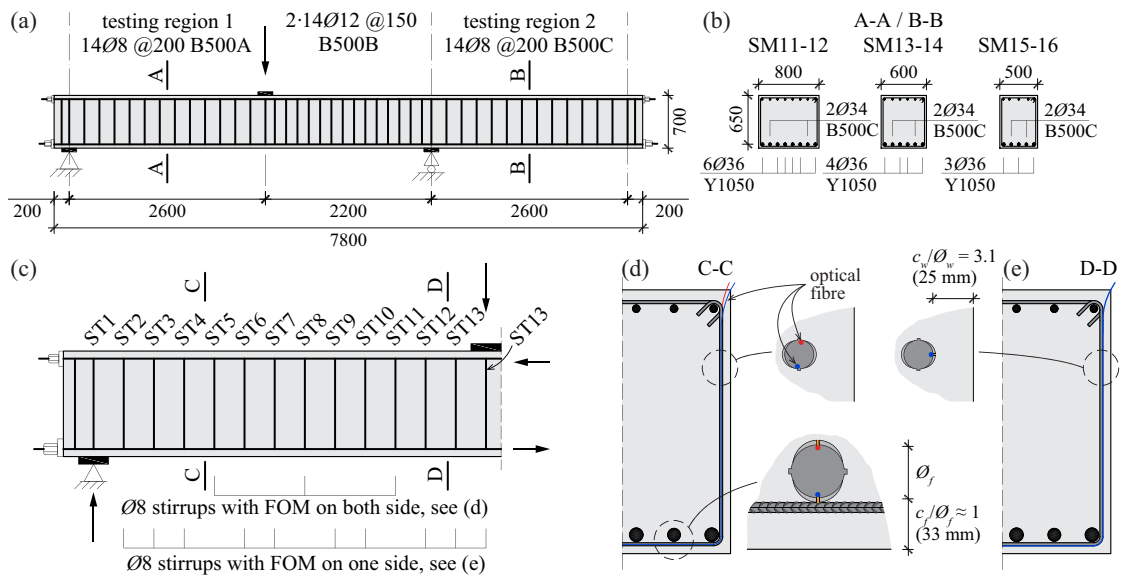


Figure 4.4: Monotonic test series SM10: (a) elevation of the test set-up; (b) cross section of the test specimens; (c) fibre instrumentation within the tested region; and details of the fibre installation in the longitudinal reinforcement and in the stirrups with (d) two sensors or (e) one sensor (for additional details, see [Mon22a]).

The two lateral faces were tracked with DIC. In each beam, the two longitudinal $\varnothing 34$ bars were instrumented with a single fibre optic installed along two opposite sides of the specimen, as illustrated in Figure 4.4d. The 125 μm polyimide-coated fibres were placed in a groove 2 mm deep in the longitudinal reinforcement and 1 mm deep in the stirrups. The stirrups ST2 to 13 were instrumented with fibres, as shown Figure 4.4c. Stirrups ST5, 8 and 11 had one fibre running along the opposite faces of the stirrup, see Figure 4.4d. The rest had only one fibre running along the perimeter of the stirrup, see Figure 4.4e. For additional details, see Monney et al. [Mon22a]

4.3.3 Beam test series SC70

Three four-point bending tests conducted by Cantone et al. [Can20] were analysed to characterize the cracking response under cyclic loading. Figure 4.5a shows the main dimensions of the test set-up. The beams had a height of 320 mm, a width of 300 mm and a longitudinal reinforcement consisting of two high-strength $\varnothing 22$ bars, see Figure 4.5b. The effective depth was 274 mm, leading to a nominal clear cover c_f of 35 mm ($1.6\varnothing_f$), see Figure 4.5c. No shear reinforcement was disposed.

The beams were loaded cyclically with three different shear force ranges. SC75 was loaded up to a maximum shear correspondent to the theoretical cracking force. SC76 was loaded up to a shear force of 55% of the shear strength V_{max} . SC77 was loaded up to the formation of the sub-horizontal branch of the shear crack. After 50 cycles, the specimens were loaded until failure, except for specimen SC77 where the propagation of the shear crack due to cyclic loading led to a premature

failure after 21 cycles. The main parameters of the tests are given in Table 4.3. Figure 4.5d shows the shear force as a function of the mid-span deflection for the three tests.

The front face of the specimen was tracked with DIC. In each beam, the longitudinal $\varnothing 22$ bar closest to the front face was instrumented with a single optical fibre installed in a 2 mm deep groove running along two opposite sides of the bar, as shown in Figure 4.5c. For additional details, see Cantone et al. [Can20]).

Table 4.3: Cyclic test series SC70 main parameters (see Notation for the definition of the parameters)

Specimen	b_w [mm]	h [mm]	ρ_f [%]	ρ_w [%]	f_{cm} [MPa]	f_{ym} [MPa]	Cycles	$V_{cyc,min}$ [kN]	$V_{cyc,max}$ [kN]	V_{max}^a [kN]
SC75	300	320	0.92	-	33.3	701	60	27.8	5.3	95.4
SC76	300	320	0.92	-	36.0	701	50	54.0	7.3	97.1
SC77	300	320	0.92	-	36.3	701	21	86.4	10.2	80.7

^a shear strength including self-weight

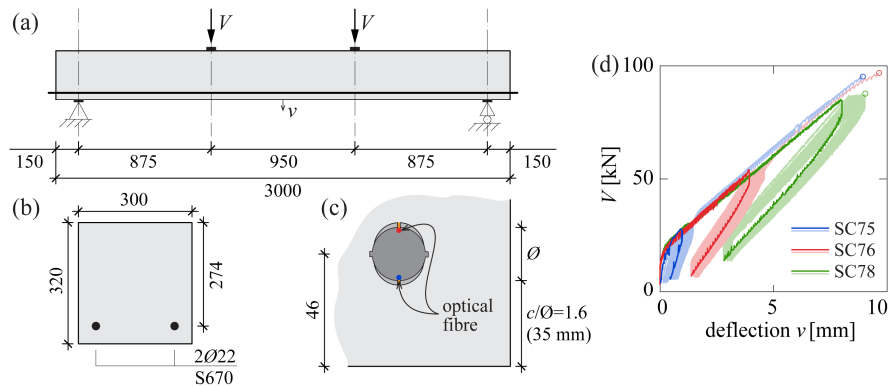


Figure 4.5: Cyclic test series SC70: (a) elevation of the test set-up; (b) cross section of the specimens; (c) fibre instrumentation within the tested region; and (d) applied shear as a function of the mid-span deflection for specimens SC75, SC76 and SC77 (for additional details, see [Can20]).

4.3.4 Measurement post-processing

The DIC results were used to detect the crack patterns and estimate crack kinematics using the Automated Crack Detection and Crack Measurement (ACDM) procedure developed by Gehri et al. [Geh22]. Therefore, the crack with measurements correspond to the value on the surface of the specimen.

The fibre strain measurements were post-processed to remove noise and the large variations due to the variable cross section and the introduction of bond stresses at the ribs [Can20, Gal21, Lem22]. For this purpose, a moving average filter over a length of two bar diameters was used. The bar strains are calculated by averaging the results from the two sides of the bar. The stresses are calculated assuming a bilinear stress-strain constitutive law assuming an elastic modulus of $E_s = 200$ GPa and a strain hardening modulus according to the respective tensile tests. Local bond stresses (τ_b) are derived from the equilibrium considerations of a finite bar element [Can20] only in the elastic range of the bar. Average bond stresses ($\tau_{b,avg}$) are computed based on the average of the local bond stresses over the relevant length. The curvature of the bar (χ_s) is calculated assuming a distance between fibres equal to the nominal bar diameter minus 4 mm, assuming that the fibre is at the bottom of the groove.

The slip considered for the estimation of the local bond-slip response is estimated from the steel strains measured with the fibres. The steel strains are integrated from the point where strains where negligible (point at approximately l_{cr} from the crack) during the crack formation phase, or from the inflection point of the strain profiles (similar to the mid-point between cracks) during the stabilized cracking stage. The cracking sequence is considered. The concrete strains are neglected.

4.4 Experimental results and discussion

4.4.1 Tensile tests

The results of the tension test series TC10 are presented in Figure 4.6. The relationship between average stress in the reinforcement (calculated as the applied force divided by the nominal steel area) and the average strain (calculated as the average of the fibre measurements divided by the tie length, namely 1250 mm) is shown in Figure 4.6a. For each specimen, the measured response (including the initial shrinkage strains) is shown with a black solid line and the bar tensile tests (grey hatch) are shown. The response after removing the initial shrinkage strains (black dashed line) is shown for visual reference. The initial shrinkage strains were around -0.14‰ and -0.25‰ for specimens TC11 and TC12, respectively. These results are in the same order of magnitude as those found in the literature [Dav17, Lem23a]. Furthermore, the difference between them is probably related to the different ratio between the element cross section and its perimeter (often referred to as notional size in standards [FIB13], 107 and 50 mm for specimens TC11 and TC12,

respectively). Elements with smaller ratios have a larger specific surface and therefore a faster drying shrinkage, in this case TC12.

Figures 4.6b and c show the crack patterns for the North and South faces of specimen TC11 at two load steps. The two faces correspond respectively to the bottom and the top faces during casting. Due to the relatively small cover, several secondary cracks originating from the conical cracks at the ribs [Got71] are visible. Some of them eventually propagated to become traversing cracks. The average crack spacings are 102 and 105 mm for the North and South faces, respectively. The corresponding value for specimen TC12 was 131 mm (similar values for both faces). The figures show the steel strain ε_s , the axial stress σ_s (calculated from the strains with the assumed stress-strain relationship) and the bond stress τ_b distributions for 6 load steps along the tie length. The strain and stress profiles show good correlation with the observed cracks. The stress distribution near the crack location and the point between cracks vary smoothly, indicating low bond stresses. This can also be observed in the bond stress distribution.

Smaller bond stresses are developed for the bar at the top of the formwork. This is a well-known effect due to the plastic settlement and bleeding voids that form under the bars [Cla49, Pér20, Moc21]. However, it is surprising to see this effect considering that the depth of the specimen TC11 is 214 mm and, consequently, both bars are in good casting conditions according to current standards [Eur04, FIB13].

The results of the DIC and fibre optical measurements allow analysing in detail each crack with a precision which was not possible with classical measurement and observation methods. Figure 4.7a shows the contribution of the secondary cracks to the crack width w for the case of crack 2 of the bottom face of specimen TC11 (TC11 North). It can be observed that the width at the initial crack (point A) does not increase after a stress of around 300 MPa. After that, a second and a third crack develop (points B and C), that concentrate additional components of the crack width. At a larger stress level, another secondary crack develops (point D) with a negligible contribution ($w \approx 0.01$ mm). The total crack width measured at the concrete surface near the bar is smaller than the corresponding width near the corners of the specimen (points E and W). This is consistent with experimental measurements that show the variation of the crack with over the concrete cover [Tam09, Bor10]. It indicates that the crack width at the bar location is likely smaller than the crack width observed on the concrete surface, particularly for large covers. For this reason, the calculated crack widths in this chapter include the neighbouring secondary cracks if present.

The bar stress (estimated from the fibre measurements) as a function of the crack width is shown in Figure 4.7b for some cracks on the bottom face of specimen TC11. Using the bond stress distributions from Figures 4.6b and c, the average bond stress at both sides of the crack (spanning between the mid-points between the studied crack and the adjacent cracks) can be calculated for each load step. Figure 4.7c shows the average bond stress as a function of the steel stress in the bar. Two cases can be observed: for crack 10 (which was a secondary crack that eventually propagated across the full section), the bond stress tends to increase with increasing steel stress and crack width; whereas in the case of cracks 2 and 6 (which developed earlier as principal cracks) the average bond stress undergoes sudden variations. These variations occur when principal or secondary cracks develop. This can be understood by looking at the bond stress diagrams in Figure 4.6b. The distribution changes significantly before and after the development

of cracks 1 and 2, which explains how the average bond on the left side of crack 3 can vary. Similar changes were observed by Cantone et al. [Can20].

Figure 4.7d shows the bar stress – crack width relationships for all the cracks on the bottom face TC11. In general, the results show rather linear trends as predicted by the stabilized crack model presented in Section 4.2.1. Some cracks show some trend variations, for example crack 6 (Figure 4.7b). This could be due to the residual tensile strength of concrete given the small crack widths or due to the fact that crack 6 did not fully propagate initially as it can be observed in Figure 4.6c. The design crack width formulations according to EC2:2004 (grey dashed line) and MC2010 (black dashed line) show that both formulations overestimate the crack width for a given stress. This can be explained by the fact that both predicted maximum crack spacings (336 and 261 mm) are larger than the experimental values.

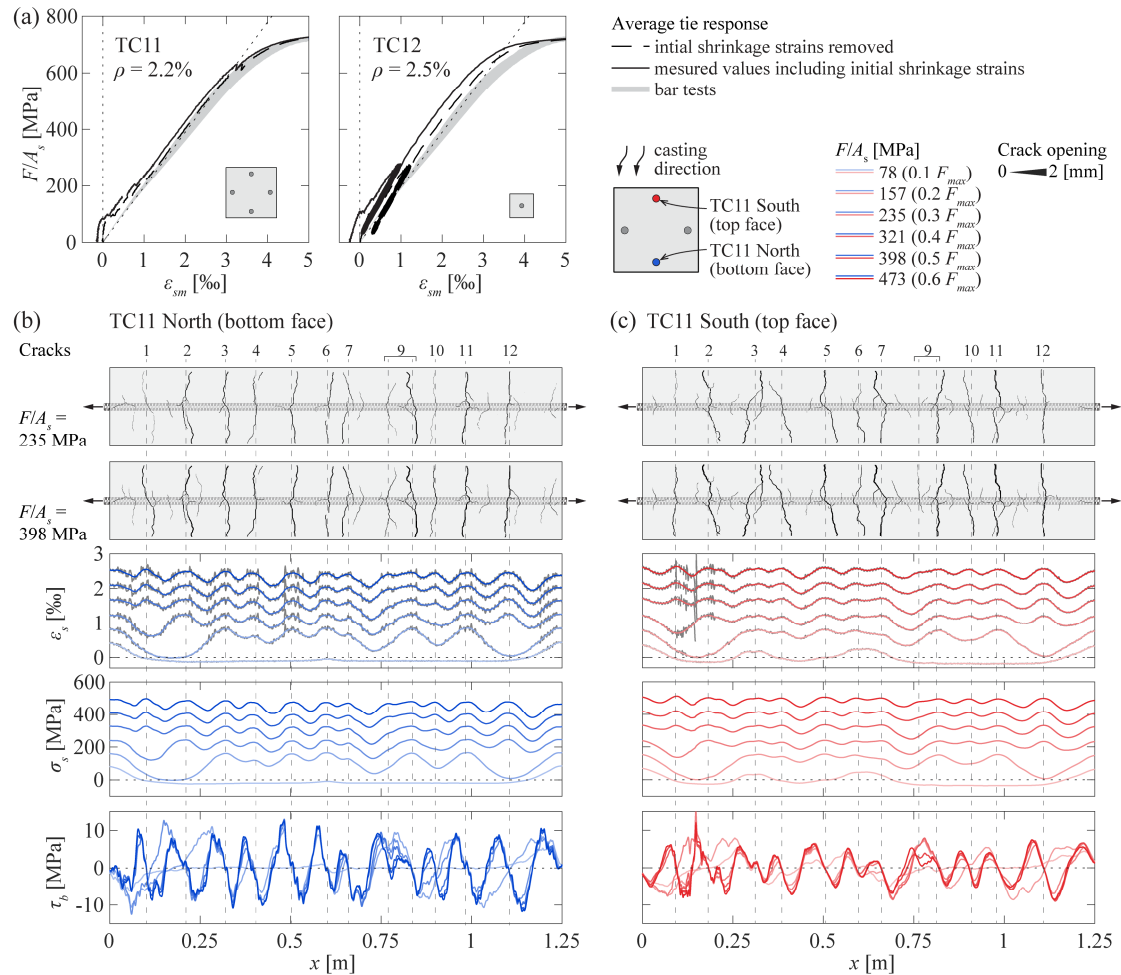


Figure 4.6: TC10 series main results: (a) steel average stress – strain diagrams for specimens TC11 and TC12; and crack patterns, steel strain, steel stress and bond stress distributions along the bonded lengths for the (b) North face and (c) South face of specimen TC11 (corresponding to the bar in the bottom and top face of the formwork respectively, see sketch in the upper right part of the figure).

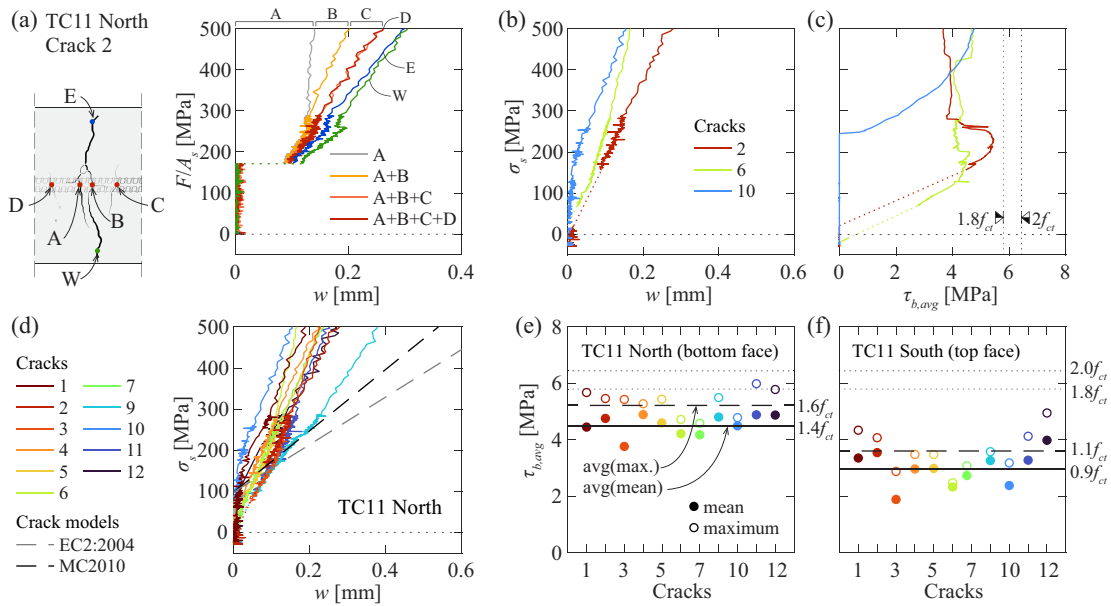


Figure 4.7: Detailed crack results from specimen TC11: (a) contributions of the secondary cracks to the crack width of crack 2 on the North face (see Figure 4.6b); (b) rebar stress – crack width and (c) rebar stress – average bond stress diagrams for selected cracks on the North face; (d) rebar stress – crack width diagrams for all cracks on the North face; and mean and maximum values of the average bond stress on both sides of the crack (in the range between $w \geq 0.1$ mm and $\sigma_s < 500$ MPa) for (e) bottom face (North), and (f) top face (South).

Figures 4.7e and f show the average bond stress in the range with $w \geq 0.1$ mm and $\sigma_s < 500$ MPa for each crack. Two values are presented: the mean value within the range (solid circular markers) and the maximum value in the range (empty circular marker). It can be observed that both values are below the values proposed by the codes. Furthermore, the values in top face (Figure 4.7f) correspond to approximately 65% of the value in the bottom face (Figure 4.7e), even though both bars are in good casting conditions [Eur04, FIB13]. This value is close to the factor typically assumed for design anchorage lengths in poor casting conditions ($\eta_2 = 0.7$) [Eur04, FIB13] and to the recently proposed factor of 0.75 for the crack width calculation [Gar22].

4.4.2 Monotonic beam tests

Figure 4.8a shows the crack pattern obtained from the DIC strain field at 90% of the maximum load for the North face of specimen SM15 (the width of the black lines is proportional to the crack width). The shear failure crack can be easily identified. It can also be observed that most of the flexural cracks occur at the location of the stirrups. In such case, the presence of transverse reinforcement does not act as confinement for the bond development between cracks.

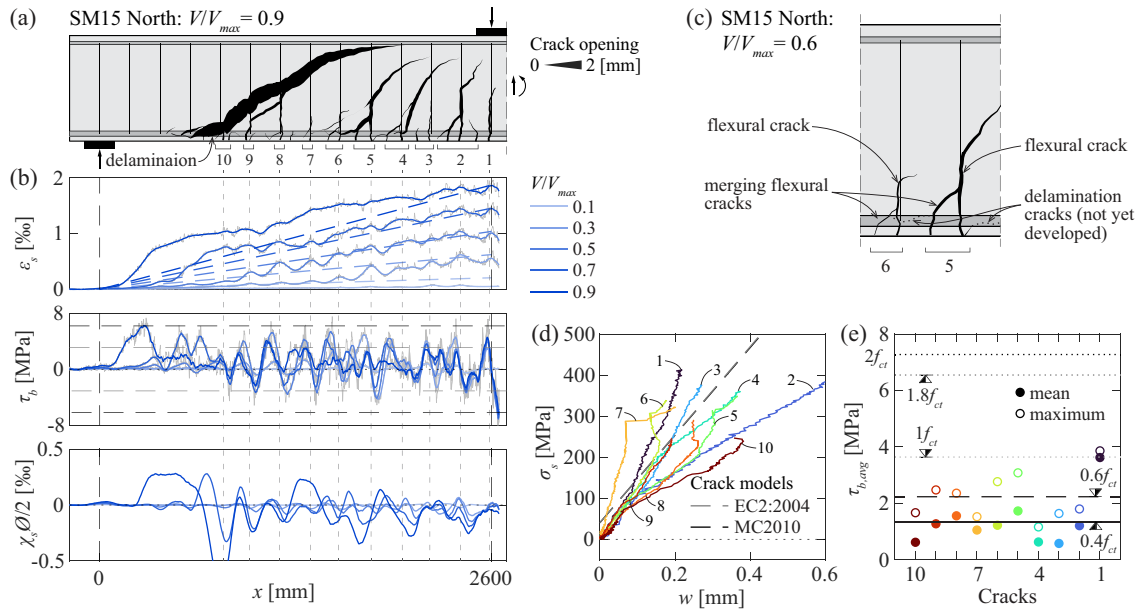


Figure 4.8: Detailed crack results of the flexural reinforcement from the North face of specimen SM15: (a) crack pattern for $V/V_{max} = 0.9$; (b) steel strain, bond stress and normalized curvature distributions for five load levels; (c) contribution of the secondary cracks to the crack width for cracks 5 and 6; (d) rebar stress – crack width diagrams for all cracks; and (e) mean and maximum values of the average bond stress at both sides of the crack (in the range between $w \geq 0.1$ mm and $\sigma_s < 500$ MPa).

Figure 4.8b shows the results of the fibre measurements including the measured steel strain, the calculated bond stress and the normalized curvature in the bar $\chi_s \cdot \varnothing/2$ (strain in bar related to local bending due to dowel action and other effects [Can20]). A good agreement between the strain peaks and the crack positions can be observed. The strains calculated assuming an elastic cracked response of the section (lever arm $z = d - h_c/3$, h_c being the depth of the compression zone assuming a linear elastic behaviour of concrete, neglecting the residual tensile strength of concrete after cracking and not considering the effect of the shear force) are indicated with a dashed line. The corresponding calculated stresses are smaller than the values derived from fibre measurements, as consistently observed in specimens subjected to shear [Cav18, Can20]. This can be explained by the inclination of the cracks (the bending moment should be calculated at the tip of the crack and accounting for the force in the stirrups) [Can20]. For shear forces closer to the shear strength, the propagation of the delamination crack due to dowel action in the flexural reinforcement [Cav15] leads to a considerable increase in the strains and stresses in the reinforcement in that region [Fer15, Can20].

The bond stress profiles in the longitudinal reinforcement presented in Figure 4.8b have the same appearance as in the ties; however, notably smaller values are observed even though the concrete strength was higher in the beam tests. The curvature profiles show that significant local bending occurs in the bars, particularly as the delamination crack develops. This bending can significantly increase the maximum stress at the surface of the bar. At the same time, stress concentrations

occur in that region due to the introduction of the bond stresses [FIB00, Can20]. This can have a negative effect on the fatigue resistance as the ribs are known to cause stress concentrations leading to the initiation of fatigue cracks [Til79, Zhe99].

Tests in reinforced concrete beams have shown that the fatigue resistance of the reinforcement bars is lower than that of bare bars [Reh69]. In regions subjected to bending, the maximum axial stress at the surface of the bar might occur at the crack location due the axial force and the local curvature of the bar. In regions subjected to bending and shear (more common in structural elements), the maximum is not necessarily at the location of the crack due to dowel action. The stress concentrations induced by the bar-to-concrete interaction will occur somewhere within the concrete between cracks as shown by the bond profiles. Further research is required to determine which of the two effects has a bigger influence on the fatigue resistance of the bar.

The bar stress as a function of the crack width is shown in Figure 4.8d. As explained in the previous section, neighbouring cracks can concentrate part of the total crack width. In most of the flexural cracks, another flexural crack developed and merged in the lower part of the beam as shown in Figure 4.8c [Cav15]. Both crack widths at the level of the reinforcement are considered. The curves also show a fairly linear response in most cases with a larger slope which is consistent with the larger crack spacings according to Section 4.2.1. In this case, the average experimental crack spacing (206 mm) is similar to the maximum crack spacing according to EC2:2004 (186 mm) and MC2010 (187 mm). Some of the experimental curves show sudden trend changes for large stresses (near the shear capacity of the specimen). This is probably related to the propagation of several small delamination and secondary cracks at the bottom of the specimen (see Figure 4.8a) that cross the other cracks, disturbing the DIC results in the points considered for the crack kinematic calculation. The average bond stress results for all the cracks presented in Figure 4.8e confirm the extremely low values of bond stresses (around $0.5f_{ct}$) compared with code formulations. Similar values were obtained for the other specimens of the series. This can be explained by the large diameter of the bars, the small cover of the longitudinal bars, the small spacing between bars and the development of splitting cracks along the bars (visible in the bottom face of the specimens). The effect of these parameters, which are not accounted for in current crack formulations, will be discussed in the following.

Figures 4.9a and b show the crack patterns and the stress profiles of the stirrups from specimens SM13 and 14. The stress profiles show the occurrence of peaks at the crack locations, leading to the yielding (red lines) in some stirrups close to the maximum load (shear strength). In most cases, the fibre measurements were lost soon after yielding (regions without measurements in the profiles).

Based on the stress distribution, the average bond stresses were calculated for crack points that were not too close to the bends of the stirrup (see Figure 4.4e) where only a single crack was traversing the stirrup. The average stress was computed for the maximum load (solid marker) or before yielding of the reinforcement (empty marker), if this was reached before the maximum load. Therefore, the average bond stresses were not calculated when the signal was lost, which was typically the case after yielding. The results presented in Figures 4.9c and d show that two cases can be distinguished: stirrups activated by an inclined crack (blue and red markers for the top and bottom parts respectively, see sketch in Figure 4.9d) and stirrups where besides the inclined crack, a flexural crack developed creating a longitudinal crack along the stirrup (green

and yellow markers for the top and bottom parts respectively). The results show that the average bond stresses are generally smaller for the stirrups that did not reach yielding. The results also indicate that the regions affected by the longitudinal cracks along the stirrups have lower average bond stresses. This can be explained on the one hand because the inclined cracks in these regions have typically smaller openings (compared with the stirrups that yielded) and because of the reduction of the contact area between the ribs and the concrete due to the crack development [Bra16, Cor23]. Similar results were found in the other specimens.

It can be observed that in most cases for the bars that reached yielding, the average bond stresses just before yielding reach values close or larger than the proposed values of current codes. The values for the bars that did not yield were lower.

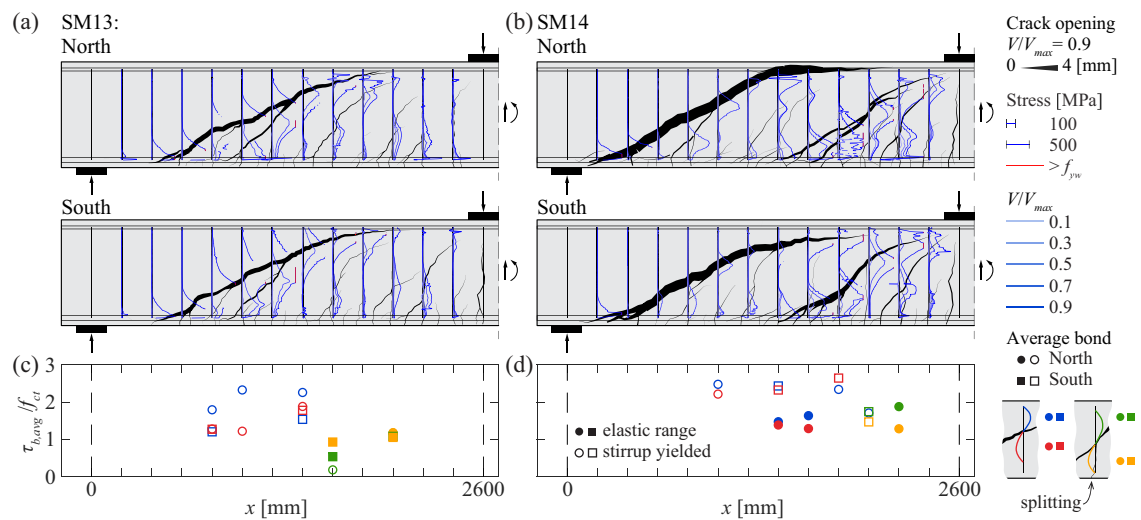


Figure 4.9: Detailed crack results of the stirrups: (a) (b) crack pattern at $V/V_{max} = 0.9$ and stirrup stress distributions for five load steps; and (c) (d) average bond stress (at V_{max} or before yielding of the stirrup) for specimens (a) (c) SM13 and (b) (d) SM14.

4.4.3 Cyclic beam tests

Figures 4.10a and b show the crack patterns and fibre measurement results for specimens SC75 (maximum load reaching the cracking load) and SC77 (maximum load reaching $0.9V_{max}$), respectively. For specimen SC75, peaks in the steel stresses in the longitudinal bars can be observed at the crack locations since the first cycle. However, not all the cracks could be detected with the DIC measurements (this is perhaps related to the fact that nonlinear concrete strains in tension can appear before reaching the tensile strength and the development of cracks [Ced81, Ced83]). In Figure 4.10a, the crack pattern for the first cycle is shown in blue (shifted to the right for clarity) and for the last cycle is shown in black. Cracks 2 and 4 did not extend beyond the reinforcement position at the 1st cycle, and cracks 3 and 5 reached only half of their final length with widths of around 0.03 mm. For specimen SC77, all the cracks were present since the first cycle and only a slight increase in the width and small propagations of some secondary cracks were observed. The bond stress distributions at $V_{max,cyc}$ indicate that bond stresses increase with the cycles in specimen SC75 and decrease for SC77.

This is more evident in the results presented in Figure 4.10c, that show the evolution of the average bond stress over the cycles. The difference can be explained by the fact that in SC75, the increase of crack width is mostly related to a propagation of the crack in the zone with residual tensile strength under the neutral axis and a reduction of the uncracked zone which leads to an increase of the tensile stress in the reinforcement and an increase of the bond stresses. For specimen SC77, the crack development is very small and the decrease of the bond is due to the load cycles that deteriorate the interface as observed by other researchers [Can20, Lem23a].

As shown in Figure 4.10c, the steepest variations occur in the first 10 to 15 cycles. At the end of the cyclic loading, the bond stresses remain fairly stable for SC75. For SC76 and SC77 a slight decreasing trend remains after the applied cycles, particularly in SC77. Bond stresses increase with the cycles in crack 5 of SC76, this is because the crack propagated from a secondary crack in the first cycles. No clear trend regarding the average bond stress and the presence or absence of splitting and secondary cracks can be observed. It must be noted that the bond stresses are in all cases lower than the values proposed by the codes. At $V_{min,cyc}$, the variations are considerably smaller.

Figure 4.10d shows the relative reduction of average bond stresses at $V_{max,cyc}$ compared with the value correspondent to the first cycle ($\tau_{b,avg0}$), in agreement with previous research [CEB79, Bal91, Can20, Lem23a]. The general trend is well captured by the reduction factor proposed by Lemcherreq et al. [Lem23a] defined by Equation 4.5.

$$k_{cyc} = 1 - 0.08 \log N \quad (4.5)$$

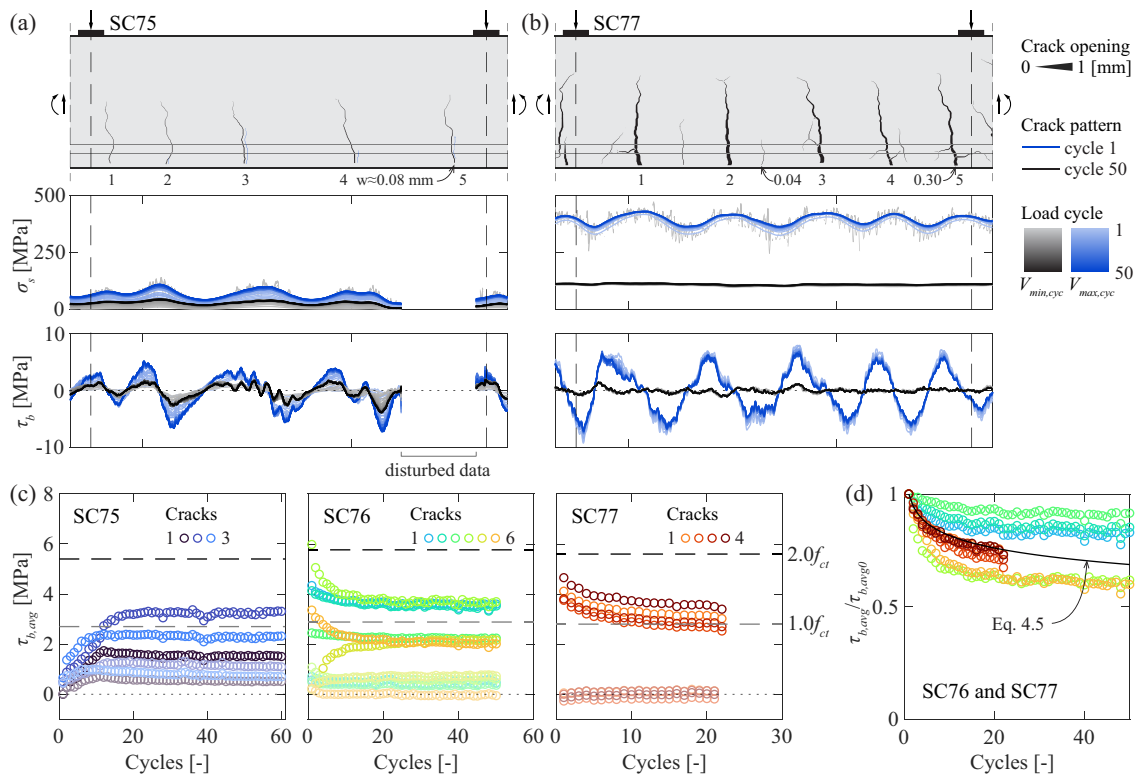


Figure 4.10: Detailed crack results of the flexural reinforcement from series SC70: crack pattern at maximum load, steel strain and bond stress distributions for all cycles for specimens (a) SC75 and (b) 77; (c) average bond stress as a function of the number of cycles for specimens SC75, 76 and 77; and (d) relative reduction of the average bond stresses with the number of cycles.

4.5 Improvement of the bond-slip relationship

Based on the principle that the underlying mechanisms in the bond response in anchorages and near cracks are the same, the local bond-slip relationship can be used to determine the bond in service conditions. A clear difference between both phenomena is the range of slips. As shown in Chapter 2, for medium bonded lengths the anchorage strength is reached for a slip in the unloaded end of 1 to 2 mm. In a cracked element, due to compatibility conditions, the mid-point between cracks should have no displacement. At the same time, near the crack (if the influence of the secondary cracks is neglected), the slip should correspond to half of the crack width. This yields maximum slips in service conditions of around 0.1 to 0.3 mm.

Another significant difference, particularly for relatively small crack spacings, is that the influence of the secondary cracks and the resulting reduction of bond near the crack is not negligible. Debernardi et al. [Deb16] adapted the model proposed by Balázs [Bal93] to account for the loss of bond near the loaded area, establishing that the average bond should remain

constant. However, recent experimental results from ties and beam tests show that average bond increases with the load in monotonic tests [Gal22, Gal23a].

In Chapter 3, the author proposed a bond-slip relationship based on mechanical considerations that shows good agreement with the results of a large test database. The relationship depends on the confinement provided by the concrete cover and the transverse reinforcement. As explained in Section 4.4.2, the confinement provided by the stirrups is not considered in this case, due fact that most of the flexural cracks appeared at the stirrup locations. Figure 4.11a shows the general formulation for each segment of the curve and the resulting bond-slip law for good casting conditions and three concrete covers. The largest bond stresses are reached for well-confined conditions ($c/\varnothing \geq 5$); and lowest for unconfined conditions ($c/\varnothing \leq 1$). Intermediate cases are considered moderately-confined conditions. More details are provided in Appendix 4B.

The ascending branch is controlled by the pull-out bond stress ($\tau_{bu,po}$) and the peak bond slip ($\delta_{sc1,po}$) in well-confined conditions that depend on the concrete compressive strength, the bar diameter and the bond index, as described in Equations 4.6 and 4.7.

$$\tau_{bu,po} = 0.5 f_{cm} \left(\frac{30}{f_{cm}} \right)^{1/6} \left(\frac{20}{\varnothing} \right)^{1/8} \quad (4.6)$$

$$\delta_{sc1,po} = 1.0 \cdot \frac{\varnothing}{20} \cdot \left(\frac{30}{f_{cm}} \right)^{1/3} \left(\frac{0.08}{f_R} \right)^{1/5} \quad (4.7)$$

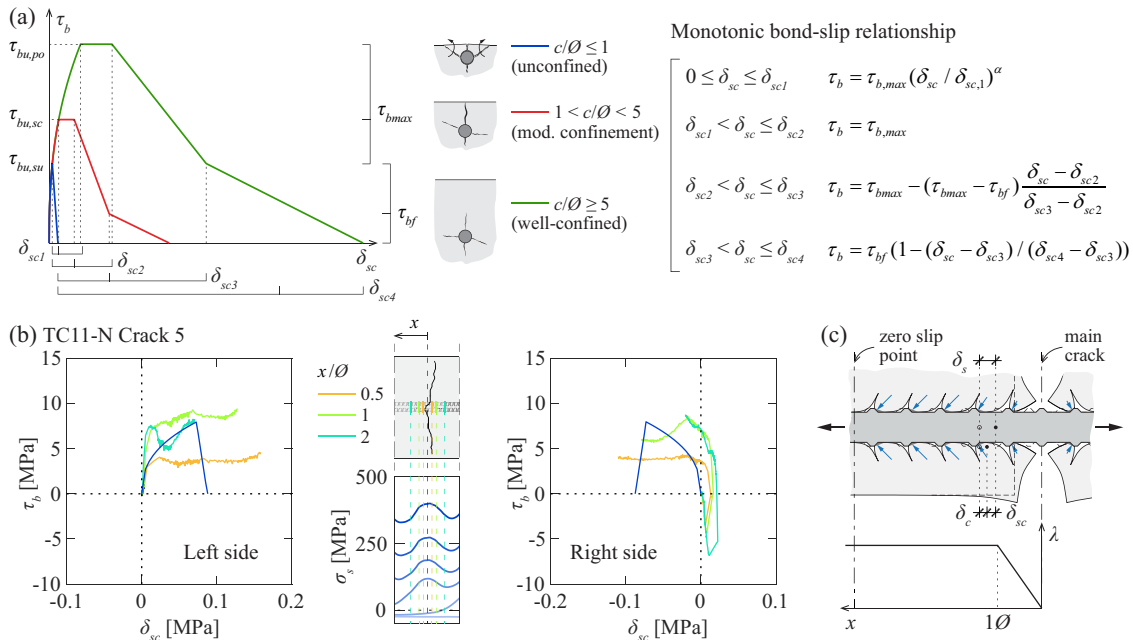


Figure 4.11: Local bond-slip response: (a) considered local bond-slip response for monotonic loading; (b) local bond-slip measurements on both sides of crack 5 of the North face of TC11; and (c) proposed reduction factor for the bond stress near the crack.

Figure 4.11b shows the local bond-slip relationship at distances of 0.5 , 1 and $2\emptyset$ from crack 5 in the North face of specimen TC11 obtained from the fibre optical measurements. In order to do so the cracking sequence was considered. This explains the results in the right side where a certain slip and bond stresses in the opposite direction are initially activated. The proposed relationship (blue curve) follows the general trend of the experimental results at 1 and $2\emptyset$ from the crack; however, the initial stiffness is slightly underestimated. The measurements show a reduction of the bond stresses at $0.5\emptyset$ from the crack. Consequently, a linear bond reduction factor (λ) acting over a distance of $1\emptyset$ from the crack is considered, as shown in Figure 4.11c.

Using the proposed bond-slip relationship (Figure 4.12a) and reduction factor to account for secondary cracks (Figure 4.11c), a numerical integration was performed as proposed by Balázs [Bal93]. The results in terms of the average bond stress as a function of the crack width are illustrated in Figures 4.12b, c and d for $\emptyset 8$, $\emptyset 18$ and $\emptyset 34$ bars. The colours correspond to different confinements. For each crack spacing (curves with different colour shades), the average bond stress before yielding of the reinforcement is represented with a solid line and the yielding point with a circular marker. The favourable effect of the confinement and the size effect are clearly visible in Figures 4.12b, c and d.

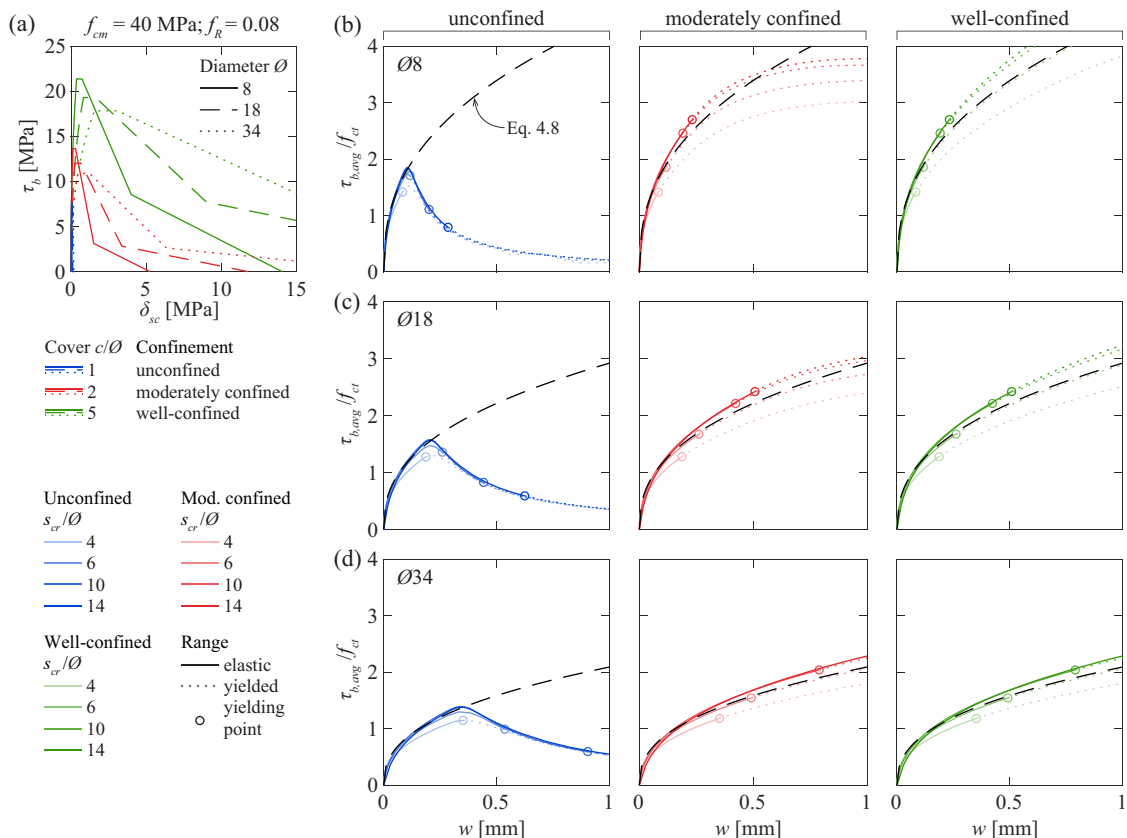


Figure 4.12: Bond in the stabilized cracking phase: (a) considered local bond-slip relationships; and average bond stress as a function of the crack width for (b) $\emptyset 8$, (c) $\emptyset 18$ and (d) $\emptyset 34$ bars.

The response in well-confined conditions (sufficient cover) is governed mostly by the ascending branch. In these conditions, the average bond stress can be estimated using Equation 4.8 (dashed curve in Figures 4.12b, c and d). This expression is derived using the analytical solution for the average bond stress as a function of the crack width in homogeneous conditions, multiplied by an adjustment factor k_{sr} depending on the crack spacing (a constant value of 1.3 is proposed):

$$\tau_{b,avg} = k_{sr} \cdot \tau_{b,max} \frac{1-\alpha}{1+\alpha} \left(\frac{w}{2 \cdot \delta_{sc1}} \right)^\alpha \quad (4.8)$$

where α is the exponent of the ascending branch of the local bond-slip relationship (a value of 0.4 as proposed in MC2010 is considered). Equation 4.8 refers to the case with good bond conditions and without the development of splitting/spalling cracks along the reinforcement bar [Cor23]. The improvements of Equation 4.8 to account for other effects are described in the following paragraphs.

As observed by Moccia et al. [Moc21], the bond performance of bars is influenced by the plastic settlement voids and cracks. The effect is directly related to the height of the bar above the bottom of the formwork. In this chapter, only results from one relatively shallow specimen are available. Based on these results, the factor of $\eta_2 = 0.7$, typically considered for short anchorages, seems to give a good estimation of the bond stress reduction. Further, research is needed to confirm these results.

Based on the work of Brantschen et al. [Bra16], the authors recently showed that the development of local bond stresses along the anchorage length is affected by the development of splitting and spalling cracks along the bar due to the reduction of contact surface between the ribs and the concrete [Cor23]. Using as reference the bond-slip relationship for well-confined conditions, the local bond stresses can be determined using a reduction factor based on the splitting and spalling crack widths. Consequently, the integration of the different local bond-slip relationships (shown in Figures 4.12b, c and d) inherently accounts for the splitting and spalling crack development. However, as Equation 4.8 accounts mostly for the ascending branch and the secondary cracks, the effects of splitting are not considered. In most cases, in existing structures, the splitting cracks can be measured. Furthermore, longitudinal cracks along the reinforcement can appear for other reasons (such as the flexural cracks along the stirrups shown in Figures 4.9a and b). Consequently, the factor proposed by Brantschen et al. [Bra16] defined by Equation 4.9 can be adopted as a reduction factor for cases where cracks along the reinforcement bar are observed on the concrete surface.

$$k_{lc} = \frac{\tau_b}{\tau_{b0}} = \frac{1}{1 + \frac{\kappa_f w_{lc}}{f_R \emptyset}} \quad (4.9)$$

where κ_f is a factor proportional to the number of lugs composing the ribs ($\kappa_f = 0.75n_l$) and w_{lc} is the crack width of the longitudinal cracks along the reinforcement. If this information is not available, the value corresponding to two rib lugs ($\kappa_f = 1.5$) and a bond index of 0.08 (average value from the database presented in Chapter 3) are recommended. Considering these two factors and the cyclic reduction factor of Equation 4.5, the expression to estimate the bond stresses is defined by Equation 4.10:

$$\tau_{b,avg} = \eta_2 \cdot k_{sr} \cdot k_{lc} \cdot k_{cyc} \cdot \tau_{b,max} \frac{1-\alpha}{1+\alpha} \left(\frac{w}{2 \cdot \delta_{sc1}} \right)^\alpha \quad (4.10)$$

After yielding, the bond stresses reduce significantly [Shi87, Fer07]. This is addressed in some models by assuming a reduction of the average bond stresses. This is the case in the TCM that proposes a reduction of the bond stress from $2f_{ctm}$ to $1f_{ctm}$ after yielding [Mar98]. Recently, Lemcherreq et al. [Lem23b] performed refined measurements using fibre optical measurements providing new insights on the subject. This topic is out of the scope of this chapter, especially as in such case, the stress in the bar is less uncertain.

4.6 Comparison of the proposed model with the experimental results

4.6.1 Average bond stresses

Figure 4.13a shows the experimental results (coloured lines) and the proposed analytical expression (black dashed line) in terms of the average bond stress as a function of the crack width. Additionally, the results of the numerical integration of the local bond-slip relationships are shown with a grey hatch. The increase in the bond stresses with the crack width is well captured. However, stresses are slightly underestimated.

Figure 4.13b shows the mean (filled marker) and maximum values (empty marker) of the average bond stresses for the flexural reinforcement of all specimens of series SM10. The corresponding predicted values are shown with black markers. The size effect and the influence of the longitudinal cracks along the bars reduce considerably the bond stresses. Nevertheless, the proposed values overestimate the experimental ones by a factor close to 2. This overestimation is likely due to the fact that the width of the delamination cracks in the lateral faces of the specimen are smaller than in the middle of the specimen due to the presence of the stirrups. The values proposed by the codes (1.8 to $2f_{ct}$) overestimate experimental results by a factor of 3 to 4.

Figure 4.13c shows the results from the stirrups not affected by the presence of cracks along the bars (flexural cracks), as explained in the previous section (see Figure 4.13e). The average bond stresses are slightly overestimated, particularly for the B500A stirrups (Figure 4.13c). This can be explained by the lower bond index of the bars and could indicate that the influence of this parameter in the proposed bond-slip relationship is underestimated. These results are coherent with the smaller crack spacings for larger bond indices observed by Galkovski et al. [Gal23a]. Figure 4.13d shows the results from the stirrups affected by the flexural cracks. In general terms, the influence of splitting is satisfactorily considered by the splitting factor (black triangular results). However, a certain tendency to overestimate the reduction can be observed. Additional experimental data is required to improve the estimation of this effect, particularly for small diameters.

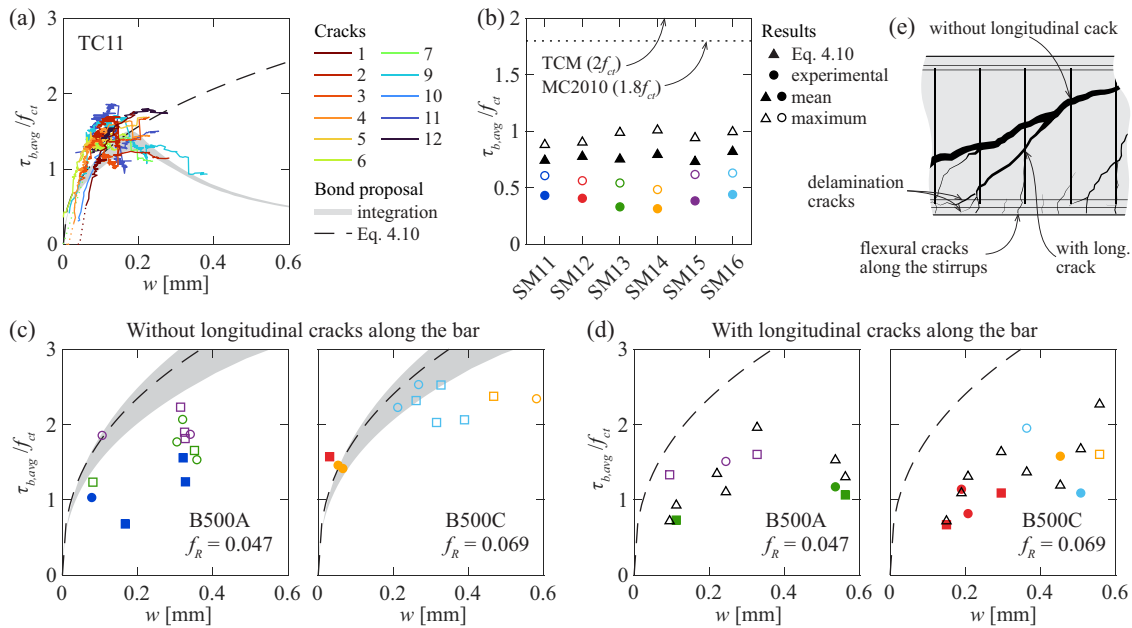


Figure 4.13: Comparison of the proposed average bond stresses and the experimental values: (a) specimen TC11; (b) flexural reinforcement of series SM10; (c) shear reinforcement without and (d) with cracks along the bar; and (e) schematic representation of stirrups with and without cracks along the bars.

4.6.2 Steel stress estimation based on the crack width

The crack width measurements obtained with DIC are used to estimate the stress in the bars. As already mentioned, the crack width was measured on the surface of the concrete. It must be noted that the clear covers in the considered tests are relatively low, therefore small differences are expected with respect to the crack width at the level of the reinforcement. Three estimations are compared with the experimental values and, in all three cases, the measured shrinkage strains are included in the relative mean strain calculation:

- Using the proposed model (Equations 4.4 and 4.10) and the measured crack spacing (distance between mid-points of consecutive cracks measured from the DIC).
- Using the relative mean strain according to EC2:2004 and the measured crack spacing.
- Using the relative mean strain and the calculated crack spacing according to EC2:2004.

Figure 4.14a shows the ratio of experimental over calculated stresses for tie TC11. The results indicate that the proposed model slightly underestimates the stress in the bar. This can be explained by the underestimation of the bond stresses (see Figure 4.13a). As explained in Section 4.2.1, for a given crack spacing and width, the code estimation yields larger bar stresses (see Figure 4.2a). Consequently, the code formulation tends to overestimate the stresses. Figure 4.14b shows the results for the flexural reinforcement of beams of series SM10. The proposed model

performs better than the code formulation for small crack widths. This is due to the bond activation expression, that gives a good estimation of the average bond stresses for smaller crack widths. For larger crack widths, both models underestimate the steel strain reduction which leads to the overestimation of the stress. The reduction of the dispersion for larger crack widths can be explained by the fact that the bond stress has a constant influence on the crack width in terms of absolute values (see Figure 4.2b) and has thus a smaller relative impact for large crack widths. As a consequence, the relative error is lower for larger stresses. The importance of an accurate estimation of the crack spacing is reflected in the poor performance of the estimations using the calculated crack spacing.

Figure 4.14c shows the results for the cyclic tests at the maximum force of each cycle. The proposed bond values lead to a certain improvement in the estimation. It must be noted that during the unloading phase bond stresses decrease and can reach negative values [Giu81, Can20, Lem23a]. Negative tension stiffening and the imperfect closure of cracks lead to stresses in the reinforcement that can be larger than the prediction according to simplified cross section analysis [Mut07, Zan10, Can20 Lem23a]. This part of the response is out of the scope of this chapter. Nevertheless, this plays a significant role in the stress variation in the reinforcement and must be considered for the fatigue assessment.

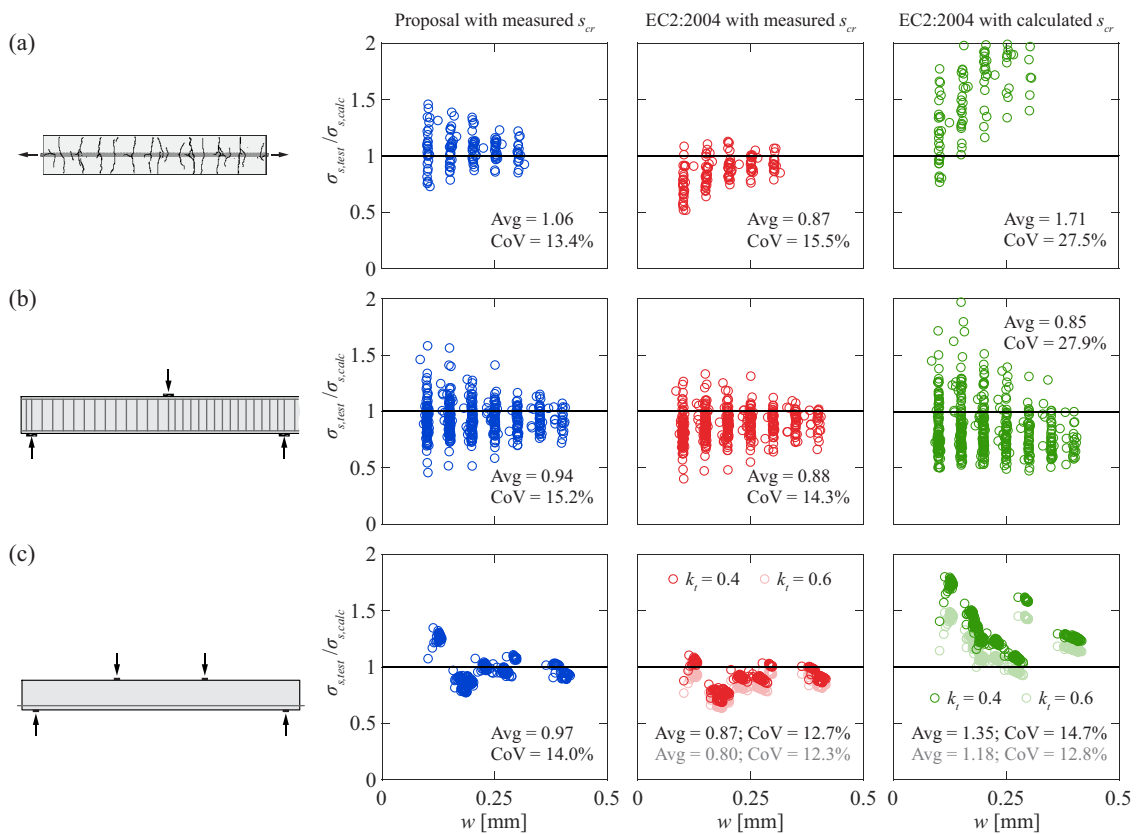


Figure 4.14: Ratio of experimental over calculated steel stress as a function of the crack width: (a) tension specimen TC11; (b) all beam specimens of series SM10; and (c) for the maximum cyclic force for specimens SC76 and SC77.

The assumption of a constant bond stress used in current code formulations is reasonable and practical given the inherent uncertainty and variability of the cracking phenomenon. However, the lower experimental bond stresses could have an influence in the crack spacing estimation. This is visible in the results from series SM10 where the calculated maximum crack spacing is actually close to the average of the experimental results (see Figure 4.8d). This explains the average results for series SM10 which is around 0.85. Further research is required to confirm this potential effect.

4.7 Conclusions

This chapter presents the results of an experimental programme and an analytical investigation to improve the current understanding of cracking in structural elements, with the aim of estimating the stress in the reinforcement based on crack width measurements. The main findings of this research are:

1. The measured average bond stresses are in most cases lower than the values proposed by current standards, with the exception of the stirrups in the beam tests that showed in some cases larger values. This could have a relevant influence in the estimation of the crack spacing.
2. The decrease of bond stresses for cyclic loading concentrates in the first 10 to 15 cycles. After that, the decrease progresses at a slower pace. This seems to depend on the stress variation range. Further research is required to confirm these findings.
3. In cases where the flexural cracks develop at the transverse reinforcement location, the presence of transverse reinforcement does not guarantee its activation as confinement for bond stress development between cracks along the longitudinal reinforcement.
4. An expression to estimate the average bond stresses considering the crack width, the casting conditions, the type of loading (monotonic or cyclic) and the presence of splitting cracks is proposed. The expression is derived from the integration of the local bond-slip relationship, accounting for the presence of secondary cracks. The estimated values show good agreement with the experimental values for short-term monotonic loading.
5. The slip-based model gives good results for the bar stress-crack width response, provided that the average bond stresses are adjusted. Using this model, a reasonable estimation of the bar stress as a function of the measured crack width can be obtained.
6. Shrinkage induced strains have a significant influence on cracking and the estimated bar stresses. However, neglecting its influence leads to an overestimation of the bar stress.
7. The estimated bar stresses using the slip-based model and the proposed expression for the average bond stresses perform better than current code formulations. The code formulations tend to overestimate the bar stress due to the inherent assumptions for the calculation of the relative mean strain.

Appendix 4A: Analytical expression development

Based on the equilibrium and compatibility conditions of the differential element shown in Figure 4.1b and assuming a linear elastic behaviour of both steel and concrete and no external forces acting on the element, the differential equation governing the tie segment response is given by Equation 4.11.

$$\frac{d^2\delta_{sc}}{dx^2} = \frac{4\tau_b(x)}{\emptyset E_s} + \frac{\pi\emptyset\tau_b(x)}{A_c E_c} \quad (4.11)$$

Assuming that the first crack appears when the concrete stress reaches f_{ct} , due to compatibility of deformations the cracking axial force is determined by Equation 4.12. The stress in the reinforcement before and after cracking can be calculated using Equation 4.13 and 4.14 at the cracked section:

$$N_{cr} = \frac{f_{ct}}{E_c} (A_c E_c + A_s E_s) \quad (4.12)$$

$$\sigma_{sB} = \frac{f_{ct}}{E_c} E_s = \varepsilon_{cr} E_s \quad (4.13)$$

$$\sigma_{sC} = \frac{f_{ct}}{\rho} [1 + (n-1)\rho] \quad (4.14)$$

Given the stress variation, the required transfer length l_{cr} as a function of the average bond stress $\tau_{b,avg}$ can be determined using Equation 4.15:

$$l_{cr} = \frac{\emptyset}{4\tau_{b,avg}} \Delta\sigma_s = \frac{\emptyset f_{ct}}{4\tau_{b,avg}} \frac{1-\rho}{\rho} \quad (4.15)$$

The crack width in the crack formation stage is therefore:

$$w = \frac{l_{cr}\sigma_{sC}}{E_s} = \frac{\emptyset f_{ct}^2}{4\tau_b E_s} \frac{(1-\rho)(1+(n-1)\rho)}{\rho^2} \quad (4.16)$$

This expression can be generalized for any stress σ_{sC} , as shown in Equation 4.17:

$$w = \frac{\emptyset\sigma_{sC}^2}{4\tau_b E_s} \frac{1-\rho}{1+(n-1)\rho} \quad (4.17)$$

In the stabilized cracking stage, the distance between cracks is smaller than the transfer length. Therefore, the tensile strength of the concrete cannot be reached between cracks and no further principal crack develops (secondary cracks may develop). In these conditions, the crack width for a given stress can be calculated considering that the maximum axial force that can be taken by the concrete as a function of the crack spacing and the average bond stress. The resulting equation is:

$$w = \frac{s_{cr}}{E_s} \left[\sigma_{sC} - \frac{s_{cr} \tau_{b,avg}}{\emptyset} \frac{1 + (n-1)\rho}{1 - \rho} \right] \quad (4.18)$$

Due to the reinforcement, the shrinkage strains ($\varepsilon_{cs} < 0$) are partially restrained, which causes tensile forces in the concrete and compression in the reinforcement. From compatibility and equilibrium conditions, the initial strain can be determined using Equation 4.19:

$$\varepsilon_{ci} = \varepsilon_{si} = \frac{1 - \rho}{1 + (n-1)\rho} \varepsilon_{cs} \quad (4.19)$$

As a consequence of this initial stress-state, the cracking force is reduced:

$$N_{cr,cs} = N_{cr} \left[1 + \frac{n\rho}{1 + (n-1)\rho} \frac{\varepsilon_{cs}}{f_{ct} / E_c} \right] \quad (4.20)$$

Nevertheless, both the cumulative difference of strains remains the same because both strain diagrams are shifted by the unrestrained shrinkage strain (see Figures 4.1c and d). Consequently, assuming the same bond distribution, the anchorage length and the crack width are the same for a lower stress in the reinforcement. For the stabilized cracking phase, the effect of shrinkage affects the average concrete strains as shown in Equation 4.21:

$$w = \frac{s_{cr}}{E_s} \left[\sigma_{sC} - \frac{s_{cr} \tau_{b,avg}}{\emptyset} \frac{1 + (n-1)\rho}{1 - \rho} - E_s \varepsilon_{cs} \right] \quad (4.21)$$

Appendix 4B: Local bond-slip relationships

The bond-slip relationships for monotonic loading were investigated by the authors in Chapter 3. The general expression of the segments composing the curve is defined in Equation 4.22 (see Figure 4.11a):

$$\begin{aligned}
 \tau_b &= \tau_{b,max} (\delta_{sc} / \delta_{sc1})^\alpha && \text{for } 0 \leq \delta_{sc} \leq \delta_{sc1} \\
 \tau_b &= \tau_{b,max} && \text{for } \delta_{sc1} < \delta_{sc} \leq \delta_{sc2} \\
 \tau_b &= \tau_{b,max} - (\tau_{b,max} - \tau_{bf}) (\delta_{sc} - \delta_{sc2}) / (\delta_{sc3} - \delta_{sc2}) && \text{for } \delta_{sc2} < \delta_{sc} \leq \delta_{sc3} \\
 \tau_b &= \tau_{bf} (1 - (\delta_{sc} - \delta_{sc3}) / (\delta_{sc4} - \delta_{sc3})) && \text{for } \delta_{sc3} < \delta_{sc} \leq \delta_{sc4}
 \end{aligned} \tag{4.22}$$

The factor to account for the cover and transverse reinforcement proposed in MC2010 is used for the definition of the confinement conditions [FIB13]. This factor is limited to a value of 1.7 [FIB14], that corresponds to the confinement when $c = 5\emptyset$. A minimum value of 1 is set, that corresponds to the confinement when $c = 1\emptyset$. The normalized factor can be determined using Equation 4.23:

$$\begin{aligned}
 k_{conf} &= \frac{1}{0.5} \left[\left(\frac{c_{min}}{\emptyset} \right)^{0.25} \left(\frac{c_{max}}{c_{min}} \right)^{0.1} - 1 \right] \quad k_{conf} \in [0,1] \\
 c_{min} &= \min(c_s / 2, c_x, c_y) \\
 c_{max} &= \max(c_s / 2, c_x, c_y)
 \end{aligned} \tag{4.23}$$

where, c_{min} and c_{max} are minimum and maximum clear covers (or half bar spacing c_s) [FIB13]. The stirrup contribution is not considered as discussed in Sections 4.4.2 and 4.5.

Three confinement conditions are defined accordingly:

- Well-confined: $k_{conf} = 1$, corresponding to covers $\geq 5\emptyset$.
- Unconfined: $k_{conf} = 0$, corresponding to cover = $1\emptyset$.
- Moderate confinement: $0 < k_{conf} < 1$, intermediate situations.

The main parameters of the proposed bond-slip relationship for the three types of confinement are summarized in Table 4.4.

Table 4.4: Bond-slip relationship parameter definition

Parameter	Well-confined	Moderate confinement	Unconfined
τ_{bu}	$\tau_{bu,po} = 0.5 f_{cm} \left(\frac{30}{f_{cm}} \right)^{1/6} \left(\frac{20}{\emptyset} \right)^{1/8}$	$\tau_{bu,sc} = \tau_{bu,su} + (\tau_{bu,po} - \tau_{bu,su}) k_{conf}$	$\tau_{bu,su} = 7.1 \left(\frac{f_{cm}}{30} \right)^{0.25} \left(\frac{20}{\emptyset} \right)^{0.2}$
τ_{bf}	$0.4 \cdot \tau_{bu}$	$\tau_{bf,sc} = \tau_{bf,su} + (\tau_{bf,po} - \tau_{bf,su}) k_{conf}$	0
δ_{sc1}	$1.0 \cdot \frac{\emptyset}{20} \cdot \left(\frac{30}{f_{cm}} \right)^{1/3} \left(\frac{0.08}{f_R} \right)^{1/5}$	$\delta_{sc1,sp} = \delta_{sc1,po} \left(\frac{\tau_{bu,sp}}{\tau_{bu,po}} \right)^{1/\alpha}$	$\delta_{sc1,su} = \delta_{sc1,po} \left(\frac{\tau_{bu,su}}{\tau_{bu,po}} \right)^{1/\alpha}$
δ_{sc2}	$2 \cdot \delta_{sc1}$	$\delta_{sc2,sc} = \delta_{sc2,su} + (\delta_{sc2,po} - \delta_{sc2,su}) k_{conf}$	δ_{sc1}
δ_{sc3}	$S_{R,clear}$	$\delta_{sc3,sc} = \delta_{sc3,su} + (\delta_{sc3,po} - \delta_{sc3,su}) k_{conf}$	$1.2 \cdot \delta_{sc1}$
δ_{sc4}	$3 \cdot S_R$	$\delta_{sc4,sc} = \delta_{sc4,su} + (\delta_{sc4,po} - \delta_{sc4,su}) k_{conf}$	$1.2 \cdot \delta_{sc1}$
α	0.4	0.4	0.4

Notation

Lower case Latin

b_R	rib width
b_w	beam width
c	clear concrete cover
d	beam effective depth
f_c	concrete compressive strength
f_{cm}	mean concrete cylinder compressive strength
f_{ct}	concrete tensile strength
f_{ctm}	mean concrete tensile strength
f_R	bond index of the reinforcement
f_{ym}	mean yield strength of the longitudinal reinforcement
f_{ywm}	mean yield strength of the shear reinforcement
h	beam height
h_c	depth of the compression zone in a section subjected to bending
k_{cyc}	average bond stress reduction factor due to cyclic loading
k_{lc}	average bond stress reduction factor due to longitudinal cracks along the bar
k_{sr}	average bond stress adjustment factor
l_{cr}	transfer length
n	ratio of the steel elastic modulus divided by the concrete elastic modulus
s	stirrup spacing
s_{cr}	crack spacing
$s_{R,clear}$	clear rib spacing at the top of the lugs
v	beam test mid-span deflection
w	crack width component in the direction of the reinforcement
w_{lc}	crack width of the longitudinal crack along the reinforcements
x	coordinate along x axis

Upper case Latin

A	transverse cross section
A_c	concrete area in the transverse cross section
E_c	elastic modulus of the concrete
E_s	elastic modulus of the reinforcement
F	tensile force applied to the concrete ties
N	number of cycles
V	shear force
$V_{cyc,max}$	maximum shear force during cyclic loading
$V_{cyc,min}$	minimum shear force during cyclic loading
V_{max}	maximum measured shear force

Lower case Greek

δ_{sc}	relative slip between the bar and the concrete
ε_c	concrete strain
ε_{cs}	unrestrained shrinkage strain
ε_s	steel strain
η_2	factor for to account for casting position
λ	bond reduction factor near the crack
ρ_f	flexural reinforcement ratio $a_s/(d \cdot b_w)$
ρ_t	tensile reinforcement ratio a_s/a
ρ_w	shear reinforcement ratio $a_{sw}/(s \cdot b_w)$
$\sigma_{cyc,max}$	maximum nominal stress in the reinforcement for the maximum force during cyclic loading
$\sigma_{cyc,min}$	minimum nominal stress in the reinforcement for the maximum force during cyclic loading
τ_b	local bond stress
$\tau_{b,avg}$	average bond stress over a certain length
$\tau_{bu,po}$	maximum bond stress for pull-out failure
$\tau_{bu,sc}$	maximum bond stress for splitting with confinement
$\tau_{bu,su}$	maximum bond stress for splitting in unconfined conditions
χ_s	reinforcement bar curvature

Other characters

\emptyset	bar nominal diameter
-------------	----------------------

5

Image-based techniques for initial and long-term characterization of crack kinematics in reinforced concrete structures

This chapter is the pre-print version of the article mentioned below, submitted for publishing to Engineering Structures:

Vincens B., Corres E., Muttoni A., *Image-based techniques for initial and long-term characterization of crack kinematics in reinforced concrete structures* [article submitted to Engineering Structures].

The work presented in this publication was performed by Baptiste Vincens and the author under the supervision of Prof. Aurelio Muttoni who provided constant and valuable feedback, proofreading and revisions of the manuscript. The work of Baptiste Vincens addresses the long-term characterization of the crack. The work of the author addresses mostly the initial crack characterization. The main contributions of the author to this article and chapter are the following:

- Comprehensive literature review on the direct detection methods for crack detection.
- Inspection of several bridges in the Lausanne region (Switzerland) to find a suitable case of study for the studied techniques.
- Execution of the laboratory tests for the validation of the technique for initial crack characterization.
- Execution of the in-situ tests to for the validation of the technique for initial crack characterization.
- Execution of the in-situ tests with DIC in collaboration with the first author.
- Redaction of the manuscript of the article, including the production of its figures and tables in collaboration with the first author.
- Conceptualization, review and edition of the manuscript.

Abstract

In the recent years, Digital Image Correlation (DIC) was applied with very promising results to monitor cracks in reinforced concrete structures. However, current DIC measurements present some limitations to characterize the existing crack (already present in the reference image) and for long-term monitoring due to the principles of the correlation algorithm. This chapter presents two techniques to complement DIC in these two cases. The first one is based on direct detection using existing algorithms. The second one is based on the detection of markers fixed around the crack. Their relative position in different images is used to compute the crack displacement that occurred between the inspections. A conventional DIC set-up can be used for this technique. Simplified and refined methods are proposed to quantify the measurement uncertainty and to determine the number and position of markers. Both techniques are validated in laboratory conditions and in-situ in an existing concrete bridge. The combination of the two presented techniques with conventional DIC is promising and could be of interest for applications with complicated crack patterns where a detailed understanding of the crack kinematics is required.

5.1 Introduction

During inspections of reinforced and prestressed concrete structures, cracks are often detected. The safety assessment of the structure based on the observed cracks is challenging since their presence does not necessarily indicate an insufficient level of safety. At the same time, small crack openings are not necessarily related to a sufficient margin of safety in cases where fragile failure modes govern [Zab19, Mon22]. Consequently, both accurate verification models and detailed measurement techniques are required to assess the condition of structures throughout their life.

Various studies have shown that the crack geometry and kinematics (crack opening and sliding, see Figure 5.1e) can be used to estimate the contribution of the different shear transfer mechanisms in reinforced concrete elements [Mih13, Cav17, Pro21, Mon22]. Furthermore, the stress-state of reinforcement bars in existing structures, which is relevant for fatigue assessment, can be estimated using the crack kinematics and the bar characteristics with appropriate mechanical models. For this reason, this chapter focuses on the measurement of crack kinematics in existing structures.

Cracks in existing structures are typically characterized by visual comparison using crack width rulers (Figure 5.1a) or microscopes (Figure 5.1b). Demountable mechanical strain gauges [Mor53] can also be used to characterize crack displacements [Cam13]. These measurement techniques can be time consuming and are susceptible to the experience of the inspector [Abd03, Oli13]. Furthermore, they cannot be used for rapid changes such as traffic loads. Gauges or extensometers (Figure 5.1c) can be used to measure the relative displacement of the crack lips when higher precision and acquisition frequencies are required. Each sensor measures the displacement in one direction at one point, therefore multiple sensors are often necessary to obtain a clear understanding of the crack kinematics.

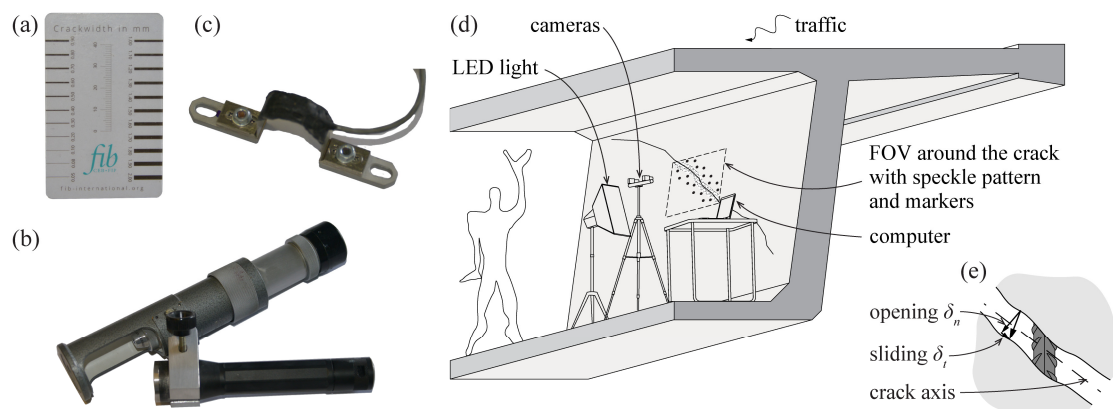


Figure 5.1: Crack width measurement tools: (a) crack width ruler; (b) crack width microscope; (c) omega gauge; (d) 3D DIC set-up; and (e) crack kinematic components.

To overcome these limitations, extensive research has focused on automated crack detection using digital images [Moh18]. Two main approaches can be distinguished: direct and indirect detection. Direct detection techniques use image processing tools to find the cracks based on the information contained in a single image. Indirect detection techniques use data obtained by comparing subsequent images to a reference image.

Direct detection algorithms typically consist of four steps: image acquisition, image pre-processing, crack detection and crack feature extraction [Wan10, Moh18]. Several image processing techniques can be used for crack detection including: thresholding or image binarization [Ito02, Fuj10, Kim17], edge-based detection (in spatial or frequency domain) [Rob63, Can86, Abd03, Jah09], morphological operations [Iye05, Jah09, Wan10, Jah12], percolation methods [Yam07] or route finder algorithms [Dar03] amongst others. Machine learning algorithms including artificial neural networks [Kas93, Mos00, Cha01] and Deep Convolutional Neural Networks (DCNN) [Dor18, Rez20, Li22] are another popular approach for direct crack detection. The need to train the neural network can be a time-consuming task; however, it provides flexibility, as the algorithms can be trained with different datasets to address specific user demands. The performance of detection algorithms is typically evaluated through pixel-wise metrics, where the detected pixels are compared with a known reference [Yam07, Dor18, Rez20, Li22]. Several comparisons can be found in the literature [Abd03, Wan10, Jah12, Li22]. Recent studies show that DCNN are amongst the most performant [Dor18].

The next step is the extraction of the relevant crack features, which requires knowing the pixel size. The pixel size can be calculated using a visual reference of known dimensions when a single camera is used. Other options are available when multiple cameras are used [Jah12, Sha15]. Several publications propose algorithms to measure crack widths in the direction perpendicular to the crack axis [Dar03, Bar09, Zhu11, Lin16, Kim17, Car21]. Detailed information about the pixel and crack sizes are not always provided, therefore the expected uncertainty or the limits of applicability of the algorithms are not always clear. Recently, Pantoja-Rosero et al. [Pan22] proposed an algorithm to calculate the crack kinematics from a binary image resulting from the segmentation of a crack image using a non-linear least squares optimization algorithm. They reported errors of less than 1 pixel (for crack widths of 6 to 20 mm) and errors of 2 to 14 pixels (for crack widths of 0.4 to 4 mm).

Digital Image Correlation (DIC) is an indirect image-based technique that is well established in several fields of research including structural engineering [Sut09, Sut17, Pan09]. The algorithm tracks groups of pixels (subsets) through a sequence of images and compares their position to the reference image. By interpolation between the centres of the subsets, continuous displacement and strain fields are obtained. A “speckle pattern” (random disposition of black dots on a white background), is typically applied to the surface to improve subset tracking [Int18, Cor20]. Using two cameras simultaneously, in-plane and out-of-plane displacements can be measured using the principle of stereovision (3D DIC, see Figure 5.1d). Typical measurement uncertainty in laboratory tests reported in the literature are around 1/30 to 1/50 pixel [Ber20, Mat20]. The displacement and strain fields obtained with DIC can be used to characterize the crack geometry and kinematics within the studied region. This can be done by manually selecting the crack and measurement points [Mon22] or automatically using the Automated Crack Detection and Crack Measurement (ACDM) procedure developed by Gehri et al. [Geh20, Geh22].

Since the early 2000s, numerous applications of DIC to monitor existing structures have been reported in the literature. Several authors used DIC to measure bridge deflections under traffic [Mur15, Zah18, Sou19, Mou21, Gar22] or displacements in other types of structures [Tun13, Bar22]. Other applications aim directly at characterizing the behaviour of a crack [Kün06, Elf12, Real18, Pop19]. Unfortunately, in most applications, the accuracy of the measurements is not mentioned. Generic values of around 1/50 pixel are occasionally provided [Kün06, Sou19].

DIC measurements present two limitations due to the fact that it relies on a comparison to a reference image. Existing crack displacements cannot be measured if they are already present in the reference image. Furthermore, its implementation for long-term monitoring is difficult as the correlation requires the sets of reference and measurement images to be captured with the same relative position of the two cameras. This relative position changes when the DIC set-up is dismantled. Consequently, long-term measurements can only be performed if the DIC system is left in place.

The detection of markers does not rely on the comparison of two images. Therefore, markers can be used to compare the position of the measurement system. Malesa et al. [Mal13] and Ruocci et al. [Ruo16] used markers around the monitored area to transform the coordinates of DIC measurements taken from different positions. However, these techniques are difficult to implement in large-scale structures and result in a significant reduction of the measurement precision. Markers can also be used to measure displacement fields if their position is compared with the reference image [Ben04, Dia11, Val13]. Other authors proposed the use of markers placed around a crack to directly measure its displacements in concrete and masonry structures [Bar09, Nis15, Ger19, Woj19, Bal21]. The crack displacement is measured by comparing the change of distance between pairs of points. In these applications, a single camera without calibration is used resulting in a measurement precision of approximately ± 1 pixel.

In order to provide a complete characterization of cracks in an existing structure using digital images, direct and indirect detection techniques need to be combined. The direct techniques can be used to characterize the initial crack. Conventional DIC provides accurate short-term measurements of the crack displacements. Marker detection looks promising to overcome the limitations of conventional DIC for long-term measurements. The literature presented in this section shows the large number of tools developed for crack detection; nevertheless, considerations on the precision of the measurements and clear limits of application are rarely provided.

In this article, two open source tools initially developed for masonry walls [Rez20, Pan22] are used for the initial crack characterization. A technique for long-term monitoring of cracks is proposed to complement short-term measurements of the crack with conventional DIC. This technique uses the conventional DIC set-up, but it relies only on tracking groups of circular markers positioned around the crack. The tools are validated for reinforced concrete structures in laboratory and in-situ conditions. Guidelines for the application of these two techniques are provided based on the limits of applicability observed in the validation tests.

5.2 Initial crack characterization

5.2.1 Objective

The technique described in this section aims to characterize the geometry and the initial crack kinematics of cracks that have been detected during inspections of existing structures. This cannot really be achieved by DIC. Traditional human inspections that are limited to measurements of the crack opening at discrete locations and can be time consuming for the characterization of the crack geometry [Abd03, Oli13].

5.2.2 Description of the technique

The first step is the crack segmentation of the cracked images to generate the corresponding binary image (pixels categorized as cracked or uncracked). For this purpose, a deep learning network implemented by Rezaie et al. [Rez20, Igl18] was used. The algorithm shows a good performance for crack segmentation of images with DIC speckles. In this chapter, crack images with and without DIC paint and speckles were analysed using the following algorithms:

- Images with DIC speckles: open-source Python code [Rez23] trained with the publicly available dataset [Rez23a].
- Images without DIC speckles: open-source Python code [Rez23b] trained with the publicly available dataset [Ozg19].

The second step is the estimation of the initial crack kinematics based on the binary images using the algorithm proposed by Pantoja-Rosero et al. [Pan22]. The open source Python code is publicly available [Pan22a]. The code performs the analysis on a 256×256 pixels window. The assumption of rigid-body displacements of both lips of the crack is valid only for small regions surrounding the crack. When the window corresponds to a surface in the specimen small enough to satisfy this assumption, the full-edge approach can be used. In this case, the full length of the crack in the window is considered. Alternatively, in cases where the window corresponds to a large specimen surface where a rigid-body crack lip displacement is unlikely to occur, the algorithm can be run by comparing partial segments of the crack.

5.2.3 Validation of the technique

A series of tests was conducted in the Structural Concrete Laboratory of the École Polytechnique Fédérale de Lausanne (Switzerland) to validate the proposed technique and to determine the accuracy under optimal conditions.

A wooden formwork panel of 27 mm was cut using a Computer Numerical Control machine MACA BC170 to simulate the presence of a crack, as shown in Figure 5.2a. The geometry of the

crack was extracted from an actual crack pattern of a concrete beam. The two panels were mounted on the fixed and moveable parts of a calibration bench (precision of $\pm 5 \mu\text{m}$). Once installed, the displacement was set to zero and two layers of white paint were applied to close the residual crack opening. The bench was progressively moved, imposing a horizontal crack opening. For each crack opening, pictures were taken from a distance ranging from 0.1 to 2.5 m using a professional digital camera and a smartphone. The camera was a Nikon D800 36.3 megapixels with an AF-S Nikkor 28-300mm f/3.5-5.6G ED VR objective [Nik23]. The smartphone was a OnePlus 6 with a Sony IMX 519 sensor and a pixel count of 16 megapixels [One23]. As shown in Figures 5.2b and c, for a given crack width (in this case 1 mm), the distance between the camera and the target determines the pixel resolution (size of the pixel in mm, mm/pixel) and the number of pixels inside the crack (25 and 2.3 for resolutions of 0.04 and 0.43 mm/pixel respectively).

Figure 5.2d shows a comparison of the measured horizontal crack openings δ_x as a function of the pixel size using each camera. The horizontal lines represent the imposed displacement whereas the points correspond to the experimental results. The colours correspond to various crack widths. Additionally, the lightly coloured hatch represents a measurement error equal to the size of one pixel. The measurements fall within the tolerance of ± 1 pixel in the left side of the graphs up to a resolution of 3 pixels per crack. This limit is represented by the dashed black line and the end of the hatch. For images where the number of pixels inside the crack is less than 3, the results show larger measurement errors. This is easy to understand looking at Figure 5.2c, having few pixels in the crack, the detection becomes more difficult due to lack of contrast. Furthermore, if the crack lips do not have sufficient features, the matching algorithm will not perform appropriately.

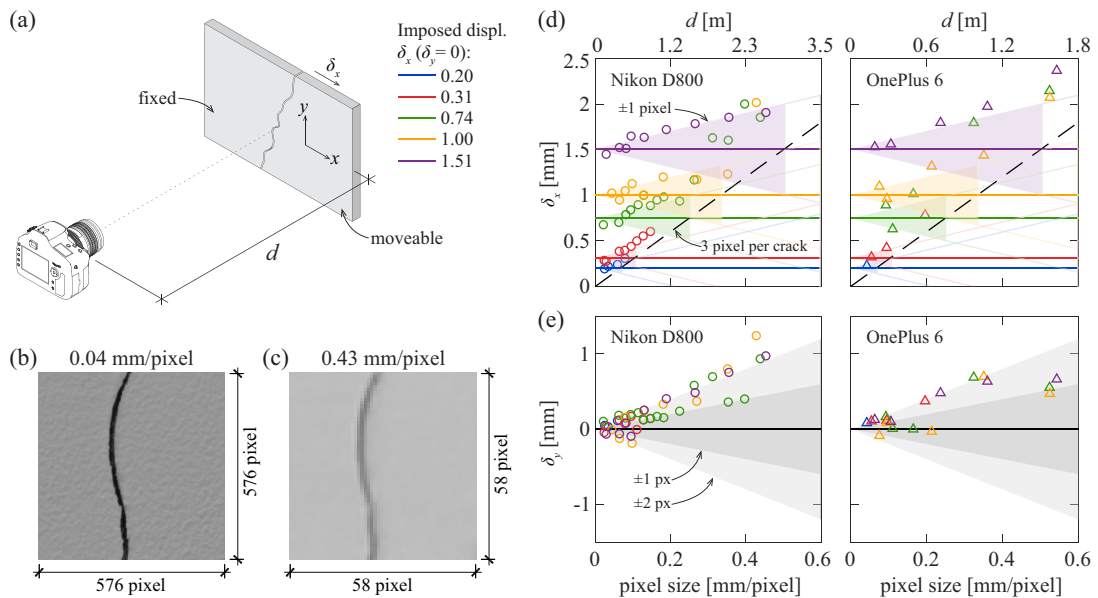


Figure 5.2: Concrete crack simulation: (a) schematic representation of the set-up; images from the studied crack with a crack width of 1 mm taken from distances of (b) 0.2 and (c) 2.5 m; (d) crack opening and (e) crack sliding as a function of the pixel size.

Figure 5.2e shows the same results for the imposed vertical crack opening δ_y , which was zero in all cases. The results show a measurement error of ± 2 pixels. The results from the two cameras are comparable for similar pixel resolutions, the only difference being the distance camera-crack needed to achieve the same pixel size.

Further validation of this approach against manual measurements and crack kinematics estimated from DIC measurements using ACDM [Geh22] can be found in work by the authors of the algorithm, see Pantoja-Rosero et al. [Pan22].

5.2.4 Recommendations and limits of applicability

The proposed technique can be used to detect cracks and estimate the crack kinematics in concrete elements with and without DIC speckles. The following recommendations are proposed to maximize the quality of the results for in-situ applications:

- The images should be taken with the camera oriented perpendicularly to the studied surface.
- For large surfaces, it is recommended to include multiple visual references for the pixel size detection as the pixel size is not uniform throughout the image.
- The resolution of the images (pixel size determined by the distance between the camera and the specimen) must be chosen to include at least 3 pixels in the crack. In such cases, the crack kinematic measurement resolution is around ± 1 pixel for the crack opening (precision of $\pm 30\%$) and ± 2 pixels for the crack sliding. However, a higher resolution of 6 to 8 pixels per crack is recommended for increased precision of around $\pm 15\%$.
- Depending on the rugosity of the surface, the use of flash or additional lighting can be beneficial. Consequently, it is recommended to acquire images with and without flash when possible as the needed time is almost the same and this could lead to better results.
- The full-edge approach should be used when the analysis window corresponds to approximately two times the maximum aggregate size. When the window size corresponds to a larger surface of the element, the finite-edge approach is recommended. A small window size can increase the measurement resolution but it requires a larger number of images and the added task of relative positioning of the different images.

5.3 Long-term crack monitoring

5.3.1 Objective

The technique described in this section aims to measure the long-term displacements of a crack by tracking and comparing the position of circular markers fixed on both sides of the crack between successive inspections. The proposed technique does not require the correlation of the speckles with the reference image of the first inspection. Therefore, the measurement system can be demounted between inspections.

5.3.2 Description of the technique

The crack geometry is defined by a sequence of l points (C_l with coordinates \underline{c}_l), as shown in Figure 5.3d. The crack defines two lips, one of which is considered fixed (used as reference between successive inspections) and the other moveable. The n markers installed on the fixed crack lip are denoted A_n with coordinates \underline{a}_n . The m markers installed on the moveable crack lip are denoted as B_m with coordinates \underline{b}_m . The centroid of a group of markers (mean of the coordinate vectors of its components) is often used in this publication. It is referred to with the same letter and a line over the top and can be calculated using Equation 5.1. For example, for the group A_n :

$$\overline{\underline{a}} = \frac{1}{n} \sum_{i=1}^n \underline{a}_i \quad (5.1)$$

The crack geometry can be obtained using the results of short-term DIC measurements of the crack or using the direct detection methods presented in the previous section. The coordinates of the centre of the markers can be obtained using any marker detection algorithm. DIC software often include marker detection algorithms. 3D coordinates of all the points are required to account for the displacements of the measurement system.

Upon the first inspection, the “reference position” of all these points is determined (the corresponding magnitudes are referred to with the subscript “ref”, light blue in Figure 5.3a). During the second inspection, the “deformed position” of the points is determined (referred to with the subscript “def”, pink in Figure 5.3b). The markers in the reference and deformed states are photographed with a different position of the camera set-up and therefore different coordinate systems. By superposing the markers on the reference side, the difference in the position of the markers in the moveable side can be used to estimate the crack displacements.

The proposed technique is based on the following assumptions:

- Crack kinematics are bidimensional. This is typically the case in reinforced concrete structures. The technique proposed in this subsection uses bidimensional coordinates assuming planar displacements of the markers. A plane fitting operation is needed to transform the 3D coordinates of the reference and deformed states into planar coordinates.

- Temperature variations result in uniform dilations of the crack lips. When the area close to the crack undergoes a difference of temperature between the two inspections, the thermal expansion of the crack lips falsely amplifies the computed crack displacements if not corrected. This effect becomes more important when the centroids of the groups of markers are far away from the crack.
- After correction of the effect of temperature, the relative positions of the markers on a given crack lip are assumed fixed between the reference and deformed states. This assumption is valid as elastic deformations of the concrete next to the crack are usually one order of magnitude smaller than the displacement of the crack [Geh20]. This means that a best-fit rigid-body displacement is a realistic simplification to characterise the required mapping operations.

Under these assumptions, the following steps are required to obtain the crack displacement $\underline{\delta}$ (considering the effect of temperature changes), that occurred at each crack point between two inspections:

1. A scaling transformation (S, \underline{t}_s) is computed according to Appendix 5A and used to scale the coordinates of the markers in the reference state to fit the markers in the deformed state. The markers with corrected coordinates $A'_{n,ref}$ and $B'_{m,ref}$ (blue in Figures 5.3a and c).
2. To realign the coordinate systems of the markers in reference and deformed state, the best-fit rigid body motion (R_0, \underline{t}_0) necessary to transform markers $A_{n,def}$ (pink in Figure 5.3b) into $A'_{n,ref}$ is computed. Detailed expressions can be found in Appendix 5B. The new coordinates of points $A'_{n,def}$ and $B'_{m,def}$ (red in Figure 5.3c) are determined by Equation 5.2:

$$\begin{aligned} \underline{a}'_{n,def} &= R_0 \cdot \underline{a}_{n,def} + \underline{t}_0 \\ \underline{b}'_{m,def} &= R_0 \cdot \underline{b}_{m,def} + \underline{t}_0 \end{aligned} \quad (5.2)$$

3. The relative displacement of the crack lips (R, \underline{t}) is computed according to Appendix 5B to transform the markers $B'_{m,ref}$ into $B'_{m,def}$ (Figure 5.3c).
4. The deformed position of the crack points is calculated with Equation 5.3 by applying the scaling transformation (S, \underline{t}_s) and the relative displacement of the crack lips (R, \underline{t}) to the coordinates of the crack points $\underline{c}_{l,ref}$:

$$\underline{c}_{l,def} = R(S\underline{c}_{l,ref} + \underline{t}_s) + \underline{t} \quad (5.3)$$

5. The translation between $\underline{c}_{l,ref}$ and the obtained coordinates $\underline{c}_{l,def}$ is the crack displacement $\underline{\delta}_l$ (Figure 3d). It can be calculated using Equation 5.4:

$$\underline{\delta}_l = \underline{c}_{l,def} - \underline{c}_{l,ref} \quad (5.4)$$

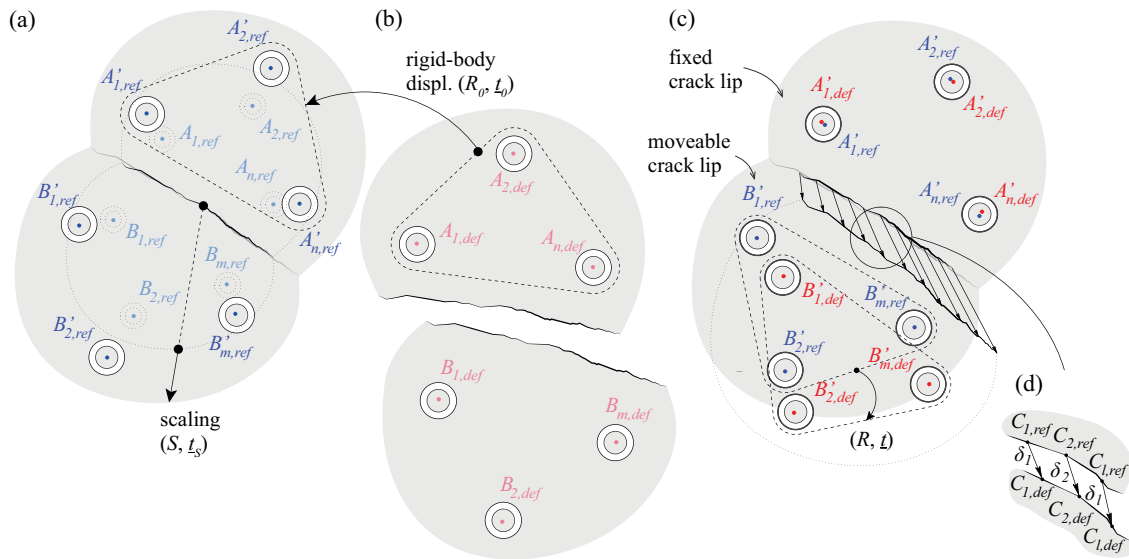


Figure 5.3: Processing of the marker coordinates: (a) markers in reference position and scaling operation; (b) markers in deformed position and re-alignment; (c) relative displacement of the crack lips; and (d) crack kinematics.

5.3.3 Measurement uncertainty

General considerations and measurement system

The measurement uncertainty in conventional DIC can be characterized by the standard deviation of the measurement errors [Int18, VDI19]. When markers are used, the measurement uncertainty resides in the detection of the coordinates of the centre of the markers which is reverberated in the crack displacement.

An experimental programme was carried out at the Structural Concrete Laboratory of the Ecole Polytechnique Fédérale de Lausanne to quantify this uncertainty. The optical set-up used comprised of two digital cameras Manta G-419 4.2 megapixels arranged with a sharp relative angle (16°). The image and pixel size were 2048×2048 pixels (620×620 mm) and 0.30 mm, respectively. Marker detection was performed using the software VIC-3D [Cor21]. A 6×6 grid of circular black markers with a diameter of 15 mm (50 pixels) printed on a sheet of paper and mounted on a rigid board was used.

The uncertainty can change for different measurement systems and types of markers. In the case of using a DIC system, the camera set-up should be ideally placed approximately parallel to the measurement surface. If the camera set-up is positioned with a sharp angle relatively to the surface, the uncertainty can significantly differ from the proposed model. This is caused by the lower out-of-plane precision.

Uncertainty of the marker coordinates

The detection of the centre of round markers is obtained by computing the centre of an ellipse fitted to the black-white transition at the edge of the marker [Ito11]. The centre of a given marker is detected in the photographs captured simultaneously by the two cameras (see Figure 5.4a) and, by triangulation, the 3D coordinates of the marker are obtained. The marker coordinate precision is influenced by a random error and a systematic error. The tests proposed in this section are adapted from their equivalent for the quantification of the uncertainty of conventional DIC measurements [VDI19].

The random error or noise is due to the internal noise of the captors [Pan09] and results in small variations in the detected coordinates of the marker, as shown in Figure 5.4b. It can be quantified with the Zero Displacement Test (ZDT). For this purpose, 10 or more images of a set of markers are captured without any applied displacement in between images. For a marker i in each picture j , the coordinates $\underline{m}_{i,j}$ are detected. The noise can be quantified by the standard deviation of the distance from each measurement to the mean position in the p images using Equation 5.5. The variations of $NV_{N,i}$ in the field of vision can generally be explained by differences in the quality of the exposure. The average value of the n markers in the field of vision NV_N calculated using Equation 5.6 is considered as the representative value.

$$NV_{N,i} = \sqrt{\frac{1}{p} \sum_{j=1}^p \|\underline{m}_i - \underline{m}_{i,j}\|^2} \tag{5.5}$$

$$NV_N = \frac{1}{n} \sum_{i=1}^n NV_{N,i} \tag{5.6}$$

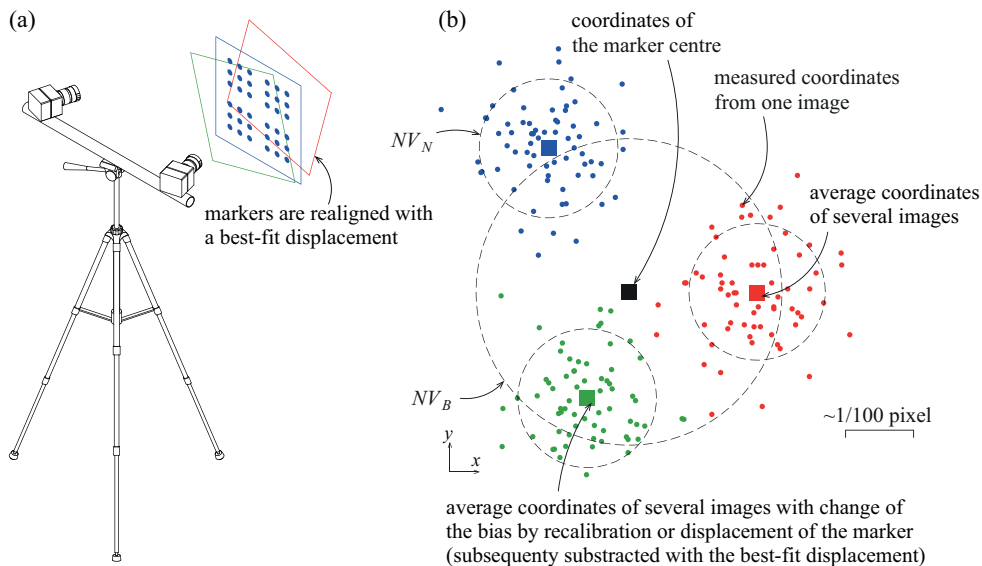


Figure 5.4: Uncertainty of the marker coordinates: (a) camera set-up and marker board used for the tests; and (b) schematic representation of the sources of error and the associated quantifications (NV).

The second type is a systematic error or bias. The consequence of this error is that the average of a large number of measurements (i.e. a measurement with little noise) does not correspond to the actual centre of the marker, as shown in Figure 5.4b. The source of this error are the imperfections of the optical model defined during the calibration [Mat20]. It can be quantified with the Zero Strain Test (ZST). In this case, rigid body translations must be applied to the markers between images, as shown in Figure 5.4a. When the rigid body displacement is removed, the measured displacements represent the systematic error. To perform the ZDT, 10 or more images must be captured with the markers in at least 10 positions. For a marker i in each position j , the coordinates in the 10 pictures can be averaged to reduce the noise resulting in the coordinates $\underline{q}_{i,j}$. The average at each position after subtracting the rigid body displacements from position 1 as described in Appendix 5B, results in coordinates $\underline{q}'_{i,j}$. Using these coordinates $NV_{B,i}$ and NV_B can be calculated using Equations 5.5 and 5.6 substituting \underline{m} by \underline{q}' .

The results from the ZDT and the ZST performed by the authors in laboratory conditions are: $NV_N = 3.3 \mu\text{m} = 1/90$ pixel and $NV_B = 8.6 \mu\text{m} = 1/35$ pixel.

Uncertainty of the crack kinematics

The measurement uncertainty of the crack kinematics is defined by the standard deviation of the crack opening and sliding. This requires separating the contribution of the uncertainty of the three components that define the relative displacement of the crack lips: the translations normal and parallel to the crack t_n and t_t , and the rotation of the crack lip θ (see Figure 5.5b).

To quantify these contributions, the experimental data gathered to estimate the uncertainty in the marker coordinates was used. Symmetrical groups of markers from the board (Figure 5.5a) were randomly chosen, and their apparent relative displacement computed. This relative displacement was used to obtain the standard deviation of the three displacement components ($\sigma(t_n)$, $\sigma(t_t)$ and $\sigma(\theta)$) assuming a fictitious vertical crack between the groups of markers, as shown in Figure 5.5b. Figure 5.5d shows that the ratio of the standard deviation of the translation normal to the crack divided by the pertinent standard deviation ($\sigma(t_n)/NV_N$ or $\sigma(t_n)/NV_B$) is strongly dependent on the number of markers n on each lip of the crack. Figures 5.5e and f show that $\sigma(\theta)$ and $\sigma(t_t)$ can be estimated from $\sigma(t_n)$ and the distances d_1 and d_2 (defined in Figures 5.5b and c).

Based on these results, a model is proposed to estimate the uncertainty of the crack kinematics for a given disposition of markers based on the following assumptions: the markers are arranged symmetrically around the crack; the axis running through the centroids of both groups of markers is approximately perpendicular to the crack; and the rotations θ are small.

Under these assumptions the following steps can be used to estimate the measurement uncertainty of the crack kinematics due to an uncertainty NV in the marker detection:

1. The uncertainty of the relative translation normal to the crack $\sigma(t_n)$ can be estimated using Equation 5.7 (see Figure 5.5d), as a function of the number of markers n :

$$\sigma(t_n) / NV = 1.35 \cdot n^{-0.5} \quad (5.7)$$

2. The uncertainty of the rotation $\sigma(\theta)$ can be estimated from $\sigma(t_n)$ and the average distance to the centre of the markers d_1 using Equation 5.8 (see Figure 5.5e):

$$\sigma(\theta) = \sigma(t_n) / d_1 \quad (5.8)$$

3. The uncertainty of the relative translation parallel to the crack $\sigma(t_i)$ can be estimated using Equation 5.9 based on $\sigma(t_n)$, $\sigma(\theta)$, d_1 , the distance between the centroid of the groups of markers d_2 and factor β . A simplified analysis with $\beta = 0.72$ is sufficient in most cases (black curve in Figure 5.5f).

$$\sigma(t_i) = \beta \left(\sigma(t_n), \sigma(\theta) \cdot \frac{d_2}{2} \right) \cdot \left(\sigma(t_n) + \sigma(\theta) \cdot \frac{d_2}{2} \right) \approx 0.72 \cdot \sigma(t_n) \cdot \left(1 + \frac{d_2}{2d_1} \right) \quad (5.9)$$

4. The uncertainty of the crack opening $\sigma(\delta_n)$ and sliding $\sigma(\delta_t)$ for a point at a distance y from the line connecting the centroids of the markers (see Figure 5.5b) can be estimated using Equations 5.10 and 5.11. For an initial estimation $\alpha = 1$ and $\beta = 0.72$ can be adopted.

$$\sigma(\delta_n) = \alpha \cdot \beta \left(\sigma(t_n), \sigma(\theta) \cdot |y| \right) \cdot \left(\sigma(t_n) + \sigma(\theta) \cdot |y| \right) \approx 0.72 \cdot \sigma(t_n) \cdot \left(1 + \frac{|y|}{d_1} \right) \quad (5.10)$$

$$\sigma(\delta_t) = \alpha \cdot \sigma(t_i) \approx \sigma(t_i) \quad (5.11)$$

5. The total uncertainty due to the noise and the bias (sub-indices “tot”, “N” and “B” respectively) for each crack opening component can be estimated using Equation 5.12. For an initial estimation $\beta = 0.72$ can be adopted.

$$\sigma(\delta)_{tot} = \beta \left(\sigma(\delta)_N, \sigma(\delta)_B \right) \cdot \left(\sigma(\delta)_N + \sigma(\delta)_B \right) \approx 0.72 \cdot \left(\sigma(\delta)_N + \sigma(\delta)_B \right) \quad (5.12)$$

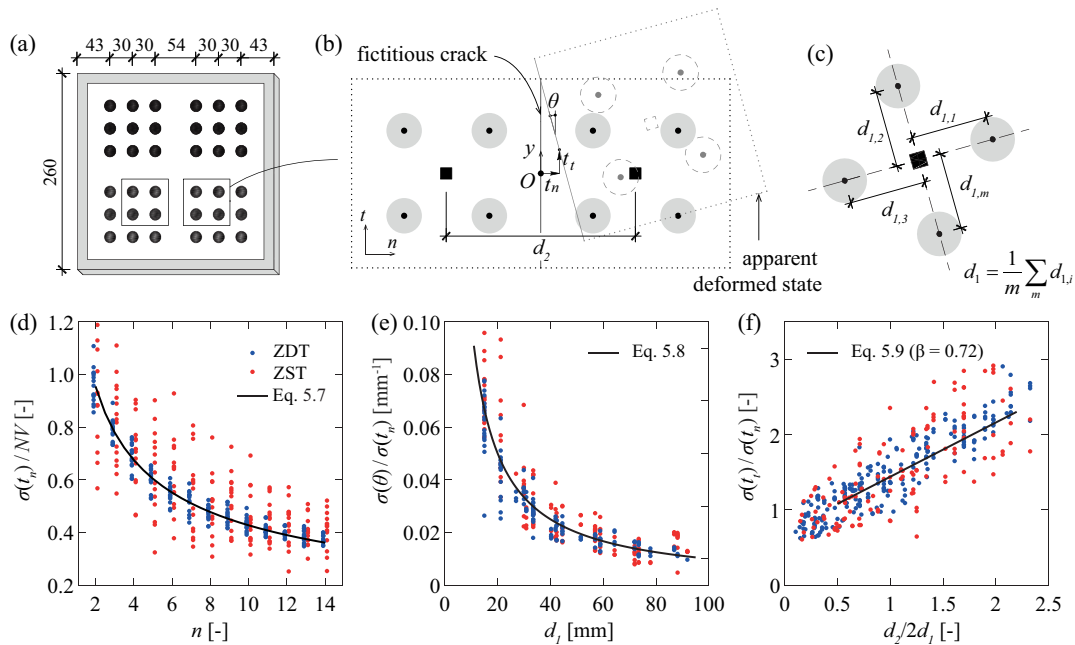


Figure 5.5: Estimation of the uncertainty of the crack kinematics: (a) board used for the tests; (b) tests principle and notation; (c) definition of distance d_i ; and results for the measurement uncertainties of (d) t_n , (e) θ and (f) t_i .

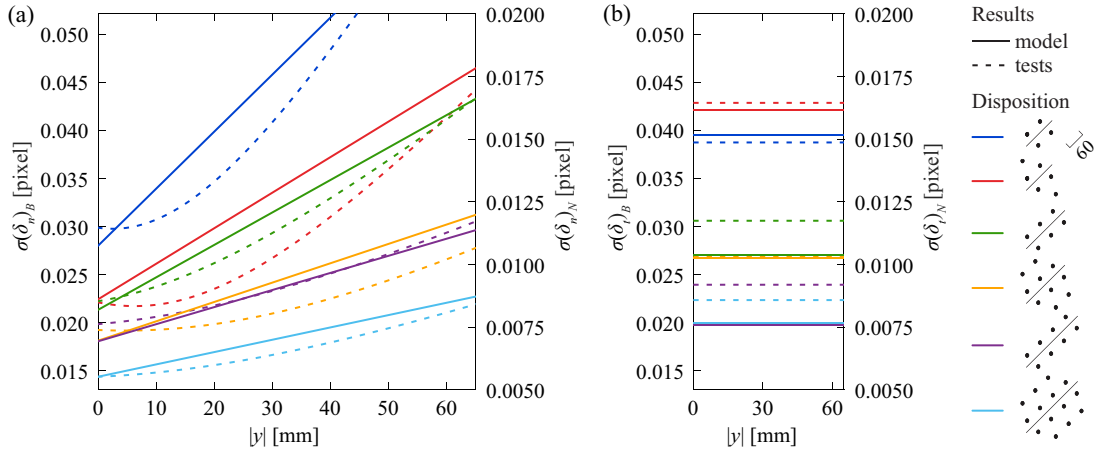


Figure 5.6: Measurement uncertainty of the crack kinematics for different marker dispositions and $\beta = 0.72$ for: (a) the crack opening; and (b) the crack sliding.

The reduction factor α is related to the effect of averaging the results of multiple images. The reduction factor β is related to the addition of two variables with different standard deviations. Refined expressions for their determination can be found in Appendix 5C.

A comparison of the uncertainty predicted with the proposed model and the experimental results is shown in Figures 5.6a and b for the crack opening and sliding, respectively. For each crack component, the standard deviations (expressed as a function of the pixel size) for different marker distributions are shown. The contributions due to the bias and the noise can be retrieved as a function of the distance y . The proposed model gives a satisfactory estimation of the uncertainty.

5.3.4 Validation of the technique

The measurement system described in Section 5.3.3 was used to monitor a four-point bending test of a rectangular reinforced concrete beam in the laboratory, see Figure 5.7a. The beam was loaded up to the end of the cracking phase and then unloaded to place two groups of 5 markers on each side of one of the cracks, see Figure 5.7b. Conventional DIC was used as a ground truth to validate the marker measurements. VIC-3D was used for the correlation and ACDM [Geh22] was used for the automatic extraction of the crack geometry and kinematics.

Reference images were acquired with the camera set-up in the three positions shown in Figure 5.7a (positions “A”, “B” and “DIC”). A displacement of the cameras was applied each time and a new calibration was performed to simulate a repositioning of the set-up for long-term measurements. In the last position (“DIC”), a reference image and regular images during loading were captured as in conventional DIC measurements. Each image of the loaded beam was used simultaneously to compute crack displacements using DIC (ground truth) and using the markers by comparing their state with the three reference states acquired before. Consequently, four sets of data were obtained at each load step: three marker measurements for the three camera positions and one measurement using DIC.

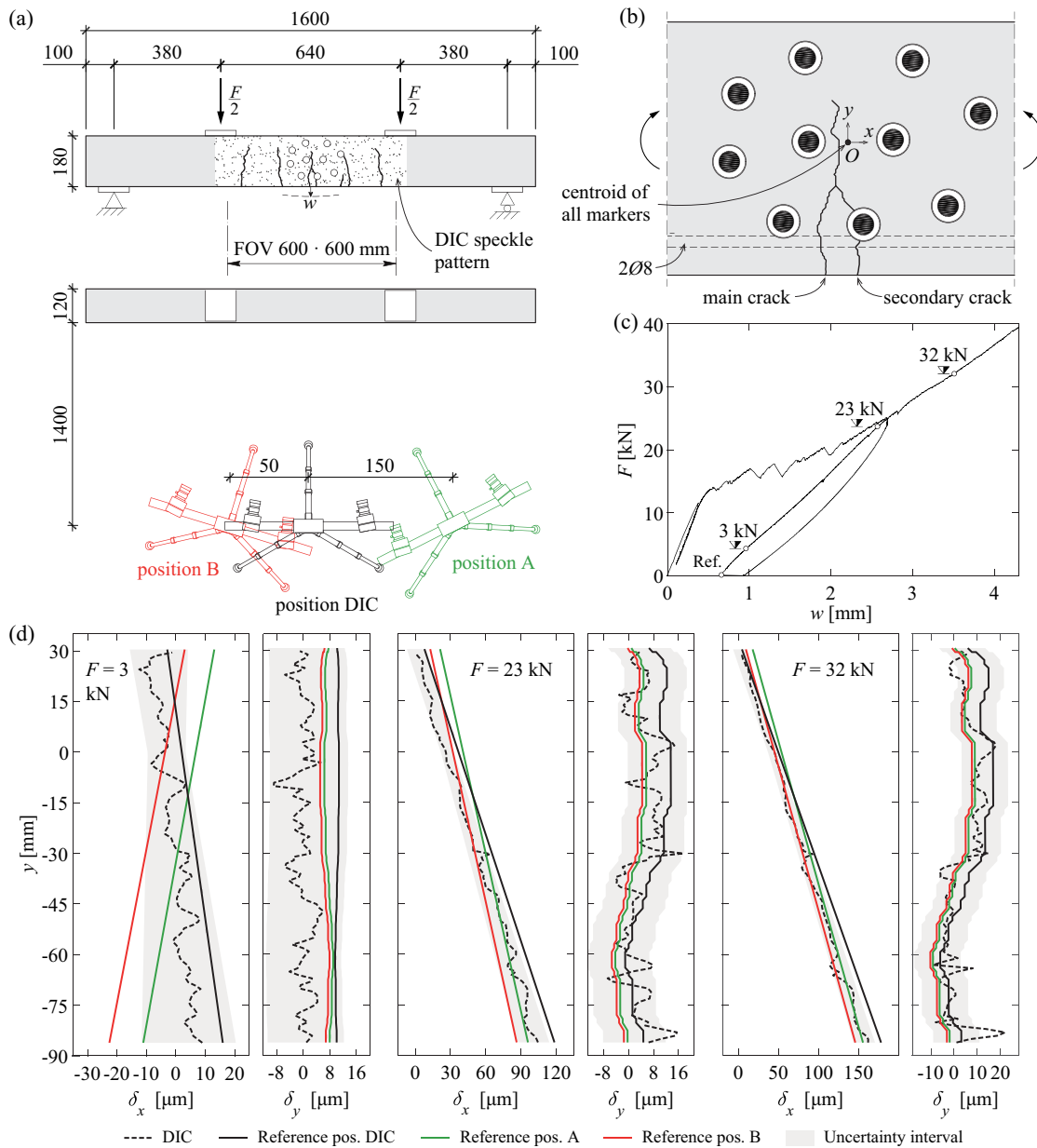


Figure 5.7: Results of the laboratory validation of the technique: (a) set-up and camera positions (the positions of the cameras are not to scale); (b) detail of the crack instrumented with markers; (c) load deformation curve; (d) crack kinematics comparison for three load steps.

Figure 5.7d shows the four measured crack displacements (different colours according to the positions in Figure 7a) for the three loading stages indicated in Figure 5.7c. The horizontal δ_x and vertical crack displacements δ_y are represented as a function of the height of the beam (coordinate system horizontally centred at the crack and vertically at the centroid of the markers, see Figure 5.7b). A secondary crack appeared probably due to the proximity of the markers to the crack. Its

kinematics were added to the kinematics of the main crack in the DIC results [Cav18]. The crack displacement uncertainty calculated according to Section 5.3.3 is shown with a grey hatch ($d_1 = 47$ mm, $d_2 = 108$ mm, $\sigma(t_n)_{tot} = 5.4$ μm , $\sigma(t_t)_{tot} = 8.1$ μm , $\sigma(\theta)_{tot} = 1.1 \cdot 10^{-4}$ rad). The kinematics obtained with DIC (ground truth for the validation) show a slight variability due to measurement uncertainties that can be smoothed using a moving average filter [Geh22]. The results show that the repositioning of the cameras has a small influence in the measurement results. For most points, the estimated crack opening and sliding fall within the estimated uncertainty interval. The interval corresponds to the standard deviation; thus, some measurements can exceed the interval. The crack opening measurements are more precise close to the centroid of the markers ($y = 0$). The precision of the crack sliding is constant as proposed in the model.

These results indicate that the discrete measurements obtained with the markers provide a good description of the crack kinematics. This technique significantly reduces the computational effort compared with the full image correlation, however a lower precision is achieved.

5.3.5 Recommendations and limits of applicability

The marker technique is practical in cases where the crack kinematics need to be accurately measured at intervals, and the use of gauge sensors is not practical (for example if a large region of an element with multiple cracks needs to be monitored). In general, when using markers, the distance d_1 should be maximized and the distance d_2 minimized. Patterns of regularly spaced markers or two staggered lines of markers were found to be suitable solutions

After the identification of the crack, the measurement system, framing of the crack and pixel size must be chosen based on the expected displacements and desired measurement uncertainty. If a measurement system similar to the one described in Section 5.3.3 is used, the following steps are recommended for the choice of the marker disposition:

1. As a first approximation, the measurement uncertainty of the marker coordinates presented in Section 5.3.3 can be used. Dividing the desired measurement uncertainty by the pixel size and estimating the value of y from the crack dimensions, the marker disposition can be determined using the values of the bias in Figure 5.6. The noise can be ignored as it is easily removed by averaging 10 images.
2. Once the marker distribution is chosen, the two tests described in Section 5.3.3 can be performed to characterize NV_N and NV_B (accounting for the type of camera, lens, markers and illumination).
3. Finally, the number and position of the markers (that determines n , d_1 and d_2) can be adjusted, so that the uncertainty of the crack kinematics according to Section 5.3.3 respects the desired limit.

When a significantly different measurement system is used it is recommended to start by step 2 and characterize the marker detection uncertainty.

5.4 In-situ application

This section presents an example of application of the proposed techniques in an existing structure. The considered crack was detected in one of the Chillon Viaducts (Switzerland). These twin viaducts are post-tensioned concrete box-girder bridges with a total length 2150 m and average span of 95 m. They were built between 1968 and 1970 by the balanced cantilever method, using precast segments produced on-site [Pig69]. The investigated crack is located on the bottom slab of the box girder at one fifth of the second span (see Figures 5.8a and b) next to the anchorage of the prestressing tendons that run along the bottom slab to carry positive bending moments. The crack is oriented at approximately 45° relative to the longitudinal axis of the bridge and is approximately 2 m long (combination of load introduction and shear between tendon and web). A segment of the crack of length 730 mm was fit inside the field of vision of 600×600 mm. It was painted with a speckle pattern and equipped with 18 markers (see Figure 5.8c).

5.4.1 Existing crack characterization

The technique discussed in Section 5.2 is applied to estimate the kinematics of the existing crack. The crack detection is performed using an image captured after cleaning the surface (Figure 5.9a) and an image after applying the white paint and speckles used for DIC measurements (Figure 5.9b). The results are similar with the exception of the region around the centre of the image where two smaller cracks were observed. Figure 5.9c presents the measured initial crack kinematics using the full-edge approach in images with speckles. It shows a crack displacement mostly perpendicular to the crack axis. This is reasonable if the studied region is considered as a shear panel reinforced in the two orthogonal directions, where an inclined stress field can develop with cracks parallel to the compression field that open perpendicularly to the compression field [Gro76, Thü79].

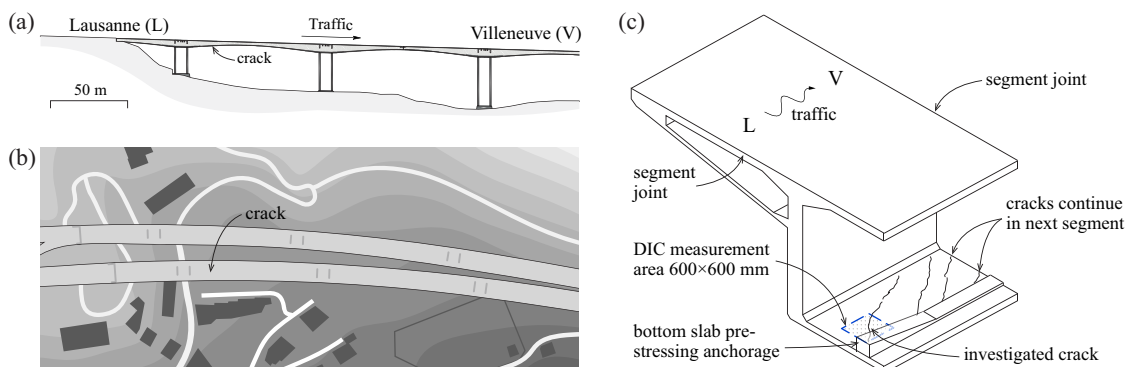


Figure 5.8: In-situ application: (a) partial elevation and (b) partial plan of the Chillon Viaducts; and (c) segment of interest with investigated crack.

To validate the results, the crack width was measured at the points between the long-term markers. Three measurements were taken using a crack microscope and a crack width ruler. Table 5.1 includes the average of three measurements ($w_{M,avg}$) and the automatic crack detection results (w_D) at each point. The results fall within the tolerance of ± 1 pixel with the exception of point D, where the difference is slightly larger. It must be noted that the crack lips in existing structures are likely to be significantly less well-defined than in tests in laboratory conditions, due to the presence of dust and erosion of the crack lips, amongst other reasons (the studied crack is probably more than 50 years old). Consequently, it is reasonable to expect a lower accuracy in such conditions.

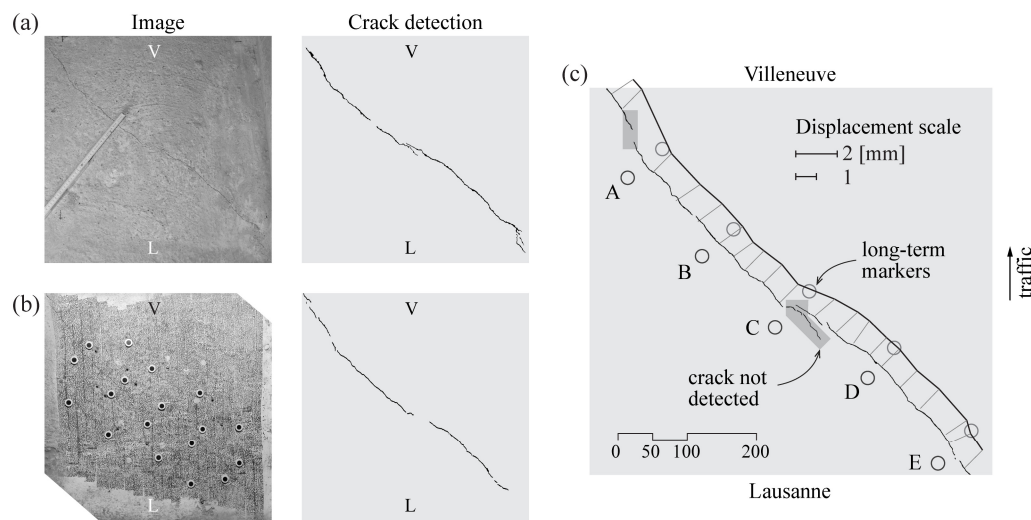


Figure 5.9: Existing crack detection and characterization: results of the crack detection for an image (a) without speckle pater and (b) with applied speckle pattern; and (c) measured initial crack kinematics.

Table 5.1: Comparison of the estimated crack width using conventional measurements and the automatic crack detection algorithm.

Point	$w_{M,avg}$ [mm]	w_D [mm]	Pixel size [mm/pixel]
A	1.20	1.29	0.323
B	1.30	1.24	0.243
C	0.75	-	-
D	0.73	1.18	0.322
E	0.80	1.07	0.242

5.4.2 Short-term measurements with DIC

As discussed in Section 5.1, DIC is particularly appropriate for short-term monitoring because it produces continuous displacement fields that can be processed to compute the crack kinematics with high accuracy.

The set-up described in Section 5.3.3 was used to measure the crack movement under a passing lorry. A set of 375 images obtained during a 15 s cycle (acquisition frequency of 25 Hz) triggered by an accelerometer was used for this purpose. The DIC analysis was performed with VIC-3D [Cor21], the crack geometry and kinematics were computed with ACDM [Geh22].

Figure 5.10a presents the crack opening measured with DIC and with an omega gauge during the passage of a heavy vehicle. A ZST for DIC [VDI19] after system installation resulted in a standard deviation of around 1/150 pixel. The DIC results fall within that measurement uncertainty from the gauge measurements. Figure 5.10b shows the crack kinematics for the selected time steps. The crack kinematics were obtained by applying smoothing operations in both space and time.

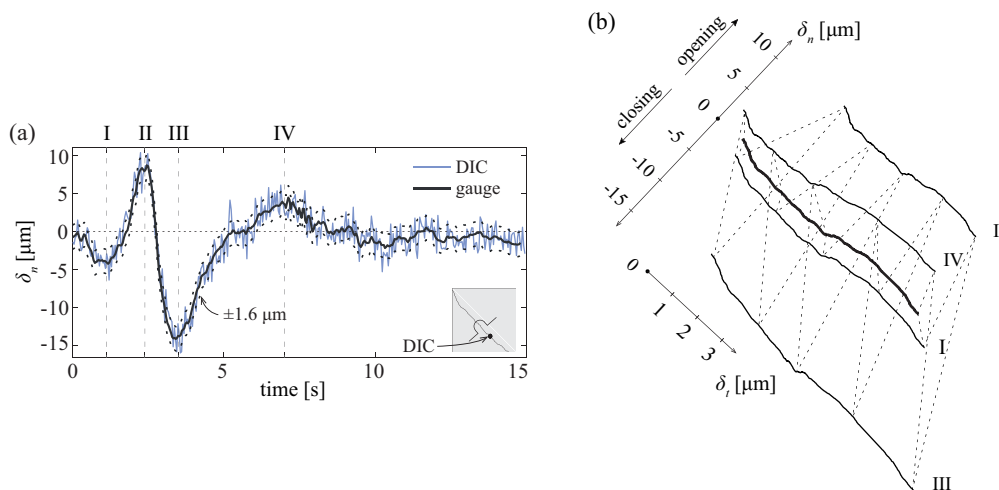


Figure 5.10: Results of the short-term in-situ application of DIC measurement: (a) comparison DIC measurements with the results of an omega gauge during the passage of a heavy vehicle; (b) crack kinematics at selected time steps.

5.4.3 Long-term measurements

Long-term monitoring of cracks requires several measurements collected at intervals for more than a year to capture the daily and seasonal temperature variations. Consequently, a permanent crack displacement can only be detected if a sufficient number of measurements is available. Due to time constraints and the lack of evidence that the studied crack presents any permanent crack displacement trend, the measurements presented in this chapter were limited to a duration of 19 hours. During this time, the crack opens and closes due to deformations of the bridge under daily temperature variations.

Figure 5.11a shows the disposition of the 18 markers around the investigated crack. The markers were screwed into metallic anchors installed in the concrete, as shown in Figure 5.11b. A set of reference images with slight displacements of the cameras was first captured. The camera set-up was then modified and recalibrated to simulate it being brought back for a second inspection. In this position, a reference image and regular images every 200 seconds for 19 hours were captured as in conventional DIC measurements.

Figures 5.11c and d show the average opening and sliding components of the crack. Figure 5.11e shows the temperature variation measured near the crack in the same period of time. Figure 5.11f shows the crack kinematics for five timesteps. For each timestep, the results of the DIC analysis (black curves) and of the marker analysis are presented simultaneously. In blue, a single image was used in the reference and deformed states for the marker measurements. In red, the measurements of ten reference images and ten deformed images were averaged as described in Appendix 5C. The uncertainty of the marker analysis (error with respect to the DIC measurements), is characterised by a systematic offset and a certain variability. As described in Section 5.3.3, the uncertainty of the measurements is due to errors in the detection of the centre of the markers. Therefore, each image (reference or deformed) carries an intrinsic error in the detection of its markers. These errors are more or less compensated when two images are compared. As the reference image is always the same, its error appears regardless of the deformed image with which it is compared. This results in the systematic offset visible in Figures 5.11c and d). The deformed images change at each timestep; therefore, their individual error varies randomly, only resulting in a variability of the measurements around an average value.

Both of these errors are reduced when multiple images are averaged. Due to the vibrations of the bridge and the camera supports, small displacements of the camera set-up occur between images. Therefore, by averaging images the bias and the noise are reduced, which explains the improvement of the results.

The ZDT and ZST resulted in $NV_N = 4.4 \mu\text{m}$ and $NV_B = 8.6 \mu\text{m}$. Compared to the results in the laboratory, the noise increased probably because the quality of the exposure was poorer. The bias was similar, as it depends mostly on the lens and the calibration. The measurement uncertainty of the crack displacements estimated according to Section 5.3.3 for one image are: $\sigma(\delta_n) = 4.8\text{-}10.0 \mu\text{m}$ (at the marker centroid and at the extremities of the field of vision respectively) and $\sigma(\delta_t) = 5.4 \mu\text{m}$. For ten images, $\sigma(\delta_n) = 1.5\text{-}3.0 \mu\text{m}$ and $\sigma(\delta_t) = 1.6 \mu\text{m}$ (reduction factor $\alpha = 0.3$ according to Appendix 5C). These values are in good agreement with the results.

In Figures 5.11c and d, the measurements obtained without considering the correction for temperature described in Section 5.3.2 are shown in light red and light blue. As expected, the value of the correction increases with the change of temperature. The corrected measurements are in close agreement with the DIC measurements, which shows the validity of the assumption of uniform dilatation of the crack lips. DIC measurements are not affected by temperature because the points used to compute the kinematics are very close to the crack and therefore insensitive to dilatations of the crack lips.

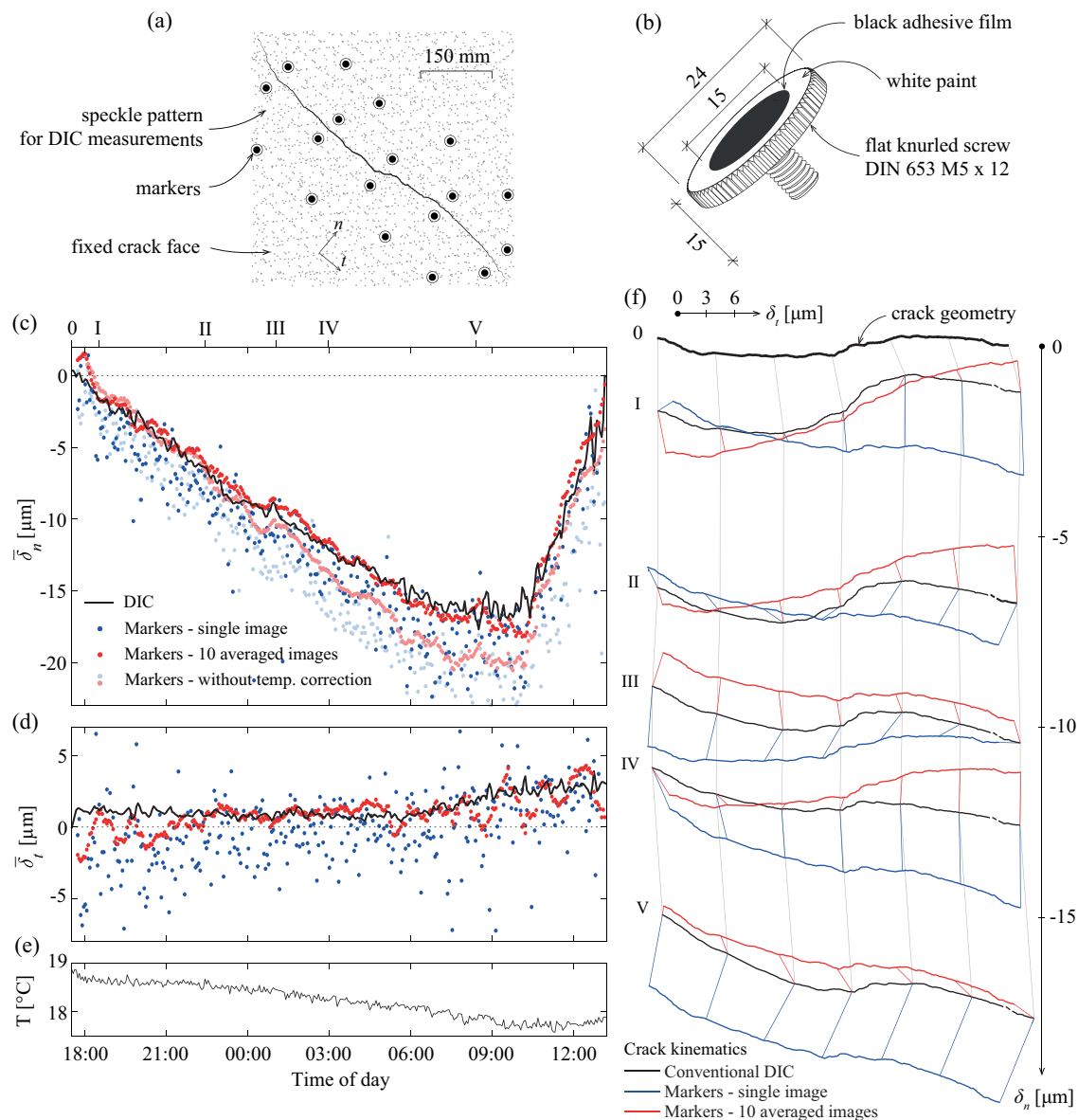


Figure 5.11: Results of the in-situ validation of the marker technique: (a) disposition of markers around the crack; (b) detail of one marker; (c) mean crack opening; (d) mean crack slip; (e) temperature; (f) crack kinematics at selected time steps.

The correction of the crack opening is approximately $2.5 \mu\text{m}$ at the coldest temperature. This is similar to the expected dilatation of the crack lips between the centroids of both of markers assuming a thermal expansion coefficient for the concrete of $\alpha_c = 10 \cdot 10^{-6}$ ($\Delta\delta_n \approx \alpha_c \cdot \Delta T \cdot d_2 = 10 \cdot 10^{-6} \cdot 1.5 \cdot 180 = 2.7 \mu\text{m}$).

These results show that the proposed marker technique can be used to characterize the crack displacements between inspections. Further validation of the measurement uncertainty is required over a longer period of time.

5.5 Conclusions

This chapter presents a contribution to the use of image-based measurements for the characterisation and monitoring of cracks in existing reinforced concrete structures. Three complementary techniques are investigated: a direct crack detection algorithm for initial crack characterization, conventional DIC for short-term high-precision measurements and a marker-based technique for long-term monitoring. The main conclusions are:

1. The tested algorithms for direct detection of crack geometry and kinematics have proven to be an effective technique to characterize the crack geometry and crack kinematics in-situ and in laboratory conditions. The achieved precision is around ± 1 pixel for the crack opening and ± 2 pixels for the crack sliding, for the evaluated conditions.
2. The automated detection results have been validated against traditional measurements, showing similar results with the clear advantage of being able to compute crack kinematics and not only crack openings. Furthermore, the resolution of the measurements is far greater than the point measurements that can be obtained using traditional measurements.
3. DIC is particularly appropriate for short-term monitoring of cracks, for instance to observe displacements due to traffic. This technique provides far more detailed information over large surfaces than traditional measurements. However, current DIC measurements present some limitations for long-term monitoring due to the principles of the correlation algorithm.
4. An alternative technique tracking markers fixed around the crack is proposed to characterize long-term changes in the crack. The proposed technique is a direct approach, thus overcomes the limitations of DIC. It can be used with any three-dimensional marker detection system. When using a high-precision marker detection system, such as a DIC measurement system and software, the marker technique can achieve crack displacement measurement precisions ranging from $1/30$ to $1/100$ pixel in optimal conditions.
5. The marker technique does not have the degree of redundancy of the DIC measurements. Therefore, the number and disposition of markers should be carefully chosen to obtain the desired measurement precision. Simplified and refined procedures are provided to predict this precision and to design a disposition of the markers. Simple tests are proposed to quantify it.

6. The three techniques were applied to monitor a crack inside a reinforced concrete bridge. Their complementary use shows promising results to obtain high-quality information about the crack geometry and displacements. The installation of the measurement system is the main disadvantage compared with simple traditional measurements. However, their use is well-justified in cases where high precision is required to characterize multiple cracks or large surfaces.

Appendix 5A: Best-fit uniform dilation

The mean distance d_3 between the centroid of a given group of markers and each of the given markers is used as an indicator of the relative change of temperature between reference and deformed states. Equation 5.13 is used to obtain $d_{3,ref}$ and $d_{3,def}$.

$$d_3 = \frac{1}{2n} \sum_n (\bar{a} - \underline{a}_n) + \frac{1}{2m} \sum_m (\bar{b} - \underline{b}_m) \quad (5.13)$$

1. The scaling matrix is:

$$S = \begin{bmatrix} d_{3,def}/d_{3,ref} & 0 \\ 0 & d_{3,def}/d_{3,ref} \end{bmatrix} \quad (5.14)$$

2. The translation vector \underline{t}_s necessary to perform the scaling operation around the centroid of the crack points $\bar{\underline{c}}_{ref}$ is:

$$\underline{t}_s = \bar{\underline{c}}_{ref} - S \cdot \bar{\underline{c}}_{ref} \quad (5.15)$$

3. The coordinates of the markers in the reference state after scaling are computed:

$$\begin{aligned} \underline{a}'_{n,ref} &= S \cdot \underline{a}_{n,ref} + \underline{t}_s \\ \underline{b}'_{m,ref} &= S \cdot \underline{b}_{m,ref} + \underline{t}_s \end{aligned} \quad (5.16)$$

Appendix 5B: Best-fit rigid body motion

This appendix presents the steps to compute the rotation matrix R and the translation vector \underline{t} to transform a group of n markers with coordinates \underline{e}_i into a group of markers with coordinates \underline{f}_i . The equations are adapted from the solution of Sorkine-Hornung [Sor17]. The equations for this type of calculations were presented by [Cam13] for use with the DEMEC and adapted by Gehri et al. [Geh20] for use with DIC measurements.

1. The coordinates of the markers relative to the centroid are computed.

$$\begin{aligned}\underline{e}_{i,rel} &= \underline{e}_i - \bar{\underline{e}} \\ \underline{f}_{i,rel} &= \underline{f}_i - \bar{\underline{f}}\end{aligned}\tag{5.17}$$

2. The covariance matrix and its singular value decomposition (U, V) are computed.

$$\begin{aligned}M &= [\underline{e}_{1,rel} \cdots \underline{e}_{n,rel}] [\underline{f}_{1,rel} \cdots \underline{f}_{n,rel}]^T \\ M &= U \Sigma V^T\end{aligned}\tag{5.18}$$

3. The rotation matrix is calculated.

$$R = V \begin{bmatrix} 1 & 0 \\ 0 & \det(VU^T) \end{bmatrix} U^T\tag{5.19}$$

4. The translation vector necessary to superpose the centroids of both groups is:

$$\underline{t} = \bar{\underline{f}} - R \bar{\underline{e}}\tag{5.20}$$

Appendix 5C: Reduction factors α and β

The reduction factor α accounts for the reduction of the uncertainty that can be achieved if the data from multiple images is considered. For the noise, the coordinates of the markers in images captured from the same position are averaged. For the bias, images with slight displacements between them are required. The rigid body motion (with respect to the first image considered in the averaging) has to be subtracted as explained in Appendix 5B before calculating their average. This is easily achieved in cases where ambient vibrations provoke small displacements of the camera set-up, as long as these displacements do not cause a “de-calibration” of the set-up. This is the case of the tests performed in the Chillon Viaducts described in Section 5.4.3. If this is not the case, the set-up needs to be recalibrated for every photograph. The reduction factor α obtained by averaging the marker coordinates collected during the ZDT as a function of the number of considered images p is shown in Figure 5.12a. Equation 5.21 is proposed for its estimation:

$$\alpha = 1 / \sqrt{p} \quad (5.21)$$

The reduction factor β results from the addition of two sets of data with different standard deviations. When adding two sets of data X and Y with different standard deviations $\sigma(X) < \sigma(Y)$, $\sigma(X + Y)$ depends on the ratio $\sigma(X)/\sigma(Y)$. If the ratio is close to 0, $\sigma(X + Y) \sim \sigma(Y)$ whereas if it is close to 1, the two sources of error have a similar scatter. In this case, a certain smoothing of the data occurs when summing them, which means that $\sigma(X + Y) < \sigma(X) + \sigma(Y)$. To quantify this effect, the marker coordinates collected during the ZDT were used as X and Y . The reduction factor β as a function of the ratio $\sigma(X)/\sigma(Y)$ is shown in Figure 5.12b. Equation 5.22 is proposed for its estimation:

$$\beta = 0.7 \cdot (\sigma(X) / \sigma(Y))^{-0.1} \quad (5.22)$$

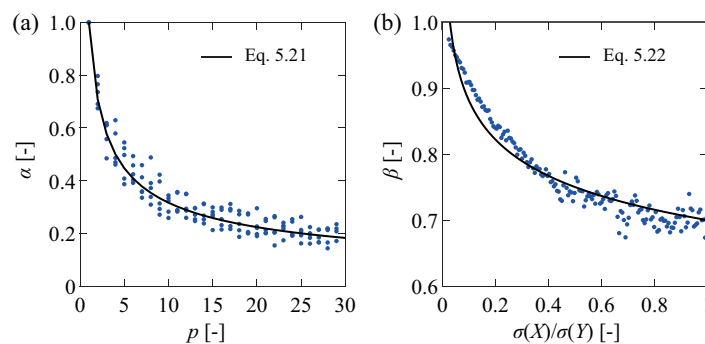


Figure 5.12: Reduction factors: (a) α as a function of the number of averaged images and (b) β as a function of the ratio $\sigma(X)/\sigma(Y)$ (where $\sigma(X) < \sigma(Y)$).

Notation

Lower case Latin characters

a_n	coordinates of the markers on the fixed crack lip
a'_n	coordinates of the markers on the fixed crack lip after correction
b_m	coordinates of the markers on the moveable crack lip
b'_m	coordinates of the markers on the moveable crack lip after correction
c_l	crack point coordinates
d	distance from the camera to the measured surface
d_1	distance from the markers to the centroid of the markers
d_2	distance between the centroids of the two groups of markers
d_3	average distance from the markers to the centroid for both groups of markers
l	number of crack points
m	number of markers on the moveable crack lip
n	number of markers on the fixed crack lip
p	number of images or positions
w_D	crack width measured using the automatic crack detection algorithm
w_{Mavg}	average of the 3 crack width measurements using traditional measurements
x	X axis
y	Y axis

Upper case Latin characters

A_n	group of markers on the fixed crack lip
A'_n	group of markers on the fixed crack lip after correction
B_m	group of markers on the moveable crack lip
B'_m	group of markers on the moveable crack lip after correction
C_l	crack points
M	covariance matrix
NV_N	standard deviation of the errors due to the noise
NV_B	standard deviation of the errors due to the bias
S	uniform scaling matrix
R	rotation matrix due to the crack displacement
R_0	rotation matrix for repositioning of the deformed coordinates
T	temperature
X	general set of data
Y	general set of data

Lower case Greek characters

α	reduction factor from averaging
β	reduction factor for different standard deviations
δ_l	displacement vector of the crack points
δ_n	crack displacement component normal to the crack axis
δ_t	crack displacement component parallel to the crack axis

δ_x	crack displacement component in the x direction
δ_y	crack displacement component in the y direction
$\sigma(X)$	standard deviation of variable X
θ	rotation

6

Conclusions and outlook

This chapter summarises the general conclusions of this thesis. In addition, an outlook on potential future research is provided.

6.1 Conclusions

Even though extensive efforts have been devoted to the research and understanding of bond between steel reinforcement, some aspects of the interaction are not fully understood. Furthermore, the refined detailed measurements available nowadays provide a big advantage for the understanding of bond with respect to conventional measurement techniques. This is particularly pertinent for the study of full-scale specimens where the reinforcement strains can be monitored with sub-millimetre spatial resolutions and the displacement field of large concrete surfaces can be measured.

The research included in this thesis focuses on the development of bond stresses in short anchorages, reinforced concrete ties and beams. This research investigates the local bond-slip relationship as the basis to understand the activation bond stresses in structural members. Using experimental evidence and mechanical considerations an existing bond-slip relationship is adapted to extend the range of applicability of the new proposal. The presented research shows that a better characterization of the local response can explain the global bond stresses activated in the structural members. The main general conclusions of this work are summarized in the following paragraphs. It must be noted that each chapter has its own specific conclusions. For this reason, in this section a more general overview is provided.

The local bond-slip relationship for well-confined conditions and good casting position can be considered as reference relationship. The local bond-slip response in other confinement and casting conditions can be explained by the presence of voids under the bar caused by plastic settlement and by the development of spalling cracks (parallel to the bar and approximately parallel to the concrete surface), splitting cracks (parallel to the bar and approximately perpendicular to the concrete surface) and conical cracks (starting at the rib lugs leading to concrete cone breakouts near the loaded end of the bar). An estimation of the reduction of bond stresses in these conditions can be provided based on the reduction of the contact area between the ribs and the concrete. For these phenomena, a simple model is proposed to quantify the bond strength reduction.

Given the relevance of the response in well-confined conditions and good casting conditions, the pull-out failure was studied in detail. The pull-out failure mechanism can be assumed to occur by the coalescence of the concrete microcracks that starts from the rib edge and progresses towards the following rib. A local bond-slip relationship is proposed to characterize the interface response in such conditions. This relationship is based on the proposal of *fib* Model Code 2010 and is adapted based on mechanical considerations and experimental evidence from a database of 159 short pull-out tests. The proposed relationship accounts for various influencing parameters that had been identified in previous studies.

As mentioned earlier, the development of cracks can explain the lower activation of bond stresses in unconfined or moderately confined conditions. Nevertheless, to apply the model proposed in Chapter 2 prior knowledge of the crack development is required. For practical purposes, a practical characterization of the local bond-slip relationship for other confinements is required. A proposal is presented in this thesis based on existing relationships from the literature and assuming that a certain transition must occur between the well-confined and the unconfined conditions.

The pertinence of the proposed relationships is evaluated to explain the activated bond stresses in cracked concrete elements. Experimental evidence indicates that typically assumed bond stresses in cracked elements overestimate the actual activated stresses. This discrepancy is confirmed in an experimental programme including beams and ties. However, in some cases the activated bond stresses are even larger than those recommended by the codes, for instance, in the shear reinforcement of the performed beam tests. An expression is proposed to estimate the activated bond stresses in service conditions based on the integration of the proposed bond-slip relationships accounting for different influencing parameters. The results provide an improvement of the estimated bond stresses with respect to current code assumptions.

With the aim of having a better characterization of the state of existing structures, the possibility of estimating the stress in the reinforcement based on crack width measurements is evaluated. For this purpose, a known cracking model based on the relative slip between the bar and the concrete is used. By using the measured crack spacing and the proposed average bond stresses in service condition, a reasonable estimation of the stress can be obtained for monotonic loading and for the maximum force during cyclic loading.

Lastly, with the same purpose, the feasibility and accuracy of DIC measurements in existing structures was studied. Conventional DIC measurements show promising results for short-term characterization of crack geometry and kinematics. However, some limitations concerning the initial crack characterization and long-term measurements were identified. These limits can be overcome by complementary techniques. The tested algorithms for direct detection of the crack have proven to be an effective technique to characterize existing crack geometry and crack kinematics. An alternative technique tracking markers fixed around the crack is proposed for long-term monitoring. Although the accuracy of this technique is lower than conventional DIC measurements, the computational cost is significantly reduced. The combination of the three investigated techniques seems promising to obtain high-quality information about the crack geometry and displacements in existing structures.

6.2 Outlook and future works

Some questions related to the topics studied in this research remain open. In the following, some of these future research lines are outlined.

Chapter 2: Bond of steel reinforcement based on detailed measurements: Results and interpretations

- The optical fibre measurements have shown great potential for the understanding of rebar-to-concrete bond. In particular, they have shown the differences in the bond stress distributions along the bonded length for bars in good and poor casting conditions. The bonded lengths studied in this research (10 to 15 \emptyset) are moderate. However, these findings should be confirmed in real anchorage lengths (around 40 \emptyset).

- The influence of the casting conditions is dependent on the distance to the bottom of the formwork. In many structures such as bridges or walls this depth can be of several meters. Pull-out tests in elements cast in such conditions could be performed to determine the bond performance and the limits of the top cast effect.
- Tests to study the redistribution of bond stresses under sustained loading using fibre optical measurements could be performed.

Chapter 3: Local bond-slip model based on mechanical considerations

- Further research is required to provide a better quantification of the local concrete strength around the rib to better estimate the pull-out strength.
- Additional research is required to better understand the response in poor bond conditions.
- Additional validation of the proposed relationships for moderate confinement is required.

Chapter 4: Estimation of the bar stress based on transverse crack width measurements in reinforced concrete structures

- The number of tests used for the validation of the model remains limited. Additional tests covering a wider range of the parameters considered in the model should be performed for validation. In particular, tests with larger concrete covers should be investigated.
- Additional tests are required to validate the average bond stress estimation in cyclic conditions. Different stress variation ranges should be considered to confirm the proposed factor.
- Further research is required to improve the estimation of the response in the unloading branch and the negative tension stiffening in order to provide a realistic estimation of the stress variations in existing structures.
- Additional tests are required with bars in poor casting conditions. Bars placed at representative heights over the formwork should be used to represent full-scale structures.
- Additional tests are required to validate current values of average bond stresses under long-term loading.
- It is well known that the rib lugs lead to stress concentrations and to the initiation of fatigue cracks. The average longitudinal steel stresses peak at the crack location where bond stresses are zero. Due to bond stresses, the steel stress diminishes with the increase of the distance from the crack. Therefore, the bar sections within the concrete have lower steel stress. However, bond stresses are introduced in the bar through the rib lugs which increases the stress concentrations in that region. Additional research is required to determine the role of bond stresses (transferred through the lugs) in the initiation of fatigue cracks.

Chapter 5: Image-based techniques for initial and long-term characterization of cracks in reinforced concrete structures

- Further validation of the proposed technique for the characterization of the initial crack in more adverse conditions are required. In existing structures, other signs of deterioration (such as corrosion traces, water, sediment marks or moss amongst others) can often be found around the cracks. The influence of these signs should be evaluated.
- The proposed technique for long-term monitoring of cracks was only validated over the duration of a day due to time constraints. Further tests to validate the technique over a long period of time are required.
- The influence of thermal deformations not resulting in uniform dilations can be assessed measuring the deformations in unrestrained steel plates in the same conditions as the monitored region. Tests combining both techniques could be useful to characterize thermal induced stresses.
- The two approaches presented in this section require the access and mastery of three different computer software. The implementation of both approaches in a single open-access program could be useful for the engineers in the practice.

Conclusions and outlook

B

Bibliography

- [Abd03] **Abdel-Qader I., Abudayyeh O., Kelly M. E.** , *Analysis of Edge-Detection Techniques for Crack Identification in Bridges*, ASCE Journal of Computing in Civil Engineering, Vol. 17, No 4, pp. 255-263, 2003.
- [Abr13] **Abrams D. A.**, *Tests of Bond between Concrete and Steel*, University of Illinois Bulletin, 71, 238 p., USA, 1913.
- [ACI92] **ACI**, *State-of-the-Art Report on Bond under Cyclic Loads*, Reported by ACI Committee 408, ACI 408.2R-92, Detroit, 1992.
- [ACI03] **ACI**, *Bond and Development of Straight Reinforcing Bars in Tension*, ACI Committee 408, ACI 408R-03, 49 p., USA, 2003.
- [ACI12] **ACI**, *Report on Bond of Steel Reinforcing Bars Under Cyclic Loading*, ACI-ASCE Committee 408, ACI 408.2R-12, 39 p., USA, 2012.
- [ACI02] **ACI Committee 318**, *Building code requirements for structural concrete (ACI 318-02) and commentary (ACI 318R-02)*, American Concrete Institute, Committee 318 Report, 443 pp. , Farmington Hills, USA, 2002.
- [And89] **Andreasen B. S., Nielsen M. P.**, *Anchorage of ribbed reinforcing bars*, Technical University of Denmark, Rapport No. R-238, 282 p., Denmark, 1989.
- [AST15] **ASTM**, *Standard Test Method for Comparing Bond Strength of Steel Reinforcing Bars to Concrete Using Beam-End Specimens*, ASTM, A944-10, 4 p., USA, 2015.
- [Au60] **Au T., Baird D. L.**, *Bearing Capacity of Concrete Blocks*, Journal of the American Concrete Institute, Vol. 56, No 3, pp. 869-880, USA, 1960.
- [Bad21] **Bado M. F., Casas J.-R., Kaklauskas G.**, *Distributed Sensing (DOFS) in Reinforced Concrete members for reinforcement strain monitoring, crack detection and bond-slip calculation*, Engineering Structures, Vol. 226, 111385, 13 p., 2021.
- [Bad21a] **Bado M. F., Casas J.-R., Dey A., Berrocal C., Kaklauskas G., Fernandez I., Rempling R.**, *Characterization of concrete shrinkage induced strains in internally-restrained RC structures by distributed optical fiber sensing*, Cement and Concrete Composites, Vol. 120, 12 p., 2021.
- [Bak90] **Bakhom M. M.**, *Shear behavior and design of joints in precast concrete segmental bridges*, PhD Thesis, Massachusetts Institute of Technology, 308 p., USA, 1990.
- [Bal21] **Bal I. E., Dais D., Smyrou E.**, *Novel invisible markers for monitoring cracks on masonry structures*, Construction and Building Materials, Vol. 300, 2021.
- [Bal91] **Balázs G. L.**, *Fatigue of Bond*, ACI Materials Journal, 99-M64, pp. 620-629, Detroit, USA, 1991.

- [Bal93] **Balázs G. L.**, *Cracking analysis based on slip and bond stresses*, ACI Materials Journal, 90 N°1, pp. 340-348, Detroit, USA, 1993.
- [Bal96] **Balázs G. L., Grosse C. U., Koch R., Reinhardt H. W.**, *Damage accumulation on deformed steel bar to concrete interaction detected by acoustic emission technique*, Magazine of Concrete Research, Vol. 48, No 177, pp. 311-320, 1996.
- [Bal90] **Baltay P., Gjelsvik A.**, *Coefficient of Friction for Steel on Concrete at High Normal Stress*, ASCE Journal of Materials in Civil Engineering, Vol.2, No 1, pp. 46-49, USA, 1990.
- [Bam07] **Bamonte P., Gambarova P.**, *High-Bond Bars in NSC and HPC: Study on Size Effect and on the Local Bond Stress-Slip Law*, ASCE Journal of Structural Engineering, Vol. 133, No 2, pp. 225-234, USA, 2007.
- [Bar09] **Barazzetti L., Scaioni M.**, *Crack measurement: Development, testing and applications of an automatic image-based algorithm*, ISPRS Journal of Photogrammetry and Remote Sensing, Vol. 64, No 3, pp. 285-296, 2009.
- [Bar22] **Barros F., Aguiar S., Sousa P.**, *Detection and measurement of beam deflection in the Madeira Airport runway extension using digital image correlation*, International Journal of Structural Integrity, Vol. 14, 2022.
- [BAS23] **BAST**, *Brückenstatistik: Datum 29/11/2023*, Bundesanstalt für Straßenwesen, <https://www.bast.de/DE/Statistik/Bruecken/Brueckenstatistik.html> (visited on 10/01/2024), German, 2023.
- [Baz95] **Bazant Z. P., Li Z., Thoma M.**, *Identification of Stress-Slip Law for Bar or Fiber Pullout by Size Effect Tests*, Journal of Engineering Mechanics, Vol. 121, No 5, pp. 587-660, USA, 1995.
- [Bel04] **Bell B.**, *European Railway Bridge Demography D1.2*, Sustainable Bridges – Assessment for Future Traffic Demands and Longer Lives, 15 p., 2004.
- [Ben04] **Benning W., Lange J., Schwermann R.**, *Monitoring crack origin and evolution at concrete elements using photogrammetry*, ISPRS Congress Istanbul Commission, 2004.
- [Ber20] **Berrocal C., Fernandez I., Rempling R.**, *Crack monitoring in reinforced concrete beams by distributed optical fiber sensors*, Structure and Infrastructure Engineering, Vol. 17, No 1, pp. 124-139, UK, 2020.
- [Bis01] **Bischoff P. H.**, *Effects of shrinkage on tension stiffening and cracking in reinforced concrete*, Canadian Journal of Civil Engineering, Vol. 21, No 3, pp. 363-374, 2001.

- [Bon75] **Bony J. C., Claude G., Soretz S.**, *Comparaison des prescriptions relatives à la résistance d'adhérence et à la surface spécifique des nervures des barres à béton*, Matériaux et constructions, Vol. 8, No 3, pp. 33-41, 1975.
- [Bor05] **Borosnyói A., Balázs G. L.**, *Models for flexural cracking in concrete: the state of the art*, Structural Concrete, Vol. 6, No 2, pp. 53-62, 2005.
- [Bor10] **Borosnyói A., Snóbli I.**, *Crack width variation within the concrete cover of reinforced concrete members*, Epitoanyag - Journal of Silicate Based and Composite Materials, Vol. 62 (3), pp. 70-74, 2010.
- [Bra16] **Brantschen F., Faria D. M. V., Fernández Ruiz M., Muttoni A.**, *Bond Behaviour of Straight, Hooked, U-Shaped and Headed Bars in Cracked Concrete*, Structural Concrete, 17 No. 5, pp. 799-810, 2016.
- [Bra16a] **Brantschen F.**, *Influence of bond and anchorage conditions of the shear reinforcement on the punching strength of RC slabs*, Thèse EPFL, n°7315, 186 p., Lausanne, Suisse, 2016.
- [Bra15] **Braut A., Hoult N. A., Lees J. M.**, *Development of a relationship between external measurements and reinforcement stress*, Proceedings of SPIE, Vol. 9435, 12 p., USA, 2015.
- [Bro65] **Broms B. B.**, *Crack width and crack spacing in reinforced concrete members*, ACI Journal Proceedings, Vol. 62, No. 10, pp. 1237-1256, USA, 1965.
- [Cai95] **Cairns J., Jones K.**, *Influence of rib geometry on strength of lapped joints: an experimental and analytical study*, Magazine of Concrete Research, Vol. 47, No 172, pp. 253-262, 1995.
- [Cai03] **Cairns J., Plizzari G.**, *Towards a harmonised European bond test*, Materials and Structures, Vol. 36, pp. 498-506, 2003.
- [Cai21] **Cairns J., Feldman L. R., Palmisano F.**, *Anchorage and lap capacity of square twisted reinforcement for assessment of existing structures*, Structural Concrete, Vol. 22, No 5, pp. 2502-3194, 2021.
- [Cai22] **Cairns J.**, *Top cast effect: Influence of bond length on splitting mode failure*, Structural Concrete, Vol. 23, No 5, pp. 2696-2709, 2022.
- [Cal15] **Calvi P. M.**, *A Theory for the Shear Behaviour of Cracks Providing a Basis for the Assessment of Cracked Reinforced Concrete Structures*, PhD Thesis, University of Toronto, 367 p., Canada, 2015.

- [Cal18] **Calvi P. M., Bentz E. C., Collins M. P.**, *Model for Assessment of Cracked Reinforced Concrete Membrane Elements Subjected to Shear and Axial Loads*, ACI Structural Journal, Vol. 115, No 2, pp. 501-509, USA, 2018.
- [Cam13] **Campana S., Fernández Ruiz M., Anastasi A., Muttoni A.**, *Analysis of shear-transfer actions on one-way RC members based on measured cracking pattern and failure kinematics*, Magazine of Concrete Research, Vol. 56, No. 6, pp. 386-404, UK, 2013.
- [Can86] **Canny J.**, *A Computational Approach to Edge Detection*, IEEE Transactions on Pattern Analysis and Machine Intelligence, Vol. 6, No 6, pp. 679-698, 1986.
- [Can20] **Cantone R., Fernández Ruiz M., Muttoni A.**, *A detailed view on the rebar-to-concrete interaction based on refined measurement techniques*, Engineering Structures, Vol. 226, 19 p., 2020.
- [Cap13] **Capros P., De Vita A., Tasios N., Papadopoulos D.**, *EU Energy, Transport and GHG Emissions Trends to 2050*, European Commission, Directorate-General for Energy, Directorate-General for Climate Action and Directorate-General for Mobility and Transport, 173 p., 2013.
- [Car15] **Carmo R. N. F., Valença J., Silva D., Dias da Costa D.**, *Assessing steel strains on reinforced concrete members from surface cracking patterns*, Construction and Building Materials, Vol. 98, pp. 265-275, 2015.
- [Car21] **Carrasco M., Araya-Letelier G., Velazquez R., Visconti P.**, *Image-Based Automated Width Measurement of Surface Cracking*, Sensors, Vol. 21, 7534, 18 p., 2021.
- [Cav15] **Cavagnis F., Fernández Ruiz M., Muttoni A.**, *Shear failures in reinforced concrete members without transverse reinforcement: An analysis of the critical shear crack development on the basis of test results*, Engineering structures, Vol. 103, pp. 157-173, UK, 2015.
- [Cav17] **Cavagnis F., Fernández Ruiz M., Muttoni A.**, *An analysis of the shear-transfer actions in reinforced concrete members without transverse reinforcement based on refined experimental measurements*, Structural concrete, Vol. 19, pp. 49-64, 2017.
- [Cav18] **Cavagnis F., Fernández Ruiz M., Muttoni A.**, *A mechanical model for failures in shear of members without transverse reinforcement based on development of a critical shear crack*, Engineering structures, Elsevier, Vol. 157, pp. 300-315, 2018.
- [CEB67] **CEB**, *Fissuration*, Comité Euro-International du béton, Bulletin d'Information, No. 61, 253 p., 1967.

- [CEB77] **CEB**, *Reinforcement, Bond and Anchorage: State of the Art Report*, CEB (Comité euro-international du béton), Bulletin d'information, 118, 240 p., 1977.
- [CEB79] **CEB**, *Structures en béton sous actions sismiques*, CEB (Comité euro-international du béton), State of the Art Report, Bulletin 131, Rome, Italy, 1979.
- [CEB93] **CEB**, *CEB-FIP Model Code 1990*, Comité Euro-International du Béton (CEB), 460 p., London, UK, 1993.
- [Ced81] **Cedolin L., Dei Poli S., Iori I.**, *Analisi sperimentale del processo di formazione della frattura nel calcestruzzo*, Studi E Ricerche, Politecnico di Milano, 3, pp. 47-74, Milan, Italy, Italian, 1981.
- [Ced83] **Cedolin L., Dei Poli S., Iori I.**, *Comportamento a trazione del calcestruzzo*, Studi E Ricerche, Politecnico di Milano, 5, pp. 23-46, Milan, Italy, Italian, 1983.
- [CEN23] **CEN**, *Final draft FprEN 1992-1-1: Design of concrete structures - Part 1-1: General rules and rules for buildings, bridges and civil engineering structures*, European Committee for Standardization (CEN), 405, Brussels, Belgium, 2023.
- [Cha01] **Chae M. J., Abraham D. M.**, *Neuro-Fuzzy Approaches for Sanitary Sewer Pipeline Condition Assessment*, Journal of Computing in Civil Engineering, Vol. 15, No 1, pp. 4-14, 2001.
- [Che69] **Chen W. F., Drucker D. C.**, *Bearing capacity of concrete blocks or rock*, Journal of Engineering Mechanics, 95, No EM 4, pp. 955-978, 1969.
- [Che75] **Chen W. F.**, *Limit analysis and soil plasticity*, Elsevier Scientific Publishing Company, 1975.
- [Choi17] **Choi O. C., Choi H.**, *Bearing Angle Model for Bond of Reinforcing Bars in Concrete*, ACI Structural Journal, Vol 114, No 1, pp. 245-253, USA, 2017.
- [Cla49] **Clark A. P.**, *Bond of Concrete Reinforcing Bars*, Journal of Research of the National Bureau of Standards, Vol. 43, pp. 565-579, USA, 1949.
- [Cor20] **Correlated Solutions**, *Vic-3D 8 Testing Guide*, 86 p., 2020.
- [Cor21] **Correlated Solutions**, *Vic-3D 8 Software Manual*, Version 8.4, 202 p., 2021.
- [Cor22] **Corres E., Muttoni A.**, *Long anchorage resistance of reinforcement bars derived from local bond-slip relationships for good and poor bond conditions*, Bond in Concrete 2022, pp. 207-216, Stuttgart, Germany, 2022.
- [Cor22a] **Corres E., Muttoni A.**, *Validation of bond models for the crack width estimation based on detailed measurements*, 14th fib International PhD Symposium in Civil Engineering, pp. 138-144, Rome, Italy, 2022.

- [Cor23] **Corres E., Muttoni A.**, *Bond of steel reinforcement based on detailed measurements: Results and interpretations*, Structural Concrete, Vol. 24, No 6, pp. 7173-7204, 2023.
- [Cro20] **Croce P.**, *Impact of Road Traffic Tendency in Europe on Fatigue Assessment of Bridges*, Applied Sciences, Vol. 10, 30 p., 2020.
- [Dah92] **Dahl K.B.**, *Constitutive model for normal and high strength concrete*, Department of structural Engineering, Technical University Denmark, Series R, No 286, 72 p., Lyngby, Denmark, 1992.
- [Dar03] **Dare P. M., Hanley H. B., Fraser C. S., Riedel B., Niemeier W.**, *An Operational Application of Automatic Feature Extraction: The Measurement of Cracks in Concrete Structures*, Photogrammetric Record, Vol. 17, No 99, pp. 453-464, 2003.
- [Dar93] **Darwin D., Graham E. K.**, *Effect of Deformation Height and Spacing on Bond Strength of Reinforcing Bars*, ACI Structural Journal, Vol. 90, No 6, pp. 646-657, USA, 1993.
- [Dav17] **Davis M. B., Hoult N. A., Bajaj S., Bentz E. C.**, *Distributed Sensing for Shrinkage and Tension Stiffening Measurement*, ACI Structural Journal, V. 114, pp. 755-766, 2017.
- [DB23] **DB**, *Facts and figures 2022*, Deutsche Bahn, 44 p., 2023.
- [Deb16] **Debernardi P. G., Taliano M.**, *An improvement to Eurocode 2 and fib Model Code 2010 methods for calculating crack width in RC structures*, Structural Concrete, Vol. 17, No 3, pp. 365-376, 2016.
- [Den96] **Den Uijl J. A., Bigaj A. J.**, *A bond model for ribbed bars based on concrete confinement*, Heron, 41 n°3, pp. 201-225, Delft, Netherlands, 1996.
- [DGC12] **DGC**, *Guía para la realización de inspecciones principales de obras de paso en la Red de Carreteras del Estado*, Dirección General de Carreteras, Ministerio de Fomento, 355 p., Spain, Spanish, 2012.
- [Dia11] **Dias da Costa D., Valença J., Júlio E. N. B. S.**, *Laboratorial test monitoring applying photogrammetric post-processing procedures to surface displacements*, Measurement, Vol. 44, No 3, pp. 527-538, 2011.
- [Dja52] **Djabry W.**, *Contribution à l'étude de l'adhérence des fers d'armature au béton*, Rapport EMPA N°184, 76 p., Zürich, Switzerland, 1952.
- [Dor18] **Dorafshan S., Thomas R. J., Maguire M.**, *Comparison of deep convolutional neural networks and edge detectors for image-based crack detection in concrete*, Construction and Building Materials, Vol. 186, pp. 1031-1045, 2018.

- [Dyb21] **Dybel P., Kucharska M.**, *X-ray CT Investigation of Bond Mechanism in Reinforced SCC Elements of Different Placement Technology*, Materials MDPI, Vol. 14, 18 p., 2021.
- [Elf12] **Elfgren L., Sas G. , Blanksvärd T.**, *Photographic strain monitoring during full-scale failure testing of Örnsköldsvik Bridge*, Structural Health Monitoring, Vol. 11 No. 4, pp. 489-498, 2012.
- [Eli83] **Eligehausen R., Popov P., Bertero V.**, *Local bond stress-slip relationships of deformed bars under generalized excitations*, UCB/EERC, 83/23, Berkeley, USA, 1983.
- [Elw95] **Elwell D. J., Fu G.**, *Compression Testing of Concrete: Cylinders vs. Cubes*, Transportation research and development bureau, New York State Department of Transportation, Special Report, 119, 30 p., USA, 1995.
- [EN105] **EN10080:2005**, *Steel for the reinforcement of concrete. Weldable reinforcing steel - General*, European Committee for Standardization (CEN), Brussels, Belgium, 2005.
- [Eur04] **Eurocode 2**, *Design of concrete structures-Part 1-1: General rules and rules for buildings*, European Committee for Standardization (CEN), 225 p., Brussels, Belgium, 2004.
- [Eur23] **Eurocode 2**, *Design of concrete structures - Part 1-1: General rules and rules for buildings, bridges and civil engineering structures*, Final draft FprEN 1992-1-1, European Committee for Standardization (CEN), 405 p., Brussels, Belgium, 2023.
- [Far95] **Farra B.**, *Influence de la résistance du béton et de son adhérence avec l'armature sur la fissuration*, Thèse EPFL, 1359, 171 p., Lausanne, Switzerland, 1995.
- [Fer07] **Fernández Ruiz M., Muttoni A., Gambarova P.**, *Analytical modelling of the pre- and post-yield behaviour of bond in reinforced concrete*, ASCE Journal of Structural Engineering, Vol. 133, N° 10, pp. 1364-1372, Reston, USA, 2007.
- [Fer15] **Fernández Ruiz M., Muttoni A., Sagaseta J.**, *Shear strength of concrete members without transverse reinforcement: A mechanical approach to consistently account for size and strain effects*, Engineering structures, Vol. 99, pp. 360-372, UK, 2015.
- [Fer66] **Ferry-Borges J.**, *Cracking and deformability of reinforced concrete beams*, Publications of the International Association of Bridge and Structural Engineering, Vol. 26, pp. 75-95, Zurich, Switzerland, 1966.
- [FIB00] **FIB**, *Bond of reinforcement in concrete*, fib bulletin, Fédération Internationale du Béton - fib Bulletin n°10; state-of-art report prepared by Task Group Bond models, 10, 427 p., Lausanne, Switzerland, 2000.

- [FIB08] **FIB**, *Constitutive modelling of high strength/ high performance concrete*, Fédération Internationale du Béton, fib bulletin, Vol. 42, 134 p., Lausanne, Switzerland, 2008.
- [FIB13] **FIB**, *fib Model Code for Concrete Structures 2010*, fib, First Edition, UK, 2013.
- [FIB14] **FIB**, *Bond and anchorage of embedded reinforcement: Background to the fib Model Code for Concrete Structures 2010*, Fédération Internationale du Béton, fib bulletin, Vol. 72, 161 p., Lausanne, Switzerland, 2014.
- [FIB22] **FIB**, *Advances on bond in concrete*, Fédération Internationale du Béton, fib bulletin, Vol. 106, 316 p., Lausanne, Switzerland, 2022.
- [Fuj10] **Fujita Y., Hamamoto Y.**, *A robust automatic crack detection method from noisy concrete surfaces*, Machine Vision and Applications, Vol. 22, pp. 245-254, 2010.
- [Fur91] **Furche J., Eligehausen R.**, *Lateral blow-out failure of headed studs near a free edge*, ACI SP-130, Anchors in concrete - Design and behavior, pp. 235-252, Detroit, USA, 1991.
- [Gal21] **Galkovski T., Lemcherreq Y., Mata Falcón J., Kaufmann W.**, *Fundamental Studies on the Use of Distributed Fibre Optical Sensing on Concrete and Reinforcing Bars*, Sensors, Vol. 21, No 22, 24 p., Switzerland, 2021.
- [Gal22] **Galkovski T., Mata Falcón J., Kaufmann W.**, *Effective reinforcement ratio of RC beams: Validation of modelling assumptions with high-resolution strain data*, Structural Concrete, Vol. 23, No 3, pp. 1353-1369, 2022.
- [Gal23] **Galkovski T., Mata Falcón J., Kaufmann W.**, *Stress field model for bond in reinforced concrete ties*, Engineering Structures, Vol. 294, 19 p., 2023.
- [Gal23a] **Galkovski T., Mata Falcón J., Kaufmann W.**, *Experimental investigation of bond and crack behaviour of reinforced concrete ties using distributed fibre optical sensing and digital image correlation*, Engineering Structures, Vol. 292, 24 p., 2023.
- [Gam89] **Gambarova P., Paolo Rostasi G., Zasso B.**, *Steel-to-concrete bond after concrete splitting: constitutive laws and interface deterioration*, Materials and Structures, Vol. 22, pp. 347-356, 1989.
- [Gam94] **Gambarova P., Rosati G., Schumm C.**, *An elasto-cohesive model for bond problems in reinforced concrete*, Proceedings Europe-US Workshop on Fracture and Damage in Quasibrittle Structures, Prague, Czech Republic, 1994.
- [Gam98] **Gambarova P., Rosati G., Schumm C.**, *Bond and splitting: a vexing question*, ACI SP-180, Bond and development of reinforcement, a tribute to Dr Peter Gergely, pp. 23-44, USA, 1998.

- [Gar22] **García R., Pérez Caldentey A.**, *Influence of casting position on cracking behavior of reinforced concrete elements and evaluation of latest proposal for EN-1992 and MC2020: Experimental study*, Structural Concrete, Vol. 23, No 5, pp. 2910-2927, 2022.
- [Gar22] **Garnica G., Lantsoght E.O.L., Yang Y.**, *Monitoring structural responses during load testing of reinforced concrete bridges: a review*, Structure and Infrastructure Engineering, Vol. 18, 2022.
- [Geh20] **Gehri N., Mata Falcón J., Kaufmann W.**, *Automated crack detection and measurement based on digital image correlation*, Construction and Building Materials, 256, 14 p., 2020.
- [Geh22] **Gehri N., Mata Falcón J., Kaufmann W.**, *Refined extraction of crack characteristics in large-scale concrete experiments based on digital image correlation*, Engineering Structures, 251-A, 21 p., UK, 2022.
- [Ger19] **Germanese D., Pascali M. A., Berton A.**, *A preliminary study for a marker-based crack monitoring in ancient structures*, Proceedings of the 2nd International Conference on Applications of Intelligent Systems, pp. 1-5, 2019.
- [Gia92] **Giaccio G., Rocco C. G., Violini D., Zappitelli J., Zerbino R.**, *High-Strength Concretes Incorporating Different Coarse Aggregates*, ACI Materials Journal, Vol. 89, No 3, pp. 242-246, USA, 1992.
- [Gil61] **Gilkey H. J.**, *Water-Cement Ratio Versus Strength-Another Look*, Journal of the American Concrete Institute, Vol. 57, No 5, pp. 1287-1312, USA, 1961.
- [Giu81] **Giuriani E.**, *Experimental Investigation on Bond-Slip Law of Deformed bars in Concrete*, IABSE Colloquium, pp. 121-142, Delft, Netherlands, 1981.
- [Giu91] **Giuriani E., Plizzari G., Schumm C.**, *Role of Stirrups and Residual Tensile Strength of Cracked Concrete on Bond*, Journal of Structural Engineering, Vol. 117, No 1, pp. 1-18, 1991.
- [Giu98] **Giuriani E., Plizzari G.**, *Interrelation of Splitting and Flexural Cracks in RC Beams*, Journal of Structural Engineering, Vol. 109, No 9, pp. 1032-1049, USA, 1998.
- [Got71] **Goto Y.**, *Cracks Formed in Concrete around Deformed Tension Bars*, ACI Journal, Vol. 68, No 4, pp. 244-251, Japan, 1971.
- [Got80] **Goto Y., Otsuka K.**, *Experimental studies on cracks formed in concrete around deformed tension bars*, Proceedings of the Japan Society of Civil Engineers, Vol. 1980, No 294, pp. 85-100, Japan, Japanese, 1980.

- [Gri07] **Gribniak V., Kaklauskas G., Bacinskas D.**, *State-Of-Art Review of Shrinkage Effect on Cracking and Deformations of Concrete Bridge Elements*, The Baltic Journal of Road and Bridge Engineering, Vol. 2, No 4, pp. 183-193, 2007.
- [Gro76] **Grob J., Thürlimann B.**, *Ultimate Strength and Design of Reinforced Concrete Beams Under Bending and Shear*, IABSE, No. 36, pp. 105-120, 1976.
- [Haj51] **Hajnal-Konyi K.**, *Comparative Tests on Various Types of Bars as Reinforcement of Concrete Beams*, The Structural Engineer, Vol. 29, No 5, pp. 133-148, 1951.
- [Han96] **Hansen E. A., Thorenfeldt E.**, *Bond Properties of Deformed Reinforcement Bars in High Strength Concrete*, Proceedings of the 4th Int. Symp. On utilization of High Strength / High Performance Concrete, pp. 1105-1114, Paris, France, 1996.
- [Han95] **Hansen T. C.**, *Triaxial Tests with Concrete and Cement Paste*, Technical University of Denmark, 54 p., Lyngby, Denmark, 1995.
- [Har95] **Harajli M. H., Hout M., Jalkh W.**, *Local Bond Stress-Slip Behaviour of Reinforcing Bars Embedded in Plain and Fibre Concrete*, ACI Materials Journal, Vol. 92 n°. 4, pp. 343-354, USA, 1995.
- [Har04] **Harajli M. H., Hamad B. S., Rteil A. A.**, *Effect of Confinement on Bond Strength between Steel Bars and Concrete*, ACI Structural Journal, Vol. 101, No 5, pp. 595-603, USA, 2004.
- [Haw82] **Hawkins N. M.**, *Local bond strength of concrete for cyclic reversed loadings*, Bond in Concrete, Applied Science Publishers Ltd., pp. 151-161, London, 1982.
- [Hes84] **Hess U.**, *Analysis of plastic solutions for the shear design of reinforced concrete beams*, Technical University of Denmark, Report No. R-137, 174 p., Denmark, Danish, 1984.
- [Hoo12] **Hool G. A.**, *Reinforced concrete construction*, McGraw-Hill Book Company, Inc, Vol. 1, 278 p., New York, USA, 1912.
- [Hor91] **Hordijk D. A.**, *Local approach to fatigue of concrete*, Delft University of Technology, Faculty of Civil Engineering, Delft, Netherlands, 1991.
- [Hua16] **Huang L., Chi Y., Xu L., Chen P., Zhang A.**, *Local bond performance of rebar embedded in steel-polypropylene hybrid fiber reinforced concrete under monotonic and cyclic loading*, Construction and Building Materials, Vol. 103, pp. 77-92, 2016.
- [Hua96] **Huang Z., Engström B., Magnusson J.**, *Experimental and analytical studies of the bond behaviour of deformed bars in high strength concrete*, Proceedings of the 4th Int. Symp. On utilization of High Strength / High Performance Concrete, pp. 1115-1124, Paris, France, Anglais, 1996.

- [Hus68] **Husain S. I., Ferguson P. M.**, *Flexural crack widths at the bars in reinforced concrete beams*, Centrale nationale d'alarme, The University of Texas at Austin, 41 p., Austin, USA, 1968.
- [Idd99] **Idda K.**, *Verbundverhalten von Betonrippenstählen bei Querkzug*, Institut für Massivbau und Baustofftechnologie, Universität Karlsruhe, 228 p., Karlsruhe, Germany, German, 1999.
- [Igl18] **Iglovikov V., Shvets A.**, *TernausNet: U-Net with VGG11 Encoder Pre-Trained on ImageNet for Image Segmentation*, ArXiv e-prints, 5 p., 2018.
- [Int18] **International Digital Image Correlation Society**, *A Good Practices Guide for Digital Image Correlation*, 110 p., 2018.
- [ISO19] **ISO**, *EN ISO 15630-1 Steel for the reinforcement and prestressing of concrete - Test methods - Part 1 : reinforcing bars, wire rod and wire*, European Committee For Standardization CEN, 36 p., 2019.
- [Ito02] **Ito A., Aoki Y., Hashimoto S.**, *Accurate Extraction and Measurement of Fine Cracks from Concrete Block Surface Image*, Proceedings of the 2002 28th Annual Conference of the IEEE Industrial Electronics, pp. 2202-2207, 2002.
- [Ito11] **Ito Y., Ogawa K., Nakano K.**, *Fast Ellipse Detection Algorithm Using Hough Transform on the GPU*, 2011 Second International Conference on Networking and Computing, pp. 313-319, 2011.
- [Iye05] **Iyer S., Sinha S. K.**, *A robust approach for automatic detection and segmentation of cracks in underground pipeline images*, Image and Vision Computing, Vol. 23, No 10, pp. 921-933, 2005.
- [Jah09] **Jahanshahi M. R., Kelly J. S., Masri S. F., Sukhatme G. S.**, *A survey and evaluation of promising approaches for automatic image-based defect detection of bridge structures*, Structure and Infrastructure Engineering, Vol. 5, No 6, pp. 455-486, 2009.
- [Jah12] **Jahanshahi M. R., Masri S. F.**, *Adaptive vision-based crack detection using 3D scene reconstruction for condition assessment of structures*, Automation in Construction, Vol. 22, pp. 567-576, 2012.
- [Kas93] **Kaseko M. S., Ritchie S. G.**, *A neural network-based methodology for pavement crack detection and classification*, Transportation Research Part C: Emerging Technologies, Vol. 1, No 4, pp. 275-291, 1993.
- [Kim17] **Kim H., Ahn E., Cho S., Shin M., Sim S.-H.**, *Comparative analysis of image binarization methods for crack identification in concrete structures*, Cement and Concrete Research, Vol. 99, pp. 53-61, 2017.

- [Kos20] **Koschemann M., Curbach M.**, *Bond stress distribution of ribbed steel bars in reinforced concrete with short bond length under various loading conditions*, Proceedings of the 13th fib International PhD Symposium in Civil Engineering, pp. 176-183, Paris, France, 2020.
- [Kos22] **Koschemann M., Curbach M., Marx S.**, *Investigation of local bond behavior using distributed optical fiber sensing*, Bond in Concrete 2022, pp. 133-145, Stuttgart, Germany, 2022.
- [Kos22a] **Koschemann M., Curbach M., Marx S.**, *Influence of the test setup on the local bond behaviour of ribbed steel bars*, fib International Congress 2022 Oslo, pp. 349-358, Oslo, Norway, 2022.
- [Kos83] **Koseki K., Breen J. E.**, *Exploratory study of shear strength of joints for precast segmental bridges*, Center for Transportation Research at The University of Texas at Austin, 106 p., USA, 1983.
- [Kre89] **Kreller H.**, *Zum nichtlinearen Trag- und Verformungsverhalten von Stahlbetonstabtragwerken unter Last- und Zwangseinwirkung*, Institut für Werkstoffe im Bauwesen, Mitteilungen, Universität Stuttgart, 214 p., German, 1989.
- [Kün06] **Küntz M., Jolin M., Bastien J.**, *Digital image correlation analysis of crack behavior in a reinforced concrete beam during a load test*, Canadian Journal of Civil Engineering, Vol. 33, No 11, pp. 1418-1425, 2006.
- [Lap18] **Lapi M., Orlando M., Spinelli P.**, *A review of literature and code formulations for cracking in R/C members*, Structural Concrete, vol. 19, No 5, pp. 1255-1535, 2018.
- [Lau99] **Laurencet P.**, *Précontrainte et armature pour contrôler l'ouverture résiduelle des fissures*, Thèse EPFL, 2028, 270 p., Lausanne, Switzerland, 1999.
- [Lei18] **Leibovich O., Yankelevsky D. Z., Dancygier A. N.**, *Direct Digital Image Analysis of Local Displacements and Strains in a Pullout Test*, Structures, Vol. 14, pp. 230-242, 2018.
- [Lei19] **Leibovich O., Yankelevsky D. Z., Dancygier A. N.**, *Circumferential strains of a concrete specimen in a pullout test*, Structural Concrete, Vol. 20, No 3, pp. 986-995, 2019.
- [Lem22] **Lemcherreq Y., Galkovski T., Mata Falcón J., Kaufmann W.**, *Application of Distributed Fibre Optical Sensing in Reinforced Concrete Elements Subjected to Monotonic and Cyclic Loading*, Sensors, Vol. 22, No 5, 28 p., Basel, Switzerland, 2022.

- [Lem23] **Lemcherreq Y., Zanuy C., Vogel T., Kaufmann W.**, *Strain-based analysis of reinforced concrete pull-out tests under monotonic and repeated loading*, Engineering Structures, Vol. 289, 19 p., 2023.
- [Lem23a] **Lemcherreq Y., Zanuy C., Vogel T., Kaufmann W.**, *Experimental and analytical assessment of fatigue damage in reinforced concrete tension members*, Engineering Structures, Vol. 289, 23 p., 2023.
- [Lem23b] **Lemcherreq Y., Haefliger S., Kaufmann W.**, *Discontinuous yielding in bare and embedded reinforcing bars: Implications on the determination of steel and bond shear stresses from strain measurements*, Engineering Structures, Vol. 278, 20 p., 2023.
- [Li22] **Li H., Wang W., Wang M., Li L., Vimlund V.**, *A review of deep learning methods for pixel-level crack detection*, Journal of Traffic and Transportation Engineering, Vol. 9, No 6, pp. 945-968, 2022.
- [Li10] **Li J.**, *An Investigation of Behavior and Modeling of Bond for Reinforced Concrete*, PhD Thesis, University of Washington, 304 p., USA, 2010.
- [Lie89] **Lieberum K. H., Reinhardt H. W.**, *Strength of Concrete on an Extremely Small Bearing Area*, ACI Structural Journal, Vol. 86, No.1, pp. 67-75, 1989.
- [Lin19] **Lin H., Zhao Y., Ozbolt J., Feng P., Jiang C., Eligehausen R.**, *Analytical model for the bond stress-slip relationship of deformed bars in normal strength concrete*, Construction and Building Materials, Vol. 198, pp. 570-586, 2019.
- [Lin11] **Lindorf A.**, *Ermüdung des Verbundes von Stahlbeton unter Querkzug*, Technischen Universität Dresden, Fakultät Bauingenieurwesen, 228 p., Dresden, Germany, German, 2011.
- [Lin16] **Lins R. G., Givigi S. N.**, *Automatic Crack Detection and Measurement Based on Image Analysis*, IEEE Transactions on Instrumentation and Measurement, Vol. 65, No 3, pp. 583-590, 2016.
- [Los79] **Losberg A., Olsson P.-A.**, *Bond Failure of Deformed Reinforcing Bars Based on the Longitudinal Splitting Effect of the Bars*, ACI Journal, Vol. 76, No 1, pp. 5-18, USA, 1979.
- [Lun20] **Luna Technologies Inc.**, *ODiSI 6000 Series User Guide*, 99 p., USA, 2020.
- [Lut67] **Lutz A. L., Gergely P.**, *Mechanics of bond and slip of deformed bars in concrete*, ACI Materials Journal, 64, pp. 711-721, Detroit, USA, 1967.

- [Ma76] **Ma S.-Y., Bertero V., Popov E.**, *Experimental and Analytical Studies on the Hysteretic Behavior of Reinforced Concrete Rectangular and T-Beams*, Earthquake Engineering Research Center, University of California, 274 p., USA, 1976.
- [Mae03] **Maekawa K., Pimanmas A., Okamura H.**, *Nonlinear Mechanics of Reinforced Concrete*, Spon Press, 768 p., 2003.
- [Mag00] **Magnusson J.**, *Bond and anchorage of ribbed bars in high-strength concrete*, PhD Thesis, Chalmers University of Technology, 300 p., Göteborg, Sweden, 2000.
- [Mah12] **Mahrenholtz C.**, *Seismic Bond Model for Concrete Reinforcement and the Application to Column-to-Foundation Connections*, Universität Stuttgart, Institut für Werkstoffe im Bauwesen, 398 p., Stuttgart, Germany, 2012.
- [Mai51] **Mains R. M.**, *Measurement of the Distribution of Tensile and Bond Stresses Along Reinforcing Bars*, Journal of the American Concrete Institute, Vol. 23, No 3, pp. 225-252, USA, 1951.
- [Mal13] **Malesa M., Kujawinska M.**, *Deformation measurements by digital image correlation with automatic merging of data distributed in time*, Applied Optics, Vol. 52, No 19, pp. 4681-4692, 2013.
- [Mar22] **Markic T., Morger F., Kaufmann W.**, *Partially loaded areas in reinforced concrete: Mechanical modelling*, Engineering Structures, Vol. 271, 18 p., Brazilian, 2022.
- [Mar98] **Marti P., Alvarez M., Kaufmann W., Sigrist V.**, *Tension chord model for structural concrete*, Structural Engineering International, IABSE, Vol. 8, No. 4, pp. 287-298, USA, 1998.
- [Mar81] **Martin H., Noakowski P.**, *Verbundverhalten von Betonstählen Untersuchung auf der Grundlage von Ausziehversuchen*, Deutscher Ausschuss für Stahlbeton, Vol. 319, 175 p., Berlin, Germany, German, 1981.
- [Mat20] **Mata Falcón J., Haefliger S., Lee M., Galkovski T., Gehri N.**, *Combined application of distributed fibre optical and digital image correlation measurements to structural concrete experiments*, Engineering Structures, Vol. 225, Page: 111309, Amsterdam, 2020.
- [Met14] **Metelli G., Plizzari G.**, *Influence of the relative rib area on bond behaviour*, Magazine of Concrete Research, Vol. 66, No 6, pp. 277-294, 2014.
- [Met23] **Metelli G., Cairns J., Plizzari G.**, *A new fib Model Code proposal for a beam-end type bond test*, Structural Concrete, Vol. 24, No 5, pp. 4446-4463, 2023.

- [Mih13] **Mihaylov B., Bentz E. C., Collins M. P.**, *Two-Parameter Kinematic Theory for Shear Behavior of Deep Beams*, ACI Structural Journal, Vol. 110, No 3, pp. 447-455, 2013.
- [Moc20] **Moccia F., Kubski X., Fernández Ruiz M., Muttoni A.**, *The influence of casting position and disturbance induced by reinforcement on the structural concrete strength*, Structural Concrete, 1, 28 p., 2020.
- [Moc20a] **Moccia F., Yu Q., Fernández Ruiz M., Muttoni A.**, *Concrete compressive strength: From material characterization to a structural value*, Structural Concrete, 21 p., 2020.
- [Moc21] **Moccia F., Fernández Ruiz M., Metelli G., Muttoni A., Plizzari G.**, *Casting position effects on bond performance of reinforcement bars*, Structural Concrete, Wiley, 21 p., 2021.
- [Moc21a] **Moccia F., Fernández Ruiz M., Muttoni A.**, *Spalling of concrete cover induced by reinforcement*, Engineering Structures, 19 p., 2021.
- [Moh18] **Mohan A., Poobal S.**, *Crack detection using image processing: A critical review and analysis*, Alexandria Engineering Journal, Vol 57, No 2, pp. 787-798, 2018.
- [Mon22] **Monney F., Yu Q., Fernández Ruiz M., Muttoni A.**, *Anchorage of shear reinforcement in beams and slabs*, Engineering Structures, Vol. 265, 114340, 32 p., 2022.
- [Mon22a] **Monney F., Fernández Ruiz M., Muttoni A.**, *Influence of amount of shear reinforcement and its post-yield response on the shear resistance of reinforced concrete members*, Structural Concrete, pp. 1-33, 2022.
- [Mor53] **Morice P. B., Base G. D.**, *The design and use of a demountable mechanical strain gauge for concrete structures*, Magazine of concrete research, Vol. 5, No 13, pp. 37-42, 1953.
- [Mör06] **Mörsch E.**, *Der Eisenbetonbau - Seine Theorie und Anwendung*, Konrad Wittwer, 2nd Edition, 252 p., Stuttgart, Germany, German, 1906.
- [Mos00] **Moselhi O., Shehab-Eldeen T.**, *Classification of Defects in Sewer Pipes Using Neural Networks*, Journal of Infrastructure Systems, Vol. 6, No 3, pp. 97-104, 2000.
- [Mos18] **Mosinska A., Marquez-Neila P., Kozinski M., Fua P.**, *Beyond the pixel-wise loss for topology-aware delineation*, Proceedings of the IEEE Conference on Computer Vision and Pattern Recognition, pp. 3136–3145, 2018.

- [Mou21] **Mousa M. A., Yussof M. M., Udi U. J.**, *Application of Digital Image Correlation in Structural Health Monitoring of Bridge Infrastructures: A Review*, *Infrastructures*, Vol. 6 No 12, p. 176, 2021.
- [Mül13] **Müller H. S., Anders I., Breiner R., Vogel M.**, *Concrete: treatment of types and properties in fib Model Code 2010*, *Structural Concrete*, Vol. 14, No 4, pp. 320 - 334, 2013.
- [Mur13] **Murcia-Delso J., Stavridis A., Shing P. B.**, *Bond Strength and Cyclic Bond Deterioration of Large Diameter Bars*, *ACI Structural Journal*, Vol. 110, No 4, pp. 659-670, 2013.
- [Mur15] **Murray C., Take W., Hout N. A.**, *Field monitoring of a bridge using digital image correlation*, *Proceedings of the ICE - Bridge Engineering*, Vol. 168, pp. 3-12, 2015.
- [Mut89] **Muttoni A.**, *Die Anwendbarkeit der Plastizitätstheorie in der Bemessung von Stahlbeton*, Dissertation ETHZ, 159 p., Zürich, Switzerland, German, 1989.
- [Mut07] **Muttoni A., Fernández Ruiz M.**, *Concrete Cracking in Tension Members and Application to Deck Slabs of Bridges*, *ASCE Journal of Bridge Engineering*, 12, pp. 646-653, USA, 2007.
- [Mut23] **Muttoni A., Cairns J., Goodchild C., Ganz H. R.**, *Background document to clauses 11.4 and 11.5 - Anchorage and laps of bars in tension and compression*, 135 p., Lausanne, Switzerland, 2023.
- [Nar19] **Naraniecki H., Marx S.**, *Zustandsentwicklung und -prognose von Eisenbahnbrücken*, 60 Forschungskolloquium des Deutschen Ausschusses für Stahlbeton, pp. 103-118, Hannover, Germany, German, 2019.
- [Nie11] **Nielsen M. P., Hoang L. C.**, *Limit Analysis and Concrete Plasticity*, CRC Press, 3rd edition, 788 p., Boca Raton, USA, 2011.
- [Nik23] **Nikon Corporation**, *Nikon D800 Tech Specs*, <https://www.nikonusa.com/en/nikon-products/product-archive/dslr-cameras/d800.html#tab-ProductDetail-ProductTabs-TechSpecs> (visited on 10/04/2023), 2023.
- [Nil72] **Nilson A. H.**, *Internal Measurement of Bond Slip*, *ACI Journal*, Vol. 69, No 7, pp. 439-441, USA, 1972.
- [Nis15] **Nishiyama S., Minakata N., Kikuchi T.**, *Improved digital photogrammetry technique for crack monitoring*, *Advanced Engineering Informatics*, Vol. 29, No 4, pp. 851-858, 2015.
- [Niy73] **Niyogi S. K.**, *Bearing Strength of Concrete - Geometric Variations*, *Journal of the Structural Division*, Vol. 99, No 7, pp. 1471-1491, USA, 1973.

- [Noa78] **Noakowski P.**, *Die Bewehrung von Stahlbetonbauteilen bei Zwangsbeanspruchung infolge Temperatur*, Deutscher Ausschuss für Stahlbeton, Vol. 296, 144 p., Germany, German, 1978.
- [Noa88] **Noakowski P.**, *Nachweisverfahren für Verankerung, Verformung, Zwangsbeanspruchung und Rissbreite*, Deutscher Ausschuss für Stahlbeton, Vol. 394, 75 p., Germany, German, 1988.
- [Nog95] **Noghabai K.**, *Splitting of concrete in the anchoring zone of deformed bars*, Lulea University of Technology, Division of Structural Engineering, Licentiate Thesis, 26L, Lulea, Sweden, 1995.
- [OFR19] **OFROU**, *Rapport sur l'état du réseau des routes nationales*, Office fédéral des routes, Édition 2019, 46 p., Switzerland, 2019.
- [OFR21] **OFROU**, *Directive ASTRA 62016: Guide pour les inspecteurs d'ouvrages d'art*, Office fédéral des routes, Édition 2021 V1.20, 85 p., Switzerland, 2021.
- [OFR22] **OFROU**, *Rapport d'état des routes nationales*, Office fédéral des routes, Édition 2021, 54 p., 2022.
- [OFR23] **OFROU**, *Rapport d'état des routes nationales*, Office fédéral des routes, Etat au 31.12.2022, Edition 2023, 56 p., Switzerland, 2023.
- [Oh07] **Oh B. H., Kim S. H.**, *Realistic Models for Local Bond Stress-Slip of Reinforced Concrete under Repeated Loading*, Journal of Structural Engineering, Vol. 133, No 2, pp. 216-224, 2007.
- [Oke20] **Okeil A., Matsumoto K., Nagai K.**, *Investigation on local bond behavior in concrete and cement paste around a deformed bar by using DIC technique*, Cement and Concrete Composites, Vol. 109, 14 p., 2020.
- [Oli13] **Oliveira H., Lobato Correia P.**, *Automatic Road Crack Detection and Characterization*, IEEE Transactions on Intelligent Transportation Systems, Vol. 14, No 1, pp. 155-168, 2013.
- [One23] **OnePlus Technology**, *OnePlus 6 Tech Specs*, <https://www.oneplus.com/us/6/specs> (visited on 11/04/2023), 2023.
- [Ozg19] **Ozgenel C. F.**, *Concrete Crack Segmentation Dataset*, Mendeley Data, <https://data.mendeley.com/datasets/jwsn7tfbrp/1> (visited on 08/05/2023), 2019.
- [Pan09] **Pan B., Qian K., Xie H.**, *Two-dimensional digital image correlation for in-plane displacement and strain measurement: a review*, Measurement Science and Technology, Vol. 20, No 6, 2009.

- [Pan22a] **Pantoja-Rosero B. G.**, *Crack Kinematics GitHub repository*, https://github.com/eesd-epfl/crack_kinematics (visited on 08/05/2023), 2022.
- [Pan22] **Pantoja-Rosero B. G., dos Santos K. R. M., Achanta R., Rezaie A., Beyer K.**, *Determining crack kinematics from imaged crack patterns*, *Construction and Building Materials*, 343, 24 p., 2022.
- [Pér13] **Pérez Caldentey A., Corres Peiretti H., Peset Iribarren J., Giraldo Soto A.**, *Cracking of RC members revisited: influence of cover, $\rho_{s,ef}$ and stirrup spacing – an experimental and theoretical study*, *Structural Concrete*, Vol. 14, No 1, pp. 69-78, 2013.
- [Pér20] **Pérez Caldentey A., García R., Gribniak V., Rimkus A.**, *Tension versus flexure: Reasons to modify the formulation of MC 2010 for cracking*, *Structural Concrete*, Vol. 21, No 5, pp. 2101-2123, 2020.
- [Pig69] **Piguet J.-C.**, *Ponts en courbe préfabriqués et construits en encorbellement (exemple de Chillon)*, *Bulletin technique de la Suisse romande*, Vol. 9, pp. 128-134, Suisse, 1969.
- [Pli22] **Plizzari G., Metelli G., Cairns J.**, *An overview of enhancements to provisions for bond in the draft Fib Model Code 2020*, *Bond in Concrete 2022*, pp. 1038-1051, Stuttgart, Germany, 2022.
- [Pol19] **Poldon J. J., Hoult N. A., Bentz E. C.**, *Distributed Sensing in Large Reinforced Concrete Shear Test*, *ACI Structural Journal*, 116(5), 235-245, 2019.
- [Pop19] **Popescu C., Sas G., Arntsen B.**, *Structural health monitoring of a buttress dam using digital image correlation*, *Sustainable and Safe Dams Around the World*, 10 p., 2019.
- [Pop73] **Popovics S.**, *A numerical approach to the complete stress-strain curve of concrete*, *Cement and Concrete Research*, 3, pp. 583-599, USA, 1973.
- [Pre09] **Preuss E.**, *Zur Frage der Haftfestigkeit zwischen Beton und Eisen*, *Armierter Beton*, No 9, pp. 336-337, German, 1909.
- [Pri13] **Prince J. R., Singh B.**, *Bond behaviour between recycled aggregate concrete and deformed steel bars*, *Materials and Structures*, Vol. 47, pp. 503–516, 2013.
- [Pro21] **Proestos G. T., Palipana D. K., Mihaylov B.**, *Evaluating the shear resistance of deep beams loaded or supported by wide elements*, *Engineering Structures*, Vol. 226, 15 p., 2021.

- [Rea18] **Reagan D., Sabato A., Niezrecki C.**, *Feasibility of using digital image correlation for unmanned aerial vehicle structural health monitoring of bridges*, Structural Health Monitoring, Vol. 17, No 5, pp. 1056-1072, 2018.
- [Reh61] **Rehm G.**, *Über die Grundlagen des Verbunds zwischen Stahl und Beton*, Deutscher Ausschuss für Stahlbeton, Vol. 138, 59 p., Berlin, Germany, German, 1961.
- [Reh69] **Rehm G.**, *Kriterien zur Beurteilung von Bewehrungsstäben mit hochwertigen Verbund*, Stahlbetonbau, Berichte aus Forschung und Praxis, Verlag Wilhelm Ernst & Sohn, pp. 79-96, Berlin, Germany, German, 1969.
- [Rei84] **Reinhardt H. W.**, *Fracture Mechanics of an Elastic Softening Material like Concrete*, Heron, Delft University of Technology, 29 nÂ², 42 p., Delft, Netherlands, 1984.
- [Rez20] **Rezaie A., Achanta R., Godio M., Beyer K.**, *Comparison of crack segmentation using digital image correlation measurements and deep learning*, Construction and Building Materials, Vol. 261, 12 p., 2020.
- [Rez23] **Rezaie A.**, *Deep Crack Segmentation GitHub repository*, <https://github.com/amirrezaie1415/Deep-DIC-Crack> (visited on 08/05/2023), 2023.
- [Rez23a] **Rezaie A., Achanta R., Godio M., Beyer K.**, *Dataset of cracks on DIC images*, <https://zenodo.org/records/4307686> (visited on 08/05/2023), 2023.
- [Rez23b] **Rezaie A.**, *Crack Segmentation in Concrete Surfaces GitHub repository*, <https://github.com/amirrezaie1415/Concrete-Crack-Segmentation> (visited on 08/05/2023), 2023.
- [RIL78] **RILEM**, *Essais portant sur l'adhérence des armatures du béton - Essai par traction*, Recommendation RILEM/CEB/FIP - RC6, Matériaux et Constructions, vol. 6, n° 32, 1978.
- [Rob63] **Roberts L. G.**, *Machine perception of three-dimensional solids*, Massachusetts Institute of Technology, Dept. of Electrical Engineering, 82 p., USA, 1963.
- [Ruo16] **Ruocci G., Rospars C., Moreau G.**, *Digital Image Correlation and Noise-filtering Approach for the Cracking Assessment of Massive Reinforced Concrete Structures*, Strain, Vol. 52, No 6, pp. 503-521, 2016.
- [Sal36] **Saliger R.**, *Hochwertige Stähle im Eisenbetonbau (High-Grade Steel in Reinforced Concrete)*, Proceedings of the 2nd congress of the International association for bridge and structural engineering (IABSE), Vol. 2, pp. 303-323, Berlin-Munich, Germany, German, 1936.

- [Sch98] **Schenkel M.**, *Zum Verbundverhalten von Bewehrung bei kleiner Betondeckung*, IBK-Bericht, PhD Thesis; Institut für Baustatik und Konstruktion; ETH Zürich, 237, 162 p., Zürich, Switzerland, German, 1998.
- [Sch84] **Schober H.**, *Ein Modell zur Berechnung des Verbunds und der Risse im Stahl- und Spannbeton*, PhD thesis; Universität Stuttgart, Fakultät für Bauingenieur- und Vermessungswesen, 208 p., Stuttgart, Germany, German, 1984.
- [Sch18] **Schoening J.**, *Anchorage and Laps in Reinforced Concrete Members under Monotonic Loading*, PhD Thesis, RWTH Aachen University, 394 p., Aachen, Germany, 2018.
- [Sha15] **Shan B., Zheng S., Ou J.**, *A Stereovision-based Crack Width Detection Approach for Concrete Surface Assessment*, KSCE Journal of Civil Engineering, Vol. 20, pp. 803-812, 2015.
- [Shi87] **Shima H., Chou L. L., Okamura H.**, *Bond characteristics in post-yield range of deformed bars*, Proceedings of JSCE, Translation, n°378/v-6, pp. 113-124, Japan, 1987.
- [Shi87] **Shima H.**, *Micro and Macro models for bond in Reinforced concrete*, University of Tokyo, Journal of the Faculty of Engineering; University of Tokyo, XXXIX n° 2, pp. 133-194, Tokyo, Japan, 1987.
- [SIA13] **SIA**, *SIA 262:2013 - Structures en béton*, Société suisse des ingénieurs et des architectes, 102 p., Zurich, Switzerland, 2013.
- [SIA24] **SIA**, *Registre des aciers d'armature conformes à la norme SIA 262:2013*, Société Suisse des Ingénieurs et Architectes, Edition 2024, 5 p., Switzerland, French, German, 2024.
- [Sig95] **Sigrist V.**, *Zum Verformungsvermögen von Stahlbetonträgern*, Dissertation, No. 11169, ETHZ, 159 p., Zürich, Switzerland, German, 1995.
- [Sor18] **Sorensen J. H.**, *Design and Modeling of Structural Joints in Precast Concrete Structures*, PhD Thesis, Technical University of Denmark, 287 p., Denmark, 2018.
- [Sor79] **Soretz S., Holzenbein H.**, *Influence of Rib Dimensions of Reinforcing Bars on Bond and Bendability*, ACI Journal Proceedings, Vol. 76, No 1, pp. 111-128, USA, 1979.
- [Sor17] **Sorkine-Hornung O., Rabinovich M.**, *Least-squares rigid motion using svd*, Department of Computer Science, ETH Zurich, 5 p., 2017.
- [Sor89] **Soroushian P., Choi Ki-Bong**, *Local Bond of Deformed Bars with Different Diameters in Confined Concrete*, ACI Structural Journal, Vol. 86, No.2, pp. 217-222, 1989.

- [Sou19] **Sousa P., Barros F., Tavares P.**, *Experimental measurement of bridge deflection using Digital Image Correlation*, *Procedia Structural Integrity*, Vol. 17, pp. 806-811, 2019.
- [Spi59] **Spieth H. B.**, *Das Verhalten von Beton unter hoher örtlicher Pressung und Teilbelastung unter besonderer Berücksichtigung von Spannbetonverankerungen*, PhD Thesis, Technische Hochschule Stuttgart, 129 p., Stuttgart, Germany, German, 1959.
- [Sto75] **Stock A. F.**, *The effect of Aggregate volume on the properties of concrete*, Thesis, University of Surrey, 152 p., UK, 1975.
- [Sut09] **Sutton M. A., Orteu J.-J., Schreier H. W.**, *Image correlation for shape, motion and deformation measurements: basic concepts, theory and applications*, Springer, 321 p., 2009.
- [Sut17] **Sutton M. A., Matta F., Rizos D.**, *Recent Progress in Digital Image Correlation: Background and Developments since the 2013 W M Murray Lecture*, *Experimental Mechanics*, Vol. 57, No 1, pp. 1-30, 2017.
- [Sys99] **Système Hennebique**, *Le béton armé*, Organe des Concessionnaires et Agents du Système Hennebique, 2e année, No. 14, 14 p., 1899.
- [Tam09] **Tammo K.**, *Crack Behavior near Reinforcing Bars in Concrete Structures*, *ACI Structural Journal*, Vol. 106, No 3, pp. 259-267, USA, 2009.
- [Tep73] **Tepfers R.**, *A theory of bond applied to overlapped tensile reinforcement splices for deformed bars*, Chalmers University, P-73:2, Division of Concrete structures, Chalmers University of Göteborg, 73 n°2, 328 p., Göteborg, Sweden, 1973.
- [Tep92] **Tepfers R., Olsson P.-A.**, *Ring test for the evaluation of bond properties of reinforcing bars*, *Bond in Concrete - From Research to Practice*, Vol. 1, pp. 89-99, Riga, Latvia, 1992.
- [Tho36] **Thomas F. G.**, *Cracking in reinforced concrete*, *The Structural Engineer*, Vol. 14, No 7, pp. 298-320, 1936.
- [Thü79] **Thürlimann B.**, *Plastic Analysis of Reinforced Concrete Beams*, *IABSE Colloquium*, Vol. 28, pp. 71-90, Copenhagen, Denmark, 1979.
- [Til79] **Tilly G. P.**, *Fatigue of steel reinforcement bars in concrete: a review*, *Fatigue of Engineering Materials and Structures*, Vol. 2, pp. 251-268, 1979.
- [Tim70] **Timoshenko S., Goodier J. N.**, *Theory of Elasticity*, McGraw-Hill Book Company, 3rd Edition, 608 p., USA, 1970.

- [Tir21] **Tirassa M., Fernández Ruiz M., Muttoni A.**, *An interlocking approach for the rebar-to-concrete contact in bond*, Magazine of Concrete Research, Vol. 73, No 8, pp. 379-393, 2021.
- [Tre15] **Treacy M. A., Brühwiler E.**, *A direct monitoring approach for the fatigue safety verification of construction joint details in an existing post-tensioned concrete box-girder bridge*, Engineering Structures, Vol. 88, pp. 189-202, 2015.
- [Tun13] **Tung S.-H., Weng M.-C., Shih M.-H.**, *Measuring the in situ deformation of retaining walls by the digital image correlation method*, Engineering Geology, Vol. 166, pp. 116-126, 2013.
- [USD16] **USDOT**, *Deficient Bridges by Superstructure Material: Data 31/12/2016*, U.S. Department of Transportation, Federal Highway Administration (FHWA), <https://www.fhwa.dot.gov/bridge/nbi/no10/mat16.cfm#b> (visited on 10/01/2024), 2016.
- [USD22] **USDOT**, *Tables of Frequently Requested NBI Information: Bridge Condition by Year Built*, U.S. Department of Transportation, FHWA, <https://www.fhwa.dot.gov/bridge/nbi/no10/yrblt23.pdf> (visited on 10/01/2024), 2022.
- [Val13] **Valença J., Dias da Costa D., Júlio E. N. B. S.**, *Automatic crack monitoring using photogrammetry and image processing*, Measurement, Vol. 46, No 1, pp. 433-441, 2013.
- [Van23] **Van der Esch A., Wolfs R., Fennis S., Roosen M., Wijte S.**, *Categorization of formulas for calculation of crack width and spacing in reinforced concrete elements*, Structural Concrete, 17 p., 2023.
- [Van90] **Van der Veen C.**, *Theoretical and Experimental Determination of the Crack Width in Reinforced Concrete at Very Low Temperatures*, PhD Thesis, Delft University of Technology, 111 p., Delft, Netherlands, 1990.
- [VDI19] **VDI**, *Optische Messverfahren - Digitale Bildkorrelation; Grundlagen, Annahme- und Überwachungsprüfung*, VDI - Verein Deutscher Ing., 51 p., Germany, German/English, 2019.
- [Vec92] **Vecchio F. J.**, *Finite Element Modeling of Concrete Expansion and Confinement*, Journal of Structural Engineering, Vol. 118, No. 9, pp. 2390-2406, 1992.
- [Wal80] **Walraven J. C.**, *Aggregate interlock: a theoretical and experimental analysis*, PhD Thesis, Delft University of Technology, Faculty of Civil Engineering, 197 p., Delft, Netherlands, 1980.
- [Wal81] **Walraven J. C.**, *Fundamental Analysis of Aggregate Interlock*, ASCE Journal of Structural Engineering, Vol. 107 No 11, pp. 2245-2270, USA, 1981.

- [Wan10] **Wang P., Huang H.**, *Comparison Analysis on Present Image-based Crack Detection Methods in Concrete Structures*, 3rd International Congress on Image and Signal Processing, pp. 2530-2533, 2010.
- [Wie98] **Wiedemann C., Heipke C., Mayer H., Jamet O.**, *Empirical Evaluation of Automatically Extracted Road Axes*, Empirical Evaluation Techniques in Computer Vision, pp. 172-187, 1998.
- [Woj19] **Wojnarowski A. E., Leonteva A. B., Tyurin S. V.**, *Photogrammetric technology for remote high-precision 3D monitoring of cracks and deformation joints of buildings and constructions*, The International Archives of Photogrammetry, Remote Sensing and Spatial Information Sciences, Vol. 42, pp. 96-101, 2019.
- [Yam07] **Yamaguchi T., Nakamura S., Saegusa R., Hashimoto S.**, *Image-Based Crack Detection for Real Concrete Surfaces*, IEEJ Transactions on Electrical and Electronic Engineering, Vol. 3, No 1, pp. 128-135, 2007.
- [Yan89] **Yannopoulos P. J.**, *Variation of the concrete concrete crack widths through cover to reinforcement*, Magazine of Concrete Research, Vol. 41, No 147, pp. 63-68, 1989.
- [Zab19] **Zaborac J., Athanasiou A., Salamone S., Bayrak O., Hrynyk T. D.**, *Evaluation of Structural Cracking in Concrete*, Center for Transportation Research at The University of Texas at Austin, Final Report (FHWA/TX-19/0-6919-1), 172 p., Austin, USA, 2019.
- [Zah18] **Zahra T., Dhanasekar M.**, *Serviceability Assessment of Masonry Arch Bridges Using Digital Image Correlation*, Journal of Bridge Engineering, Vol. 24, 2018.
- [Zan10] **Zanuy C., De la Fuente P., Albajar L.**, *Estimation of parameters defining negative tension stiffening*, Engineering Structures, 32(10), 3355-3362, 2010.
- [Zha97] **Zhang J.-P.**, *Strength of Cracked Concrete, Part 2 - Micromechanical Modelling of Shear Failure in Cement Paste and in Concrete*, Technical University of Denmark, Series R, No 17, 139 p., Lyngby, Denmark, 1997.
- [Zha17] **Zhao W., Zhu B.**, *Theoretical model for the bond–slip relationship between ribbed steel bars and confined concrete*, Structural Concrete, Vol. 19, No 2, pp. 548-558, 2017.
- [Zhe99] **Zheng H., Abel A. A.**, *Fatigue Properties of Reinforcing Steel Produced by TEMPCORE Process*, Journal of Materials in Civil Engineering, Vol. 11, No 2, pp. 158-165, USA, 1999.
- [Zhu11] **Zhu Z., German S., Brilakis I.**, *Visual retrieval of concrete crack properties for automated post-earthquake structural safety evaluation*, Automation in Construction, Vol. 20, No 7, pp. 874-883, 2011.

Enrique Corres Sojo

Date of birth: 05/12/1993
 Phone number: +41 76 240 06 88
 Email: e.corres.sojo@gmail.com
 LinkedIn: Enrique Corres



Education

- 2020-2024 **PhD Candidate at the Structural Concrete Laboratory**
 Swiss Federal institute of Technology (EPFL), Lausanne, Switzerland
- 2017-2019 **Double Master's Degree in Civil Engineering**
 Technical University of Madrid (UPM), Madrid, Spain
- 2015-2016 **Double Master's Degree in Civil Engineering**
 École des Ponts ParisTech (ENPC), Paris, France
- 2014-2015 **Exchange program as part of the Bachelor's Degree**
 Swiss Federal institute of Technology (EPFL), Lausanne, Switzerland
- 2011-2014 **Bachelor of Science in Civil Engineering**
 Technical University of Madrid (UPM), Madrid, Spain

Professional experience

- 2020-2024 **PhD research and teaching assistant**
 Swiss Federal institute of Technology (EPFL), Lausanne, Switzerland
- 2019-2020 **Engineer at Sumitomo Mitsui Construction Co. Ltd.**
 Technical and Engineering Service Division, Tokyo, Japan
- 2016-2017 **Internship at Guy Nordenson and Associates**
 Guy Nordenson and Associates, New York, United States
- 2014 **Internship at Ferrovial Agroman**
 Technical Department of Ferrovial Agroman, Madrid, Spain

Awards and scholarships

- 2022 Best paper award in the field of Structural analysis and design in the *fib* PhD Symposium in Rome
- 2017 Scholarship for the Double Degree Students, awarded by UPM
- 2015 Best academic record at graduation, awarded by TYPSA
- 2012 Award for the best students of the first year, awarded by Caja de Ingenieros and UPM

Languages

Spanish (native), English (proficient), French (proficient), Portuguese (basic)

Bibliography